

NUMERICAL SIMULATIONS OF TURBULENT FLOWS

by

Craig T. Johansen

B. Eng (Mechanical)

A thesis submitted to the Faculty of Graduate
Studies and Research in the partial fulfilment
of the requirements for the degree of

Master of Applied Science in Aerospace Engineering

(M.A.Sc.Aerospace)

Ottawa-Carleton Institute for Mechanical
and Aerospace Engineering

Department of Mechanical and Aerospace Engineering

Carleton University

Ottawa, Ontario

Canada

January, 2005

Copyright © 2005

Craig T. Johansen



Library and
Archives Canada

Bibliothèque et
Archives Canada

Published Heritage
Branch

Direction du
Patrimoine de l'édition

395 Wellington Street
Ottawa ON K1A 0N4
Canada

395, rue Wellington
Ottawa ON K1A 0N4
Canada

Your file *Votre référence*

ISBN: 0-494-00744-3

Our file *Notre référence*

ISBN: 0-494-00744-3

NOTICE:

The author has granted a non-exclusive license allowing Library and Archives Canada to reproduce, publish, archive, preserve, conserve, communicate to the public by telecommunication or on the Internet, loan, distribute and sell theses worldwide, for commercial or non-commercial purposes, in microform, paper, electronic and/or any other formats.

The author retains copyright ownership and moral rights in this thesis. Neither the thesis nor substantial extracts from it may be printed or otherwise reproduced without the author's permission.

AVIS:

L'auteur a accordé une licence non exclusive permettant à la Bibliothèque et Archives Canada de reproduire, publier, archiver, sauvegarder, conserver, transmettre au public par télécommunication ou par l'Internet, prêter, distribuer et vendre des thèses partout dans le monde, à des fins commerciales ou autres, sur support microforme, papier, électronique et/ou autres formats.

L'auteur conserve la propriété du droit d'auteur et des droits moraux qui protègent cette thèse. Ni la thèse ni des extraits substantiels de celle-ci ne doivent être imprimés ou autrement reproduits sans son autorisation.

In compliance with the Canadian Privacy Act some supporting forms may have been removed from this thesis.

Conformément à la loi canadienne sur la protection de la vie privée, quelques formulaires secondaires ont été enlevés de cette thèse.

While these forms may be included in the document page count, their removal does not represent any loss of content from the thesis.

Bien que ces formulaires aient inclus dans la pagination, il n'y aura aucun contenu manquant.


Canada

to my family

Abstract

This study involves the evaluation of several turbulence models in Reynolds-averaged Navier Stokes (*RANS*) simulations and large eddy simulations (*LES*) using the commercial *CFD* code, *CFX^{TR}*. The types of flows investigated include confined swirling flow, isotropic decay of homogeneous turbulence, and inclined-jet-in-cross-flow. The turbulence models investigated include the k - ϵ turbulence model, a differential Reynolds-stress turbulence model, and Smagorinsky's sub-grid turbulence model.

LES using Smagorinsky's sub-grid model proved to be superior to *RANS*-based turbulence models in predicting flows characterised by vortical streamline patterns. Sensitivity of the *LES* predictions to the Courant number, to the constant used in Smagorinsky's sub-grid model, and the discretization scheme is highlighted through these benchmarks. In the inclined-jet-in-cross-flow benchmark, the role of large scale turbulence on the wandering of the streamwise vortex is explored through the *LES* computations.

As an example to utilizing *LES* in a practical design exercise, the thesis concludes with a design of a vortex generator, with *LES* used to predict the streamwise decay of the generated vortex.

Acknowledgements

I would like to thank my thesis supervisor, Dr. M.I. Yaras, for his guidance and advice during the course of this work. I extend my thanks to Dr. B. Lee, my co-supervisor, for suggestions and advice on this thesis. The financial support of NSERC is also acknowledged. Finally, I owe a great debt to my family for their unconditional support during my education.

Table of Contents

Abstract	iv
Acknowledgements	v
Table of Contents	vi
List of Figures	xiii
List of Tables	xxi
Nomenclature	xxii
1.0 Introduction	1
2.0 Vortex Dominated Flows	4
2.1 Vorticity	4
2.2 Vortex Dynamics	6
2.3 Vortical Structure	9
2.4 Examples of Vortical Flows	13
2.4.1 Confined Swirling Flow	13
2.4.2 Wingtip Vortices	17
2.4.3 Inclined-Jet-in-Cross-Flow	21
2.4.3.1 Vortical Structures in <i>IJICF</i>	23
2.4.3.2 The Momentum Ratio	27
2.5 Stability of Vortical Flows	29
2.5.1 Two-Dimensional Instability	30

2.5.2 Long-Wave Instability	31
2.5.3 Short-Wave Instability	33
2.6 Turbulence in Vortical Flows	35
2.6.1 Reynolds Number, Stability, and Turbulence Production	36
2.6.2 Vorticity, Vortical Structures, and Diffusion in Turbulence	37
2.6.3 Dissipation and the Energy Cascade	37
2.6.4 Turbulence Measurements in Aircraft Vortices	38
3.0 Modelling of Turbulence	41
3.1 Direct Numerical Simulation.....	41
3.1.1 Computational Grid Requirements	42
3.1.2 Time-Step Requirements	44
3.2 Large Eddy Simulation	46
3.2.1 Overview of Filtering Process	46
3.2.2 Filtering of the Governing Equations of Fluid Flow	50
3.2.3 Sub-grid Turbulence Modelling	52
3.3 Reynolds-Averaged Navier-Stokes Models	58
3.3.1 Reynolds-Averaging of Governing Equations	59
3.3.2 Reynolds-Stress Models	61
3.3.2.1 Algebraic Reynolds-Stress Models	62
3.3.2.2 Differential Reynolds-Stress Models	65
3.3.2.2.1 Diffusion Term	66
3.3.2.2.2 Pressure-Strain Term	68

3.3.2.2.3 Dissipation Term	72
3.3.2.2.4 Methods of Higher Moments	76
3.3.3 Two-Equation Models	77
3.3.3.1 Standard k - ϵ Model	78
3.3.3.2 Other Two-Equation Eddy-Viscosity Models	82
3.3.4 One-Equation Models	84
3.3.5 Zero-Equation Models	85
4.0 Confined Swirling Flow	86
4.1 Description of Test Case	86
4.2 Turbulence Models	88
4.2.1 k - ϵ Turbulence Model	88
4.2.2 <i>SST</i> Reynolds-Stress Turbulence Model	89
4.3 Computational Domain	92
4.4 <i>CFX</i> Algorithm	95
4.5 Boundary Conditions	97
4.6 Initial Conditions	103
4.7 Computational Grid Requirements for k - ϵ Simulations	104
4.8 Computational Grid Requirements for Reynolds-Stress Simulations	107
4.9 Solution Convergence	109
4.10 Simulation Results	110
5.0 Decay of Turbulence	120
5.1 Description of Test Case	120

5.2 Theory of Decay of Homogeneous Isotropic Turbulence	122
5.2.1 Turbulence Length and Time Scales	122
5.2.2 Analytical Equations for the Decay of Homogeneous Turbulence	124
5.3 Comparison of Analytical Results to Experimental Data	126
5.4 <i>LES</i> and Smagorinsky's Turbulence Model	128
5.5 Computational Domain and Discretization	129
5.6 Boundary Conditions	130
5.7 Initial Conditions	131
5.8 Spatial and Temporal Resolution	133
5.8.1 Spatial Resolution	133
5.8.2 Temporal Resolution	136
5.9 Solution Convergence	137
5.10 Simulation Results	140
5.10.1 Effects of Numerical Dissipation	140
5.10.2 Effects of Computational Grid Structure	143
6.0 Inclined-jet-in-cross-Flow	146
6.1 Description of Test Case	146
6.2 Turbulence Models	149
6.2.1 <i>RANS</i> Reynolds-Stress Turbulence Model	149
6.2.2 <i>LES</i> Smagorinsky Turbulence Model	151
6.3 Computational Domain and Discretization	153
6.4 Boundary Conditions	155

6.5 Initial Conditions	162
6.6 Spatial Resolution	163
6.6.1 Spatial Resolution for <i>RANS</i> Simulations	163
6.6.2 Spatial Resolution for <i>LES</i>	169
6.7 Temporal Resolution	170
6.7.1 Temporal Resolution for <i>RANS</i> Simulations	170
6.7.2 Temporal Resolution for <i>LES</i>	171
6.8 Solution Convergence	171
6.8.1 Solution Convergence for <i>RANS</i> Simulations	171
6.8.2 Solution Convergence for <i>LES</i>	172
6.9 Flow Physics	173
6.10 Simulation Results	179
6.10.1 Mean Flow Distribution	180
6.10.2 Vorticity Distribution and Decay	183
6.10.3 Turbulence Distribution	186
7.0 Vortex Generator	193
7.1 Configuration of the Vortex Generator	194
7.1.1 Vortex Generator General Setup	194
7.1.2 Vortex Generator Inflow and Outflow Conditions	195
7.1.3 Choices of Overall Design Configuration, Blade Aspect Ratio and Pitch-to-Chord Ratio	199
7.1.4 Quantitative Functional Analysis	203
7.1.5 Selection of Hub and Tip Radii and Blade Chord Length	204

7.1.6 Blade Outlet Angle Calculations	205
7.1.7 Blade Profile	207
7.2 Simulation of the Vortex-Generator Downstream Flow	209
7.2.1 Computational Domain and Discretization	209
7.2.2 Boundary Conditions	210
7.2.3 Initial Conditions	212
7.2.4 Spatial Resolution	213
7.2.5 Temporal Resolution	215
7.2.6 Solution Convergence	215
7.2.7 Simulation Results	216
8.0 Conclusions and Recommendations	221
References	224
Appendices	244
Appendix A: Vortex Generator Design Specifications	245
Appendix B: 3D Isometric View of Vortex Generator (using BladeGen)	246
Appendix C: Monitor Point Generation Program (Matlab)	247
Appendix D: <i>LES</i> Inclined Jet Data Reduction Program (Matlab)	249
Appendix E: Simulation Fact Sheet	254
Appendix F: Practical Issues in Turbulence Modelling	255
F.1 Numerical Stability	255
F.2 Computational Cost and Solution Accuracy	257
F.3 The Future of <i>LES</i> in Vortical Flow Predictions	260

Appendix G: <i>CFX</i> Tips	262
G.1 Getting Technical Help	262
G.2 Turbulence Intensity at Boundaries for <i>LES</i>	263
G.3 Conservative and Hybrid Values Near Boundaries	264
G.4 Output Control Options	264
G.5 <i>CFX</i> on Linux Workstations	265
Appendix H: Numerical Truncation Error	266

List of Figures

Figure 2.2.1: Schematic of a vortex	6
Figure 2.2.2: Flow field enclosed by curve Z	7
Figure 2.3.1 Free-vortex motion	9
Figure 2.3.2: Forced-vortex motion	11
Figure 2.3.3: Rankine's vortex model	12
Figure 2.4.1.1: Schematic of confined swirling flow	13
Figure 2.4.1.2: Experimental setup of swirl combustor model, reproduced from Ahmed (1998)	15
Figure 2.4.1.3: Evolution of velocity (A) U_z/U_0 (B) U_r/U_0 (C) U_t/U_0 ; reproduced from Ahmed (1998)	15
Figure 2.4.1.4: Evolution of Reynolds-stresses (A) u'^2/U_0^2 ; (B) v'^2/U_0^2 ; (C) w'^2/U_0^2 ; (D) $\overline{u'v'}/U_0^2$; (E) $\overline{u'w'}/U_0^2$; (F) k/U_0^2 ; reproduced from Ahmed (1998)	16
Figure 2.4.2.1: Initial rollup of a wingtip vortex, reproduced from Chow <i>et al.</i> (1997).....	17
Figure 2.4.2.2: Tangential velocity distribution, reproduced from Traub <i>et al.</i> (1998)	19
Figure 2.4.2.3: Tangential velocity distributions, reproduced from Devenport <i>et al.</i> (1996)	20
Figure 2.4.2.4: Toroidal Vortex	21
Figure 2.4.3.1: Development of an <i>IJICF</i>	22
Figure 2.4.3.1.1: Vortical structures produced by <i>JICF</i> , reproduced from New <i>et al.</i> (2003)	24

Figure 2.4.3.1.2: Vortical structures of inclined jet-in-cross-flow, reproduced from Bray and Garry (2000)	25
Figure 2.4.3.1.3: a) Jet-shear-layer vortices and horseshoe vortex, b) Horseshoe vortex at the upstream edge of jet orifice, reproduced from Kelso <i>et al.</i> (1995)	26
Figure 2.5.1.1: Von Kármán vortex street ($Re = 140$), reproduced from Von Dyke (1982)	30
Figure 2.5.2.1: Vortex pair evolution under combined action of long-wave and short-wave instabilities, reproduced from Leweke and Williamson (1998)	32
Figure 2.5.3.1: Short-wave instability ($Re = 2500$), reproduced from Eloy (2000) ..	33
Figure 3.2.1.1: Decomposition of the energy spectrum using a filter in <i>LES</i> , reproduced from Sagaut (2002)	47
Figure 3.2.1.2: Top-hat filter shown in a) physical space normalized by $\bar{\Delta}$, and in b) Fourier space, reproduced from Sagaut (2002)	48
Figure 3.2.1.3: Gaussian filter shown in a) physical space normalized by $\bar{\Delta}$, and in b) Fourier space, reproduced from Sagaut (2002)	48
Figure 3.2.1.4: Sharp cut-off filter shown in a) physical space normalized by $\bar{\Delta}$, and in b) Fourier space, reproduced from Sagaut (2002)	49
Figure 3.2.1.5: Energy spectrum of unfiltered and filtered solutions using Gaussian and sharp cut-off filters, reproduced from Sagaut (2002)	50
Figure 3.2.3.1: Decay of isotropic turbulence: inviscid case, reproduced from Hughes <i>et al.</i> (2001)	57
Figure 3.2.3.2: Decay of isotropic turbulence: viscous case, reproduced from Hughes <i>et al.</i> (2001)	57
Figure 3.3.1: Symbolic decomposition of the energy spectrum using Reynolds-averaged techniques, reproduced from Sagaut (2002)	58
Figure 3.3.2.1.1: Evolution of turbulence kinetic energy, (— explicit <i>ASM</i> , --- <i>SSG</i> , - - - <i>k - ε</i> , ○ <i>LES</i>), reproduced from Gatski and Speziale (1993)	64

Figure 3.3.2.2.2.1: Axial velocity distribution comparisons for $k-\varepsilon$, <i>SSG</i> , <i>IPCM</i> , and experimental data at low swirl, reproduced from Chen and Lin (1999)	70
Figure 3.3.2.2.2.2: Axial velocity distribution comparisons for $k-\varepsilon$, <i>SSG</i> , <i>IPCM</i> , and experimental data at high swirl, reproduced from Chen and Lin (1999)	70
Figure 3.3.2.2.3.1: Sensitivity of centerline axial velocity variation to turbulence models, reproduced from Lin and Lu (1994)	75
Figure 3.3.3.1.1: Radial velocity profiles of radial velocities at 77.5° stream-wise station (\bullet experimental data, — $k-\varepsilon$, - - - <i>RNG k-ε</i> , — <i>RNG k-ε</i> model with C_μ modification), reproduced from Yin <i>et al.</i> (1996)	81
Figure 3.3.3.2.1: The skin friction coefficient along the straight and curved wall, reproduced from Hellsten (1998)	83
Figure 4.1: Geometry of experimental setup	86
Figure 4.3.1: Cylindrical computational domain.....	93
Figure 4.3.2: Wedge-shaped computational domain	94
Figure 4.3.3: Sensitivity of the tangential velocity distribution to the shape of the computational domain ($z/D_j = 14$)	95
Figure 4.5.1: Boundaries for the cylindrical computational domain	97
Figure 4.5.2: Boundaries for the wedge-shaped computational domain	98
Figure 4.5.3: Mean velocity distributions at the inflow boundary ($z/D_j=1$)	99
Figure 4.5.4: Turbulence kinetic energy distribution at the inflow boundary ($z/D_j=1$)	100
Figure 4.7.1: Optimized grid-node distribution in the cross-section plane	105
Figure 4.7.2: Streamwise distribution of grid nodes	106
Figure 4.7.3: Sensitivity of predictions to domain length	106

Figure 4.8.1: Streamwise distribution of grid nodes	107
Figure 4.8.2: Optimized grid-node distribution in the cross-section plane	108
Figure 4.8.3: Sensitivity of the predictions to spatial resolution ($z/D_j = 14$)	109
Figure 4.10.1: Radial distribution of tangential velocity component at $z/D_j = 1$	114
Figure 4.10.2: Radial distribution of tangential velocity component at $z/D_j = 14$	114
Figure 4.10.3: Velocity distribution in the $z-r$ plane near the inflow boundary ($k-\varepsilon$ turbulence model)	115
Figure 4.10.4: Velocity distribution in the $z-r$ plane near the inflow boundary (Reynolds-stress turbulence model)	115
Figure 4.10.5: Radial distributions of tangential velocity component at $z/D_j = 40$..	116
Figure 4.10.6: Radial distributions of axial velocity component at $z/D_j = 40$	116
Figure 4.10.7: Radial distributions of tangential velocity component at $z/D_j = 14$..	117
Figure 4.10.8: Radial distributions of tangential velocity component at $z/D_j = 40$..	117
Figure 4.10.9: Radial distribution of axial velocity component at $z/D_j = 14$	118
Figure 4.10.10: Radial distribution of axial velocity component at $z/D_j = 40$	118
Figure 4.10.11: Predictions compared to Yaras and Grosvenor (2003) - radial distribution of tangential velocity component at $z/D_j = 14$...	119
Figure 4.10.12: Predictions compared to Yaras and Grosvenor (2003) - radial distribution of tangential velocity component at $z/D_j = 40$...	119
Figure 5.1.1: Geometry of experimental setup, reproduced from Comte-Bellot and Corrsin (1971)	120
Figure 5.2.1.1: Energy cascade, reproduced from Gatski et al. (1996)	123
Figure 5.2.2.1: Time dependent three dimensional turbulence energy spectrum, reproduced from Skrbek and Stalp (1999)	125
Figure 5.3.1: Measured and predicted rates of turbulence decay	127

Figure 5.5.1: Computational domain	129
Figure 5.6.1: Boundary conditions	131
Figure 5.7.1: Simulation initialization process	132
Figure 5.7.2: Sensitivity of decay rate to initialization ($\nu = 1.55 \times 10^{-5} \text{ m}^2/\text{s}$, $C_s = 0.18$, $\nu = 0.009$)	133
Figure 5.8.1.1: Decomposition of turbulence kinetic energy ($\nu = 1.55 \times 10^{-5} \text{ m}^2/\text{s}$, $C_s = 0.18$, $\nu = 0.009$), reproduced from Misra and Pullin (1997)	135
Figure 5.8.1.2: Computational grid for isotropic decay of turbulence	136
Figure 5.9.1: Solution sensitivity to time-step convergence criteria ($\nu = 1.55 \times 10^{-5} \text{ m}^2/\text{s}$, $C_s = 0.18$, $\nu = 0.009$)	138
Figure 5.9.2: Typical residual plot for <i>LES</i> of turbulence decay ($\nu = 1.55 \times 10^{-5} \text{ m}^2/\text{s}$, $C_s = 0.18$, $\nu = 0.009$, 2 iterations/time-step)	139
Figure 5.10.1.1: The effects of Courant number on turbulence decay ($C_s = 0$)	141
Figure 5.10.1.2: The effects of sub-grid model on the rate of turbulence decay ($\nu = 0.05$, $\nu = 1.55 \times 10^{-5}$)	142
Figure 5.10.2.1: Spatial resolution for anisotropic grid (expansion factor = 3)	144
Figure 5.10.2.2: The effects of stretch ratio on the decay of turbulence ($\nu = 1.55 \times 10^{-5} \text{ m}^2/\text{s}$, $C_s = 0.18$, $\nu = 0.009$)	145
Figure 6.1.1: Geometry of experimental test section	147
Figure 6.3.1: Computational domain for inclined jet-in-cross-flow	154
Figure 6.4.1: Boundary conditions for inclined-jet-in-cross-flow using <i>RANS</i>	155
Figure 6.4.2: Mean velocity distributions at the inflow boundary	156
Figure 6.4.3: Turbulence intensity distribution at the cross-flow inflow boundary ..	157

Figure 6.4.4: Mean velocity distributions at the jet-inflow boundary ($y/D_j = 0.044$).	160
Figure 6.4.5: Jet-inflow boundary	161
Figure 6.4.6: Turbulence intensity distribution at the jet-inflow boundary ($y/D_j = 0.044$)	161
Figure 6.6.1.1: Computational grid for inclined jet-in-cross-flow, reproduced from Grosvenor (2000)	164
Figure 6.6.1.2: Optimized grid-node distribution in $y-z$ plane at $x/D_j = 0$	166
Figure 6.6.1.3: Optimized grid-node distribution in $x-y$ plane at $z/D_j = 0$	166
Figure 6.6.1.4: Optimized grid-node distribution in $x-z$ plane at $y/D_j = 0.5$	167
Figure 6.6.1.5: Predicted streamwise velocity; sensitivity to grid resolution	168
Figure 6.6.1.6: Predicted tangential velocity; sensitivity to grid resolution	168
Figure 6.8.2.1: Location of monitor points	173
Figure 6.9.1: Flow topology of inclined jet-in-cross-flow, reproduced from Barberopoulos and Garry (1998)	174
Figure 6.9.2: Vortical structures of inclined jet-in-cross-flow, reproduced from Bray and Garry (2000)	175
Figure 6.9.3: Formation of horseshoe vortex upstream of jet discharge.....	176
Figure 6.9.4: Streamlines around lower (a) and upper (b) side of jet inflow	177
Figure 6.9.5: x -component vorticity distribution predicted using <i>LES</i>	179
Figure 6.10.1.1: Velocity field of the vortex produced by the inclined jet-in-cross-flow interaction at $x/D_j = 7.5$ (a) experimental data of Yaras (2004), (b) <i>LES</i> , (c) <i>RANS</i>	181
Figure 6.10.1.2: Velocity field of the vortex produced by the inclined jet-in-cross-flow interaction at $x/D_j = 13.0$ (a) experimental data of Yaras (2004), (b) <i>LES</i> , (c) <i>RANS</i>	182
Figure 6.10.1.3: Velocity distributions through the center of the vortex	183

Figure 6.10.2.1: x -component vorticity distribution from (a) experimental data of (a) Yaras (2004) and (b) <i>LES</i>	185
Figure 6.10.2.2: Streamwise decay of peak vorticity and spanwise movement of vortex center	186
Figure 6.10.3.1: Movement of a vortex produced by an inclined jet-in-cross-flow ($x/D_j = 4.5$)	188
Figure 6.10.3.2: Turbulence distributions through the center of the vortex	192
Figure 7.1.1.1: Vortex generator general setup	195
Figure 7.1.2.1: Tangential velocity distribution for Q and K vortices	198
Figure 7.1.2.2: Flow angularity in a Q -vortex	199
Figure 7.1.3.1: Cascade notation for vortex generator, reproduced from Cohen <i>et al.</i> (1972)	200
Figure 7.1.3.2: Profile loss coefficient variation with pitch/chord ratio, reproduced from Cohen <i>et al.</i> (1972)	201
Figure 7.1.3.3: Optimum pitch/chord ratio as a function of efflux angle, reproduced from Cohen <i>et al.</i> (1972)	202
Figure 7.1.3.4: Vortex-generator design options	203
Figure 7.1.5.1: Blade dimensions	205
Figure 7.1.6.1: Outlet flow and blade angles	207
Figure 7.1.7.1: <i>T6</i> Airfoil selection, reproduced from Cohen <i>et al.</i> (1972)	208
Figure 7.1.7.2: Blade profile of vortex generator, produced using BladeGen	208
Figure 7.2.1.1: Computational domain of vortex generator simulation	210
Figure 7.2.2.1: Boundary conditions for vortex generator simulation	211
Figure 7.2.4.1: Radial grid-node distribution for vortex generator downstream flow simulation	214

Figure 7.2.4.2: Axial grid-node distribution for vortex generator downstream flow simulation	215
Figure 7.2.7.1: Streamwise location of data-analysis planes	217
Figure 7.2.7.2: Decay of tangential velocity component	218
Figure 7.2.7.3: Decay of vorticity	219
Figure B.1: 3D isometric view of vortex generator	247
Figure H.1: Effects of dissipation and dispersion. (a) exact solution, (b) dissipation error, (c) dispersion error, reproduced Tannehill (1997)	267

List of Tables

Table 3.1.1.1: <i>DNS</i> node count requirements	44
Table 3.1.2.1: <i>DNS</i> time-step requirements	45
Table 5.1.1: Experimental data of Comte-Bellot and Corrsin (1971)	121
Table 7.1.4.1: Quantitative functional analysis of vortex design options	204
Table A.1: Vortex generator design specifications	246
Table E.1: Simulation fact sheet	255
Table F.1.1 Simulation complexity	256
Table F.2.1: Computational cost and solution accuracy	259

Abbreviations

<i>AR</i>	aspect ratio
<i>ASM</i>	algebraic-stress model
<i>BSL</i>	two-equation closure model of Menter (1994)
<i>CFD</i>	computational fluid dynamics
<i>CVP</i>	counter-rotating vortex
<i>DNS</i>	direct numerical simulation
<i>FRV</i>	free vortex
<i>IJICF</i>	inclined jet in cross-flow
<i>IPCM</i>	Reynolds-stress closure model of Launder <i>et al.</i> (1975) – Isotropization of Production
<i>JICF</i>	jet in cross-flow
<i>LDA</i>	laser-doppler anemometry
<i>LES</i>	large eddy simulation
<i>LPS</i>	modified dissipation equation of Launder <i>et al.</i> (1977)
<i>LRR-IP</i>	Reynolds-stress closure model of Launder <i>et al.</i> (1975) – Isotropization of Production
<i>LRR-IPϵ</i>	Reynolds-stress closure model of Lin and Lu (1994) and Launder <i>et al.</i> (1977)
<i>LRR-QI</i>	Reynolds-stress closure model of Launder <i>et al.</i> (1975) – Quasi Isotropic
<i>NACA</i>	National Advisory Committee for Aeronautics
<i>QFD</i>	quantitative functional analysis
<i>RANS</i>	Reynolds-averaged-Navier-Stokes
<i>RDT</i>	rapid distortion theory
<i>RNG</i>	renormalization group

<i>RCSST</i>	modified two equation shear transport model of Hellsten (1998)
<i>FOV</i>	forced vortex
<i>SSG</i>	Reynolds-stress closure model of Speziale <i>et al.</i> (1991)
<i>SST</i>	two-equation shear stress-transport model
<i>VR</i>	velocity ratio
<i>V/STOL</i>	vertical/ short take-off and landing

English Symbols

A	circulation variable
A_i	modified dissipation extra strain term
A_{ij}	Reynolds-stress slow pressure/rate-of-strain term (m^2/s^3)
b_{ij}	Reynolds-stress anisotropy tensor
c_f	wall-skin-friction coefficient
c_w	chord length
C	log-layer constant (=5)
C_1	turbulence closure coefficient (=3.4)
C_1^*	turbulence closure coefficient (=1.8)
C_2	turbulence closure coefficient (=4.2)
C_3	turbulence closure coefficient (=0.8)
C_3^*	turbulence closure coefficient (=1.3)
C_4	turbulence closure coefficient (=1.25)
C_5	turbulence closure coefficient (=0.4)
C_{ij}	Cross-stress tensor (m^2/s^2)
C_k	Kolmogorov constant
C_s	Smagorinsky constant

C_{ijk}	turbulent transport tensor (m^2/s^2)
C_s^*	triple velocity correlation constant of Hanjalic and Launder (1972)
$C_{\varepsilon 1}^S$	modified dissipation-equation constant of Shih <i>et al.</i> (1995)
$C_{\varepsilon 2}^S$	modified dissipation-equation constant of Shih <i>et al.</i> (1995)
$C_{\varepsilon 1}$	turbulence closure coefficient (=1.44)
$C_{\varepsilon 2}$	turbulence closure coefficient ($k - \varepsilon$, =1.92; Reynolds-stress,=1.83)
d_{ij}	Reynolds-stress turbulence diffusion term (m^2/s^3)
D	enclosure diameter (m)
D_j	jet diameter (m)
f	external force vector
f	mathematical variable (Section 3.1)
\bar{f}	filtered variable
f'	fluctuating/sub-grid variable
E	Energy per unit mass (m^2/s^2)
F	Reynolds-averaged variable
F_{TR}	temporally-averaged variable
F_{SR}	spatially-averaged variable
F_{ER}	ensemble-averaged variable
g	acceleration due to gravity (=9.81 m/s^2)
G	kernel filter
H	step height (m)
k	turbulence kinetic energy (m^2/s^2)
k_1	vortex-generator tangential-velocity constant (Eqn. 7.1.2.1)
k_2	vortex-generator tangential-velocity constant (Eqn. 7.1.2.3)
k_3	vortex-generator tangential-velocity constant (Eqn. 7.1.2.7)
K_1	equation constant for free vortex (Eqn. 2.3.1)

K_2	equation constant for free vortex (Eqn. 2.3.2)
K_3	equation constant for forced vortex (Eqn. 2.3.6)
K_4	equation constant for forced vortex (Eqn. 2.3.7)
l_{mix}	turbulence mixing length (m)
L	largest turbulence length scale (m)
L_{char}	characteristic turbulence length scale (m)
L_{ij}	Leonard-stress tensor (m^2/s^2)
L_{char}	characteristic length scale
L_{scale}	simulation length scale (m)
L_{vol}	volume length scale (m)
L_{ext}	computational domain length scale (m)
L	computational domain extent (m)
M_{ij}	Reynolds-stress rapid rate-of-strain term (m^2/s^2)
N_R	number of measurements in reference to Reynolds ensemble averaging
N_d	Number of nodes in computational domain
N_s	Number of time steps
p	pressure (Pa)
p'	fluctuating pressure component (Pa)
P	temporally averaged static pressure (Pa)
\overline{p}	filtered static pressure (Pa)
P_{ij}	Reynolds-stress turbulence production term (m^2/s^3)
P_k	Reynolds-stress turbulence production tensor (m^2/s^3)
\overline{q}^2	resolved kinetic energy
r_c	vortex core radius (m)
r_m	jet to cross-flow momentum ratio

R	vortex radius (m)
R_{ij}	<i>SGS</i> Reynolds-stress tensor (m^2/s^2)
Re	Reynolds number
S	swirl number
S_{ij}	mean rate of strain tensor (1/s)
\bar{S}_{ij}	resolved rate of strain tensor (1/s)
T	Life cycle time of largest turbulent structure (s)
T_{ij}	Reynolds-stress third-order-diffusion term (m^2/s^3)
T_R	Reynolds averaging time (s)
u	velocity vector (m/s)
u'	fluctuating/sub-grid velocity component (m/s)
u^+	dimensionless velocity (u/u_τ) near the wall
u_τ	friction velocity (m/s)
u_s	near-wall velocity (m/s)
\bar{u}	filtered velocity vector (m/s)
U	temporally averaged velocity vector (m/s)
U_b	bulk exit velocity (m/s)
U_{bc}	velocity scale based on area averaged velocities on boundaries (m/s)
U_{node}	velocity scale based on arithmetic mean of nodal velocities (m/s)
U_{char}	characteristic velocity scale (m/s)
U_0	upstream velocity (m/s)
U_∞	free-stream velocity (m/s)
$(U_t)_{FOV}$	tangential velocity in solid-body-rotation section of a vortex (m/s)
$(U_t)_{FRV}$	tangential velocity in free-vortex section of a vortex (m/s)
$(U_z)_j$	velocity of jet in the z direction (m/s)

$(\bar{U}_z)_a$	area-averaged axial velocity at inflow boundary (m/s)
\bar{V}_j	spatially-averaged jet velocity (m/s)
\bar{V}_{cf}	spatially-averaged cross-flow velocity (m/s)
V_R	Reynolds averaging volume (m ³)
W_{ij}	angular velocity tensor (1/s)
y_p	distance from the wall to the first node (m)
y^+	dimensionless distance from the wall to the first node
Y_p	profile loss coefficient for turbine blade
Z	closed curve in space

Greek Symbols

α_1	inlet flow angle (deg)
α_2	outlet flow angle (deg)
α_ω	modified dissipation equation constant (Eqn. 3.3.3.2.1)
β_1	inlet metal angle (deg)
β_2	outlet metal angle (deg)
β_ω	modified dissipation equation constant (Eqn. 3.3.3.2.1)
δ	toe-in-angle (deg)
δ_{ij}	Kronecker's delta function
δ_{TOF}	toe-in-angle of wing (deg)
Δ	grid size (m)
$\bar{\Delta}$	filter width (m)
Δt	simulation time scale (s)

Δt_u	minimum time scale calculated from average nodal and boundary velocity values (s)
Δt_g	buoyancy time scale (s)
Δt_{rot}	rotational time scale (s)
ε	dissipation rate of turbulence kinetic energy (m^2/s^3)
$\bar{\varepsilon}$	resolved dissipation rate of turbulence kinetic energy (m^2/s^3)
ζ	vorticity vector (1/s)
η	Kolmogorov length scale (m)
θ	blade camber angle (deg)
θ_j	jet skew angle for inclined-jet-in-cross flow (deg)
κ	von- Kármán's constant (=0.41)
κ_c	cut-off wave number
μ	dynamic laminar viscosity (Ns/m^2)
μ_T	dynamic turbulent viscosity (Ns/m^2)
ν	kinematic laminar viscosity (m^2/s)
ν_a	artificial viscosity (m^2/s)
ν_T	kinematic turbulent viscosity (m^2/s)
ν'_T	modified kinematic turbulent viscosity (m^2/s)
ξ	$\frac{1}{2}$ of the spatial filter width, $\bar{\Delta}$ (m)
Π_{ij}	pressure-strain correlation tensor (m^2/s^3)
ρ	fluid density (kg/m^3)
$\overline{\rho u'_i u'_j}$	Reynolds stress tensor (m^2/s^2)
σ_k	turbulence closure coefficient (Eqn. 3.3.3.4)
σ_ε	turbulence closure coefficient (Eqn. 3.3.3.1.2)
σ_ω	modified dissipation equation constant (Eqn. 3.3.3.2.1)

τ	shear stress (N/m ²)
τ_w	wall shear stress (N/m ²)
$\overline{\tau_c}$	cut-off time scale (s)
τ_{ij}	sub-grid-stress tensor (m ² /s ²)
ν	Courant number
ϕ_{ij}	Reynolds-stress pressure-strain term (m ² /s ³)
$\phi_{ij,1}$	Rotta's linear 'return to isotropy' pressure-strain term (m ² /s ³)
$\phi_{ij,2}$	'isotropization of production' pressure-strain term (m ² /s ³)
$\phi_{ij,3}$	wall reflections pressure-strain term (m ² /s ³)
Φ_j	jet pitch angle for inclined-jet-in-cross flow (deg)
$\boldsymbol{\Omega}$	angular velocity vector (rad)
∇	del operator
Γ	circulation (1/s)

Subscripts

d	computational domain
i, j, k	index counts in the three grid directions; x, y, and z components of a quantity; also used in the Einstein notation for summation
x, y, z	Cartesian spatial co-ordinates (m)
r, t, z	cylindrical spatial co-ordinates (m)

Chapter 1

INTRODUCTION

Solutions to the Navier-Stokes equations, which govern fluid flow in a continuum, can be obtained through closed form (analytical) or numerical means. Due to the non-linearity of the Navier-Stokes equations, the presence of turbulence at high Reynolds-numbers often negates the closed form option. Three common approaches for numerical computation include direct numerical simulation (*DNS*), large eddy simulation (*LES*), and Reynolds-averaged-Navier-Stokes (*RANS*) simulation. Since *DNS* computes the entire turbulence spectrum directly, it is unrivalled in accuracy and level of description it provides (Pope, 2000). However, since the computational requirements are proportional to the flow Reynolds-number, the type of flows that can be computed is severely restricted. At the other side of the spectrum, *RANS* simulations integrate the Navier-Stokes equations over long time durations, resulting in the Reynolds-averaged-Navier-Stokes equations. Due to the nonlinearity of the Navier-Stokes equations, the averaging process produces additional terms, known as Reynolds-stresses, which represent statistical effects of turbulence on the time-mean flow field. Although the *RANS* approach substantially reduces the computational load, quantifying the Reynolds-stresses with consistent accuracy continues to be a challenge. Since the effects of turbulence on the mean flow field are similar to effects of molecular viscosity, Bousinessq (1877) proposed to scale the Reynolds-stresses to the mean-strain-rate through a scaling factor referred to as the eddy-viscosity. Various methods have been proposed to

quantify the eddy-viscosity, ranging from simple algebraic expressions to partial differential equations. Certain weaknesses of eddy-viscosity-based Reynolds-stress models, such as the assumption of isotropic turbulence, inability of representing stress relaxation, and difficulties in accounting for the effects of streamline curvature on turbulence, led to the development of full Reynolds-stress models, where each component of the Reynolds-stress tensor is modeled by a separate partial differential equation. While these models are potentially more accurate than eddy-viscosity-based models, significantly larger computational overhead is needed for their operation. In addition, the generality of Reynolds-stress models are limited by extensive calibration of empirical constants appearing in the Reynolds-stress transport equations and approximations built into the accompanying transport equation for the dissipation rate of turbulence (Gatski *et al.*, 1993).

As a compromise, large eddy simulation (*LES*) alleviates the severe Reynolds-number restriction associated with *DNS* by filtering the Navier-Stokes equations (Leonard, 1974). Large scale eddies are computed directly, and smaller eddies are modeled as sub-grid stresses, which are similar to Reynolds-stresses modeled in *RANS* simulations. It can be argued that modeling sub-grid stresses are more straightforward since turbulence at smaller scales is closer to being isotropic, and is localized, in that it is dominated by production and dissipation (i.e. negligible convection and diffusion). Additionally, since only a portion of the turbulence is modeled as sub-grid stresses, the impact of any shortcomings of the turbulence model on the predicted mean-flow field is reduced. While *LES* may offer such advantages in turbulence closure over the *RANS*

approach, the requirement of directly computing large-scale turbulence activity in *LES* introduces considerable computational overhead. It is only with the most recent advances in computing power that *LES* is beginning to be considered for use in industrial design activities where fast turn over is critical.

It is necessary for any computational algorithm using *RANS*- or *LES*-based turbulence models to be extensively tested against carefully-measured flows (postdiction) before being used in the prediction of similar flow fields. The work presented in this thesis caters to this objective by evaluating a number of *RANS* turbulence closures and an *LES* sub-grid model in the context of a series of flows. Majority of the chosen benchmark flows involve vortical streamline patterns and proximity to solid walls, for these features are considered to be particularly challenging in turbulence modeling. Additionally, since the commercial computational-fluid-dynamics software, *ANSYS-CFX*, is used in the present study, unknown features of the numerical algorithm, which may affect the accuracy of the integration of the governing differential equations, need to be investigated and evaluated. Extensive parametric studies are therefore performed for each test case of this study to identify and eliminate any inaccuracies in the solution caused by factors other than those associated with turbulence closure.

Chapter 2

VORTEX DOMINATED FLOWS

In this chapter, literature is surveyed on the dominant mechanisms involved in the development and decay of vortex-dominated flows. The chapter begins with a discussion of vorticity transport and its role in the laws governing vortex dynamics. This follows with a review of vortex-flow applications, including confined swirling flows, wingtip vortices, and vortices generated by inclined jets in cross-flow. Finally, the effects of turbulence and instability mechanisms on vortex decay are reviewed.

2.1 Vorticity

One of the determining characteristics that distinguish solids from fluids is how they respond to stresses. A solid responds to an applied load by deforming internally or undergoing strain. Due to Hooke's law of elastic solids, this displacement results in the generation of internal stresses that balance the applied load. Fluids do not respond in the same manner in that they continue to deform as long as an applied load exists. The rate of deformation is important when analyzing fluid motion. Motion of fluid particles can be classified into three groups: translation, solid-body rotation, and deformation. Local particle velocity is the translational rate; extension and shear are types of deformation. The rates of deformation and rotation are key components of vorticity.

The relative velocity of two fluid particles can be represented by a combination of

pure straining motion and rigid body motion. In rigid-body rotation, elements rotate with an angular velocity $\boldsymbol{\Omega}$:

$$\boldsymbol{\Omega} = \frac{1}{2} \boldsymbol{\zeta} \quad (2.1.1)$$

where $\boldsymbol{\zeta}$ is the vorticity vector. Vorticity is a measure of curl or rotation that exists in a flow at a given point. Mathematically, vorticity, $\boldsymbol{\zeta}(x,t)$, is defined as the curl of the velocity vector, $\boldsymbol{U}(x,t)$:

$$\boldsymbol{\zeta} = \nabla \times \boldsymbol{U} \quad (2.1.2)$$

Organized vorticity can be observed by placing small objects in the flow field. The flow is considered to have vorticity if the object rotates when placed in the flow field. Regions in which there is no fluid rotation, $\boldsymbol{\Omega} = 0$, the fluid is irrotational.

Understanding mechanisms of vorticity production, dissipation, convection and diffusion are often beneficial in fluid-flow analysis. The Navier-Stokes equations can be represented in terms of vorticity to further understand these mechanisms. The general vorticity transport equation is expressed as:

$$\frac{D\boldsymbol{\zeta}}{Dt} = \underbrace{\frac{\partial \boldsymbol{\zeta}}{\partial t}}_{\text{Time Derivative}} + \underbrace{(\boldsymbol{U} \cdot \nabla) \boldsymbol{\zeta}}_{\text{Convective Term}} = \underbrace{\nabla \frac{1}{\rho} \times \nabla p}_{\text{Pressure-Density Term}} + \underbrace{\nabla \times \boldsymbol{f}}_{\text{External-Force Term}} + \underbrace{\nu \nabla^2 \boldsymbol{\zeta}}_{\text{Viscous Term}} \quad (2.1.3)$$

where ρ , p , \boldsymbol{f} , ν are the density, pressure, conservative force, and kinematic viscosity, respectively. The convection term in Eqn. 2.1.3 is responsible for the transfer of vorticity from one part of a fluid system to another and includes two processes: stretching and tilting of vortex lines. The pressure-density term is zero if surfaces of constant pressure are parallel to surfaces of constant density and is also zero if the flow field is of constant

density or pressure. A flow is termed barotropic when surfaces of constant pressure are parallel to surfaces of constant density. The external force term is zero for conservative forces, which are path-independent. Some electromagnetic and magnetic forces are non-conservative and are able to produce and modify vorticity. The viscous term is responsible for the diffusion of vorticity.

2.2 Vortex Dynamics

A vortex is defined as a mass of fluid whose elements are rotating about a common axis.

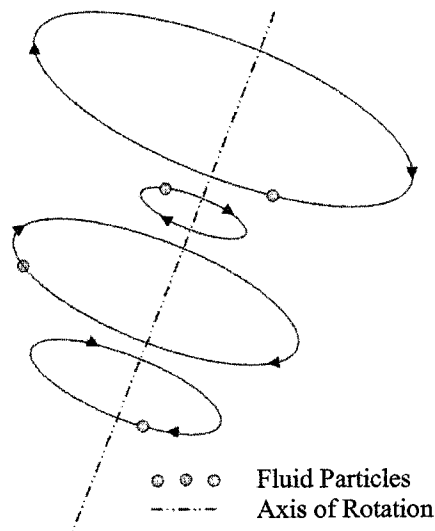


Figure 2.2.1: Schematic of a vortex

The terms vortex and vortices are to be distinguished from vorticity, with the latter being the rotation of infinitesimal fluid elements. Vorticity can exist without vortex motion.

The boundary layer is an example of a flow in which there is no vortex motion although the velocity distribution confirms the presence of vorticity.

A vortex filament is a vortex tube of infinitesimal cross section. Vortex tubes are a collection of vortex lines which follows that the flux of vorticity through these tubes is constant. A scalar function describing the collective strength of the vorticity field contained by a closed curve is called circulation:

$$\Gamma = \int_Z \mathbf{U} \cdot d\mathbf{l} \quad (2.2.1)$$

where Z and $d\mathbf{l}$ represent a closed curve and an infinitesimal length along that curve, respectively.

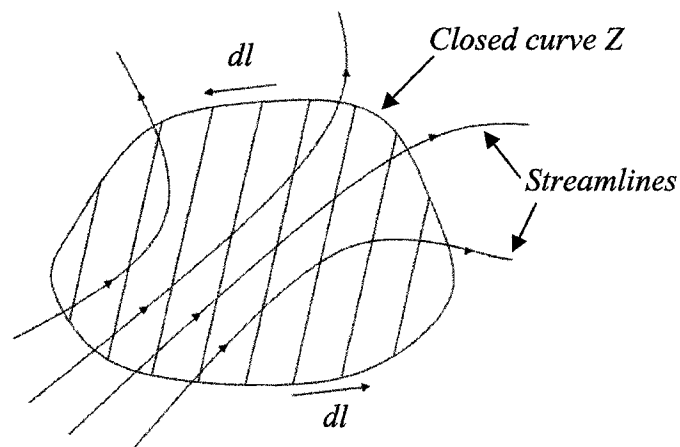


Figure 2.2.2: Flow field enclosed by curve Z

Another parameter to assess the strength of a vortex tube is the swirl number. The swirl number is defined as:

$$S = \frac{\int_0^{\frac{D}{2}} U_z U_t r^2 dr}{\frac{D}{2} \int_0^{\frac{D}{2}} U_z^2 r dr} \quad (2.2.2)$$

where U_z is the axial velocity component, U_t is the tangential velocity component, and D is the vortex-tube diameter. Typically, high swirl numbers are associated with strong and large recirculation zones. Related issues regarding vortex stability are discussed in Section 2.5.

Three theorems explaining the behaviour of vortex motion were proposed by Helmholtz assuming an inviscid, barotropic fluid under the action of conservative external body forces:

1. Fluid particles originally free of vorticity remain free of vorticity.
2. Although fluid particles may be translated, they belong to a unique vortex line at all instances in time.
3. The strength of a vortex filament is constant along its entire length and does not vary with time during the motion of the fluid.

As explained by Saffman (1992), the solenoidal structure of a vorticity field and Theorem 3 requires that vortex tubes or lines go to infinity or end on solid boundaries. The toroidal vortex model presented in Section 2.4.2 is an example of a vortex tube which goes to infinity by ending in a loop.

The types of vortical flows investigated in this thesis often deviate from

Helmholtz's laws since diffusion of vorticity plays a significant role in determining vortex dynamics.

2.3 Vortical Structure

Understanding vortex structure is essential when trying to control or predict vortical flows. Due to variation of initial and boundary conditions, the types of vortex systems are virtually limitless. Therefore, the velocity, pressure, and vorticity distributions of only free-vortex and forced-vortex motion will be presented herein. Free-vortex motion in a barotropic environment exhibits a flow distribution shown in Figure 2.3.1.

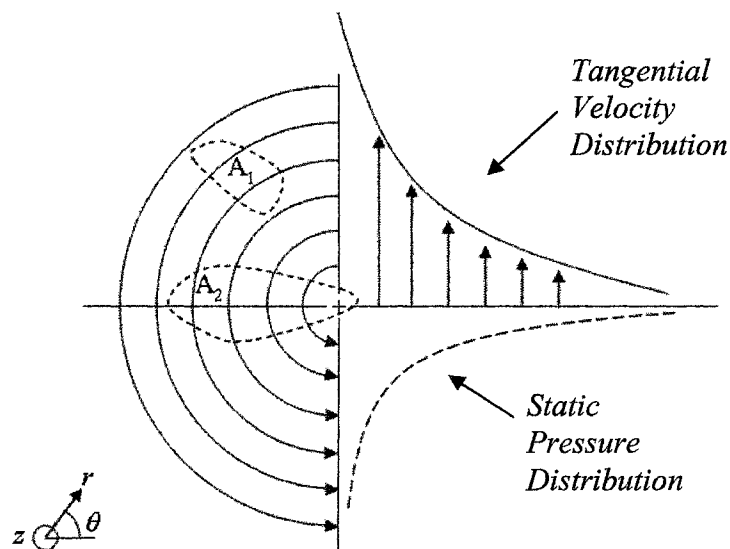


Figure 2.3.1: Free-vortex motion

Corresponding to the flow field shown in Figure 2.3.1, the tangential velocity $[(U_t)_{FRV}]$

static pressure [P_{FRV}] and vorticity [ζ_{FRV}] distributions are defined as:

$$(U_t)_{FRV} = \frac{K_1}{r} \quad (2.3.1)$$

$$P_{FRV} = K_2 - \frac{\rho K_1^2}{2r^2} \quad (2.3.2)$$

$$\zeta_{FRV} = 0 \quad (2.3.3)$$

where K_1 and K_2 are arbitrary constants, and FRV denotes free-vortex. The equations for circulation of the outlined regions (A_1 & A_2) in Figure 2.3.1 are:

$$\Gamma_1 = 0 \quad (2.3.4)$$

$$\Gamma_2 = 2\pi K_1 \quad (2.3.5)$$

The velocity distribution experiences a singularity at $r = 0$, and the circulation of the region enclosing this point is non-zero (Eqn. 2.3.5). This type of vortical motion is completely governed by the laws of Helmholtz, as fluid particles originally free from vorticity remain free of vorticity. Vortex intensification by stretching does not apply to this idealized inviscid vortex. This is due to the fact that vorticity is concentrated on a line located at the center of the vortex and the distribution of vorticity is not affected by convection. In comparison, if a vortex tube undergoes deformation and undergoes a change in cross-sectional area, the vorticity will increase or decrease accordingly. This is due to the conservation of angular momentum of the vortex filament. Another type of vortex motion that is common to many vortex models is forced-vortex motion shown in Figure 2.3.2.

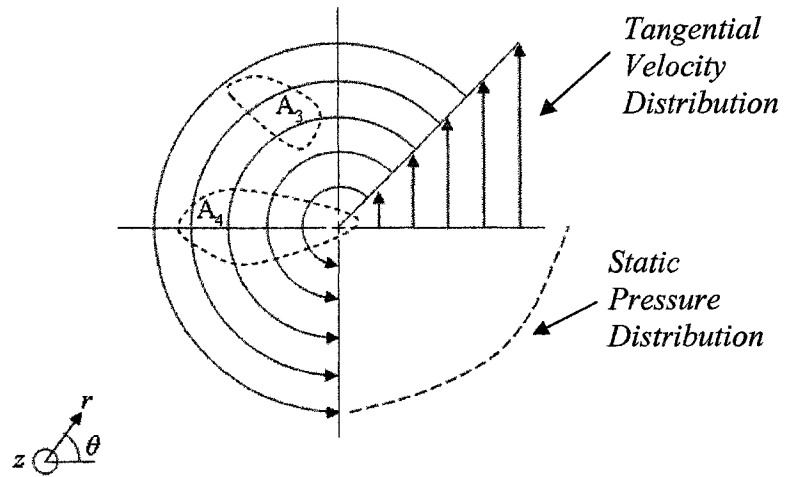


Figure 2.3.2: Forced-vortex motion

In Figure 2.3.2, the tangential velocity $[(U_t)_{FOV}]$ pressure $[P_{FOV}]$ and vorticity $[\zeta_{FOV}]$ distributions are defined as:

$$(U_t)_{FOV} = K_3 r \quad (2.3.6)$$

$$P_{FOV} = K_4 + \frac{\rho K_3^2 r^2}{2} \quad (2.3.7)$$

$$\zeta_{FOV} = 2K_3 \quad (2.3.8)$$

where K_3 and K_4 are arbitrary constants and FOV denotes forced-vortex-rotation. The equations for circulation of the outlined regions (A_3 & A_4) in Figure 2.3.2 are:

$$\Gamma_3 = \int_{A_3} \zeta_{FOV} ds \quad (2.3.9)$$

$$\Gamma_4 = \int_{A_4} \zeta_{FOV} ds \quad (2.3.10)$$

Since this type of vortex motion is considered to be rotational, the vorticity distribution and circulation of region A_4 is non-zero. Therefore, in contrast to free-vortex motion,

vortex intensification by stretching does apply to this type of vortex motion as vorticity is not concentrated at a single point at the vortex center.

A simple vortex model which represents many real-life vortex systems is the Rankine vortex model. Rankine's vortex is very typical of a wingtip vortex, which will be discussed in Section 2.4.2. This type of vortex has a forced type rotation in the core and a free type rotation outside of the core. Essentially, this vortex is a combination of the motions shown in Figures 2.3.1-2. Figure 2.3.3 illustrates Rankine's vortex model.

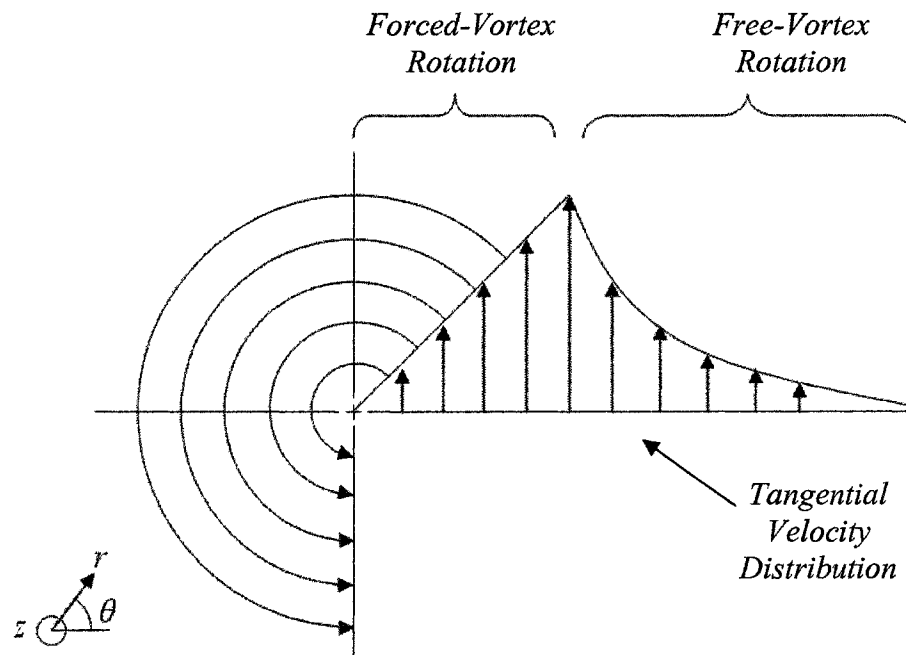


Figure 2.3.3: Rankine's vortex model

Most isolated vortices have a similar structure to the Rankine-vortex shown in Figure 2.3.3. Three dimensional effects along with complex geometrical environments lead to deviations from the distributions of velocity, pressure, and vorticity corresponding

to the Rankine-vortex model.

2.4 Examples of Vortical Flows

2.4.1 Confined Swirling Flow

Confined swirling flows have many practical engineering applications such as in the combustion processes of gas turbine engines, industrial furnaces, and diesel engines. In these combustion systems, swirl is a major factor in determining the combustion efficiency and affects flame stabilization and mixing. Figure 2.4.1.1 shows a schematic of swirling flow, or a vortex, enclosed by a solid surface.

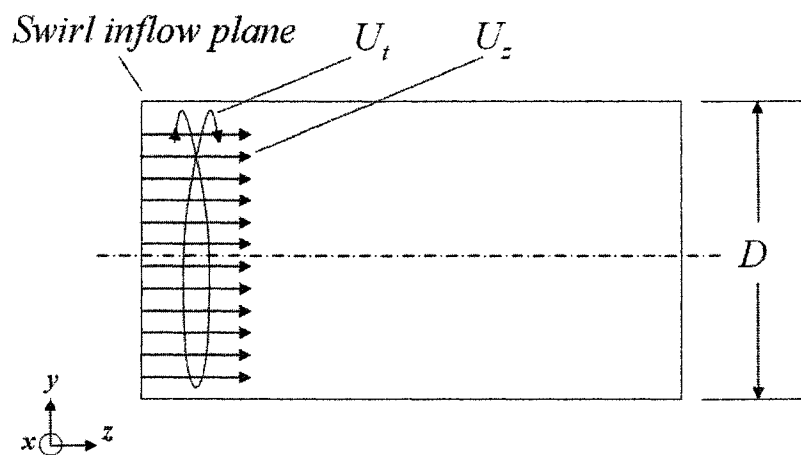


Figure 2.4.1.1: Schematic of confined swirling flow

In this figure, U_t , U_z , and D are the tangential component of velocity, axial component of velocity, and diameter of the enclosure, respectively. The solid boundary provides a no-

slip condition, which affects the axial and cross-stream velocity, and turbulence distributions. The shear stress on this surface applies a torque on the flow, thereby reducing vortex strength (angular momentum) as the vortex develops in the streamwise direction. Due to the reduction of tangential velocity, a rise in vortex core pressure results. The resultant adverse pressure gradient can lead to flow reversal and vortex breakdown (Gupta *et al.*, 1984).

Figures 2.4.1.3 and 2.4.1.4 show the mean-velocity and turbulence properties of an isothermal swirling flow measured by Ahmed (1998) for a Reynolds number of 1.5×10^5 based on the outer diameter of the swirl generator. The fluctuating components of velocity, u' , v' , w' are measured in the axial, radial, and tangential planes, respectively. The data is normalized by the upstream velocity, $U_0 = 16$ m/s and the test section radius is normalized by the step height, $H = 25.4$ mm (Figure 2.4.1.2). The step height is the thickness of the swirl-generator housing. The recirculation zone due to flow reversal is detected from the negative radial and axial velocities. For all three components of normal Reynolds-stresses, the maximums were located within the inner and outer shear-layers. This is expected as the shear layer is the largest source of turbulence production in this vortex.

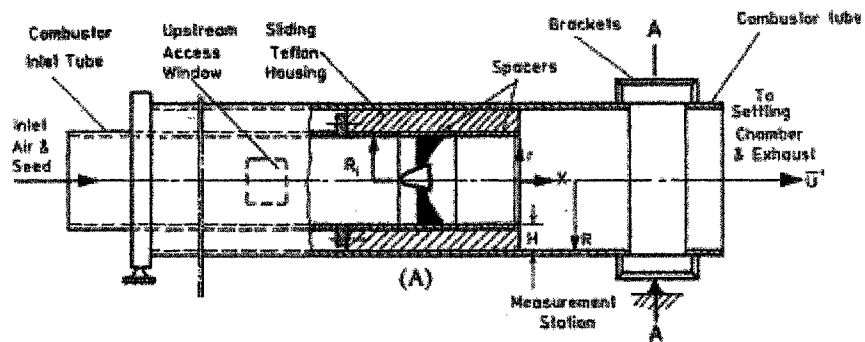


Figure 2.4.1.2: Experimental setup of swirl combustor model, reproduced from Ahmed (1998)

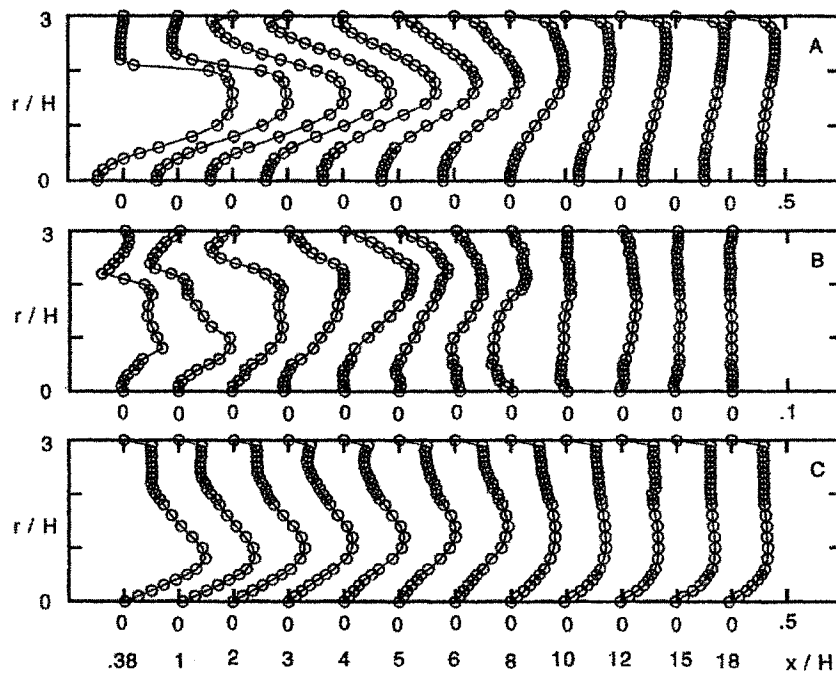


Figure 2.4.1.3: Evolution of velocity (A) U_z/U_0 (B) U_r/U_0 (C) U_t/U_0 ; reproduced from Ahmed (1998)

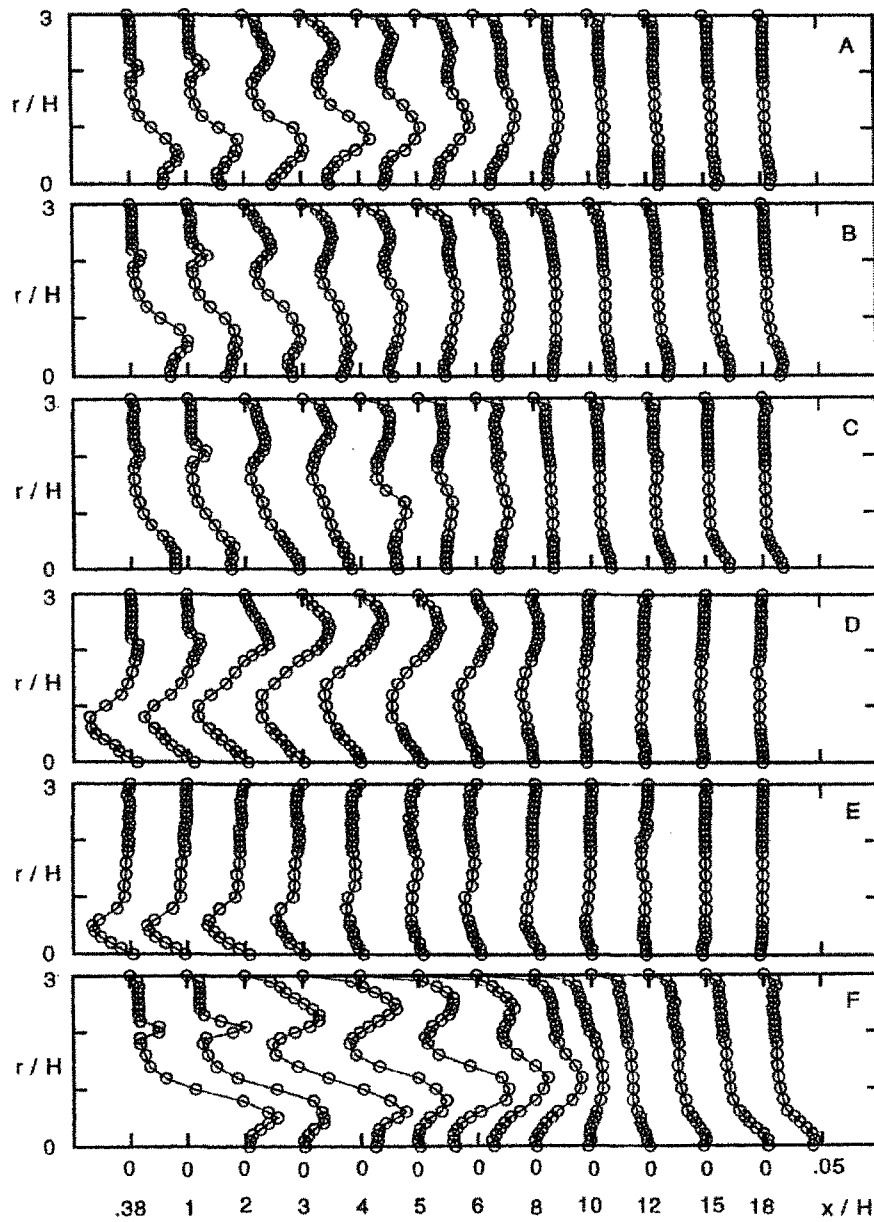


Figure 2.4.1.4: Evolution of Reynolds-stresses (A) u'^2/U_0^2 ; (B) v'^2/U_0^2 ; (C) w'^2/U_0^2 ; (D) $\overline{u'v'}/U_0^2$; (E) $\overline{u'w'}/U_0^2$; (F) k/U_0^2 ; reproduced from Ahmed (1998)

2.4.2 Wingtip Vortices

The wingtip vortex is of great importance because of its effect on practical problems such as aerodynamic drag, hazard posed to following aircraft, blade/vortex interactions on helicopter blades, and control of propeller cavitation on ships. Wingtip vortex studies date back to the work of Betz (1932). Through theoretical reasoning, based on conservation of circulation and vortical dispersion, Betz developed a wake convection model. His model demonstrated that the vorticity distribution on a lifting surface developed into the spirals of a tip vortex as it evolved downstream of the wing. Figure 2.4.2.1 shows the development of a typical wingtip vortex.

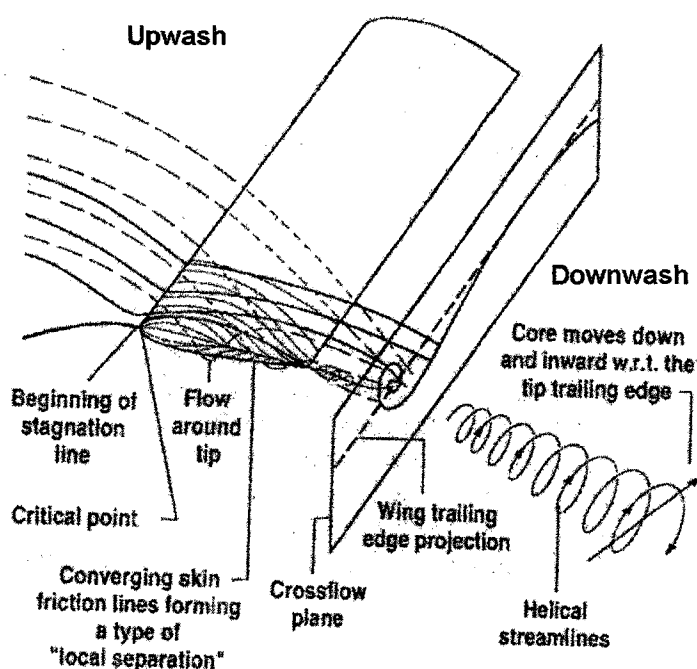


Figure 2.4.2.1: Initial rollup of a wingtip vortex, reproduced from Chow *et al.* (1997)

Measurements of the near-field vortex-roll-up process show that the aircraft wingtip vortex is initially fully turbulent. The highly unstable shear layer from the wing trailing edge winds up around the core, while turbulence in the vortex core is strongly suppressed. It has been observed numerically and experimentally that turbulence production approaches zero near the core. This characteristic explains the relatively slow diffusion of the core in time. Outside the core, the flow follows a free-vortex velocity distribution in which the tangential velocity varies inversely with radius. Traub *et al.* (1998) completed a study on wingtip vortex development off of a rectangular wing of aspect ratio 6.5. This data is reproduced in Figure 2.4.2.2, where the radius shown is normalized by the wingspan, b . The experimental data was collected 23 chord lengths, c_w , downstream from the wing's trailing edge at a chord Reynolds number of 2×10^5 . This experiment included testing different wing shapes, and δ_{TOE} refers to the toe-in angle of the wing. The toe-in angle is the angle between the wingtip and the leading edge. For the basic wing, the δ_{TOE} was equal to zero. Devenport *et al.* (1996) completed a study on the development of a wingtip vortex behind a rectangular *NACA* 0012 half-wing at an angle of attack of 5° and a Reynolds number of 6×10^5 . The experimental data was measured at a series of axial locations downstream from the trailing edge of the wing from $z/c_w = 5$ to $z/c_w = 30$. Figure 2.4.2.3 shows the data for this experiment, where the tangential velocity is normalized by the free-stream velocity, U_∞ , and the radius is normalized by the chord length, c_w .

Velocity measurements at 30 chord lengths downstream of the wing test-section for both Devenport *et al.* (1996) and Traub *et al.* (1998) indicate a maximum tangential velocity equal to about 25% of the free-stream velocity. Also, both of the maximum tangential velocities occur at approximately 4% of the chord length from the center of the vortex.

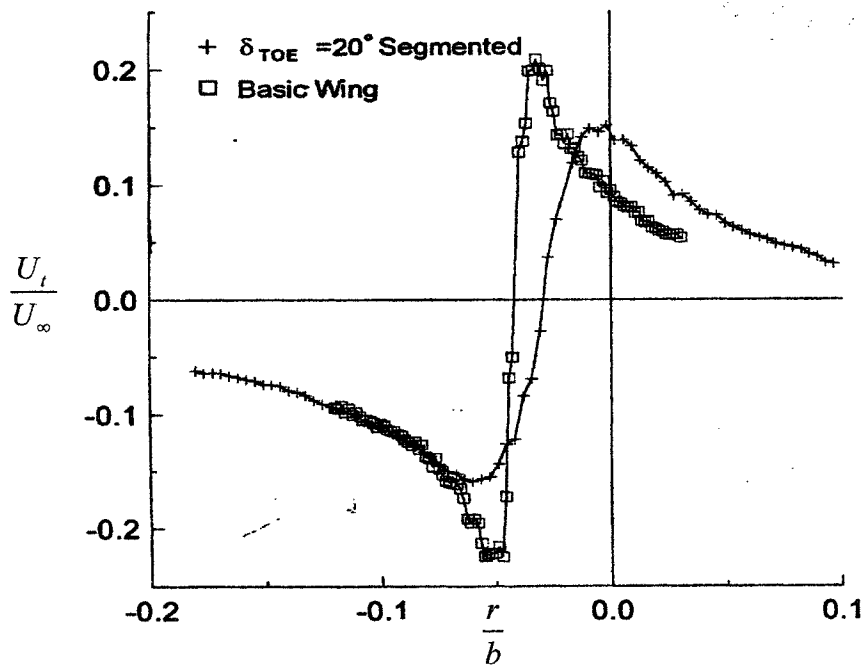


Figure 2.4.2.2: Tangential velocity distribution, reproduced from Traub *et al.* (1998)

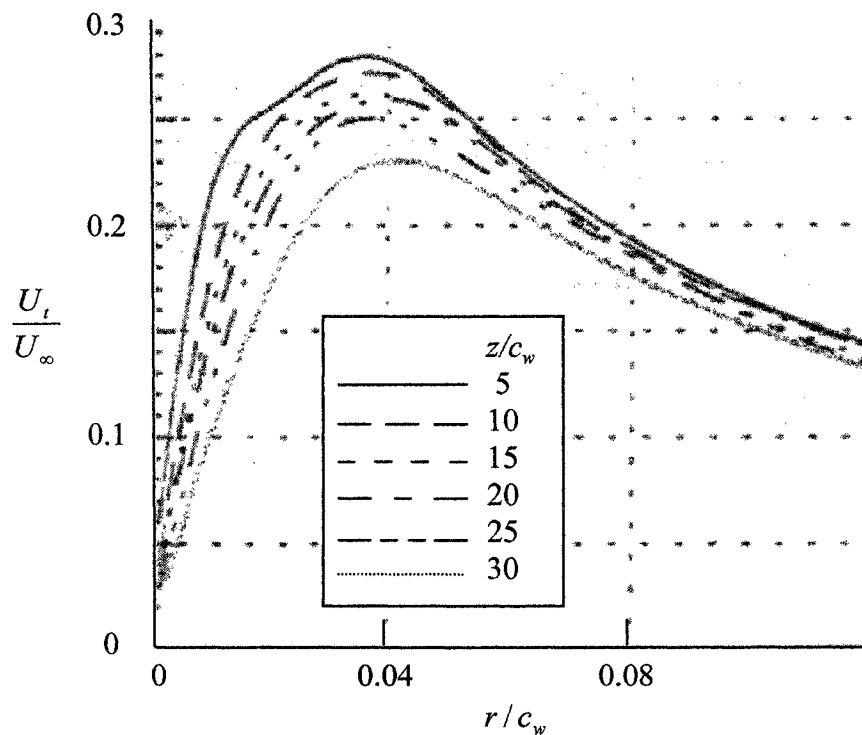


Figure 2.4.2.3: Tangential velocity distributions, reproduced from Devenport *et al.* (1996)

Due to the absence of shear in the vortex core, turbulence production is considered to be negligible. Bandyopadhyay *et al.* (1991) investigated the turbulence structure in a turbulent trailing vortex and concluded that the inner core region is not a complete laminar region; instead it is a re-laminarizing region where patches of turbulent fluid are intermittently brought in from the outer region.

Wingtip vortices leave the aircraft as a pair of parallel vortices rotating in opposite directions. Due to instabilities, the parallel vortices eventually touch, break, and finally recombine into toroidal vortices. A toroidal vortex is a circular vortex ring, as shown in Figure 2.4.2.4, and will propel itself forward due to the rotating motion. In

inviscid fluid, the radius of the vortex will remain constant with time. The viscosity of a real fluid will cause the toroidal radius to increase.

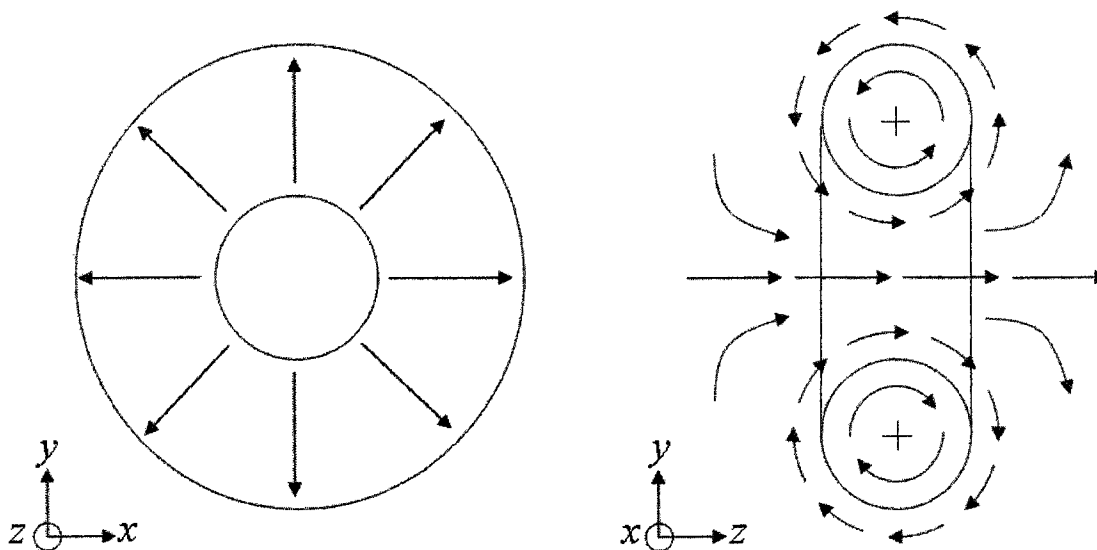


Figure 2.4.2.4: Toroidal Vortex

2.4.3 Inclined-Jet-in-Cross-Flow

Inclined-jet-in-cross-flow (*IJICF*) research is relevant to applications such as boundary-layer control, turbine blade cooling, *V/STOL* aircrafts, roll control of missiles, and mixing in combustors. The *IJICF* is a very effective mixing mechanism for two fluids in a limited space and limited time. Broadwell and Breidenthal (1984) claim that this type of mixing is considered superior to other flow constellations such as a mixing layer or jet in co-flow.

The first investigations of a normal jet in cross-flow (*JICF*) began with the study of the mixing of chimney plumes (Sutton, 1932). Numerous investigators including Scorer (1958), Kamotani and Greber (1972), and Fric and Roshko (1994), have concluded that neither *JICF* nor *IJICF* can be generalized in terms of self similarity or Reynolds number dependence, in contrast to mixing flow configurations such as a jet. As can be expected, the velocity and turbulence characteristics of an *IJICF* share some of the properties of both wingtip vortices and confined vortices. The vortex produced from an *IJICF*, shown in Figure 2.4.3.1, is bounded by a solid wall and the free-stream.

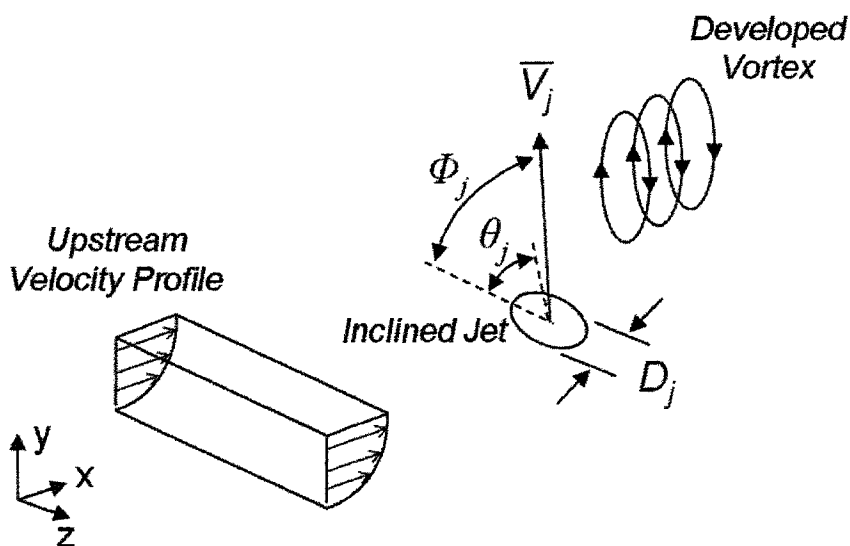


Figure 2.4.3.1: Development of an *IJICF*

In Figure 2.4.3.1, Φ_j , θ_j , \bar{V}_j , and D_j are the jet-pitch angle, jet-skew angle, spatially-averaged jet velocity, and jet diameter, respectively. Further understanding of *IJICF*

requires investigating the effects of the ratio of jet momentum to boundary layer momentum and jet-inflow geometry on vortex development.

2.4.3.1 Vortical Structures in *IJICF*

Most types of jet-inflow geometry produce the same types of vortical structures. The simplest type of jet-inflow geometry for a *JICF* is that of a circular cross section with the flow axis perpendicular to the cross flow ($\Phi_j = 0^\circ$ and $\theta_j = 0^\circ$). The five most dominant vortical structures produced in a *JICF* are the leading-edge vortices, lee-side vortices, counter-rotating vortex pairs (*CVP*), horseshoe vortices, and wake vortices. In Figure 2.4.3.1.1, New *et al.* (2003) show a schematic of the main vortical structures produced by a *JICF*. This figure is similar to an interpretation of Fric and Roshko (1994), although Fric and Roshko group the lee-side and leading-edge vortices into vortical structures called jet-shear-layer vortices.

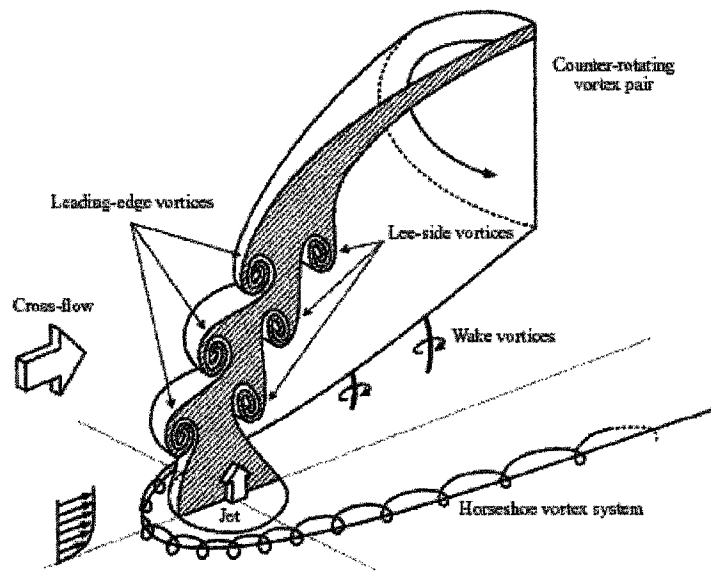


Figure 2.4.3.1.1: Vortical structures produced by *JICF*, reproduced from New *et al.* (2003)

Of the relevant vortical structures, the most dominant vortex system in a *JICF* is the counter-rotating vortex pair. Jet-shear-layer vortices, wake vortices and horseshoe vortices are often called secondary vortices and play a minor role. Although these vortical structures do not significantly affect the flow system, their effects are not negligible in the near field of the jet.

The mechanism for the formation of the counter rotating vortex pair (*CVP*) is not fully understood. It is generally accepted that the vorticity of the *CVP* has its origin at the sidewalls of the jet. The jet-shear-layer vortices are produced directly at the jet orifice. The jet and cross-flow stream form a mixing layer with a Kelvin-Helmholtz instability, which causes a roll-up near the edges of the jet. As shown in Figure 2.4.3.1.2, for an

IJICF, the main counter rotating vortex pair is significantly altered into a single dominant vortex.

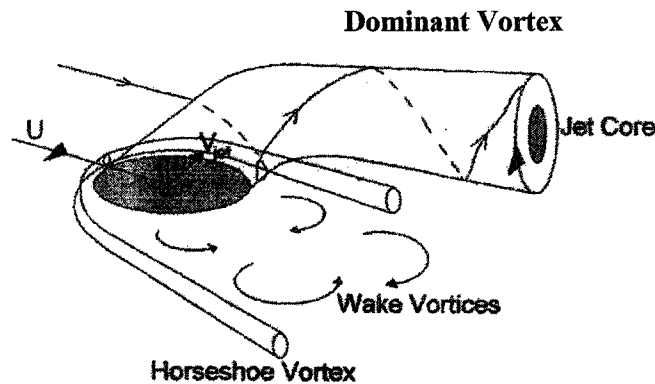


Figure 2.4.3.1.2: Vortical structures of inclined jet-in-cross-flow, reproduced from Bray and Garry (2000)

As the jet is pitched closer to the test surface, one vortex from the counter-rotating pair is forced closer to the test surface (lower side). Close proximity to the test surface increases the dissipation of that vortex, reducing its strength to the point of destruction. The strength distributed between the counter rotating vortex pair becomes progressively non-uniform resulting a single vortex (upper side). As the weaker vortex is destroyed, it wraps around the dominant vortex. Secondary vortical structures such as jet-shear-layer vortices and the horseshoe vortex continue to exist when the jet is inclined (Figure 2.4.3.1.2).

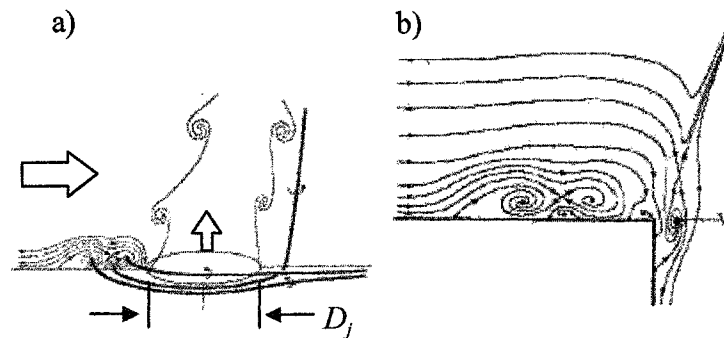


Figure 2.4.3.1.3: a) Jet-shear-layer vortices and horseshoe vortex, b) Horseshoe vortex at the upstream edge of jet orifice, reproduced from Kelso *et al.* (1995)

As shown in Figure 2.4.3.1.3, upstream of the *IJICF*, a horseshoe vortex forms. This vortex is convected and stretched by the jet flow and wraps around the jet nozzle like a necklace. This same phenomenon occurs in flow configurations where a boundary layer hits a solid obstruction in the flow (Baker, 1979).

Andreopoulos (1982) measured the velocity profiles of the jet-pipe interior and found that they were non-symmetrical. Kelso *et al.* (1995) observed that the cross-flow affects the jet-pipe flow up to $2D_j$ upstream of the nozzle, which is illustrated in Figure 2.4.3.1.3b. A separation bubble develops inside the jet-pipe near the jet exit due to the interaction of the jet and cross-flow.

The production mechanism for the wake vortices is also controversial. The mechanism first thought to be responsible for their production was the shedding process behind the jet. It was thought that the jet was similar to the obstruction of a solid cylinder and the wake vortices were similar to that of a Kármán vortex street (Section 2.5.1). This conclusion was later refuted by Perry (1993), who showed that in an incompressible

fluid, internal vorticity production is impossible. The vorticity transport equation for incompressible fluids consists of only convection and diffusion terms. Any vorticity in the flow must be convected from the imposed boundaries. Therefore the shedding process cannot be responsible for the wake vortices observed in *JICF*. Fric and Roshko (1994) claimed that the production of wake vortices was due to a separation event that occurred at the test surface at the sides of the jet nozzle. The wake vortex rotates into a vertical orientation due to convection from the jet trajectory.

With this review of the main vortical structures that exist in an *IJICF*, the discussion will move to the effects of jet momentum on vortex development.

2.4.3.2 The Momentum Ratio

The momentum ratio, r_m , of an *IJICF* is defined as:

$$r_m = \sqrt{\frac{\bar{\rho}_j \bar{V}_j^2}{\bar{\rho}_{cf} \bar{V}_{cf}^2}} \quad (2.4.3.2.1)$$

where $\bar{\rho}_j$, $\bar{\rho}_{cf}$, and \bar{V}_{cf} are the spatially-averaged jet-density, spatially-averaged cross-flow density, and spatially-averaged magnitude of cross-flow velocity. If the jet fluid and cross-flow fluid are of the same species, at the same temperature, and at subsonic conditions, the momentum ratio in Eqn. 2.4.3.2.1 simplifies to the incompressible velocity ratio:

$$VR = \frac{\bar{V}_j}{\bar{V}_{cf}} \quad (2.4.3.2.2)$$

The impact of VR on the flow regime is quite significant for *IJICF*. Analysis of these regimes can be grouped into three main ranges of velocity ratio:

$$VR < 1 : \text{weak jet} \quad (2.4.3.2.3a)$$

$$1 < VR < 10 : \text{jet of intermediate strength} \quad (2.4.3.2.3b)$$

$$VR > 10 : \text{strong jet} \quad (2.4.3.2.3c)$$

The first flow regime based upon the criteria in Eqn. 2.4.3.2.3a involves the interaction of a weak jet and a strong cross-flow. This type of flow regime is typical of turbine blade cooling applications (Benz *et al.*, 1993). In this flow regime, the relatively small amount of momentum available in the jet is not sufficient to break through the wall boundary layer of the cross-flow. The far-field of the jet is primarily governed by the oncoming boundary layer of the cross-flow. This type of flow regime can occur up to a velocity ratio of $VR = 1$, and it is also dependent on the cross-flow boundary layer thickness. The range of velocity ratios in Eqn. 2.4.3.2.3b are common flow regimes for combustion applications. For this range, the boundary layer plays a minor role as the jet has enough momentum to penetrate through the boundary layer. In this flow configuration, the *JICF* is determined by freestream turbulence characteristics and is easier to model. The flow characteristics associated with a velocity ratio range shown in Eqn. 2.4.3.2.3c are similar to those of free jets. This similarity becomes more apparent with increasing velocity ratio.

2.5 Stability of Vortical Flows

Excitation of certain instability modes can cause vortex breakdown. Understanding the mechanisms responsible for this process is very important to predict or control vortical flows. The following is a list of vortex breakdown theories assembled by Jacob (1995). Vortex breakdown is:

1. a separation phenomenon (Talbot, 1954)
2. a standing wave phenomenon (Squire, 1960)
3. a result of a hydrodynamic instability (Bossel, 1967)
4. the onset of a transition between two conjugate flow states (Benjamin, 1962)
5. the result of external influences affecting the axial flow in the core (Tsai and Widnall, 1976)

Considerable attention has been given to the instability mechanisms resulting in vortex breakdown. The stability of vortex configurations to small perturbations can be classified into three main categories: two dimensional, three-dimensional long-wave, and three-dimensional short-wave instabilities.

2.5.1 Two-Dimensional Instability

Examples of two-dimensional-instability investigations include a row of point vortices, a Kármán vortex street (Kármán, 1911, 1912), and a ring of N -point vortices (Havelock, 1931). These studies conclude that vortex strength and position are the only relevant properties to 2-D stability. Details such as vortex core size and distribution of vorticity do not affect the stability of two dimensional motions. Figure 2.5.1.1 shows the development of a Von Kármán vortex street.

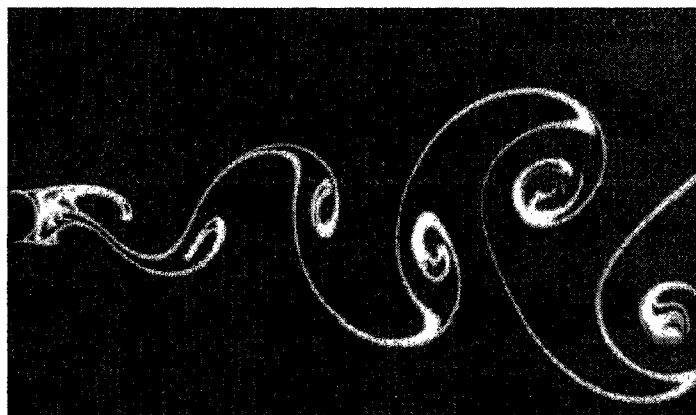


Figure 2.5.1.1: Von Kármán vortex street ($Re = 140$), reproduced from Von Dyke (1982)

Kármán showed that the vortex street is unstable to infinitesimal two-dimensional disturbances. For most cases, disregarding three dimensional instabilities result in inaccurate predictions in vortex development. Graham (1984) found that three dimensional instabilities distorted the vortex filament in the case of vortices shed from a cylinder (Kármán vortex street). Only when three-dimensional distortions were included

in Graham's vortex model, were accurate agreement between experiment and predictions achieved.

2.5.2 Long-Wave Instability

Three-dimensional long wave instabilities, an example of which is shown in Figure 2.5.2.1, are usually only relevant to systems that involve more than one vortex. The characteristic wavelength associated with a long-wave or Crow instability is of the order of the separation distance between the two vortex cores in a vortex pair, such as that existing in the wake of an aircraft. In the analysis of long-wave instability the vortex is treated as a filament. The self-induced motion of a vortex filament is governed by the core size and a shape constant dependent upon the vorticity distribution. All long-wave instability problems can be described in terms of vortex configuration, wavelength, and an effective core size.

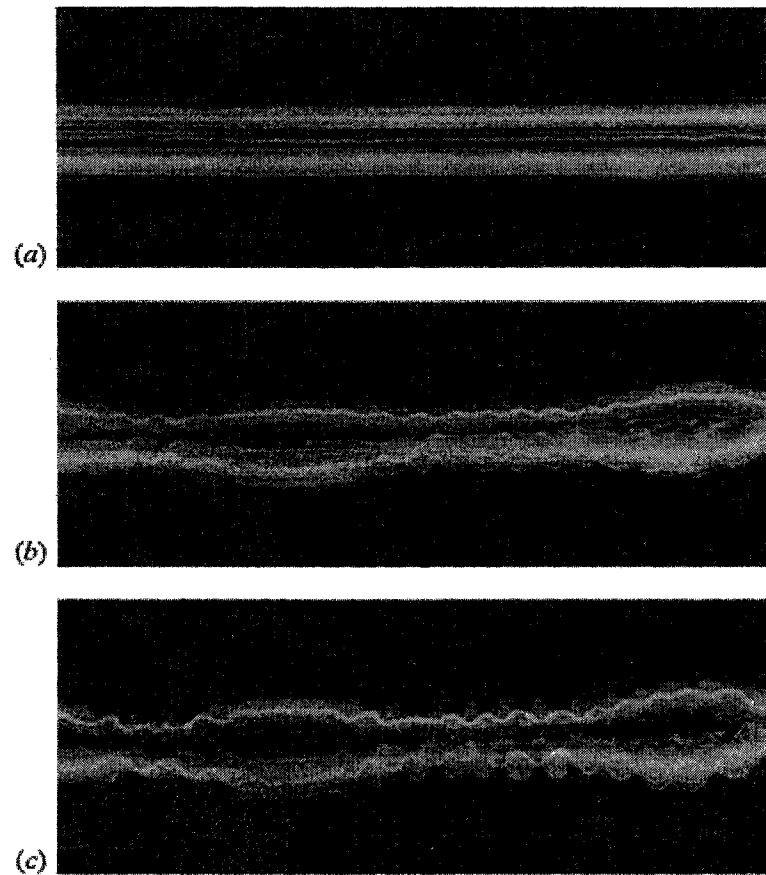


Figure 2.5.2.1: Vortex pair evolution under combined action of long-wave and short-wave instabilities, reproduced from Leweke and Williamson (1998)

Three-dimensional instability of vortex filaments can be understood as a balance between the destabilizing effects of local strain field at the vortex location and the self-induced velocity due to local curvature. Instability occurs when the destabilizing effects of strain overcome the stabilizing effects of self-induced rotation. Another effect important for long-wave instability is the velocity induced on the vortex filament by the displacement perturbations of the distant filament. These velocities determine what wave length will be most unstable for a given configuration and core size. Crow (1971)

investigated long-wave stability and concluded that a vortex pair of equal and opposite strength is unstable to both symmetric and anti-symmetric perturbations.

2.5.3 Short-Wave Instability

Three-dimensional short-wave or elliptic instabilities can appear on a single vortex since they are linked to the presence of an external straining field. An example of a short-wave instability is shown in Figure 2.5.3.1, where a vortex under external strain is enclosed in a cylinder of a height-to-radius ratio of 8.2.

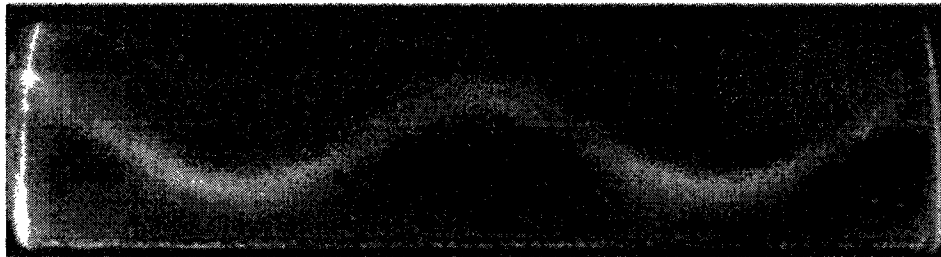


Figure 2.5.3.1: Short-wave instability ($Re = 2500$), reproduced from Eloy (2000)

The wavelength scale associated with a short-wave instability is of the order of the vortex core diameter, D_c . Any vortex with distributed vorticity is linearly unstable to short-wave disturbances with an amplification rate proportional to the local strain, with the exception of straight, isolated vortices in an infinite fluid. This mechanism of instability is linked to the periodic straining experienced by plane-wave disturbances that are advected by the rotating base flow. This can lead to a resonant amplification if the wave and straining

frequencies match. Pierrhumbert (1986) and Bayly (1986) were the first to show that two-dimensional flows with elliptical streamlines are unstable with respect to three-dimensional disturbances. Also, they found that there is no low-wavelength cut-off for the band of unstable perturbations in the case of inviscid flow.

Thomas and Auerbach (1994) showed the existence of short waves on one vortex of a non-symmetric pair generated by the periodic rotation of a single flat plate. Their visualizations showed that the perturbations on one of their vortices had a close resemblance with the Kelvin mode proposed by Widnall et al (1974) as the source of short-wavelength instability.

Widnall *et al.* (1971, 1974) investigated short-wave instabilities on vortex rings and identified a connection between the short-wave modes of vortex oscillation that have no self-induced rotation and the short-wave instabilities of vortices. Solutions for the short-wave modes depend upon core size and vorticity distribution. A specific example is the Kelvin mode which was discovered in relation to long-wave instability. This mechanism is defined as the resonance of a long, bending Kelvin wave on the vortex filament with the external straining field imposed by the other vortex filament. Widnall *et al.* (1974) predicted that this mechanism should also excite short-wavelength Kelvin modes distinguished by their complicated structure within the vortex core. This was confirmed by Moore and Saffman (1975) in the context of a general axisymmetric vortex distribution distorted by an externally imposed straining field. This external field caused the streamlines to become slightly elliptical. It was concluded that the strain destabilizes the helical wave, which does not propagate on the vortex core.

Mayer and Powell (1992) conducted extensive studies on the linear stability response of a q -vortex to helical perturbations or Kelvin waves. In their study, the Batchelor similarity model, also referred to as the q -vortex, was used to represent trailing vortices. The initial velocity distributions are given by:

$$U_t = \frac{q}{r}(1 - e^{-r^2}) \quad (2.5.3.1)$$

$$U_z = 1 - e^{-r^2} \quad (2.5.3.2)$$

where q and r are the instability parameter and radial coordinate, respectively. They indicate that q is a determining parameter of instability and the vortex is generally stabilized for values of q greater than 1.5.

2.6 Turbulence in Vortical Flows

The flow field, diffusion rate, stability, wandering, and breakdown of a vortex are affected by the presence of turbulence. The increased mixing associated with turbulence provides a mechanism to dissipate energy from the vortex. Turbulence is also a primary source of the short- and long-wave instabilities discussed in Section 2.5. During transition towards breakdown, the velocity profiles in the vortex core slowly change until they reach a critical shape which suddenly leads to breakdown.

To predict the behaviour of most practical flows, including vortical flows, turbulence characteristics must be modelled. Due to the difficulty of solving the governing equations of motion, a complete definition of turbulence cannot be formulated.

As stated by Tennekes and Lumely (1972), turbulence is a characteristic of fluid flow and not a characteristic of the fluid. Therefore, turbulence can only be described in a series of behaviours and characteristics that are common to all turbulent flows. These characteristics include randomness of the flow variables, diffusivity, a broad-banded spectrum, and vorticity.

2.6.1 Reynolds Number, Stability, and Turbulence Production

The Reynolds number is the ratio of inertial-to-viscous forces in a fluid flow, and is stated as:

$$\text{Re} = \frac{U_{char} L_{char}}{\nu} \quad (2.6.1.1)$$

where U_{char} is a characteristic velocity scale of the flow field, L_{char} is a characteristic length scale, and ν is the kinematic viscosity. In vortical flows, it is often more relevant to specify the vortex Reynolds number:

$$(\text{Re})_{vortex} = \frac{\Gamma}{\nu} \quad (2.6.1.2)$$

Turbulence occurs at high Reynolds numbers and is often initiated by an instability in laminar flow. Instabilities in a flow are often related to the interaction between the viscous and inertia forces. The mechanisms for turbulence production include shear, buoyancy, and density differences in a centripetal field. For wall-bounded shear-layers and free shear-layers, the most common turbulence production mechanism is shear.

2.6.2 Vorticity, Vortical Structures, and Diffusion in Turbulence

All turbulence is rotational and is associated with high levels of three-dimensional fluctuations, irregularities, or randomness of the flow field. Often, turbulence is characterized by three-dimensional vorticity fluctuations that are maintained through vortex stretching. Vortex stretching is a three-dimensional mechanism implying that turbulence cannot exist in two-dimensions. Turbulent eddies, considered to be vortical structures, account for a small portion of the turbulent kinetic energy, but are responsible for a large portion of the transport of properties such as species, mass, momentum, and energy (Tennekes and Lumely, 1972). This process is called turbulent diffusion and is responsible for the prevention of flow separation on airfoils and increased heat transfer to or from the airfoil surface. The vortical structures do not appear regularly in time or space, which accounts for the randomness of turbulent flows.

2.6.3 Dissipation and the Energy Cascade

The production mechanisms of turbulence, which are discussed in Section 6.2.1, involve a strain rate. The strain rate is indirectly caused by viscous shear stresses, which perform deformation work on the time-mean flow field resulting in both turbulence production and turbulence dissipation. When dissipation exceeds production, the turbulence field is said to be in a state of decay. All turbulent flows experience energy dissipation and the existence of turbulence is dependent on a constant flow of energy

from the time-mean flow field. Conservation of energy can be used to explain the cascade of turbulence kinetic energy from large scales to small scales. As the energy is transferred to these smaller scales, a critical scale is reached where smaller scales of turbulence cannot exist. At this critical scale, the Kolmogorov scale, kinetic energy of the turbulent eddies is transformed into thermal energy. Therefore, turbulence is considered to exist in a continuum governed by the equations of fluid mechanics and has the potential to operate on all time and length scales. Turbulent behaviour is dependent on the environment which it exists in, and therefore current turbulence theory is tailored to specific situations (Wilcox, 1993).

2.6.4 Turbulence Measurements in Aircraft Vortices

Proctor (1998), Sarpkaya and Daly (1987), and Sarpkaya (1998) indicate that the decay mechanism for aircraft trailing vortices is influenced by ambient atmospheric turbulence and stratification, three-dimensional vortex pair dynamic instabilities, ground effects, and self-generated turbulence in the vortex. Furthermore, Wallin and Girimaji (2000) indicate that in typical aircraft trailing vortices, the Reynolds number is of the order of 10^7 , which means that molecular diffusion is of lesser importance compared to turbulent diffusion.

Chow et al. (1997) completed a study on the turbulence characteristics in the near field of a wingtip vortex with a Reynolds number based on the chord length of 4.6×10^6 . The turbulence intensity, Tu , measured in and around the vortex core was initially the

same order of magnitude as levels measured outside of the core. The presence of turbulence inside the core was primarily due to entrainment from the wing's boundary layer during the roll-up process. Although additional turbulence was generated by the mean axial velocity gradients downstream of the trailing edge, the re-laminarizing influence of the forced-vortex region of the core reduced overall turbulence levels.

In the far field, it has been observed experimentally and numerically that the Reynolds-shear-stress and turbulence production tend to zero in the vortex core. Decay therefore begins at the outer edges of the vortex and propagates inward due to the diffusive properties of turbulence.

Gerz and Holzapfel (1999) investigated the turbulence levels in wingtip vortices using large eddy simulation. Three cases were analyzed to establish the role of turbulence in the time evolution of the vortex. These included wingtip vortex decay without turbulence, with aircraft boundary layer turbulence, and with the combination of atmospheric turbulence and aircraft boundary layer turbulence. It was discovered that the presence of turbulence decreases the life of the wingtip vortex as it promotes instability mechanisms.

One of the main concerns in experimental studies of vortical flows is the issue of vortex meandering or vortex wandering. Low frequency motion of a vortex can be misinterpreted as turbulence. Westphal and Mehta (1989) completed a study on the turbulence measurements downstream of oscillating and stationary vortices. It was found that the contours of Reynolds-shear-stresses were altered considerably for the meandering vortex. Devenport *et al.* (1995) performed turbulence measurements behind a rectangular

NACA 0012 wing and found that high Reynolds-stresses in the core were attributed primarily to vortex meandering. They also found that meandering amplitudes increased approximately linearly with downstream distance and decreased angle of attack. Baker *et al.* (1974) estimated the measurement error in the peak tangential velocity due to meandering to be as much as 35%.

Chapter 3

MODELLING OF TURBULENCE

The numerical solution of the Navier-Stokes equations for turbulent flows can be characterized by how turbulence is quantified. The spectrum of choices discussed in this section consists of direct numerical simulation (*DNS*), large eddy simulation (*LES*), and Reynolds-averaged-Navier-Stokes (*RANS*) simulation.

3.1 Direct Numerical Simulation

The most exact approach available to model turbulence is to solve the Navier-Stokes equations directly without averaging, filtering, or using approximations. The conservation of mass and momentum equations assuming incompressible flow of a Newtonian fluid are given below:

$$\frac{\partial u_i}{\partial x_i} = 0 \quad (3.1.1)$$

$$\rho \frac{\partial u_i}{\partial t} + \rho \frac{\partial (u_i u_j)}{\partial x_j} = -\frac{\partial p}{\partial x_i} + \mu \frac{\partial}{\partial x_j} \left(\frac{\partial u_i}{\partial x_j} + \frac{\partial u_j}{\partial x_i} \right) \quad (3.1.2)$$

With the development of powerful computers, direct numerical simulation (*DNS*) is becoming a viable option for simulating turbulent flows. Since this approach avoids the problems of statistical correlations for turbulence that are often based upon weak assumptions, it is the most accurate choice for computing turbulent flows. Unfortunately,

there are two major problems that prohibit the use of *DNS* for most engineering flows.

First, the *DNS* spatial resolution requirements for any flow simulation of engineering interest are extremely high and increase with the Reynolds number of the flow. This is attributed to one of the fundamental aspects of turbulence, in that it operates on a wide range of time and length scales. Accurate *DNS* requires the computational grid to be large enough to encompass the domain of interest while at the same time have a fine enough resolution to capture the physics at the smallest scales of turbulence. Second, as *DNS* is a transient type of simulation that aims to capture the temporal development of all turbulent motions, such simulations require a sufficient amount of time increments to capture the life cycles of turbulence structures of all scales.

3.1.1 Computational Grid Requirements

The ratio between the largest and smallest turbulence length scales will give an insight into the spatial grid requirements for *DNS*. The smallest turbulence length scale of importance is the Kolmogorov scale, η , and is defined as:

$$\eta = \left(\frac{\nu^3}{\varepsilon} \right)^{\frac{1}{4}} \quad (3.1.1.1)$$

where ν is the kinematic viscosity and ε is the turbulence energy dissipation rate per unit mass. The size of the largest turbulence structures correlate with the overall dimensions of the flow path, L . The required amount of nodes on a computational grid is proportional to the ratio of the largest and smallest length scales of turbulence (L/η):

$$\frac{L}{\eta} = \frac{\text{Re}^{\frac{3}{4}}}{(2/c_f)^{\frac{1}{4}}} \quad (3.1.1.2)$$

$$c_f = \frac{\tau_w}{\frac{1}{2}\rho U^2} \quad (3.1.1.3)$$

where c_f , U , and τ_w are the wall-skin-friction coefficient, characteristic velocity scale of turbulence, and wall-shear-stress respectively. Since the wall-skin-friction coefficient, c_f , is only weakly correlated to Reynolds number, Eqn. 3.1.1.2 can be simplified to:

$$\frac{L}{\eta} \propto \text{Re}^{\frac{3}{4}} \quad (3.1.1.4)$$

Table 3.1.1.1 gives estimates of the number of nodes required for duct flow at different Reynolds numbers. Gatski *et al.* (1996) suggests that a mean grid-node spacing of $\Delta=3\eta$ is adequate to capture all of the important structures at the small turbulence scales. Assuming a simple cubic computational domain with the length of each side equal to L , the number of nodes is then given as:

$$N_d = \left(\frac{L}{\Delta}\right)^3 \quad (3.1.1.5)$$

Re	L/Δ	N_d
5.0E+03	1.98E+02	7.79E+06
1.0E+04	3.33E+02	3.70E+07
5.0E+04	1.11E+03	1.38E+09
1.0E+05	1.87E+03	6.59E+09
5.0E+05	6.27E+03	2.46E+11

Table 3.1.1.1: *DNS* node count requirements

With currently available computing capabilities (10^{10} floating point operations per second, 10^9 words storage), *DNS* for a Reynolds number below 5×10^4 is possible.

3.1.2 Time-Step Requirements

The number of time-steps, N_s , required to follow one realization time, T , also depends on Reynolds number. The realization time refers to the lifetime of an eddy for a particular flow. Assuming a Courant number, ν , less than 1.0, the time-step Δt is roughly limited to:

$$\Delta t \leq \frac{\nu \Delta}{U} \quad (3.1.2.1)$$

where the Courant number, ν , is defined as:

$$\nu = \frac{U \Delta t}{\Delta} \quad (3.1.2.2)$$

Eqn. 3.1.2.1 assures that turbulence is adequately resolved in time and is based upon a

length scale that adequately resolves turbulence in space. Using the same assumptions as in the grid-node spacing requirements (i.e. $\Delta=3\eta$), the time-step size is calculated as:

$$\Delta t \leq \frac{3L}{U \text{Re}^{\frac{3}{4}}} \quad (3.1.2.3)$$

Gatski *et al.* (1996) assumes that an adequate realization of time required to obtain reliable flow statistics is approximately $T = 100L/U$. Based on this, the number of time-steps can be determined as:

$$N_s = \frac{T}{\Delta t} \geq \frac{100}{3} \text{Re}^{\frac{3}{4}} \quad (3.1.2.4)$$

Re	N_s
5.0E+03	1.98E+04
1.0E+04	3.33E+04
5.0E+04	1.11E+05
1.0E+05	1.87E+05
5.0E+05	6.27E+05

Table 3.1.2.1: *DNS* time-step requirements

As all of the turbulence in *DNS* is completely resolved by the temporal and spatial grids, *DNS* is considered to be the most accurate method of predicting fluid flows. The computational requirements for *DNS* severely limit the range of engineering flows this technique can be used for. From Tables 3.1.1.1 and 3.1.2.1, *DNS* of a flow with a Reynolds number of 5×10^5 requires approximately 2×10^{11} nodes and 6×10^7 time-steps.

Although computer technology is continuously improving, the present situation requires a method of reducing the computational requirements below those of *DNS*.

3.2 Large Eddy Simulation

Large eddy simulation (*LES*) is an attempt to reduce the computational requirements of *DNS* by using statistical models to represent turbulence at the small scales. More specifically, the *LES* approach is to represent the largest scales of turbulence explicitly while the small scales are treated by some approximate parameterization or model. In terms of turbulence modeling, *LES* can be thought of as the first step into moving away from *DNS*, allowing for the investigation of problems at much higher Reynolds numbers. However, as most of the scales of turbulence are resolved explicitly, *LES* is still computationally expensive. In essence, *LES* can be considered a compromise between *DNS* and *RANS* models. *RANS* models will be discussed later.

3.2.1 Overview of Filtering Process

Since a separation of both length and time scales is required for *LES*, the equations of motion need to be appropriately filtered. Figure 3.2.1.1 shows a symbolic representation of how a typical filter is applied to the turbulence energy spectrum.

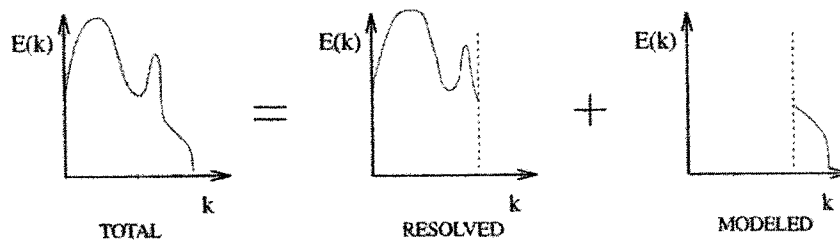


Figure 3.2.1.1: Decomposition of the energy spectrum using a filter in *LES*, reproduced from Sagaut (2002)

A variable, $f(x,t)$, can be decomposed into a resolved, large scale, component, $\bar{f}(x,t)$, and an unresolved, small scale, component, $f'(x,t)$:

$$f = \bar{f} + f' \quad (3.2.1.1)$$

The resolved, large scale, component, \bar{f} , is obtained by passing $f(x,t)$ through:

$$\bar{f}(x_i, t) = \int_{-\infty}^{+\infty} \int_{-\infty}^{+\infty} G(x_i - x'_i, t - t') f(x'_i, t') dt' d^3 x'_i \quad (3.2.1.2)$$

where G is the convolution kernel which is dependent on the type of the filter used. It should be noted that filters operate in both space and time and therefore each convolution kernel requires a cut-off time scale, $\bar{\tau}_c$, and a cut-off length scale, $\bar{\Delta}$. Figures 3.2.1.2 – 4 give a visual representation of three common convolution filters in both physical and Fourier space. The range in which the kernel is activated is denoted by $\pm \xi$ centered about $x - \xi = 0$ and is related to the filter width, $\bar{\Delta} = 2\xi$.

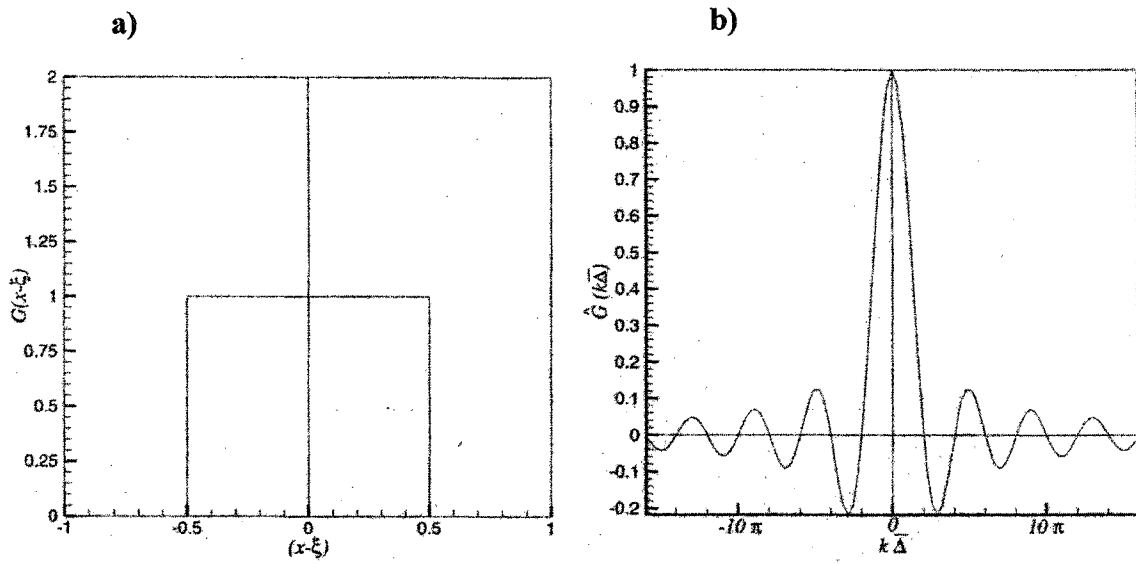


Figure 3.2.1.2: Top-hat filter shown in a) physical space normalized by $\bar{\Delta}$, and in b) Fourier space, reproduced from Sagaut (2002)

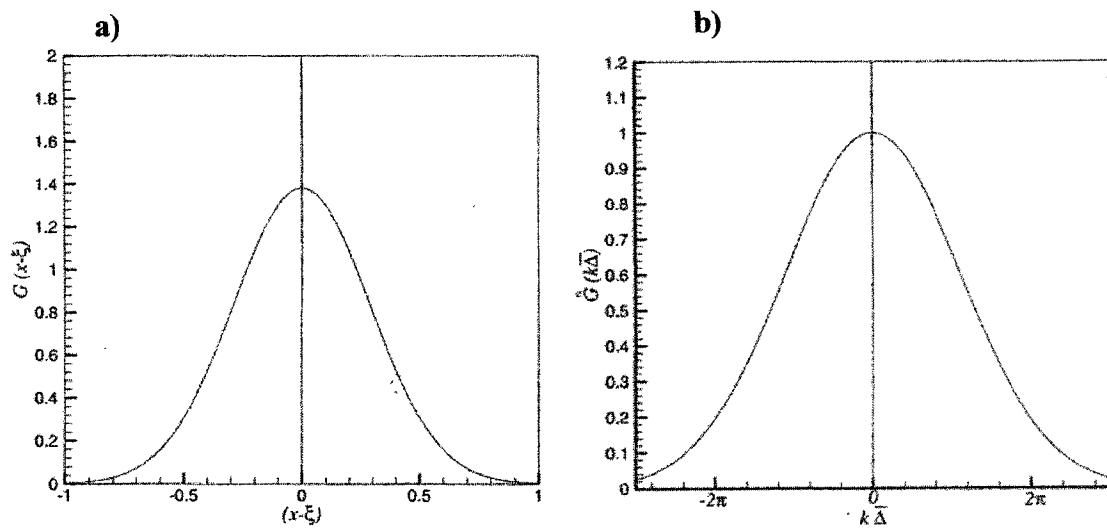


Figure 3.2.1.3: Gaussian filter shown in a) physical space normalized by $\bar{\Delta}$, and in b) Fourier space, reproduced from Sagaut (2002)

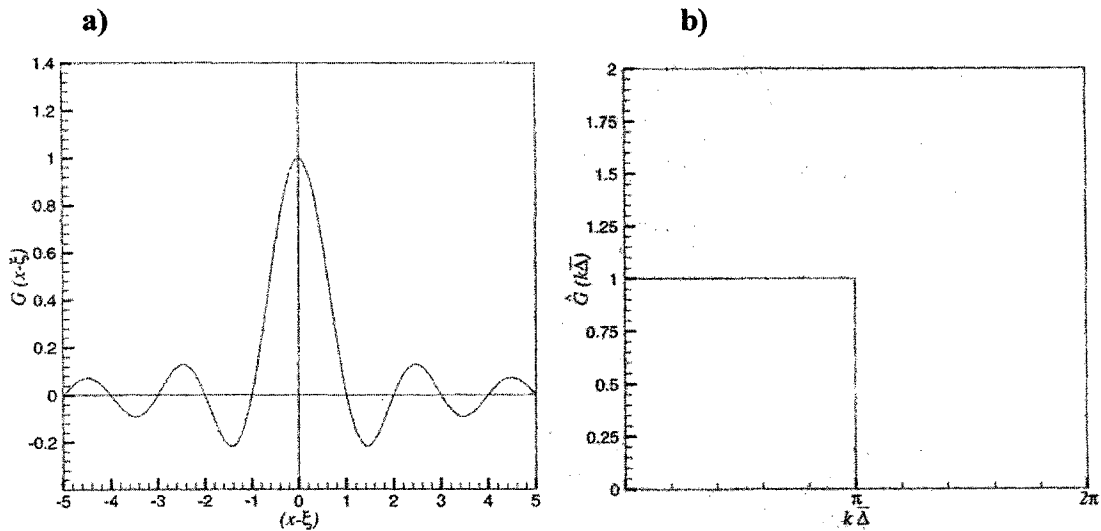


Figure 3.2.1.4: Sharp cut-off filter shown in a) physical space normalized by $\bar{\Delta}$, and in b) Fourier space, reproduced from Sagaut (2002)

It can be seen from Figures 3.2.1.2-4 that variables are explicitly filtered in space while they are implicitly filtered in time. Other filters, which will not be discussed here, filter the variables explicitly in time and implicitly in space. The type of filter has large consequences on the responsibilities of the turbulence model (sub-grid model) used in *LES*. Figure 3.2.1.5 shows the energy spectrum filtered using a Gaussian and sharp cut-off filter. It is noted that unlike the sharp cut-off filter, the Gaussian filter does not have a clear distinction between the large and small scales. Physically, this means that when the Gaussian filter is used, the sub-grid turbulence model must account for large-small scale interactions. This will also be demonstrated mathematically in the next section.

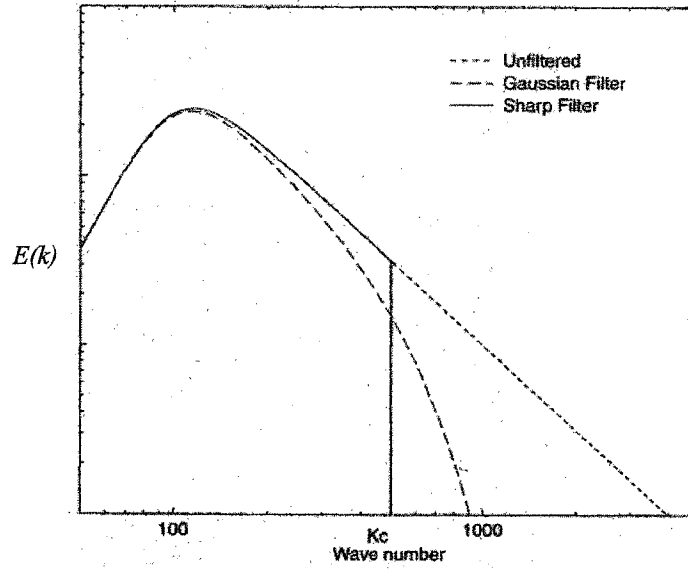


Figure 3.2.1.5: Energy spectrum of unfiltered and filtered solutions using Gaussian and Sharp-cut-off filters, reproduced from Sagaut (2002)

3.2.2 Filtering of the Governing Equations of Fluid Flow

As the kernel filter is applied to the governing equations of fluid flow, the result is the version of these equations applicable to the resolvable scales of motion only:

$$\frac{\partial \bar{u}_i}{\partial x_i} = 0 \quad (3.2.2.1)$$

$$\rho \frac{\partial \bar{u}_i}{\partial t} + \rho \frac{\partial (\overline{u_i u_j})}{\partial x_j} = -\frac{\partial \bar{p}}{\partial x_i} + \mu \frac{\partial}{\partial x_j} \left(\frac{\partial \bar{u}_i}{\partial x_j} + \frac{\partial \bar{u}_j}{\partial x_i} \right) \quad (3.2.2.2)$$

It is well known that these filtered equations are not of direct use unless the non-linear term, $\overline{u_i u_j}$, is further decomposed. As a fundamental part of filtering, the following rule must be adhered to:

$$\overline{u_i u_j} \neq \bar{u}_i \bar{u}_j \quad (3.2.2.3)$$

Leonard (1974) expressed the non-linear term by the following double decomposition:

$$\overline{u_i u_j} = \overline{(\bar{u}_i + u'_i)(\bar{u}_j + u'_j)} = \overline{\bar{u}_i \bar{u}_j} + \overline{\bar{u}_i u'_j} + \overline{\bar{u}_j u'_i} + \overline{u'_i u'_j} = \bar{u}_i \bar{u}_j + L_{ij} + C_{ij} + R_{ij} \quad (3.2.2.4)$$

where L_{ij} , C_{ij} , and R_{ij} are referred to as the Leonard stresses, cross stresses, and sub-grid scale Reynolds-stresses respectively, and are defined as:

$$L_{ij} = \overline{\bar{u}_i \bar{u}_j} - \bar{u}_i \bar{u}_j \quad (3.2.2.5)$$

$$C_{ij} = \overline{\bar{u}_i u'_j} + \overline{\bar{u}_j u'_i} \quad (3.2.2.6)$$

$$R_{ij} = \overline{u'_i u'_j} \quad (3.2.2.7)$$

By convention, L_{ij} , C_{ij} and R_{ij} are called stresses since their units are similar to that of the viscous stress tensor on the right side of Eqn. 3.2.2.2. Similar to viscous stresses, L_{ij} , C_{ij} and R_{ij} affect mass, momentum, and energy exchange in the flow field. Therefore, the convention of naming these terms is based upon both mathematical and physical arguments. Furthermore, the absence of the density term in the definition of each of these stresses in Eqns. 3.2.2.5-7 suggests that, in fact, they should be called specific stresses. The author's choice to call these terms 'stresses' is in order to avoid confusion with well-accepted conventions (Pope, 2000 and Gatski *et al.*, 1996).

The purpose of Eqn. 3.2.2.4 is to represent the non-linear term with resolved and unresolved components so they can be used in *LES*. Also, by re-arranging and grouping Eqn. 3.2.2.4, a physical meaning can be given to each stress. The Leonard-stress term represents interactions between the large resolved scales and between these large-scale eddies and the mean flow. The cross-stress term represents interaction between large and small scales of turbulence, and is usually responsible for the energy transfer from the

resolved to sub-grid scales. The Leonard- and cross-stresses indirectly account for the dissipative effects of the sub-grid model. Finally, the *SGS* Reynolds-stress term represents interaction among the sub-grid scales and is responsible for energy transfer from the sub-grid scales back to the resolved scales in a process known as backscatter. In order to close the system of filtered equations, the terms in Eqn. 3.2.2.4 need to be modeled.

3.2.3 Sub-grid Turbulence Modelling

It is obvious that C_{ij} and R_{ij} require sub-grid turbulence models as they contain terms representing sub-grid flow activity. It can be argued that L_{ij} only contains resolved terms and therefore can be calculated explicitly from the computed flow field. This only holds true when the filter width, $\bar{\Delta}$, is several orders of magnitude larger than the grid size, Δ . Otherwise, the term $\bar{u}_i \bar{u}_j$ will not be calculated accurately as it needs a finer spatial resolution than that of $\overline{\bar{u}_i \bar{u}_j}$. Sagaut (2002) explains that $\bar{u}_i \bar{u}_j$ is a quadratic term and it contains frequencies that are in theory higher than each of the terms composing it. Therefore, in most cases, when the filter width, $\bar{\Delta}$, is equal to the grid size, Δ , L_{ij} also needs to be modeled.

Although there is much debate as to which sub-grid model is best, the simplest approach is to group all of the stress terms in Eqn. 3.2.2.4 into a single sub-grid stress term, τ_{ij} :

$$\rho \frac{\partial \bar{u}_i}{\partial t} + \rho \frac{\partial (\bar{u}_i \bar{u}_j)}{\partial x_j} = -\frac{\partial \bar{p}}{\partial x_i} + \mu \frac{\partial}{\partial x_j} \left(\frac{\partial \bar{u}_i}{\partial x_j} + \frac{\partial \bar{u}_j}{\partial x_i} \right) - \rho \frac{\partial \tau_{ij}}{\partial x_j} \quad (3.2.3.1)$$

where τ_{ij} is defined as:

$$\tau_{ij} = L_{ij} + C_{ij} + R_{ij} \quad (3.2.3.2)$$

Often τ_{ij} is quantified using the eddy viscosity approach (Boussinesq, 1877). The use of the eddy viscosity to close the system of filtered governing equations is probably the most controversial aspect to turbulence modeling. Eddy viscosity, ν_T , and momentum transfer in turbulence are often explained with analogies to molecular viscosity and momentum transfer at the molecular level. Molecular viscosity is a property of the fluid and is defined as the ratio of viscous stress to strain rate. In laminar flows, energy dissipation and transport of mass, momentum and energy across streamlines are all mediated by the viscosity, so it is natural to assume that the effect of turbulence can be represented as an increase in effective viscosity. The mean free path in a gas is described as the average distance particles travel between collisions, thus defining a length scale for molecular momentum transfer. The similarity between representing the viscous stress tensor through random molecular fluctuations and representing the sub-grid stress tensor through sub-grid turbulence fluctuations is the essence of the Boussinesq approximation. Prandtl (1925) put forth a mixing length model which defined eddy viscosity as a product of a mixing length and a velocity scale:

$$\nu_T = l_{mix}^2 \left| \frac{\partial U}{\partial y} \right| \quad (3.2.3.3)$$

where l_{mix} is a characteristic length scale of turbulence analogous to the mean free path in

a gas, and $l_{mix} \left| \frac{\partial U}{\partial y} \right|$ is a characteristic velocity scale analogous to molecular velocity.

Applying these ideas to *LES* provides one way to close the system of filtered governing equations.

In the well known sub-grid model, proposed by Smagorinsky (1963), the sub-grid stress tensor, τ_{ij} , is correlated to the resolved strain rate tensor, \bar{S}_{ij} , using the eddy viscosity, ν_T :

$$\tau_{ij} - \frac{1}{3} \delta_{ij} \tau_{kk} = -2\nu_T \bar{S}_{ij} = -\nu_T \left(\frac{\partial \bar{u}_i}{\partial x_j} + \frac{\partial \bar{u}_j}{\partial x_i} \right) \quad (3.2.3.4)$$

The addition of $\frac{1}{3} \delta_{ij} \tau_{kk}$ is to ensure that when Eqn. 3.2.3.4 is contracted on the free indices, the result is $\tau = \tau_{ii}$, as otherwise it would be zero due to continuity. The eddy viscosity, ν_T , is determined from dimensional analysis:

$$\nu_T = (C_s \bar{\Delta})^2 |\bar{S}| \quad (3.2.3.5)$$

where C_s is the Smagorinsky constant and the resolved strain-rate magnitude is $|\bar{S}| = (2\bar{S}_{ij}\bar{S}_{ij})^{\frac{1}{2}}$. The filter width, $\bar{\Delta}$, is the characteristic length scale of the sub-grid motion. This length scale along with the velocity scale $\bar{\Delta}|\bar{S}|$ is analogous to Prandtl's mixing length model discussed above. It is often desirable to calibrate model constants using well-established benchmarks. The decay of isotropic turbulence is an often-used benchmark to calibrate turbulence models. The energy distribution in the inertial sub range for isotropic turbulence is:

$$E(k) = C_k \varepsilon^{\frac{2}{3}} \kappa^{-\frac{5}{3}} \quad (3.2.3.6)$$

where $C_k \approx 1.6$, ε , κ are the Kolmogorov constant, dissipation rate, and wave number, respectively. The resolved kinetic energy equation, which is similar to the turbulence kinetic energy equation, is defined as:

$$\begin{aligned} \frac{\partial \bar{q}^2}{\partial t} + \frac{\partial (\bar{q}^2 \bar{u}_j)}{\partial x_j} = \frac{\partial}{\partial x_j} \left(-2 \bar{p} \bar{u}_j - 2 \bar{u}_j \tau_{ij} + \frac{1}{\text{Re}} \frac{\partial \bar{q}^2}{\partial x_j} \right) \\ - \frac{2}{\text{Re}} \frac{\partial \bar{u}_i}{\partial x_j} \frac{\partial \bar{u}_i}{\partial x_j} + 2 \tau_{ij} \bar{S}_{ij} \end{aligned} \quad (3.2.3.7)$$

where $\bar{q}^2 = \bar{u}_i \bar{u}_i$ is the resolved kinetic energy. In Eqn. 3.2.3.7, the resolved dissipation represents the energy transfer between resolved and sub-grid scales and is defined as:

$$\bar{\varepsilon} = \nu_T |\bar{S}|^2 = (C_s \bar{\Delta})^2 |\bar{S}|^3 \quad (3.2.3.8)$$

Furthermore, the strain rate can be estimated to be:

$$|\bar{S}| = 2 \int_0^{\kappa_c} k^2 E(\kappa) d\kappa = \frac{3}{2} C_k \varepsilon^{\frac{2}{3}} \kappa_c^{\frac{4}{3}} \quad (3.2.3.9)$$

Lilly (1966) assumed that $\pi / \bar{\Delta} = \kappa_c$ and $\bar{\varepsilon} = \varepsilon$ since, at the resolved scales, energy dissipated through molecular viscosity is considered negligible compared to the energy transferred to smaller sub-grid turbulence scales. Smagorinsky's constant calibrated for isotropic turbulence is:

$$C_s = \frac{1}{\pi} \left(\frac{2}{3 C_k} \right)^{\frac{3}{4}} = 0.18 \quad (3.2.3.10)$$

Caution must be used when using eddy-viscosity-based sub-grid models. For instance,

with Smagorinsky's model, it must be assumed that the sub-grid stress tensor, τ_{ij} , is always aligned with the resolved strain-rate tensor, \bar{S}_{ij} . The Smagorinsky model is considered to be one of the simplest sub-grid models for *LES* and therefore it is not computationally expensive. If the computed flow is such that the sub-grid stress tensor can be assumed to align with the resolved strain rate tensor, and the percentage of turbulence allocated to the sub-grid model is small, the use of the Smagorinsky model can be justified.

Hughes *et al.* (2001) investigated the prediction capability of several sub-grid models on the decay of homogeneous isotropic turbulence including the Smagorinsky, dynamic Smagorinsky, Small-Small, and Large-Small models. The dynamic Smagorinsky model uses a procedure developed by Germano *et al.* (1991) and Lilly (1992), where the Smagorinsky coefficient is allowed to vary in space and time. The Small-Small and Large-Small models refer to multi-scale formulations for the eddy-viscosity term:

$$v'_T = (C'_s \Delta')^2 \nabla \bar{u}_i \quad (3.2.3.11)$$

$$v'_T = (C'_s \Delta')^2 \nabla u'_i \quad (3.2.3.12)$$

where Eqns. 3.2.3.11 and 3.2.3.12 correspond to the Large-Small and Small-Small models, respectively.

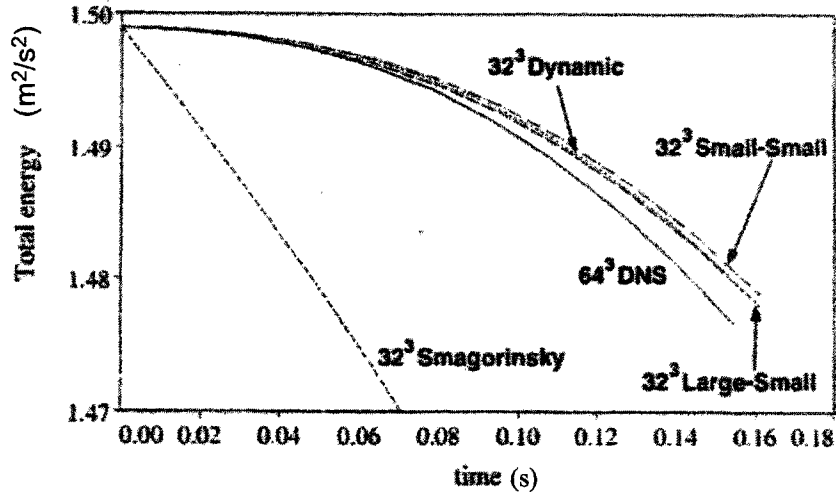


Figure 3.2.3.1: Decay of isotropic turbulence: inviscid case, reproduced from Hughes *et al.* (2001)

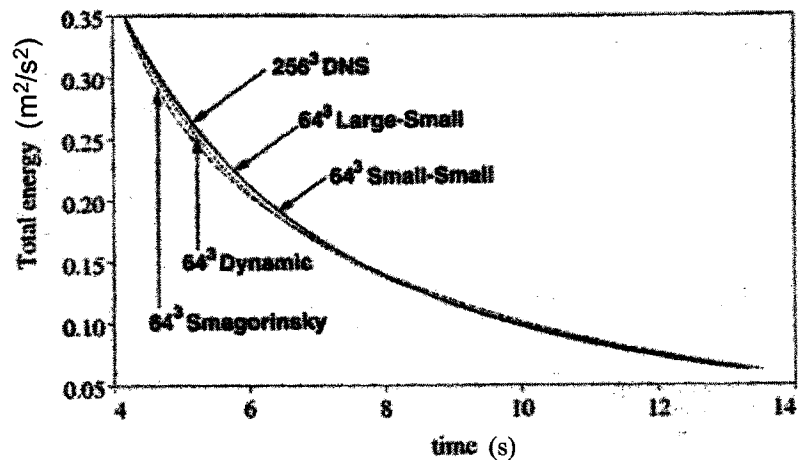


Figure 3.2.3.2: Decay of isotropic turbulence: viscous case, reproduced from Hughes *et al.* (2001)

The inconsistent prediction capability of the Smagorinsky model is shown in Figures 3.2.3.1 and 3.2.3.2. The discrepancy between the Smagorinsky model and *DNS* data in Figure 3.2.3.1 is due to excess dissipation from the eddy-viscosity approximation. For the viscous case in Figure 3.2.3.2, the eddy viscosity model performs quite well

compared to *DNS* data. The improved accuracy is attributed to the refined computational grid, as less of the turbulence spectrum is allocated to the sub-grid model.

3.3 Reynolds-Averaged Navier-Stokes Models

Due to current capabilities of computational resources, Reynolds-averaged-Navier-Stokes (*RANS*) models have been the most widely used turbulence models for engineering applications. Similar to *LES*, *RANS* simulations attempt to reduce computational resources by allocating turbulence to a model. A major difference between *LES* and *RANS* simulations is the percentage of turbulence allocated to the model. As shown in Section 3.2, *LES* uses a kernel filter to resolve a large portion of the turbulence and only allocates a small portion of turbulence to a sub-grid model. As visually illustrated in Figure 3.3.1, *RANS* simulations allocate all of the turbulence to the model.

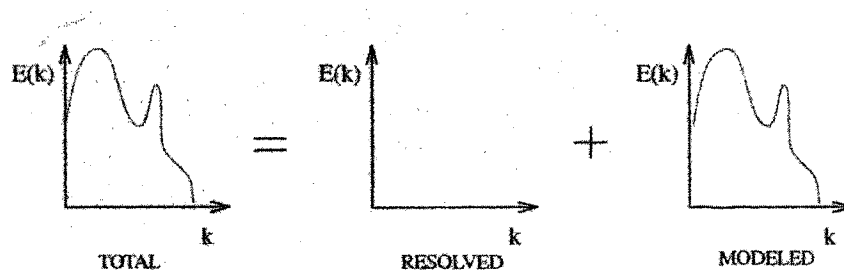


Figure 3.3.1: Symbolic decomposition of the energy spectrum using Reynolds-averaged techniques, reproduced from Sagaut (2002)

3.3.1 Reynolds-Averaging of Governing Equations

Similar to decomposition in *LES*, the Reynolds-averaging process entails decomposing each variable in the governing equations into mean and fluctuating components:

$$f = F + f' \quad (3.3.1.1)$$

where f is an instantaneous variable which can vary both in space and time, F is a Reynolds-averaged value of f , and f' is the fluctuating component of f . The type of Reynolds operator determines exactly how the variables will be decomposed and averaged. Temporal, F_{TR} ; spatial, F_{SR} ; or ensemble averages, F_{ER} ; are all viable operators:

$$F_{TR}(x) = \lim_{T_R \rightarrow \infty} \frac{1}{T_R} \int_t^{t+T_R} f(x,t) dt \quad (3.3.1.2)$$

$$F_{SR}(x) = \lim_{V_R \rightarrow \infty} \frac{1}{V_R} \iiint_{V_R} f(x,t) dV_R \quad (3.3.1.3)$$

$$F_{ER}(x,t) = \lim_{N_R \rightarrow \infty} \frac{1}{N_R} \sum_{n=1}^{N_R} f_n(x,t) \quad (3.3.1.4)$$

where T_R , V_R , and N_R are the averaging time, volume, and number of samples, respectively. All of these averages are considered to be identical as long as each of the respective values T_R , V_R , and N_R approach infinity. For the temporal average, the requirement of T_R approaching infinity is equivalent to specifying a large separation of time scales between the mean and fluctuating components. Only temporal or time averages will be considered from this point forward.

The Reynolds-operator is applied to the governing equations in the same manner as the kernel filter was applied to the governing equations in *LES*. In contrast to filtering, Reynolds-averaging contains the following rules due to the large separation of scales between t and T_R :

$$\lim_{T_R \rightarrow \infty} \frac{1}{T_R} \int_t^{t+T_R} F(x) dt = F(x) \quad (3.3.1.5)$$

$$\lim_{T_R \rightarrow \infty} \frac{1}{T_R} \int_t^{t+T_R} f'(x) dt = 0 \quad (3.3.1.6)$$

$$\lim_{T_R \rightarrow \infty} \frac{1}{T_R} \int_t^{t+T_R} F(x) f'(x) dt = \left(\lim_{T_R \rightarrow \infty} \frac{1}{T_R} \int_t^{t+T_R} F(x) dt \right) \left(\lim_{T_R \rightarrow \infty} \frac{1}{T_R} \int_t^{t+T_R} f'(x) dt \right) = 0 \quad (3.3.1.7)$$

As the Reynolds operator is applied to the governing equations, the result is the Reynolds-Averaged Navier-Stokes equations, which are defined as:

$$\frac{\partial \overline{U}_i}{\partial x_i} = 0 \quad (3.3.1.8)$$

$$\rho \frac{\partial \overline{U}_i}{\partial t} + \rho \frac{\partial \overline{u_i u_j}}{\partial x_j} = -\frac{\partial P}{\partial x_i} + \mu \frac{\partial}{\partial x_j} \left(\frac{\partial \overline{U}_i}{\partial x_j} + \frac{\partial \overline{U}_j}{\partial x_i} \right) \quad (3.3.1.9)$$

for an incompressible flow. Similar to the filtered Navier-Stokes equations, the non-linear term, $\overline{u_i u_j}$, must be further decomposed:

$$\overline{u_i u_j} = \overline{(U_i + u'_i)(U_j + u'_j)} = \overline{U_i U_j} + \overline{U_i u'_j} + \overline{U_j u'_i} + \overline{u'_i u'_j} = U_i U_j + \overline{u'_i u'_j} \quad (3.3.1.10)$$

It should be noted that Eqn. 3.3.1.10 looks very similar to Eqn. 3.2.2.4 with the exception that L_{ij} and C_{ij} are equal to zero due to the rules of the Reynolds-operator specified in Eqns. 3.3.1.5-7. The last term in Eqn. 3.3.1.10 is simply called the Reynolds-stress

tensor instead of *SGS* Reynolds-stress tensor. In contrast to filtering, most literature that use Reynolds-averaging techniques refer to $\overline{\rho u'_i u'_j}$ as the Reynolds-stress tensor as it has the same units as the viscous stress term in the Navier-stokes equation (Pope, 2000 and Gatski *et al.*, 1996). The most recognized form of the Reynolds-averaged-Navier-Stokes equation is stated as:

$$\rho \frac{\partial U_i}{\partial t} + \rho \frac{\partial (U_i U_j)}{\partial x_j} = -\frac{\partial P}{\partial x_i} + \mu \frac{\partial}{\partial x_j} \left(\frac{\partial U_i}{\partial x_j} + \frac{\partial U_j}{\partial x_i} \right) - \rho \frac{\partial \overline{u'_i u'_j}}{\partial x_j} \quad (3.3.1.11)$$

Modeling the Reynolds-stress term, $\overline{\rho u'_i u'_j}$, remains the most difficult task of the *RANS* approach. The complexity of turbulence makes it difficult for any single model to represent all turbulent flows. Generally, the *RANS* approach to modeling turbulence can be grouped into two main categories. These include models that calculate each of the Reynolds-stresses directly and models that use an eddy viscosity to relate the Reynolds-stresses to the local strain rates. Turbulence models can be further distinguished based upon the amount of differential equations they solve in addition to the Navier-Stokes equations. Examples include two-equation, one-equation, and zero-equation (i.e. algebraic) models.

3.3.2 Reynolds-Stress Models

As Reynolds-stress models evaluate each Reynolds-stress component independently, these models are considered to be the most elaborate *RANS* turbulence closures. Although the variations of Reynolds-stress models are quite numerous, they

can be grouped into two main categories. Algebraic Reynolds-stress models calculate each component of the Reynolds-stress tensor from an algebraic equation. Although they are considered to be computationally inexpensive, they are not universal in their application range. Differential Reynolds-stress models use a partial differential equation to calculate each Reynolds-stress. These models are considered the most computationally expensive *RANS* models, but in theory have the highest potential for solution accuracy.

3.3.2.1 Algebraic Reynolds-Stress Models

As described above, algebraic Reynolds-stress models are the family of turbulence models that solve an algebraic equation for each of the Reynolds-stresses. In certain cases, models using algebraic equations for the Reynolds-stresses have proven to predict flows just as accurately as differential Reynolds-stress models. An advantage for these models is that they do not use the Boussinesq eddy-viscosity approximation in representing the Reynolds-stress tensor (the eddy-viscosity is used in the diffusion term of some differential Reynolds-stress models, Section 3.3.2.2.1). As will be explained later, eddy viscosity models fail in the presence of sudden changes in the mean strain rate or extra rates of strain due to stream line curvature such as rotating or swirling flows. Optimized algebraic stress models have produced fairly accurate results for more complicated flows, including flows with streamline curvature.

Armfield and Fletcher (1989) used experimental data from Clausen (1987) of moderate swirling flow through a 20° diffuser to compare two-equation models with

algebraic Reynolds-stress models. Two-equation models are described in detail in Section 3.3.3. The two-equation models used in Armfield and Fletcher's study were the standard k - ε model and a k - ε model with a swirl modification to the ε equation. It was concluded from this study that both the k - ε and algebraic Reynolds-stress models could be adapted to this particular flow. Although the two algebraic Reynolds-stress models examined by the authors performed better than the k - ε model for the mean flow quantities, they failed to capture the anisotropy of the Reynolds-stress tensor. This failure could be attributed to the fact that algebraic relations were used instead of solving the differential transport equations for each Reynolds-stress.

Gatski and Speziale (1993) demonstrated the problems associated with using algebraic Reynolds-stress models for complex flows using a variation of Pope's model (Pope, 1975). The performance of this model, termed explicit algebraic stress model (*ASM*), is shown in Figure 3.3.2.1.1 for a rotating homogeneous shear flow.

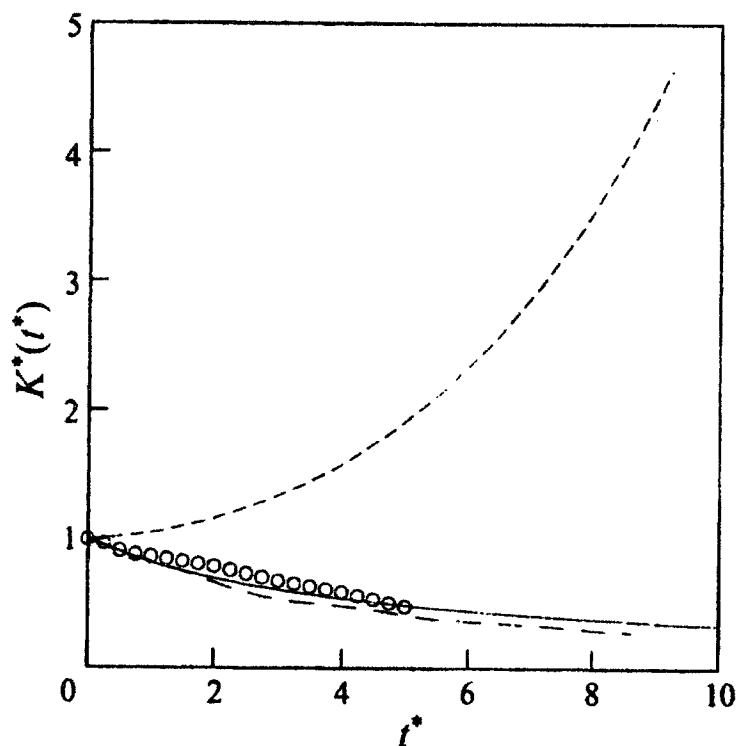


Figure 3.3.2.1.1: Evolution of turbulence kinetic energy, (— explicit ASM , --- SSG , · · · $k-\epsilon$, ○ LES), reproduced from Gatski and Speziale (1993)

In Figure 3.3.2.1.1, t^* , K^* , and SSG , represent the normalized time, normalized turbulence kinetic energy, and a differential Reynolds-stress model of Speziale *et al.* (1991), respectively. The ASM predicts values of turbulence kinetic energy close to the predicted values of the SSG model and LES . As expected, the $k-\epsilon$ model performs poorly in determining the turbulence kinetic energy for this swirling flow. For this particular flow, this study confirms that algebraic stress models can be modified to perform at the same level as differential Reynolds-stress models and LES in terms of accuracy. For a more universal model, accurately predicting the Reynolds-stress tensor requires the use of additional partial differential equations.

3.3.2.2 Differential Reynolds-Stress Turbulence Models

Differential Reynolds-stress models use a differential equation for each Reynolds-stress, thus requiring much more computing power than any other *RANS* model, but claim to be the most accurate for complex flows. Differential Reynolds-stress models date back to 1951 when Rotta (1951) proposed the first variant. These closures account for the convection, diffusion, production, and dissipation of the Reynolds-stresses allowing the model to capture effects such as streamline curvature, system rotation and stratification. The differential equations for the Reynolds-stresses are determined by taking moments of the Navier-Stokes equations, which involves multiplying them by a fluctuating component of velocity and then time averaging the product:

$$\begin{aligned} \frac{\partial \overline{u'_i u'_j}}{\partial t} + U_k \frac{\partial \overline{u'_i u'_j}}{\partial x_k} = & -\overline{u'_i u'_k} \frac{\partial U_j}{\partial x_k} - \overline{u'_j u'_k} \frac{\partial U_i}{\partial x_k} \\ & + \varepsilon_{ij} + \Pi_{ij} + \frac{\partial}{\partial x_k} \left[\nu \frac{\partial \overline{u'_i u'_j}}{\partial x_k} + C_{ijk} \right] \end{aligned} \quad (3.3.2.2.1)$$

where

$$\Pi_{ij} = -\overline{\frac{p'}{\rho} \left(\frac{\partial u'_i}{\partial x_j} + \frac{\partial u'_j}{\partial x_i} \right)} \quad (3.3.2.2.2)$$

$$\varepsilon_{ij} = 2\nu \overline{\frac{\partial u'_i}{\partial x_k} \frac{\partial u'_j}{\partial x_k}} \quad (3.3.2.2.3)$$

$$\rho C_{ijk} = \overline{\rho u'_i u'_j u'_k} + \overline{p' u'_i} \delta_{jk} + \overline{p' u'_j} \delta_{ik} \quad (3.3.2.2.4)$$

The Reynolds-stress equation is closed by modelling the specific dissipation rate tensor, ε_{ij} , the turbulent transport tensor, C_{ijk} , and the pressure-strain correlation tensor, Π_{ij} . The Reynolds-stress equation can be regrouped in a more compact form:

$$\rho \frac{\partial}{\partial x_k} \left(U_k \overline{u'_i u'_j} \right) = \underbrace{P_{ij}}_{\text{production}} + \underbrace{d_{ij}}_{\text{diffusion}} + \underbrace{\Pi_{ij}}_{\text{pressure-strain}} + \underbrace{\varepsilon_{ij}}_{\text{dissipation}} \quad (3.3.2.2.5)$$

where the production term, P_{ij} , can be calculated explicitly:

$$P_{ij} = -\rho \overline{u'_i u'_k} \frac{\partial U_j}{\partial x_k} - \rho \overline{u'_j u'_k} \frac{\partial U_i}{\partial x_k} \quad (3.3.2.2.6)$$

3.3.2.2.1 Diffusion Term

The diffusion term in Eqn. 3.3.2.2.5 is defined as follows:

$$d_{ij} = -\frac{\partial}{\partial x_k} \left[\underbrace{\overline{u'_i u'_j u'_k}}_{\text{turbulent diffusion}} + \frac{1}{\rho} \left(\underbrace{\overline{p' u'_j} \delta_{ik} + \overline{p' u'_i} \delta_{jk}}_{\text{pressure diffusion}} \right) - \underbrace{\nu \frac{\partial \overline{u'_i u'_j}}{\partial x_k}}_{\text{Reynolds-stress diffusion}} \right] \quad (3.3.2.2.1.1)$$

Hytopoulos and Simpson (1993) claim that the diffusion term, d_{ij} , is difficult to modify, and it is equally difficult to monitor its success. Almost all current differential Reynolds-stress models rely on the gradient-type diffusion hypothesis for this term:

$$d_{ij} = \frac{\partial}{\partial x_k} \left(\frac{\mu_T}{\sigma_k} \frac{\partial \overline{u'_i u'_j}}{\partial x_k} \right) \quad (3.3.2.2.1.2)$$

where μ_T and σ_k are the eddy viscosity and closure constant, respectively. Speziale (1991) showed that this method is valid only if there is a definite separation of scales between mean and fluctuating fields at the third-moment level. Unfortunately, obtaining experimental data of higher-moment information is extremely difficult, and therefore

comparing the capability of different diffusion models is also difficult.

To advance the modelling of diffusion transport, d_{ij} , more attention needs to be given to the turbulent diffusion term in Eqn. 3.3.2.2.1.1. A closure method specified by Speziale (1991) assumes that turbulent diffusion can be grouped with pressure diffusion terms to form a third-order-diffusion term, T_{ij} . In modeling the third-order-diffusion term, T_{ij} , the pressure diffusion terms are often considered to be negligible. Again, this assumption requires a clear-cut separation of scales between mean and fluctuating fields. Hanjalic and Launder (1972) developed a dynamic equation for the third-order diffusion term in which the pressure-diffusion term was considered to be negligible:

$$\overline{u'_i u'_j u'_k} = -C_s^* \frac{k}{\varepsilon} \left[\overline{u'_i u'_l} \frac{\partial \overline{u'_l u'_k}}{\partial x_l} + \overline{u'_j u'_l} \frac{\partial \overline{u'_l u'_k}}{\partial x_l} + \overline{u'_k u'_l} \frac{\partial \overline{u'_l u'_j}}{\partial x_l} \right] \quad (3.3.2.2.1.3)$$

where C_s^* is a constant. In their derivation, they assumed that the convection, mean field velocity gradient production, pressure transport, and dissipation terms in the turbulent diffusion transport equation were negligible. Also, it was assumed that the distribution of velocity fluctuations is Gaussian.

Lumley (1978) developed a model for the triple velocity correlation and for the pressure diffusion term. This model was based on the assumption that turbulence tends to relax to a Gaussian state in the absence of inhomogeneity. It is also assumed that the length scale of turbulence is small compared to the length scale of any inhomogeneity. This model is more complicated, but Lumley considers it to be more complete.

Hytopoulos and Simpson (1993) claim the failure of conventional models for the triple products of velocity are an important cause for the limited success of differential

Reynolds-stress models. They also claim that appropriate modelling of the turbulent diffusion terms in the differential Reynolds-stress models need a new approach differing from the gradient-diffusion-type hypothesis. Most turbulence models tailored for swirling flow applications use the gradient diffusion hypothesis for the diffusion term.

3.3.2.2.2 Pressure-Strain Term

The pressure- strain term, Π_{ij} , plays the most crucial role in differential Reynolds-stress models. Most models for the pressure-strain term that have been used in conjunction with differential Reynolds-stress models are based on the assumption of local homogeneity. For homogeneous turbulent flows, where the mean velocity gradients are spatially uniform, the pressure-strain term can be written as follows:

$$\Pi_{ij} = A_{ij} + M_{ijkl} \frac{\partial U_k}{\partial x_l} \quad (3.3.2.2.1)$$

where A_{ij} involves a triple correlation of fluctuating velocity, and is called the slow pressure/rate-of-strain term. M_{ijkl} involves the interaction of fluctuating velocities and the mean velocity gradient, and is called the rapid-strain term. The pressure-strain correlation can be separated into the slow and rapid terms because the correlation between rapid and slow fluctuating pressures for homogenous flow is quite low (Rogers *et al.*, 1986).

Usually the pressure-strain, or redistribution term, Π_{ij} , can be broken down into three contributions:

$$\Pi_{ij} = \Pi_{ij,1} + \Pi_{ij,2} + \Pi_{ij,3} \quad (3.3.2.2.2)$$

where $\Pi_{ij,1}$ is Rotta's linear "return to isotropy" term, $\Pi_{ij,2}$ is the "isotropization of productions" term, and $\Pi_{ij,3}$ is the "wall reflections" term. Wall reflection terms are used to inhibit the tendency of $\Pi_{ij,1}$ and $\Pi_{ij,2}$ to excessively isotropize the turbulence field near walls and fluid interfaces. The main difference between most models that modify the pressure-strain term is the order of the correlation. The *LRR-IP* and *LRR-QI*, which are models developed by Launder *et al.* (1975), have a linear correlation for the pressure-strain term. The *SSG* model developed by Speziale *et al.* (1991) uses a quadratic relationship for this.

Chen and Lin (1999) performed research on strongly swirling pipe flows comparing differential Reynolds-stress models to the standard $k-\varepsilon$ two-equation model (Figure 3.3.2.2.1). Each turbulence model was tested at swirl numbers of 2.25 and 0.85. Experimental data from Kitoh (1991) was used for low swirl number model evaluations and data from So *et al.* (1984) was used for high swirl number model evaluations. Fu *et al.* (1987) developed a differential Reynolds-stress model denoted as *IPCM*, which is an adapted version of the model proposed by Launder *et al.* (1975).

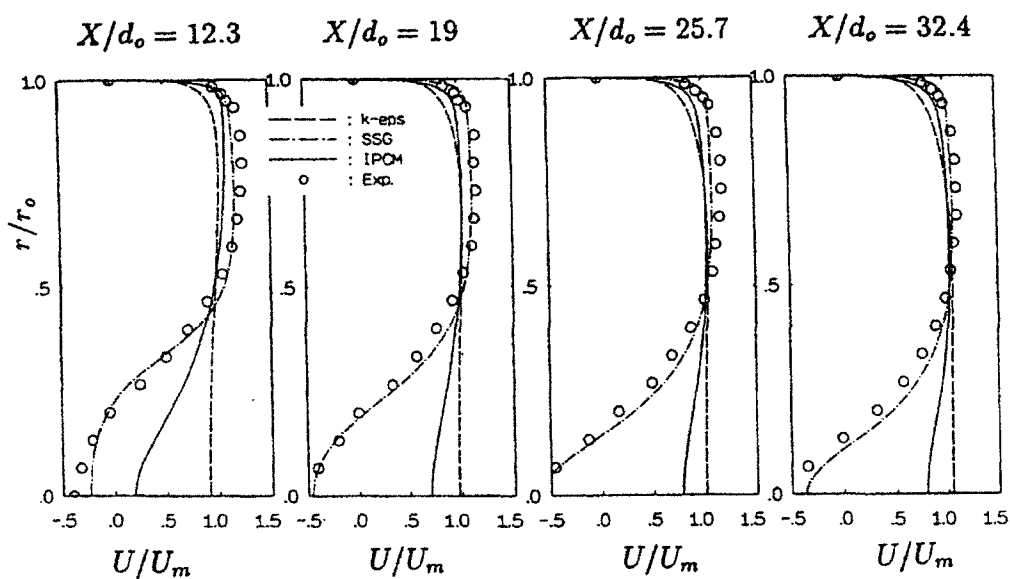


Figure 3.3.2.2.1: Axial velocity distribution comparisons for $k-\epsilon$, SSG, IPCM, and experimental data at low swirl, reproduced from Chen and Lin (1999)

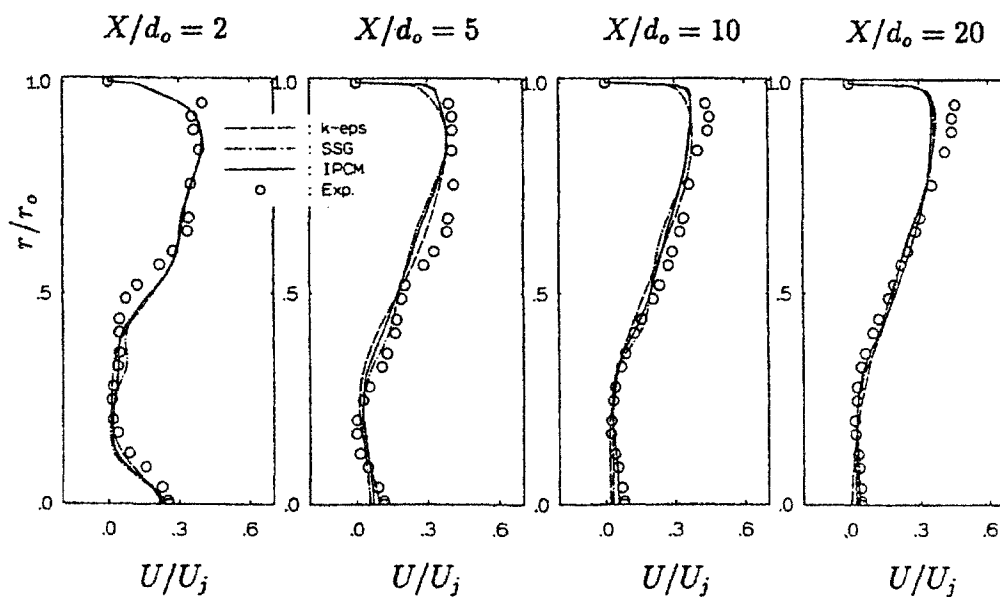


Figure 3.3.2.2.2: Axial velocity distribution comparisons for $k-\epsilon$, SSG, IPCM, and experimental data at high swirl, reproduced from Chen and Lin (1999)

Chen and Lin (1999) concluded that at the higher swirl number of 2.25, both the linear pressure-strain model (*IPCM*) and the quadratic pressure-strain model (*SSG*) predicted the flow adequately (Figure 3.3.2.2.2.2). At the lower swirl number of 0.85, the *IPCM* model showed excessively diffusive flow fields while the *SSG* predicted the flow accurately (Figure 3.3.2.2.2.1). The *k-ε* model, however, predicted excessively diffusive flow fields at both swirl numbers. The inherent capability of the differential Reynolds-stress models to capture strong swirl and turbulence interaction was evident at high swirl numbers.

The *SSG* Reynolds-stress model that includes a quadratic pressure-strain correlation produced superior results than differential Reynolds-stress models with a linear pressure-strain term. This general trend leads to the conclusion that the order of the pressure-strain correlation has an effect on solution accuracy. Launder and Craft (1991) developed a cubic pressure strain correlation as a function of the anisotropy tensor. Laurence (1992) compared the cubic pressure-strain model to a linear pressure-strain model and concluded that the cubic pressure-strain model predicted velocity and Reynolds-stress distributions more accurately.

Although modifications to the pressure-strain term can produce improvements in the model's predictive capability, these refined models tend to become specialized towards certain conditions and cannot perform in other flow environments. Basara *et al.* (1995) compared the *SSG* Reynolds-stress model specified by Speziale (1991) with the standard *k-ε* model. It was concluded that both models failed to predict the flow characteristics in two and three dimensional turn-around ducts.

3.3.2.2.3 Dissipation Term

The dissipation term, ε_{ij} , is defined as:

$$\varepsilon_{ij} = \frac{2}{3} \rho \varepsilon \delta_{ij} \quad (3.3.2.2.3.1)$$

where ε is the scalar dissipation rate often calculated by the following transport equation:

$$\rho \frac{\partial \varepsilon}{\partial t} + \rho U_j \frac{\partial \varepsilon}{\partial x_j} = C_{\varepsilon 1} \frac{\varepsilon}{k} \overline{\rho u'_i u'_j} \frac{\partial U_i}{\partial x_j} - C_{\varepsilon 2} \rho \frac{\varepsilon^2}{k} \quad (3.3.2.2.3.2)$$

The dissipation term, ε_{ij} , is usually considered to be isotropic, enabling component dissipation rates to be expressed in terms of the dissipation rate of turbulence energy, ε . Direct numerical simulations performed by Kim *et al.* (1987) suggest that at the fine scales where dissipation is known to exist, the nature of the dissipation is anisotropic. Therefore, there is room to improve differential Reynolds-stress models by modifying the dissipation term.

Lumely (1983) claims that the dissipation equation is the weakest point of differential Reynolds-stress models. Leschziner (1990) states, “the semi-intuitive nature of this equation does not only make it a weak, if not the weakest, element in the present modelling strategy, but also makes it difficult to introduce rationally and physically sound modifications designed to cure defects known to originate from the equation.” He goes on to say that one such defect is the prediction of excessive levels of length scale $k^{3/2} / \varepsilon$ in high shear regions in the presence of an adverse pressure gradient. Length scales are known to be insensitive to such regions of departure from equilibrium

conditions.

Barlow and Johnson (1988) claim that the failure of differential Reynolds-stress models to accurately capture turbulence in concave boundary layers can be attributed to the inadequacy of the ε equation. Therefore, Luo and Lakshminarayana (1997) studied the ability of differential Reynolds-stress models with modified dissipation equations to predict flow characteristics on surfaces with concave curvature. Launder *et al.* (1977) modified the generation term of the standard dissipation equation to include an additional sink term. The modified dissipation equation is termed *LPS*, and is defined as:

$$\rho \frac{\partial \varepsilon}{\partial t} + \rho U_j \frac{\partial \varepsilon}{\partial x_j} = C_{\varepsilon 1} \frac{\varepsilon}{k} \nu_T \left(\frac{\partial U_i}{\partial x_j} \right)^2 - C_{\varepsilon 2} \rho \frac{\varepsilon^2}{k} + \frac{\varepsilon}{k} A_i \quad (3.3.2.2.3.3)$$

where $C_{\varepsilon 1}$ and $C_{\varepsilon 2}$ are empirical constants, and the extra strain rate term is defined as:

$$A_i = \frac{U_i / x_j}{\frac{\partial U_i}{\partial x_j}} \quad (3.3.2.2.3.4)$$

Lumley (1992) developed a new dissipation equation based on the concept of spectral energy transfer for non-equilibrium flows. Similar to the dissipation equation proposed by Launder *et al.* (1977), the source term is modelled with the invariant strain rate, $|S|$. Taking one step further, Shih *et al.* (1995) modelled the dynamic equation of the mean-square vorticity fluctuation to derive a transport equation for the dissipation rate, ε . This new dissipation equation is termed *Shih- ε* , and is defined as:

$$\rho \frac{\partial \varepsilon}{\partial t} + \rho U_j \frac{\partial \varepsilon}{\partial x_j} = \rho C_{\varepsilon 1}^S |S| \varepsilon - \rho C_{\varepsilon 2}^S \frac{\varepsilon^2}{k + \sqrt{\nu \varepsilon}} \quad (3.3.2.2.3.5)$$

where $C_{\varepsilon 1}^S$ and $C_{\varepsilon 2}^S$ are empirical constants, and the invariant strain rate defined as:

$$|S| = \sqrt{S_{ij}S_{ij}} \quad (3.3.2.2.3.6)$$

The differential Reynolds-stress models with the *LPS- ε* and *Shih- ε* dissipation equations provided excellent predictions of Reynolds-stresses throughout the boundary layer on the outer (concave) wall of a 90 degree curved duct (Luo and Lakshminarayana, 1997). Although differential Reynolds-stress models with the standard dissipation equation failed to capture the entire Reynolds-shear stress profile, the standard *k- ε* model failed to capture the profile completely. The study concluded that modifying the dissipation term can provide better predictions of wall-bounded flows with streamline curvature.

Modelling the flow along concave surfaces requires modifications to the dissipation equation if accurate Reynolds-stresses are to be predicted. Lin and Lu (1994) compared two differential Reynolds-stress models with the standard *k- ε* equation model at two different swirl numbers in a can-type gas-turbine combustor. The amount of fuel injected into the swirling stream was large and lead to a very strong interaction between the two flows. The two differential Reynolds-stress models were the *IP* model specified by Gibson and Launder (1978) and the *IP ε* model. The *IP ε* is a variant of the *IP* model with an anisotropic modified ε source term combined with a quadratic approximation of convection fluxes. The two swirl numbers investigated were 0.74 and 0.85.

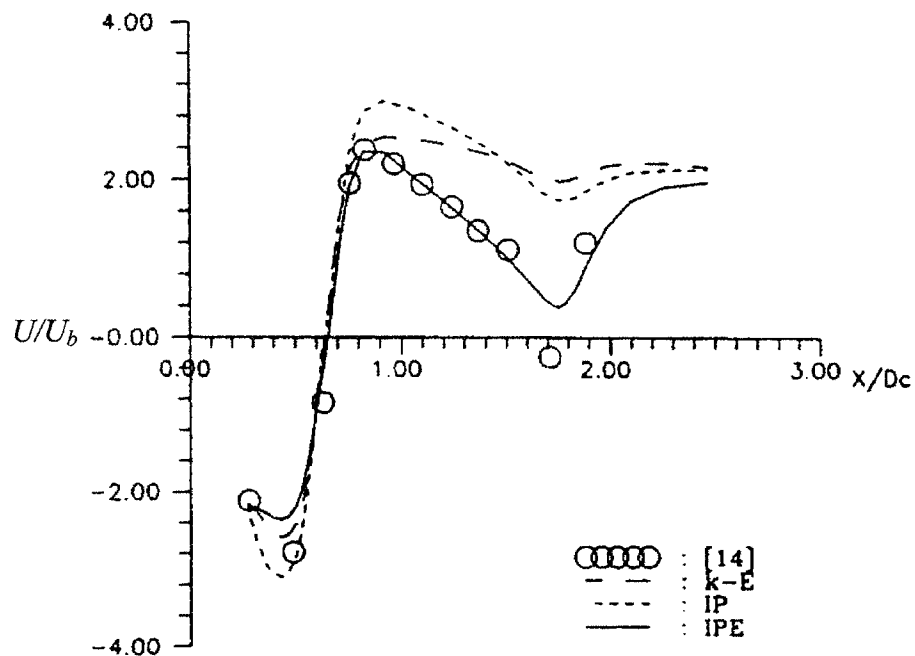


Figure 3.3.2.2.3.1: Sensitivity of centerline axial velocity variation to turbulence models, reproduced from Lin and Lu (1994)

As shown in Figure 3.3.2.2.3.1, the $IP\epsilon$ model performed the best at both swirl numbers while the $k-\epsilon$ model overestimated the diffusive nature of the flow and predicted an intense vortex core near the centerline region. The mean axial velocity, U , and axial location, x , are normalized by the bulk exit velocity, U_b , and the jet diameter, D_c , respectively.

Chaouat (1999) compared $k-\epsilon$, algebraic and differential Reynolds-stress models for fully developed channel flow in non-rotating and rotating frames of reference. The pressure-strain term used in the latter two models included wall reflection terms that were used to damp the isotropization of turbulence near the wall. The differential Reynolds-stress model included both modified pressure-strain and dissipation equations tailored for

rotating frames of reference. The predictions obtained from these models were compared to the results of *DNS* and *LES*. All three models adequately predicted the mean flow characteristics but the k - ϵ model failed to predict the Reynolds-stresses for both rotating and non-rotating flows due to the flawed Boussinesq approximation. The differential Reynolds-stress model performed the best in predicting mean velocity profiles and Reynolds-stresses in both rotating and non-rotating frames of reference. These results were in good agreement with the results of *DNS* and *LES*.

3.3.2.2.4 Methods of Higher Moments

Due to the non-linearity of the Navier-Stokes equation, taking higher moments will only yield additional equations along with additional constants (Wilcox, 1993). Calibrating a higher order model is much more difficult than calibrating a lower-order model simply due to the higher number of unknown constants. When properly calibrated, higher order models have a higher potential of accurately predicting a flow scenario than lower order models. However, due to the large amount of empirical constants, higher order models tend to be tailored for specific flow conditions and are not universal in their application. In general, higher moment models also tend to be more unstable requiring relaxation schemes, making them less robust in comparison to lower-moment models.

If the computational load required by differential Reynolds-stress models is too large, it is possible to reduce the number of equations used in predicting the transport of

turbulence. Two equation models are an alternative to the computationally expensive differential Reynolds-stress models.

3.3.3 Two-Equation Models

Eddy-viscosity-based two-equation models are an attempt to further reduce the computational load while still obtaining the important physics of the flow. Two-equation models calculate the Reynolds-stress tensor using the Boussinesq approximation:

$$\overline{u'_i u'_j} = -\nu_T \left(\frac{\partial U_i}{\partial x_j} + \frac{\partial U_j}{\partial x_i} \right) + \frac{2}{3} \delta_{ij} k \quad (3.3.3.1)$$

where k is the turbulence kinetic energy and is defined as:

$$k = \frac{1}{2} \overline{u'_i u'_i} \quad (3.3.3.2)$$

The addition of $\frac{2}{3} \delta_{ij} k$ is to ensure that when Eqn. 3.3.3.1 is contracted on the free indices, the result is k , as otherwise it would be zero due to continuity. The differential equation used to calculate k is obtained by taking the trace of the Reynolds-stress equation:

$$\rho \frac{\partial k}{\partial t} + \rho U_j \frac{\partial k}{\partial x_j} = \overline{\rho u'_i u'_i} \frac{\partial U_i}{\partial x_j} - \rho \varepsilon + \frac{\partial}{\partial x_j} \left[\mu \frac{\partial k}{\partial x_j} - \frac{1}{2} \overline{\rho u'_i u'_i u'_j} - \overline{p' u'_j} \right] \quad (3.3.3.3)$$

which includes unsteady, convection, production, dissipation, molecular diffusion, turbulence transport, and pressure diffusion terms, respectively. An assumption that the turbulent transport and pressure diffusion term can be grouped and behaves as a gradient-

transport process yields the following equation:

$$\frac{1}{2} \overline{\rho u'_i u'_i u'_j} + \overline{p' u'_j} = - \frac{\mu_T}{\sigma_k} \frac{\partial k}{\partial x_j} \quad (3.3.3.4)$$

Using this in Eqn. 3.3.3.3, the most common form of the turbulence kinetic energy transport equation is obtained:

$$\rho \frac{\partial k}{\partial t} + \rho U_j \frac{\partial k}{\partial x_j} = \overline{\rho u'_i u'_j} \frac{\partial U_i}{\partial x_j} - \rho \varepsilon + \frac{\partial}{\partial x_j} \left[\left(\mu + \frac{\mu_T}{\sigma_k} \right) \frac{\partial k}{\partial x_j} \right] \quad (3.3.3.5)$$

The transport equation for turbulence kinetic energy provides the velocity scale information for the turbulence. As recalled from Section 3.2.3, as per Prandtl's mixing length theory, the eddy-viscosity is based upon characteristic length and velocity scales of turbulence. For Smagorinsky's sub-grid model in *LES*, the length scale is determined from the filter width, $\bar{\Delta}$. As turbulence in *RANS* closure models is completely modelled, the local grid size, Δ , is not appropriate as a characteristic length scale. Generally, the choice of differential equation representing the length scale of turbulence is what differs among two-equation models.

3.3.3.1 Standard k - ε model

The most popular two-equation eddy-viscosity turbulence model is the standard k - ε model. The standard k - ε model is based on partial differential transport equations for turbulence kinetic energy, k , and turbulence dissipation rate, ε :

$$\rho \frac{\partial k}{\partial t} + \rho U_j \frac{\partial k}{\partial x_j} = \overline{\rho u'_i u'_j} \frac{\partial U_i}{\partial x_j} - \rho \varepsilon + \frac{\partial}{\partial x_j} \left[\left(\mu + \frac{\mu_T}{\sigma_k} \right) \frac{\partial k}{\partial x_j} \right] \quad (3.3.3.1.1)$$

$$\rho \frac{\partial \varepsilon}{\partial t} + \rho U_j \frac{\partial \varepsilon}{\partial x_j} = C_{\varepsilon 1} \frac{\varepsilon}{k} \overline{\rho u'_i u'_j} \frac{\partial U_i}{\partial x_j} - C_{\varepsilon 2} \rho \frac{\varepsilon^2}{k} + \frac{\partial}{\partial x_j} \left[\frac{\mu_T}{\sigma_\varepsilon} \frac{\partial \varepsilon}{\partial x_j} \right] \quad (3.3.3.1.2)$$

The values of the empirical constants appearing in these equations are:

$$C_{\varepsilon 1} = 1.44, C_{\varepsilon 2} = 1.92, \sigma_k = 1, \sigma_\varepsilon = 1$$

with k and ε obtained through Eqns. 3.3.3.1.1 and 3.3.3.1.2, the eddy-viscosity is calculated from the following equation:

$$\mu_T = \rho C_\mu \frac{k^2}{\varepsilon} \quad (3.3.3.1.3)$$

where $C_\mu = 0.09$ is a constant.

The dissipation equation, Eqn. 3.3.3.1.2, is identical to that used in differential Reynolds-stress models. For both types of models, it is assumed that the dissipation of Reynolds-stresses is isotropic. Since eddy-viscosity models often over-predict turbulence kinetic energy levels, correction terms can be included to either limit turbulence production or amplify the dissipation rate of turbulence. Adding a source term to the dissipation equation will have this effect, although it may provide misleading results.

The coefficients of the standard k - ε model are determined from series of assumptions. For example, the constant $C_\mu = 0.09$ is derived assuming an anisotropy ratio of 0.3 and equality of turbulence production and dissipation in a thin shear layer. Although the standard k - ε model provides reasonable results for simple non-rotating flow, it has difficulty predicting flows with anisotropic turbulence and streamline curvature. Laurence (1992) performed a simple test case of comparing differential Reynolds-stress

models with the standard k - ε model. The study illustrated the poor predictions of the eddy-viscosity model for the production of turbulence for flow around a cylinder.

Since the standard k - ε model is considered to be the preferred turbulence model in industrial applications due to its robustness in achieving fast convergence of the solution, several modifications have been made to predict swirling flows more accurately. The constant C_μ can be modified to account for the effects of streamline curvature. Yin *et al.* (1996) completed a study exploring the effects of a modified C_μ term in duct flow around a 90° bend with strong curvature. This study also compared the standard k - ε model with the *RNG* k - ε model. The *RNG* k - ε model is based on the renormalization group analysis of the Navier-Stokes equations. The transport equations for dissipation and turbulence production are identical to the standard model with the exception of the constants. Also, the *RNG* k - ε model calculates $C_{\varepsilon 1}$ as a function of the Reynolds-shear stresses, dissipation, and turbulence production.

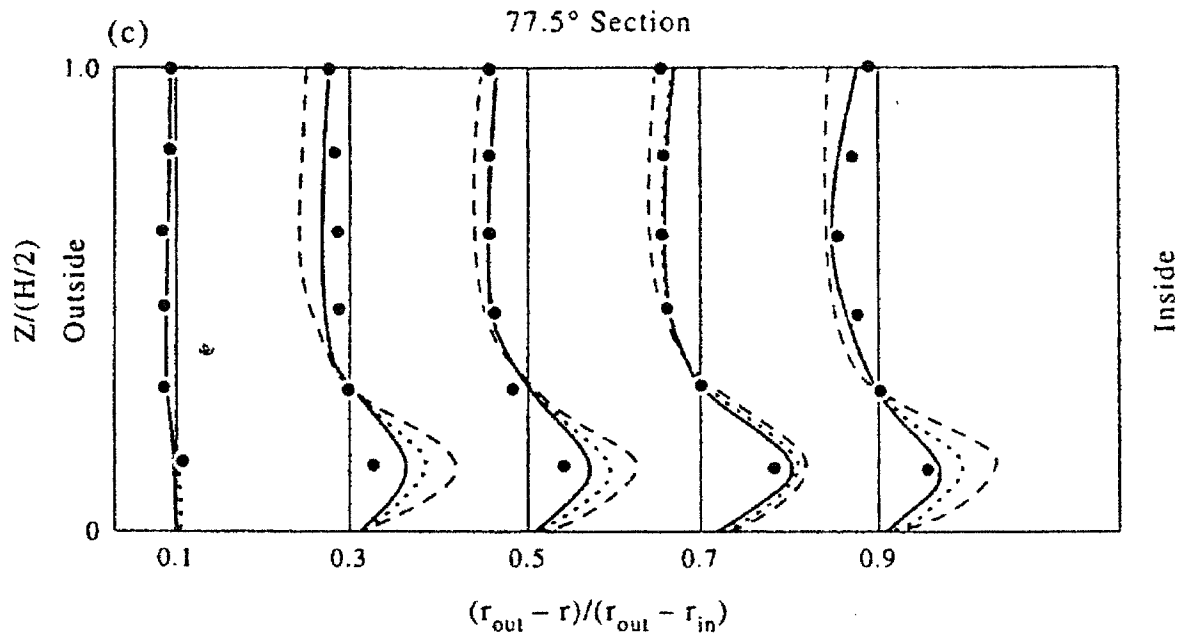


Figure 3.3.3.1.1: Radial velocity profiles of radial velocities at 77.5° stream-wise station (• experimental data, — $k-\epsilon$, - - - RNG $k-\epsilon$, — RNG $k-\epsilon$ model with C_μ modification), reproduced from Yin *et al.* (1996)

The radial velocities near the outer radius are predicted very consistently by each model included in the study. However, near the inner radius, it appears that models using a constant C_μ fail to predict radial velocity.

Gallardo and Lakshminarayana (1993) used algebraic approximations for the Reynolds-stress equations and derived an expression for C_μ . These models were tested for two-dimensional flow in a high-deflection turbine nozzle passage. The expression for C_μ accounts for the effects of streamline curvature and the pressure-strain in the flow. Although the dynamic C_μ model agreed well with experimental velocity data, it consistently over predicted the level of turbulence kinetic energy on the convex wall.

3.3.3.2 Other Two-Equation Eddy-Viscosity Models

The $k-\omega$ model for turbulence is based on the transport equation for turbulence kinetic energy, k , and specific-dissipation rate of turbulence, ω . The advantage of the $k-\omega$ model lies in the near wall treatment for low-Reynolds number computations. The $k-\omega$ model performs better in predicting flows near the wall than the standard $k-\varepsilon$ model (Wilcox, 1998). The specific dissipation transport equation is defined as:

$$\rho \frac{\partial \omega}{\partial t} + \rho U_j \frac{\partial \omega}{\partial x_j} = \alpha_\omega \frac{\omega}{k} \overline{\rho u'_i u'_j} \frac{\partial U_i}{\partial x_j} - \beta_\omega \rho \omega^2 + \frac{\partial}{\partial x_j} \left[(\mu + \sigma_\omega \mu_T) \frac{\partial \omega}{\partial x_j} \right] \quad (3.3.3.2.1)$$

where α_ω , β_ω , and σ_ω are constants (Wilcox, 1998). The relationship between ε and ω is given as:

$$\varepsilon = k\omega \quad (3.3.3.2.2)$$

The Wilcox $k-\omega$ model is the most widely tested version of this type of model. Menter (1994) concluded that the Wilcox $k-\omega$ model performs well for low-Reynolds number computations deep in the boundary layer, but is extremely sensitive to free stream conditions. To solve this problem, a blended $k-\omega$ and $k-\varepsilon$ turbulence model was created called the Baseline ($B-L$) $k-\omega$ model. The $k-\varepsilon$ model is used in the outer part of the boundary layer due to its insensitivity to free stream conditions. The $k-\omega$ model is used near the surface due to the fact that it does not involve the complex non-linear damping functions required for applying the $k-\varepsilon$ model in the vicinity of solid surfaces. The blended treatment results in a more robust model that can achieve faster convergence. Menter (1994) concluded that the $B-L$ $k-\omega$ model captures the benefits of

both the Wilcox $k-\omega$ and standard $k-\varepsilon$ model but still fails to accurately predict the onset and extent of flow separation from smooth surfaces.

The Shear Stress Transport (*SST*) $k-\omega$ model proposed by Menter (1994) incorporates a blending function that limits the turbulent shear stress and therefore performs better in predicting the onset and amount of flow separation from smooth surfaces.

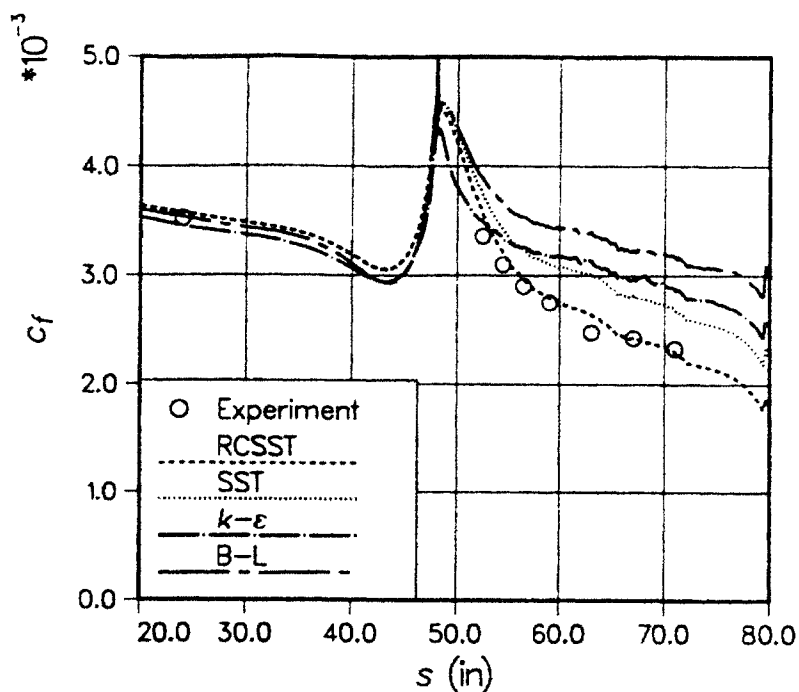


Figure 3.3.3.2.1: The skin friction coefficient along the straight and curved wall, reproduced from Hellsten (1998)

Modifications to the *SST* $k-\omega$ model have been carried out by Hellsten (1998) to sensitize the model to the effects of system rotation and streamline curvature. The modified model is called the $k-\omega$ *RCSST* model, and it is found to be in better agreement with

experimental data of rotating channel flow than both k - ε and the original k - ω SST model.

Although using a specific dissipation equation for near wall flow simulations provides more accurate results, all two equation models share a few common faults. The simplified turbulence kinetic energy equation over-predicts the Reynolds-stresses in situations of high shear and streamline curvature. This robust turbulence model is satisfactory for simple flow situations but is unacceptable for complex flows such as swirling flow (Hogg and Leschziner, 1989).

3.3.4 One-Equation Models

Further reduction in computational load can be achieved by reducing the amount of differential equations utilized by the turbulence model. Indicative of the name, one-equation models solve a single differential equation to model turbulence. Prandtl (1945) and Kolmogorov (1942) proposed a one-equation model based upon the turbulence kinetic energy equation. The eddy-viscosity was determined from the following equation:

$$\nu_T = k^{\frac{1}{2}} l_{mix} \quad (3.3.4.1)$$

where $k = \frac{1}{2} \overline{u_i' u_i'}$ is the turbulence kinetic energy and l_{mix} is the turbulence mixing length,

which needs to be specified by an algebraic equation or by empirical means. Spalart and Allmaras (1992) proposed a one-equation model based upon a differential transport equation for the eddy-viscosity.

3.3.5 Zero-Equation Models

The simplest type of turbulence model determines the Reynolds-stress tensor through eddy-viscosity, ν_T , which is computed algebraically. This method is similar to the Smagorinsky model used in *LES* to correlate the sub-grid stress, τ_{ij} , to the resolved strain rate, $\overline{S_{ij}}$. When using zero-equation models, the velocity scale is also determined from the mean strain rate, but the length scale must be specified explicitly as there is no filter width in *RANS*. Therefore, it is widely accepted that zero-equation models are incomplete turbulence models for the governing equations (Wilcox, 1993). The most famous zero-equation model is that of Baldwin and Lomax (1978):

$$\nu_T = l_{mix}^2 (\omega_i \omega_i)^{\frac{1}{2}} \quad (3.3.5.1)$$

where ω_i is the mean vorticity vector.

Although considered incomplete closures, zero-equation models can provide accurate results in very simple flow environments. Cebeci and Meier (1979) and Cebeci *et al.* (1986) concluded that such models are effective design aids for airfoils. Since algebraic equations are solved much faster than differential equations, zero-equation models are computationally more efficient. Unfortunately, zero-equation models have to be calibrated for each flow configuration and therefore cannot be used as a general turbulence model.

Chapter 4

CONFINED SWIRLING FLOW

In this chapter, the investigation of confined swirling flow is undertaken using the standard $k-\varepsilon$ and SSG Reynolds-stress turbulence models. The simulation results are compared to the experimental data of So *et al.* (1984).

4.1 Description of Test Case

The flow consists of an annular swirling stream introduced into a circular pipe of diameter $D = 0.125\text{m}$, in conjunction with a non-swirling jet of diameter $D_j = 0.00873\text{m}$.

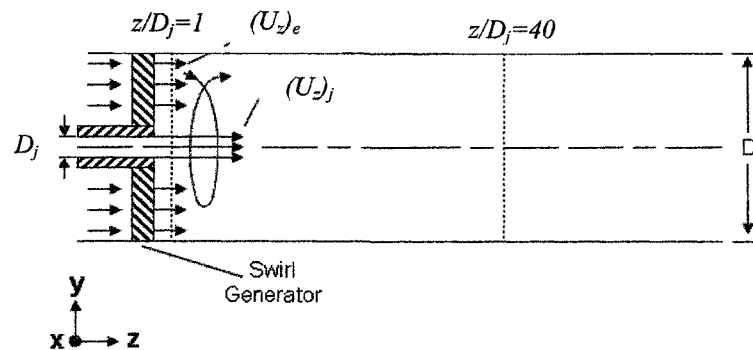


Figure 4.1: Geometry of experimental setup

The flow is characterized by an inflow axial velocity ratio of $(U_z)_j / (\overline{U_z})_a = 3.9$, a flow Reynolds number of 164000, and a swirl number of 2.25. The Reynolds number is based on the spatially-averaged inflow velocity of 19.8m/s and the diameter D of the test section. The swirl number, S , is defined as:

$$S = \frac{\int_0^{\frac{D}{2}} U_z U_t r^2 dr}{\frac{D}{2} \int_0^{\frac{D}{2}} U_z^2 r dr} \quad (4.1)$$

where U_z is the axial velocity component and U_t is the tangential velocity component. The swirl number of 2.25 corresponds to the region just downstream of the swirl generator. This is considered to be a high swirl number where the streamwise variation of centrifugal forces causes an adverse streamwise pressure gradient in the vortex core. The non-swirling jet of $(U_z)_j = 25.4\text{m/s}$ velocity is introduced at the core to counteract the flow reversal tendency due to the adverse pressure gradient.

A *DISA* Model 55L laser-Doppler anemometer (*LDA*) was used to measure the tangential and axial velocity profiles at different axial locations. This particular model was limited to only measuring a single velocity component at a time. At each streamwise location, the profile was given through measurements at different radial positions. The fluctuations in the tangential and axial velocity components were also included in the published data set. Both mean radial velocity and radial fluctuations were not measured due to difficulties associated with translating the sample volume in the vertical direction.

A blower powered by a 25 hp motor was used to generate a pressure differential to drive the flow through the test section. Although the motor was considered to be a

constant-speed motor, experimental results revealed that the blower fluctuated 8% from its mean specified flow rate over the duration of the experiment. The swirler used in the experiment consisted of vanes set at an angle of 66° to the axial flow direction. These vanes were flat plates and did not extend through the entire cross-section. The center nozzle was designed with a backward facing step to ensure a fully turbulent jet.

All fluids were kept at room temperature including the compressed air used as the centerline jet. Also, at each axial location, velocity and turbulence measurements at different circumferential positions were used to confirm that the flow remained axisymmetric throughout the entire test section.

Due to the aforementioned variations in the blower flow rate, the data set in its unaltered form did not satisfy the conservation of mass between the multiple measurement planes. Accordingly, in the present study, the spatially-averaged axial velocity is used in each measurement plane to normalize the velocity measurements in that plane.

4.2 Turbulence Models

4.2.1 k - ε Turbulence Model

The first simulation in this study used the standard k - ε turbulence model to predict the experimental data of So *et al.* (1984). With the standard k - ε turbulence model, the Reynolds-stresses are evaluated using Boussinesq's assumption:

$$-\overline{u'_i u'_j} = \nu_T \left(\frac{\partial U_i}{\partial x_j} + \frac{\partial U_j}{\partial x_i} \right) - \frac{2}{3} \delta_{ij} k \quad (4.2.1.1)$$

where ν_T is the eddy viscosity and δ_{ij} is Kronecker's delta function. The standard k - ε model is based on partial differential transport equations for turbulence kinetic energy, k , and turbulence dissipation rate, ε :

$$\rho \frac{\partial k}{\partial t} + \rho U_j \frac{\partial k}{\partial x_j} = \overline{\rho u'_i u'_j} \frac{\partial U_i}{\partial x_j} - \rho \varepsilon + \frac{\partial}{\partial x_j} \left[\left(\mu + \frac{\mu_T}{\sigma_k} \right) \frac{\partial k}{\partial x_j} \right] \quad (4.2.1.2)$$

$$\rho \frac{\partial \varepsilon}{\partial t} + \rho U_j \frac{\partial \varepsilon}{\partial x_j} = C_{\varepsilon 1} \frac{\varepsilon}{k} \overline{\rho u'_i u'_j} \frac{\partial U_i}{\partial x_j} - C_{\varepsilon 2} \rho \frac{\varepsilon^2}{k} + \frac{\partial}{\partial x_j} \left[\frac{\mu_T}{\sigma_\varepsilon} \frac{\partial \varepsilon}{\partial x_j} \right] \quad (4.2.1.3)$$

where the diffusion term in both Eqn. 4.2.1.2 and 4.2.1.3 use Einstein summation notation. The values of the empirical constants appearing in these equations are:

$$C_{\varepsilon 1} = 1.44, C_{\varepsilon 2} = 1.92, \sigma_k = 1, \sigma_\varepsilon = 1$$

With k and ε obtained through Eqn. 4.2.1.2 and 4.2.1.3, the eddy viscosity is calculated from the following equation:

$$\mu_T = \rho C_\mu \frac{k^2}{\varepsilon} \quad (4.2.1.4)$$

where $C_\mu = 0.09$.

4.2.2 SSG Reynolds-Stress Turbulence Model

The second order turbulence model selected for this simulation study is the *SSG* model developed by Speziale *et al.* (1991). Second order models solve a partial

differential equation for each of the Reynolds-stresses in addition to a partial differential equation for the turbulence dissipation rate, ε . The transport equations for the Reynolds-stresses are defined as:

$$\rho \frac{\partial(\overline{u'_i u'_j})}{\partial t} + \rho U_k \frac{\partial(\overline{u'_i u'_j})}{\partial x_k} = d_{ij} + P_{ij} + \varepsilon_{ij} + \Pi_{ij} \quad (4.2.2.1)$$

In this equation d_{ij} is the diffusion term, P_{ij} is the production term, ε_{ij} is the dissipation term, Π_{ij} is the pressure-strain term, and they are defined as:

$$d_{ij} = \frac{\partial}{\partial x_k} \left[\frac{v_t}{\sigma_k} \frac{\partial \overline{u'_i u'_j}}{\partial x_k} \right] \quad (4.2.2.2)$$

$$P_{ij} = -\overline{\rho u'_i u'_k} \frac{\partial U_j}{\partial x_k} - \overline{\rho u'_j u'_k} \frac{\partial U_i}{\partial x_k} \quad (4.2.2.3)$$

$$\varepsilon_{ij} = \frac{2}{3} \varepsilon \delta_{ij} \quad (4.2.2.4)$$

ε , appearing in Eqn. 4.2.2.4, is the scalar dissipation rate and is determined through the solution of the following transport equation:

$$\rho \frac{\partial \varepsilon}{\partial t} + \rho U_k \frac{\partial \varepsilon}{\partial x_k} = C_{\varepsilon 1} \frac{\varepsilon}{k} P_{kk} - C_{\varepsilon 2} \rho \frac{\varepsilon^2}{k} + \frac{\partial}{\partial x_k} \left[\frac{v_T}{\sigma_\varepsilon} \frac{\partial \overline{u'_i u'_j}}{\partial x_k} \right] \quad (4.2.2.5)$$

Eqn. 4.2.2.5 is identical to Eqn. 4.2.1.3 with the exception that the diffusion term is anisotropic. The constants appearing in Eqn. 4.2.2.5 are very similar to those appearing in Eqn. 4.2.1.3:

$$C_{\varepsilon 1} = 1.44, C_{\varepsilon 2} = 1.83, \sigma_\varepsilon = 1$$

The model of Speziale et al. (1991) uses a quadratic relationship for the pressure-strain term, Π_{ij} :

$$\Pi_{ij} = \Pi_{ij,1} + \Pi_{ij,2} \quad (4.2.2.6)$$

where

$$\Pi_{ij,1} = -(C_1 \varepsilon + C_1^* P_k) b_{ij} + C_2 \varepsilon \left(b_{ik} b_{kj} - \frac{1}{3} b_{kl} b_{kl} \right) \quad (4.2.2.7)$$

$$\begin{aligned} \Pi_{ij,2} = & \left(C_3 - C_3^* \sqrt{b_{kl} b_{kl}} \right) k S_{ij} + C_4 k \left(b_{ik} S_{jk} + b_{jk} S_{ik} - \frac{2}{3} b_{kl} S_{kl} \delta_{ij} \right) \\ & + C_5 k (b_{ik} W_{jk} + b_{jk} W_{ik}) \end{aligned} \quad (4.2.2.8)$$

In these expressions, k is the turbulence kinetic energy, S_{ij} is the mean strain-rate tensor, W_{ij} is the angular velocity tensor, P_k is the production tensor, and b_{ij} is a tensor representing the Reynolds-stress anisotropy.

$$S_{ij} = \frac{1}{2} \left(\frac{\partial U_i}{\partial x_j} + \frac{\partial U_j}{\partial x_i} \right) \quad (4.2.2.9)$$

$$W_{ij} = \frac{1}{2} \left(\frac{\partial U_i}{\partial x_j} - \frac{\partial U_j}{\partial x_i} \right) \quad (4.2.2.10)$$

$$b_{ij} = \frac{\overline{u'_i u'_j}}{\overline{u'_k u'_k}} - \frac{1}{3} \delta_{ij} \quad (4.2.2.11)$$

$$P_k = -\overline{\rho u'_i u'_j} \frac{\partial U_i}{\partial x_j} \quad (4.2.2.12)$$

The seven empirical constants were determined to be:

$$C_1 = 3.4, C_1^* = 1.8, C_2 = 4.2, C_3 = 0.8, C_3^* = 1.3, C_4 = 1.25, C_5 = 0.4$$

Sarkar and Speziale (1990) claim that linear pressure-strain models have two main deficiencies. They predict the same rate of decay for each component of the anisotropy tensor, and the predicted rate is independent of the initial state of anisotropy. Lumley and Newman (1977) and Lumley (1978) have concluded that linear pressure strain models are not supported by experimental data. The *SSG* model is only quadratically nonlinear in the anisotropy tensor, b_{ij} , hence it has the advantage of being topologically equivalent to more general pressure-strain models in plane homogenous turbulence such as those developed by Launder *et al.* (1975) and Gibson and Launder (1978).

The *SSG* pressure-strain correlation along with the empirical constants were determined and optimized to be consistent with a series of constraints developed by Speziale *et al.* (1990). The equations and constants are asymptotic consistent in the limit of small anisotropies. They are also consistent with Rapid Distortion Theory (*RDT*) for homogeneously strained turbulent flows that are initially isotropic, with the equilibrium values for homogeneous shear flows measured by Tavoularis and Corrsin (1981), the *RDT* results of Bertoglio (1982) for rotating shear flows, and return to isotropy of an initially anisotropic, homogeneous turbulence.

4.3 Computational Domain

Two computational domains were used in this investigation. The first domain consisted of a cylinder of diameter D and $45D_j$ ($3.14D$) length, which was used for

simulations with the $k-\varepsilon$ turbulence model. The second computational domain consisted of a wedge-shaped geometry of $\frac{1}{2} D$ radius and $45D_j$ length, and was used with the Reynolds-stress turbulence model. The smaller domain size for the Reynolds-stress turbulence model was dictated by the availability of computational resources. The two computational domains are shown in Figures 4.3.1 and 4.3.2.

The computational time and memory requirements are substantially greater for the Reynolds-stress turbulence model than for the $k-\varepsilon$ turbulence model. This is due to the fact that the Reynolds-stress model solves seven partial differential equations for turbulence closure while the $k-\varepsilon$ model only solves two partial differential equations.

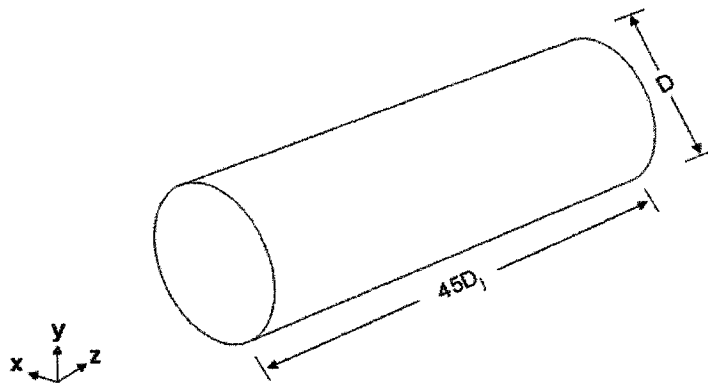


Figure 4.3.1: Cylindrical computational domain

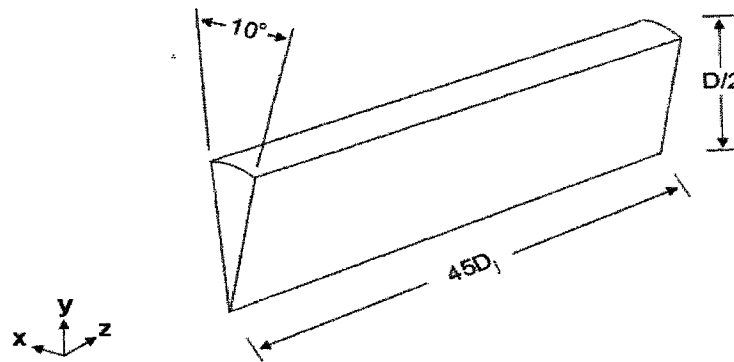


Figure 4.3.2: Wedge-shaped computational domain

With the wedge-shaped computational domain, the side faces are treated as periodic boundaries. This should not result in any deviation of the predicted flow from the cylindrical computational domain since the flow is axisymmetric. The predictions based on the $k-\varepsilon$ model were compared for the two computational domains to observe equality of the results (Figure 4.3.3). It can be seen that the wedge-shaped domain gives essentially the same results for the tangential velocity distribution as the cylindrical domain.

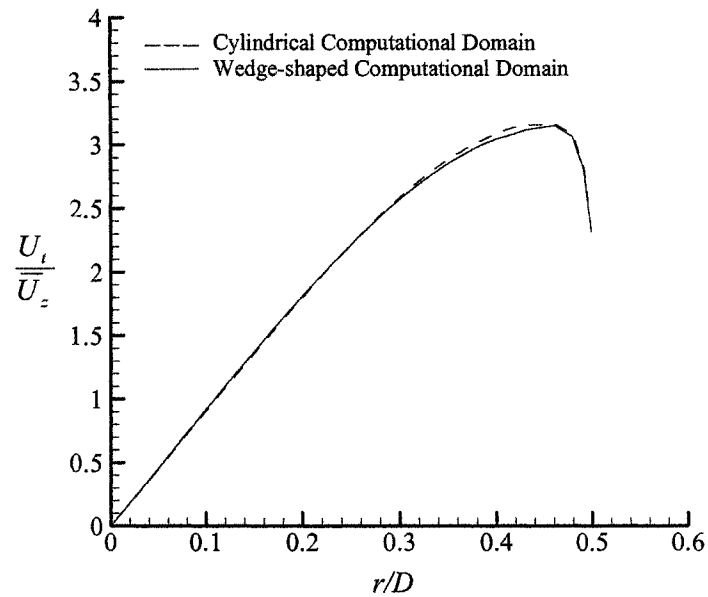


Figure 4.3.3: Sensitivity of the tangential velocity distribution to the shape of the computational domain ($z/D_j = 14$).

4.4 CFX Algorithm

Both convective and diffusive space derivatives were discretized with second order accuracy. For simulations with the $k-\varepsilon$ turbulence model, a number of iterations were performed with a first order discretization of the convective derivatives before restarting the solution with a second-order accurate discretization.

For steady-state problems, the *CFX* algorithm uses a fully implicit formulation so that iterations through time marching can be performed with as large time steps as possible. The time step for each $k-\varepsilon$ simulation run was calculated to be 0.001 seconds. The *CFX* algorithm calculates the time step based upon characteristic length and velocity

scales determined from the domain geometry, initial flow conditions, and boundary conditions. For incompressible flows, the time scale is calculated using the following equation:

$$\Delta t = 0.3 \frac{L_{scale}}{\max(U_{bc}, U_{node})} \quad (4.4.1)$$

where L_{scale} is defined as:

$$L_{scale} = \min(L_i) \quad (4.4.2)$$

$$U_{bc} = \max|\bar{U}_{bc}| \quad (4.4.3)$$

$$U_{node} = |\bar{U}_{node}| \quad (4.4.4)$$

where \bar{U}_{bc} is the arithmetic mean of the velocity on a boundary and \bar{U}_{node} is the arithmetic mean of initial nodal velocities. Eqn. 4.4.3 determines the maximum velocity scale from a set of velocity scales calculated at all boundaries.

The global time step calculated for the Reynolds-stress simulations was identical to that calculated for the $k-\varepsilon$ simulation. However, during Reynolds-stress simulations, a local time step factor was used to avoid divergent solutions. The local time step factor is specified by the user and is a multiplier of the local element-based timescale. When this option is used, the *CFX* algorithm allows the local time step to deviate about the mean time step calculated in Eqn. 4.4.1. The magnitude of the time step variance is determined by the local element length scale and the local time step factor. The local time step factor used for the Reynolds-stress simulations was 5.

4.5 Boundary Conditions

The inflow boundary conditions for the mean velocity and turbulence properties were specified using a one-dimensional interpolation function available in *CFX*. The function executes by interpolating from a list of point coordinates and a list of values at those points. This type of function allows the user to specify discrete values at arbitrary locations. Due to the axisymmetric nature of the present simulations, it was sufficient for all discrete values to be specified along the radial axis.

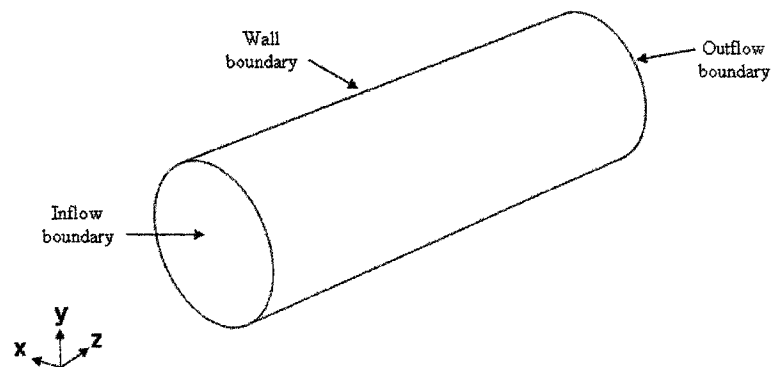


Figure 4.5.1: Boundaries for the cylindrical computational domain

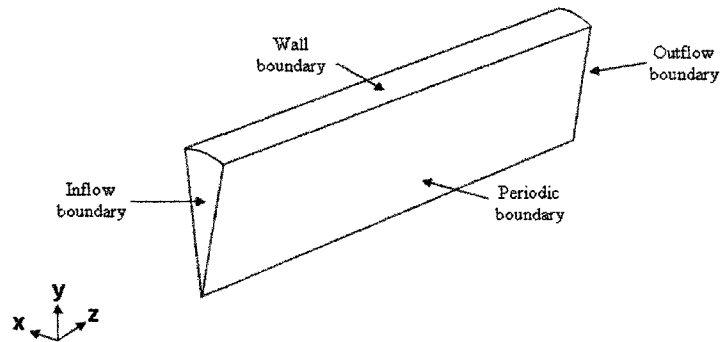


Figure 4.5.2: Boundaries for the wedge-shaped computational domain

The inflow boundary was located $1D_j$ downstream from the experimental swirl generator; this swirl generator is shown in Figure 4.1.1. This choice was dictated by the availability of the flow measurements. The velocity distribution imposed at the inflow boundary is given in Figure 4.5.3. The radial velocity component was set to 0 m/s since this quantity was not measured in the experiments of So *et al.* (1984). Such an approximation may not be justified; hence the simulation results have to be compared to the experimental results in this context.

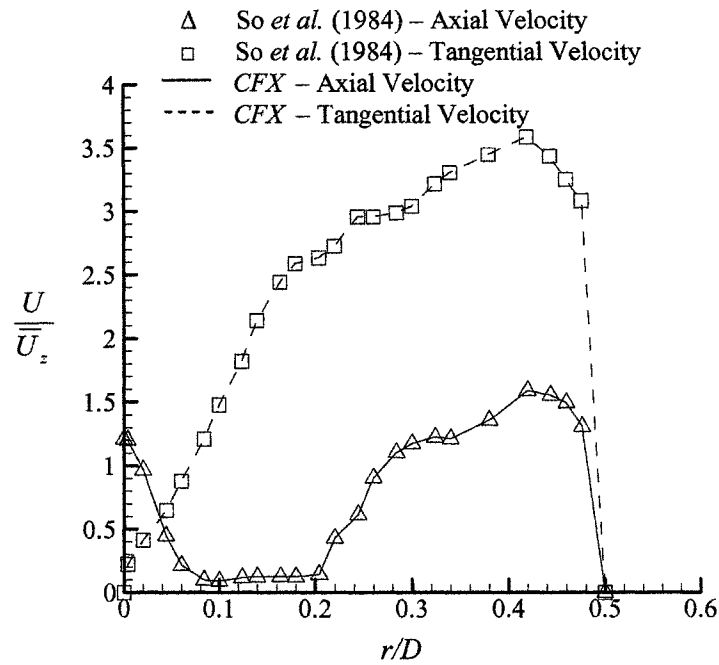


Figure 4.5.3: Mean velocity distributions at the inflow boundary ($z/D_j=1$)

The tangential and axial velocity fluctuations provided in the experimental data set made it possible to determine the turbulence kinetic energy at the inflow boundary. The turbulence kinetic energy is defined as:

$$k = \frac{1}{2} \overline{(u'_i u'_i)} \quad (4.5.1)$$

The experimental data set did not include velocity fluctuations in the radial direction. The normal Reynolds normal stresses in the radial direction were therefore assumed to be the average of the Reynolds normal stresses in the tangential and axial directions.

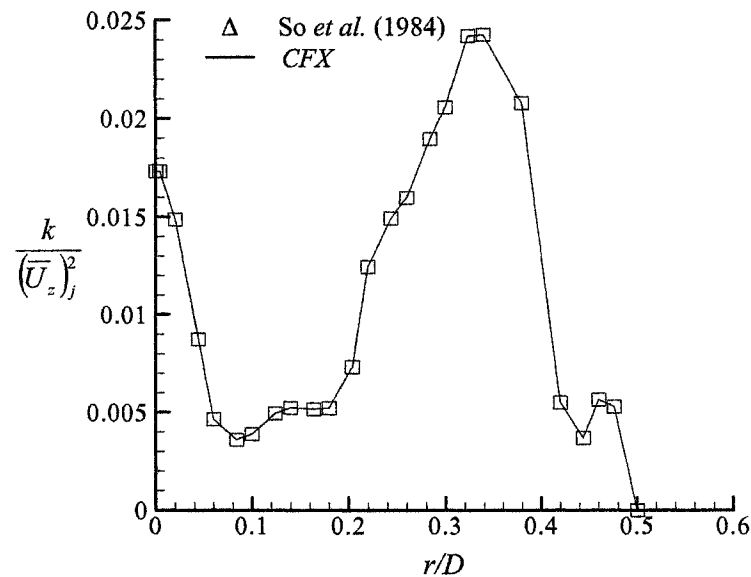


Figure 4.5.4: Turbulence kinetic energy distribution at the inflow boundary ($z/D=1$)

Due to the absence of experimental data for the rate dissipation of turbulence, this quantity was determined from the equation:

$$\varepsilon = \frac{k^{\frac{3}{2}}}{0.2D} \quad (4.5.2)$$

which is conventionally used for estimating ε in confined flow paths.

A no-slip (zero velocity) boundary condition was applied to the wall boundary. Scalable wall functions were used to establish the boundary conditions for turbulence properties and wall shear stress near the wall. In the specified grid, the precise placement of the first node near the wall was controlled by scalable wall functions. The first node was placed at a y^+ of 11 which corresponds to the intersection of the logarithmic and linear near-wall u^+ profile. The wall function approach in *CFX* is an extension of the

model of Launder and Spalding (1974). For standard wall functions, the near-wall velocity distribution is given by the logarithmic relation:

$$u^+ = \frac{U_t}{u_\tau} = \frac{1}{\kappa} \ln(y^+) + C \quad (4.5.3)$$

where

$$y^+ = \frac{y_p u_\tau}{\nu} \quad (4.5.4)$$

$$u_\tau = \left(\frac{\tau_w}{\rho} \right)^{\frac{1}{2}} \quad (4.5.5)$$

u^+ is the non-dimensional near wall velocity, u_τ is the friction velocity, U_t is the velocity tangent to the wall at a distance of y_p from the wall, y^+ is the dimensionless distance from the wall, τ_w is the wall shear stress, κ is the von-Kármán constant, and C is a log-layer constant that takes on the value of 5 for smooth surfaces. u^+ in Eqn. 4.5.3 becomes singular at separation points where the near wall velocity, U_t , approaches zero. Scalable wall functions use an alternative velocity scale, u_n , to avoid this problem and solve the following set of equations instead:

$$u_n = C_\mu^{\frac{1}{4}} k^{\frac{1}{2}} \quad (4.5.6)$$

$$u_\tau = \frac{U_t}{\frac{1}{\kappa} \ln(y^*) + C} \quad (4.5.7)$$

$$\tau_w = \rho u_n u_\tau \quad (4.5.8)$$

$$y^* = \frac{u_n y_p}{\nu} \quad (4.5.9)$$

u_n is the near-wall velocity, u_τ is the friction velocity, U_t is the velocity tangent to the wall at a distance of y_p from the wall, y^* is the dimensionless distance from the wall, and τ_ω is the wall shear stress. It is assumed that u_n is equal to u_τ for the valid range of u^+ in order to use the logarithmic relation shown in Eqn. 4.5.7. The turbulence dissipation rate at the first node near the wall is calculated assuming local equilibrium between turbulence production and dissipation:

$$\varepsilon_{wall} = \frac{u_n^4}{\kappa y^* \nu} \quad (4.5.10)$$

The turbulence kinetic energy is calculated from the following equation:

$$k_{wall} = \frac{u_n^2}{C_\mu^{\frac{1}{2}}} \quad (4.5.11)$$

The range of y^* is limited by the following equation:

$$y^* = \max(y^*, 11.06) \quad (4.5.12)$$

where 11 is the intersection of the logarithmic and linear near wall profile, and therefore the grid point at which the wall function is imposed remains outside of the viscous sublayer. During simulations using the Reynolds-stress turbulence model, the fluxes of the Reynolds-stresses at the wall were set to zero, and normal stresses were assumed to be isotropic and calculated from the turbulence kinetic energy.

On the outflow boundary, pressure was maintained at atmospheric level on a spatially-averaged basis. The *CFX* algorithm allows for non-uniform pressure

distribution within the outflow boundary, which it extrapolates from the adjacent set of interior nodes.

For periodic boundaries, the one-to-one connection option was specified in *CFX*. For a one-to-one connection, the grid on each side of the interface is identical with respect to both the number of nodes and the relative location of the nodes. This type of connection allows the nodal values from one periodic surface to be applied to the nodal values at the other surface without the need for spatial interpolation.

4.6 Initial Conditions

The initial distributions of flow variables within the computational domain for both Reynolds-stress and k - ε simulations were identical to those specified at the inflow boundary. The tangential and axial velocities within the entire domain were initialized to the profiles shown in Figure 4.5.3. Similar to the inflow boundary condition, the initial radial velocity within the domain was set to 0m/s. The initial turbulence kinetic energy was specified using the experimental profile shown in Figure 4.5.4, while the initial dissipation values were calculated from Eqn. 4.5.2. The pressure distribution was initialized at standard atmospheric level throughout the computational domain.

4.7 Computational Grid for k - ϵ Simulations

The initial spatial grid resolution was set to resemble the optimum grids for this test case presented by Yaras and Grosvenor (2003a,b). That study specified 73 nodes in the radial direction and 61 nodes in the axial direction. *CFX* allows for the use of a hybrid grid to minimize spatial resolution requirements in attaining a grid independent solution. For the present simulation a structured grid is used near the wall to resolve the boundary layer, and an unstructured grid consisting of tetrahedral elements is used elsewhere.

The structured grid is created by applying inflation layers to boundaries. An inflation layer is created by ‘inflating’ a two dimensional triangle into a three dimensional prism. The purpose of inflation layers is to minimize resolution requirements while still resolving the flow where spatial gradients are greatest normal to the boundary.

Grid controls are used to cluster nodes to reduce the total node count, hence memory requirements without sacrificing accuracy. Each grid control consists of a length scale, a radius of influence, and an expansion factor. The length scale determines the amount of nodes to be created within the radius of influence. The rate at which this refined length scale returns to the global length scale is determined by the expansion factor. The range of expansion factors to produce smooth or coarse transitions on the present grids was approximately 1.05 to 1.2.

As the spatial resolution was adjusted, both tangential and axial velocity profiles were monitored until a grid independent solution was obtained. When the variation in velocity profiles from one grid to the next fell below one percent, the solution was deemed grid independent. The final grid independent solution had a total of 144,659 nodes. This consisted of approximately 50 nodes in each of the tangential, radial, and axial directions. The grid optimization study led to the clustering of nodes near the vortex core. Although the wall boundary layer in Figure 4.7.1 appears to be resolved with only a few nodes, increasing the resolution near the wall had negligible effects on the flow field where experimental data is available. The simulation results using the cylindrical domain were compared to the more refined wedge-shaped domain, where the boundary layer was fully resolved. The two results agreed confirming that the resolution of the boundary layer in the cylindrical domain was sufficient to produce realistic frictional effects along the wall.

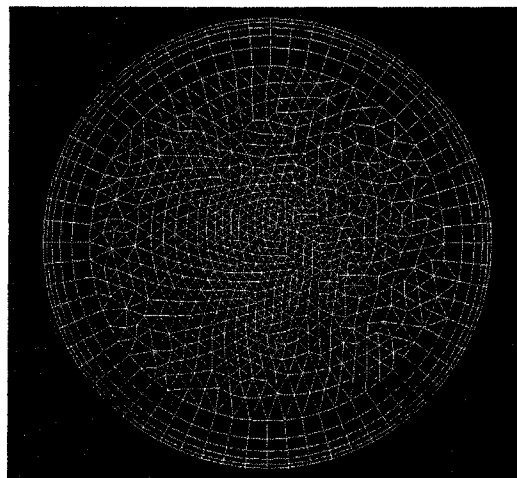


Figure 4.7.1: Optimized grid-node distribution in the cross-section plane

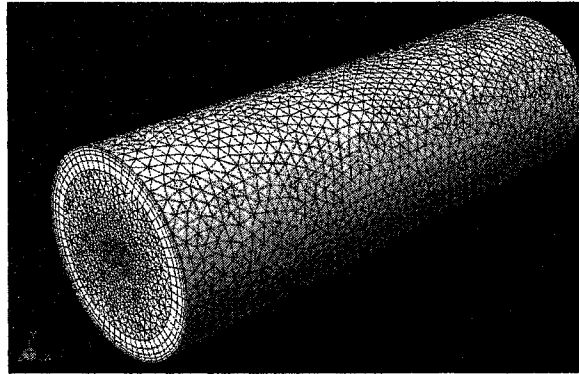


Figure 4.7.2: Streamwise distribution of grid nodes

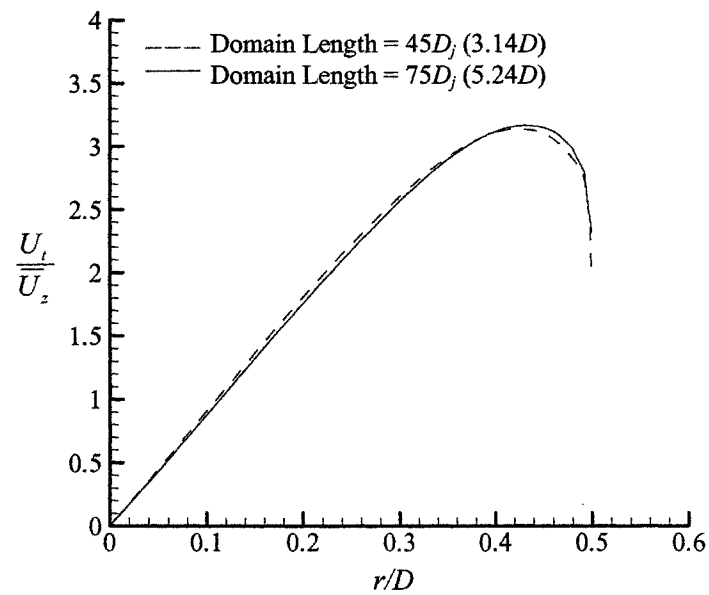


Figure 4.7.3: Sensitivity of predictions to domain length

The cross-stream pressure distribution is non-uniform in the computational domain due to the swirling nature of the flow which is reflected onto the outflow

boundary. The procedure for extrapolating the interior pressure distribution on to the outflow boundary used in *CFX* is not known, and therefore a sensitivity study was performed by varying the domain length from $45D_j$ to approximately $75D_j$. The results, as shown in Figure 4.7.3, indicate that the solution is independent of domain length. The effects of domain radius and shape were not investigated as they were determined by geometry constraints.

4.8 Computational Grid for Reynolds-Stress Simulations

Since a different computational domain shape and turbulence equations were used in the Reynolds-stress simulations, a separate grid sensitivity study was conducted for those cases. As the grid resolution was adjusted, both tangential and axial velocity profiles were monitored until a grid independent solution was obtained.

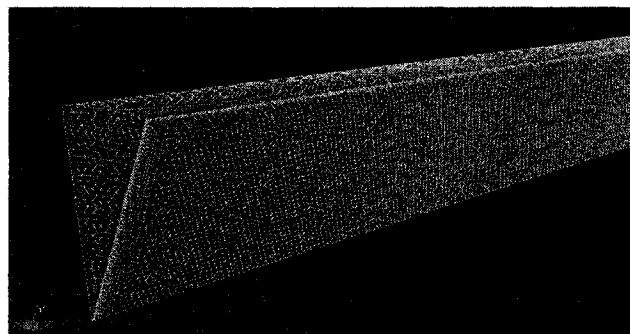


Figure 4.8.1: Streamwise distribution of grid nodes

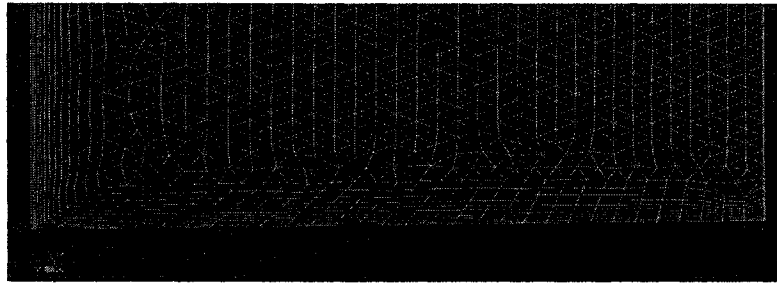


Figure 4.8.2: Optimized grid-node distribution in the cross-section plane

The computational grid consisted of two inflation layers and one grid control. The first inflation layer was placed at the inflow boundary and was necessary since high spatial gradients near the inflow boundary caused solution divergence for simulations with the Reynolds-stress model. As with the $k-\varepsilon$ model, an inflation layer was used at the wall to resolve the boundary layer. Both inflation layers had 15 nodes with an expansion factor of 1.2. The grid control was used to cluster nodes near the inflow boundary since the level of spatial gradients decreased as the vortex decayed downstream. The grid control was placed at the inflow boundary and had a radius of influence of $22D_j$ ($1.54D$), an expansion factor of 1.05, a local length scale of $0.2D_j$ ($0.014D$), and a global length scale of D_j ($0.07D$). This allowed for a smooth transition between elements of small scales specified by the grid control and elements of larger scales specified by the global length scale.

The grid-independent solution had a total of 62000 nodes. This consisted of approximately 40 nodes in the radial direction, 15 in the tangential direction, and 230 in the axial direction. The wedge-shaped domain is only a ten degree section of the pipe. If

the same grid density were used for the cylindrical domain as shown in Figure 4.5.1, the total node count would be approximately 2,000,000 nodes. Using the wedge-shaped domain allowed for a grid with both a high node density and small total node count.

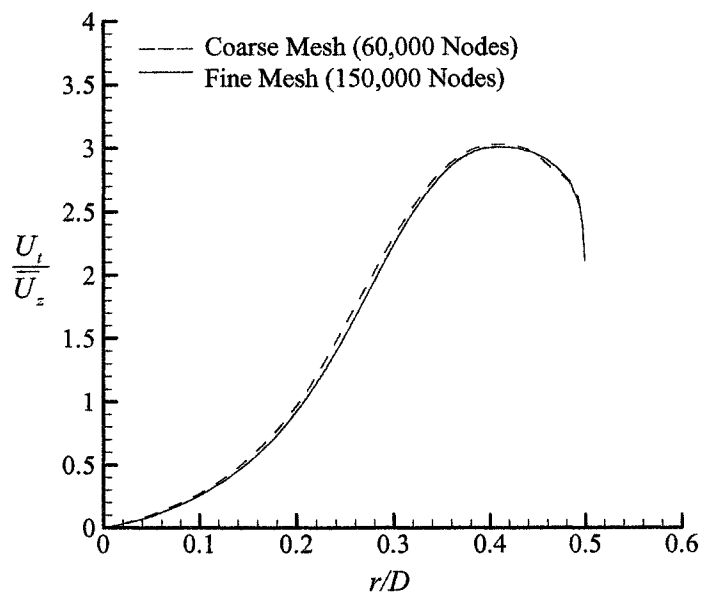


Figure 4.8.3: Sensitivity of the predictions to spatial resolution ($z/D_j = 14$)

4.9 Solution Convergence

The criteria involved in determining solution convergence includes monitoring the *RMS* residuals of all governing equations solved for the flow simulation in question, checking solution development with iterations, and checking for global conservation of mass. The number of iterations required to reach converged solutions for the laminar, k -

ε , and Reynolds-stress simulations were 300, 400, and 3000, respectively. The Reynolds-stress model required the implementation of a local time step factor to prevent solution divergence, and therefore required many more iterations to reach a converged solution. Each simulation was executed until the *RMS* residuals levelled off to their respective values.

Typical residual values for continuity, momentum, and turbulence equations were of the order 10^{-7} . After the residual levels subsided, the simulation was continued for approximately 200 and 1000 iterations for the *k- ε* and Reynolds-stress simulations, respectively. After the solution was determined to be independent of iterations, five cross-sectional planes were chosen along the computational domain to conduct a conservation of mass analysis. For each simulation the error in mass flow rate was less than one percent.

4.10 Simulation Results

In this section, predictions of mean flow and turbulence quantities are presented and compared to the experimental results of So *et al.* (1984). Because of the unsteadiness of the flow-rate in their experiments, So *et al.* (1984) decided to normalize the axial velocity component by the local spatially-averaged axial velocity. However, they neglected to normalize the tangential velocity in the same manner. Instead, the tangential velocity was normalized by a spatially-averaged axial velocity obtained just downstream

of the swirl generator. This is a poor choice for comparing results since all velocity components must be scaled appropriately and consistently. For the current results, both the experimental tangential and axial velocity profiles were normalized by their local spatially-averaged axial velocities, $\overline{U_z}$. All computational results were normalized by the inflow average axial velocity since the mass flow rate for each simulation was constant. It should be noted that the experimental spatially-averaged axial velocity varied by as much as eleven percent from inflow to outflow planes. According to So *et al.* (1984), this variation cannot be completely allocated to the unsteadiness associated with the blower. It was hypothesized that the error was partly due to the low sampling resolution near the wall.

Figures 4.10.1 and 4.10.2 show the tangential velocity distribution of the $k-\varepsilon$ model, Reynolds-stress model, and the laminar case at $z/D_j = 1$ and $z/D_j = 14$. At $z/D_j = 1$, all three models strongly deviate from the velocity profile specified at the inflow boundary. The deviation of the laminar model suggests that the change in velocity profile for all three simulations is not related to turbulent diffusion. The diffusion of momentum for the laminar model is due to interaction of molecules only, and is typically much smaller than turbulent diffusion. Therefore, it is argued that the computed result is due to the redistribution of mass near the inflow boundary caused by a re-circulation zone that was not present in the experimental results. A visual representation of the flow re-circulation in the $r-z$ plane is shown in Figures 4.10.3 and 4.10.4. The size of the re-circulation zone in the solution with the Reynolds-stress model is large compared to the

k - ε model. The extent by which the flow near the inflow boundary is affected by flow reversal can clearly be seen in Figure 4.10.4.

It is important to note that the failure of both Reynolds-stress and k - ε simulations in predicting the velocity distribution further downstream of the swirler is due to the initial deviation occurring immediately after the inflow boundary. The existence of a recirculation zone near the inflow boundary for Reynolds-stress, k - ε , and laminar simulations imply that the boundary conditions used were not completely accurate. For the experimental results, it is quite likely that a radial component of velocity at the inflow boundary prevented flow reversal throughout the experimental domain. Due to difficulties associated with taking measurements in the radial direction, the radial component of velocity was omitted from the published data set of So *et al.* (1984). The assumption of a negligible radial velocity component at the inflow boundary was incorrect and is most likely responsible for the development of a recirculation zone in the computational results. Therefore, any assessment of the turbulence models used for both simulations is difficult since the flow field is quite different than experimental results regardless of the turbulence model used.

Hogg and Leschziner (1989) completed a study comparing Reynolds-stress and k - ε turbulence model's ability to predict the experimental results of So *et al.* (1984). A Reynolds-stress model with a linear pressure-strain term was used in their study while a quadratic correlation was used in the present study. They were confronted with the same problem of flow reversal even though a centerline jet existed to prevent this flow

structure. Only when an explicit velocity profile was specified at the outflow boundary were adequate results obtained. This confirms that the assumption of zero radial velocity at the inflow boundary was incorrect and the development of a recirculation zone in simulations was independent of the algorithm used.

The importance of advection scheme on simulation results is shown in Figures 4.10.7-10. The first order advection scheme consistently predicts lower tangential velocity profiles compared to a second order advection scheme. The standard $k-\varepsilon$ model overestimates the transfer of angular momentum of the stream tubes in the radial direction for both first and second order advection schemes. The first order advection scheme shows a faster rate of vortex decay than the second order advection scheme. This decay in tangential velocity allows the core pressure to rise more rapidly and causes stronger reversed flow.

As shown in Figure 4.10.11 and 4.10.12, an alternative numerical algorithm used by Yaras and Grosvenor (2003) to predict the data of So *et al.* (1984), agrees completely with the results obtained from *CFX*. Both algorithms over-predict the decay of the vortex structure near the core and over-predict the velocity magnitude near the wall. This comparison strengthens the notion that the solution is independent of both the specifics of the solution algorithm and grid structure used.

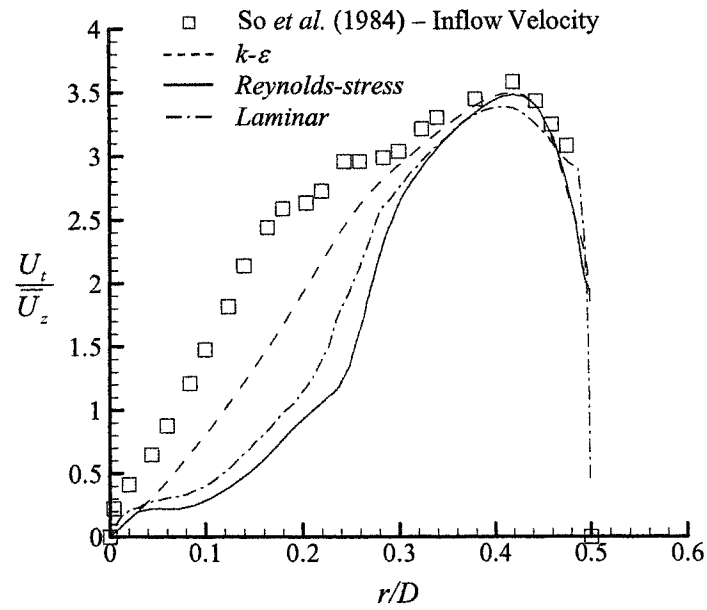


Figure 4.10.1: Radial distribution of tangential velocity component at $z/D_j = 1$

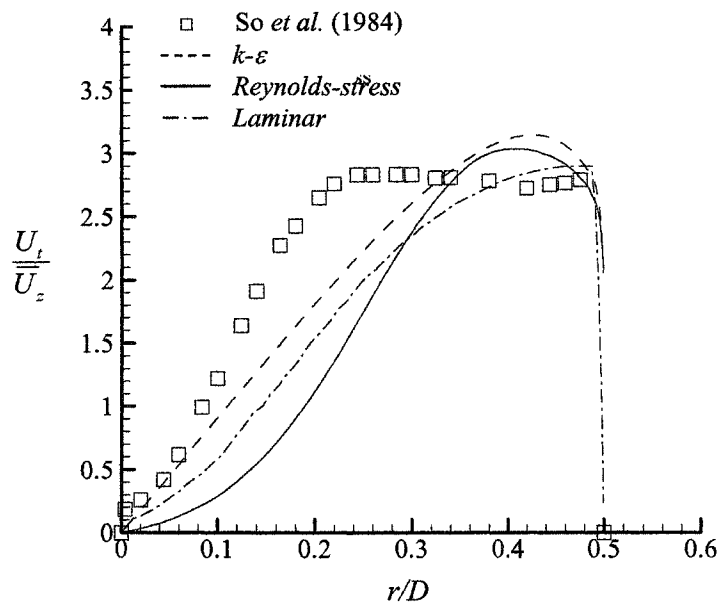


Figure 4.10.2: Radial distribution of tangential velocity component at $z/D_j = 14$

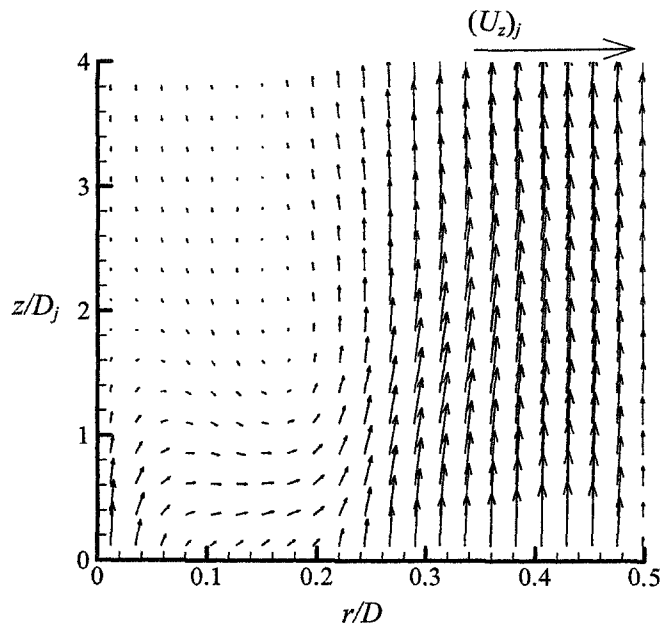


Figure 4.10.3: Velocity distribution in the $z-r$ plane near the inflow boundary ($k-\varepsilon$ turbulence model)

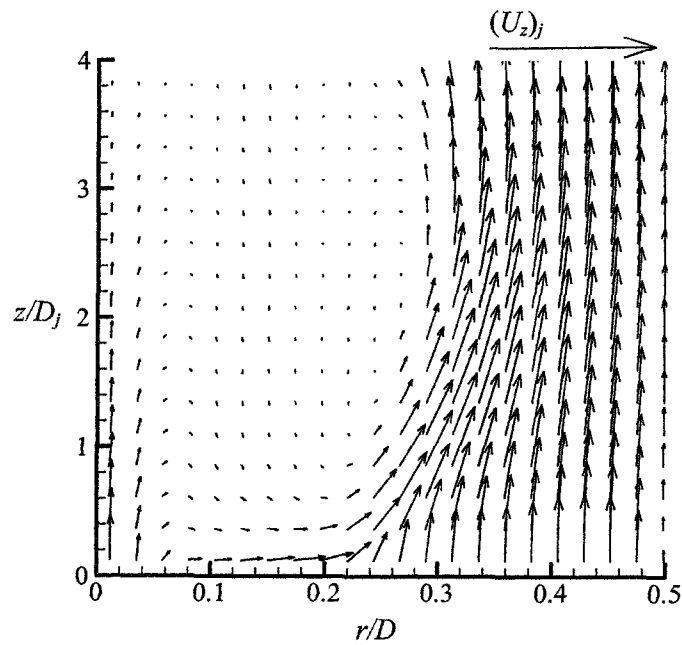


Figure 4.10.4: Velocity distribution in the $z-r$ plane near the inflow boundary (Reynolds-stress turbulence model)

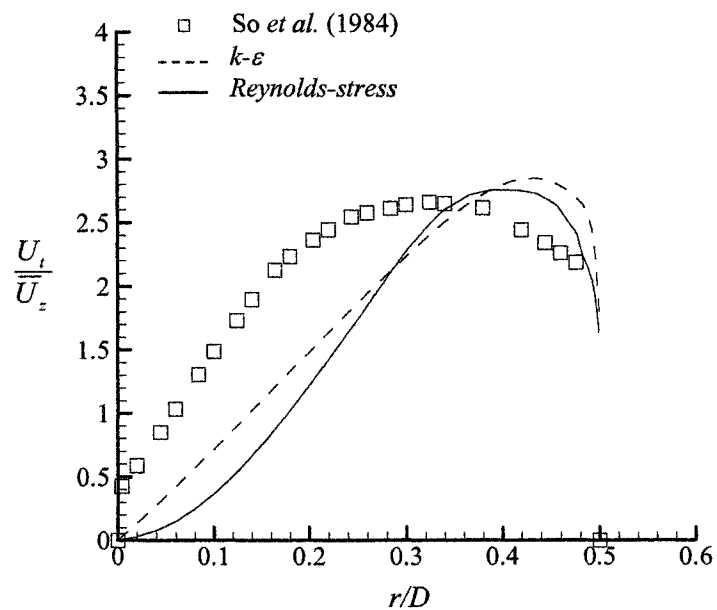


Figure 4.10.5: Radial distributions of tangential velocity component at $z/D_j = 40$

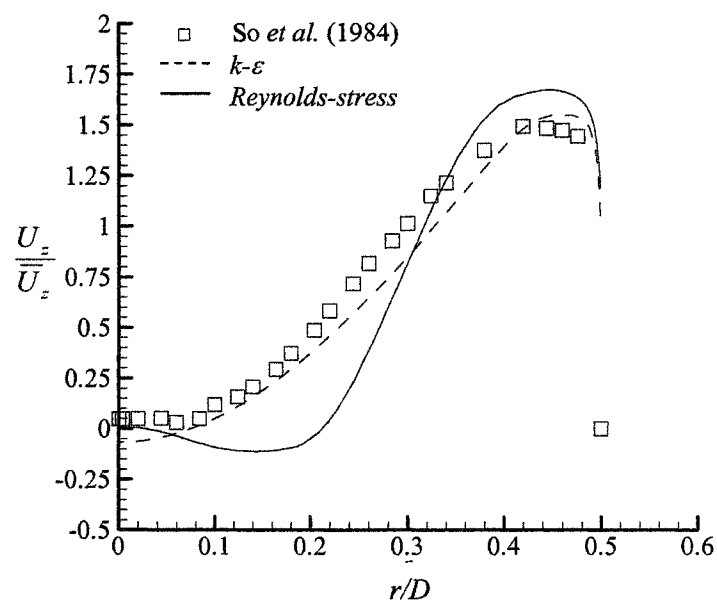


Figure 4.10.6: Radial distributions of axial velocity component at $z/D_j = 40$

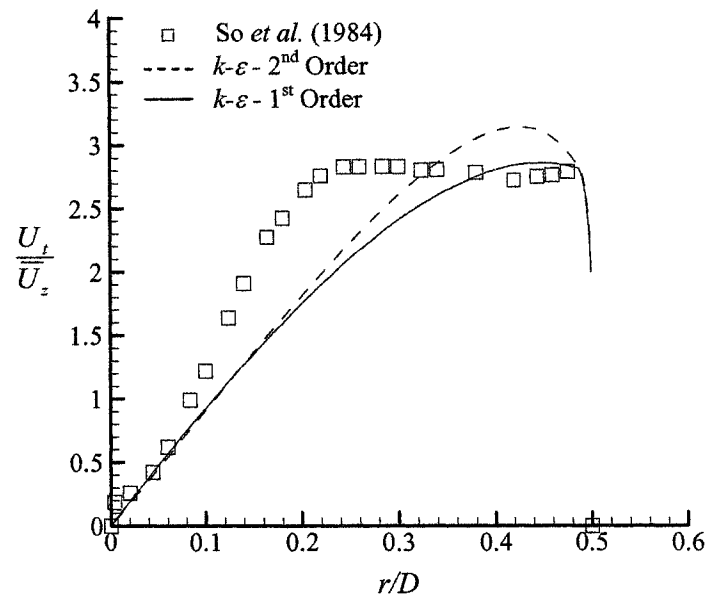


Figure 4.10.7: Radial distributions of tangential velocity component at $z/D_j = 14$

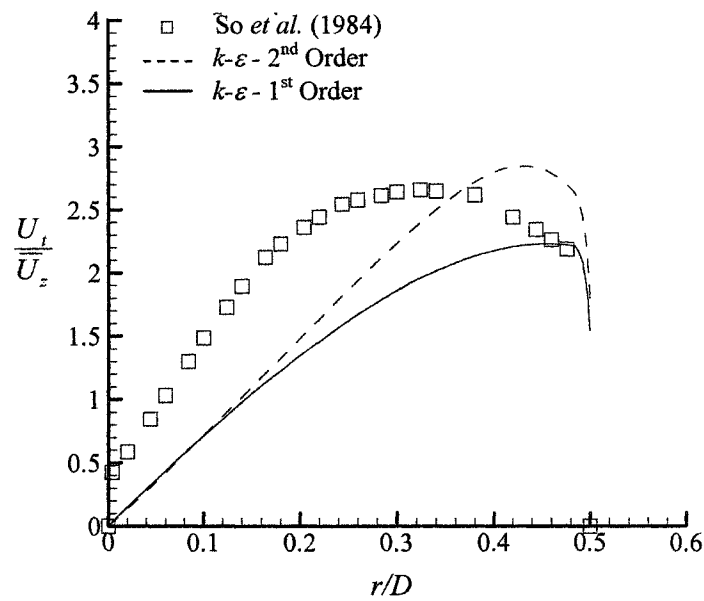


Figure 4.10.8: Radial distributions of tangential velocity component at $z/D_j = 40$

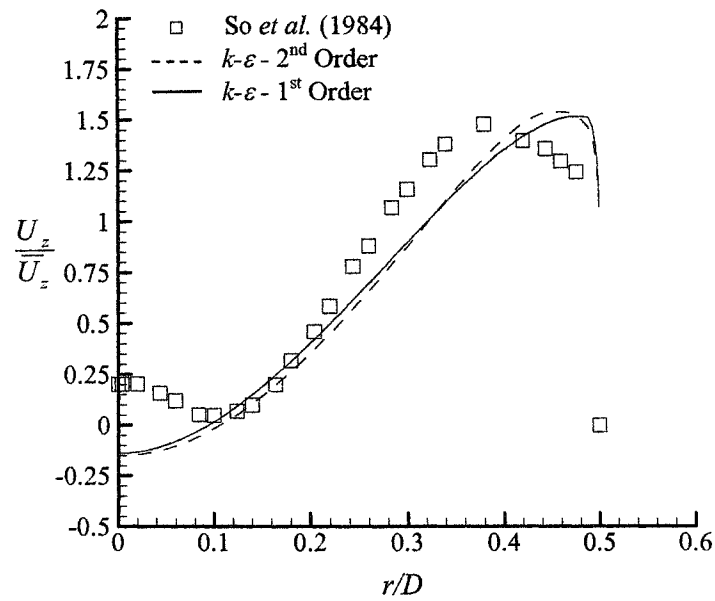


Figure 4.10.9: Radial distribution of axial velocity component at $z/D_j = 14$

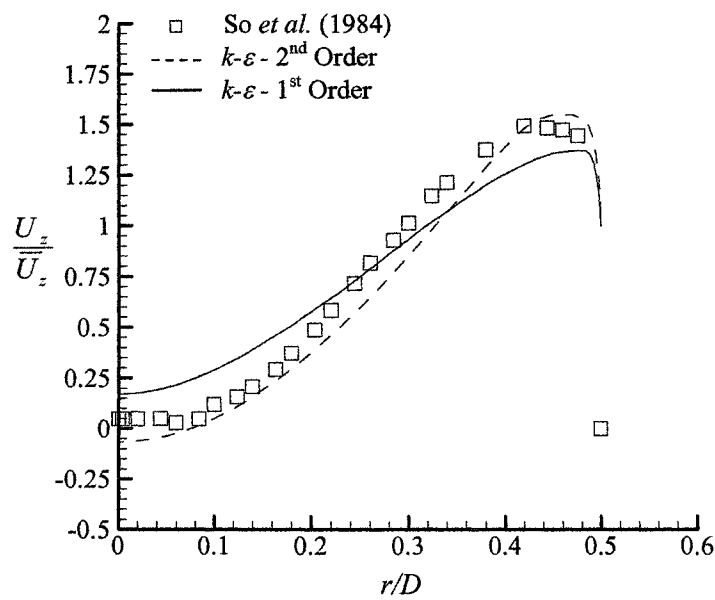


Figure 4.10.10: Radial distribution of axial velocity component at $z/D_j = 40$

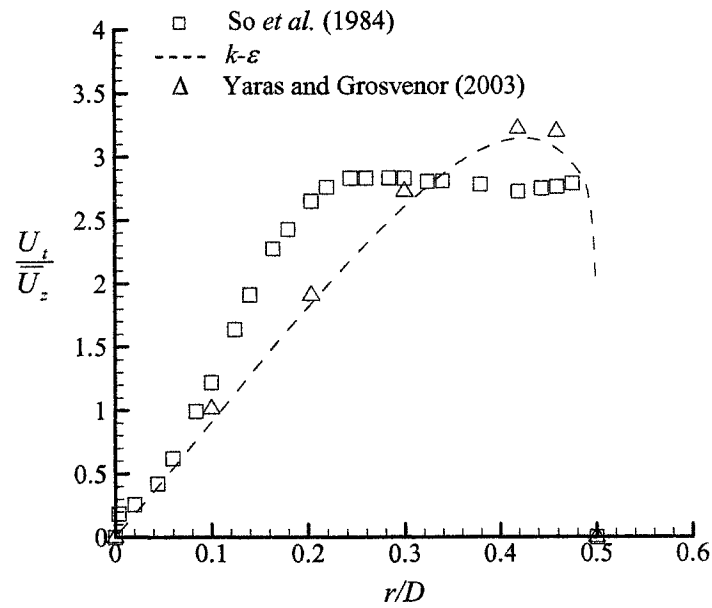


Figure 4.10.11: Predictions compared to Yaras and Grosvenor (2003) - radial distribution of tangential velocity component at $z/D_j = 14$

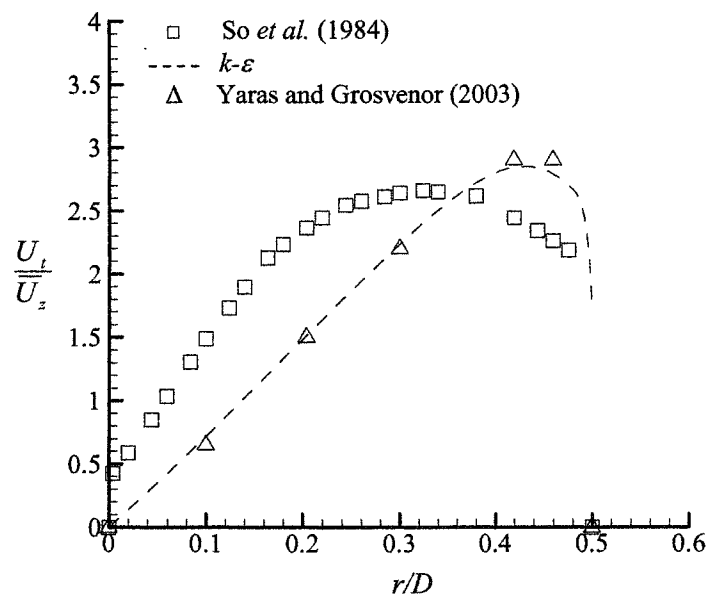


Figure 4.10.12: Predictions compared to Yaras and Grosvenor (2003) - radial distribution of tangential velocity component at $z/D_j = 40$

Chapter 5

DECAY OF TURBULENCE

In this chapter, the decay of homogeneous isotropic turbulence is investigated using large eddy simulation with Smagorinsky's sub-grid model. The simulation results are compared to the experimental data of Comte-Bellot and Corrsin (1971).

5.1 Description of Test Case

Comte-Bellot and Corrsin (1971) measured the energy spectrum at three streamwise locations downstream of a turbulence-generating mesh. The geometry of the experimental setup used by Comte-Bellot and Corrsin is shown in Figure 5.1.1.

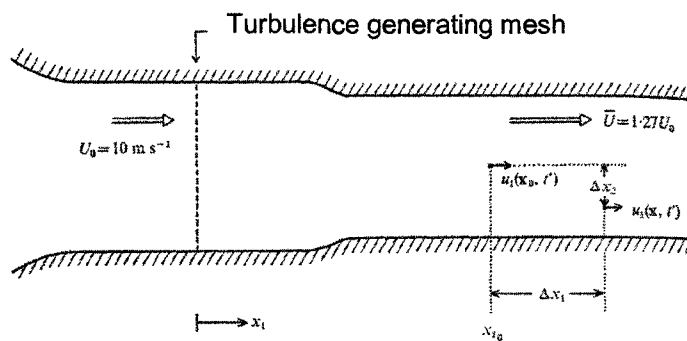


Figure 5.1.1: Geometry of experimental setup, reproduced from Comte-Bellot and Corrsin (1971)

The decay of turbulence as it is convected downstream is simulated in a computational domain with periodic boundary conditions moving with the mean flow speed. The convection time, t , is defined as:

$$t = \int_0^{x_1} \frac{dx'}{\bar{U}(x')} \quad (5.1.1)$$

where x_1 is the downstream distance from the turbulence generating-mesh, and $\bar{U}(x)$ is the free-stream velocity spatially averaged over the cross-section of the tunnel. Data of Comte-Bellot and Corrsin (1971) collected at three streamwise locations correspond to computed convection times of 0.213, 0.498, and 0.869 seconds, respectively. Herein, both experimental data (Table 5.1.1) and numerical results are presented with reference to non-dimensional times, $U_0 t / M_g$. At the location of the turbulence-generating mesh ($x_1 = 0$ m), the free-stream flow velocity is $U_0 = 10$ m/s, and the spacing of turbulence generating mesh is $M_g = 0.0508$ m. Comte-Bellot and Corrsin normalized their data by a characteristic length scale:

$$L_{ref} = 11M_g \quad (5.1.2)$$

This length scale was chosen to contain approximately four integral scales of turbulence.

$\frac{U_0 t}{M}$	$\sqrt{u_1^2}$ (cm sec ⁻¹)	ϵ Dissipa- tion rate (cm ² sec ⁻³)	η Kolmo- gorov micro- scale (cm)	λ	L	L_l	$\frac{R_\lambda}{\nu}$	$\frac{\lambda}{L} R_\lambda$
				Taylor trans- verse micro- scale (cm)	trans- verse integral scale (cm)	longi- tudinal integral scale (cm)		
42	22.2	4740	0.029	0.484	1.27	2.40	71.6	27.3
98	12.8	633	0.048	0.764	1.88	3.45	65.3	26.5
171	8.95	174	0.066	1.02	2.28	4.90	60.7	27.1

Table 5.1.1: Experimental data of Comte-Bellot and Corrsin (1971)

5.2 Theory of Decay of Homogeneous Isotropic Turbulence

5.2.1 Turbulence Length and Time Scales

One of the key characteristics of turbulence is the existence of several time and length scales. The ranges of scales which can exist are bounded by the flow domain geometry and by the diffusive action of molecular viscosity. Three dimensional rotating eddies are structures used to describe turbulence. When a flow becomes turbulent, a finite range for both time and length scales exist for these turbulent eddies. The energy transfer between the mean flow and turbulence is dictated by the dynamics of the larger eddies. The majority of energy enters the turbulence spectrum at the integral scale L_c , which is defined as the scale associated with the largest coherent turbulent structure or eddy in the flow. Dissipation mostly occurs at scales comparable to the Kolmogorov length scale, η . This implies that the general direction of energy transfer in turbulence must be from the large scales to the small scales. The process of energy transfer is usually referred to as the energy cascade. A representation of the energy cascade or spectral flux is given in Figure 5.2.1.1.

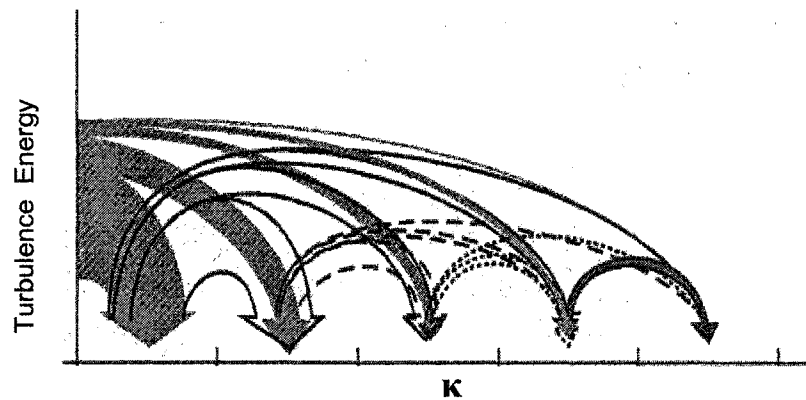


Figure 5.2.1.1: Turbulence energy cascade, reproduced from Gatski *et al.* (1996)

Although the majority of energy transfer occurs between eddies of relatively equal size, it also occurs between all scales. For the decay of isotropic homogeneous turbulence, unidirectional energy transfer is generally observed. However, energy transfer can also occur in the reverse direction in a process called back-scatter.

The horizontal axis in Figure 5.2.1.1 refers to the corresponding wave number of an eddy. The smallest wave number, κ_η , corresponds to eddies at the Kolmogorov length scale where viscous effects dominate the flow dynamics and kinetic energy is dissipated into thermal energy. The wave number, κ_e , is associated with the length scale of the large eddies, which hold the most kinetic energy. The largest possible eddies that can exist in a domain are dictated by the geometry dimensions and have an associated wave number, κ_c . Mathematically, each of these wave numbers is defined as:

$$\kappa_\eta = 2\pi / \eta \quad (5.2.1.1)$$

$$\kappa_e = 2\pi / L_c \quad (5.2.1.2)$$

$$\kappa_c = 2\pi / d \quad (5.2.1.3)$$

where d is the restricting dimension of the domain. With these parameters defined, attention will now shift to deriving analytical equations for turbulence decay.

5.2.2 Analytical Equations for the Decay of Homogeneous Turbulence

As explained by Hinze (1975), the energy spectrum of homogeneous isotropic turbulence at small wave numbers can be described as:

$$E(\kappa) = A\kappa^m \quad (5.2.2.1)$$

where A is a constant with units of $(\text{length})^{m+3}/(\text{time})^2$ and m is a constant determined from the initial conditions. The treatment of m is widely debated. From a theoretical standpoint, it has been argued that $m = 4$ is a constant based upon Loitsianskii's invariant (Loitsianskii, 1939). Due to Proudman and Reid (1954), Loitsianskii's integral was proven to vary with time at large Reynolds numbers, thus no longer being appropriate for determining m . Saffman (1967) proposed an alternative dynamic invariant which yields the value of $m = 2$.

In the inertial range ($\kappa_e \leq \kappa \leq \kappa_\eta$) of wave numbers, the turbulence energy spectrum follows the behavior of:

$$E(\kappa) = C_k \varepsilon^{\frac{2}{3}} \kappa^{-\frac{5}{3}} (\kappa L_e)^{-\mu^*} \quad (5.2.2.2)$$

where C_k , ε , and μ^* are the dimensionless Kolmogorov constant, dissipation rate, and intermittency exponent, respectively. Fluid structures with wave numbers below κ_e and above κ_η have zero turbulent kinetic energy. As turbulence decays, the energy-containing

length scale grows until it reaches the size of the domain and saturates. This is illustrated in Figure 5.2.2.1.

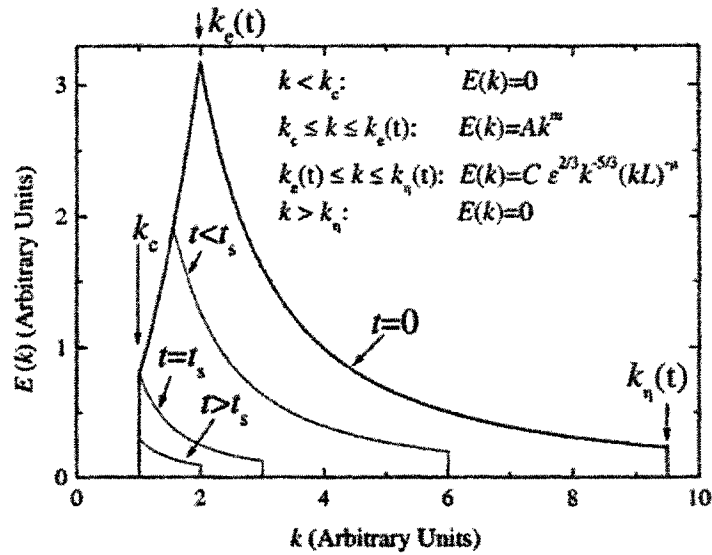


Figure 5.2.2.1: Time dependent three dimensional turbulence energy spectrum, reproduced from Skrbek and Stalp (1999)

The decay properties of turbulence before and after saturation are quite different. Skrbek and Stalp (1999) showed that the total energy of turbulence before saturation decays according to the following:

$$E < (t) = A \int_{k_c}^{k_s} k^m dk + C \epsilon^{\frac{2}{3}} \int_{k_s}^{k_n} k^{-\frac{5}{3}} (kL_c)^{-\mu} dk \quad (5.2.2.3)$$

In the extreme case of infinite Reynolds number, and using Saffman's invariant, Eqn. 5.2.2.3 can be evaluated to be:

$$E < (t) \propto t^{\frac{6}{5}} \quad (5.2.2.4)$$

After the saturation of turbulence occurs, Skrbek and Stalp (1999) showed that the decay of turbulence kinetic energy, $E > (t)$, follows:

$$E > (t) = C \varepsilon^{\frac{2}{3}} \int_{\kappa_e}^{\kappa_\eta} \kappa^{-\frac{5}{3}} (\kappa L_c)^{-\mu} d\kappa \quad (5.2.2.5)$$

Also, in the case of infinite Reynolds number and using Saffman's invariant, Eqn. 5.2.2.5 can be evaluated to be:

$$E > (t) \propto t^{-2} \quad (5.2.2.6)$$

Skrbek and Stalp (1999) showed how the intermittency coefficient, μ^* , has a negligible effect on the predicted turbulence decay rate. It was also shown that by setting $\mu^* = 0$ in Eqns. 5.2.2.3 and 5.2.2.5, the power law (Eqn. 5.2.2.1) was unaffected. Therefore, assuming that the intermittency coefficient is independent of Reynolds number, intermittency does not affect the power decay law. Furthermore, viscosity corrections are neglected since they have negligible effects on the decay rate, saturation time, and saturation energy levels.

5.3 Comparison of Analytical Results to Experimental Data

Comte-Bellot and Corrsin's (1971) experimental data presented in Section 5.1 agrees well with the analytical results based on the equations derived in Section 5.2. This comparison is shown in Figure 5.3.1. The total energy of turbulence before saturation in Eqn. 5.2.2.4 is compared to the turbulence kinetic energy of the data of Comte-Bellot and Corrsin (1971) through the estimate:

$$k = \frac{3}{2} u'^2 \quad (5.3.1)$$

where one component of the velocity fluctuation, u' , is representative of all components due to the isotropic state of the turbulence. The turbulence energy decomposition shown in Figure 5.3.1 was provided by Misra and Pullin (1997) by integrating the turbulence spectrum of Comte-Bellot and Corrsin (1971) over the relevant scale ranges (L_c , Δ , and η). In Figure 5.3.1, k_{res} and k_{sub} correspond to the resolved and sub-grid turbulence kinetic energy components, respectively:

$$k = k_{res} + k_{sub} \quad (5.3.2)$$

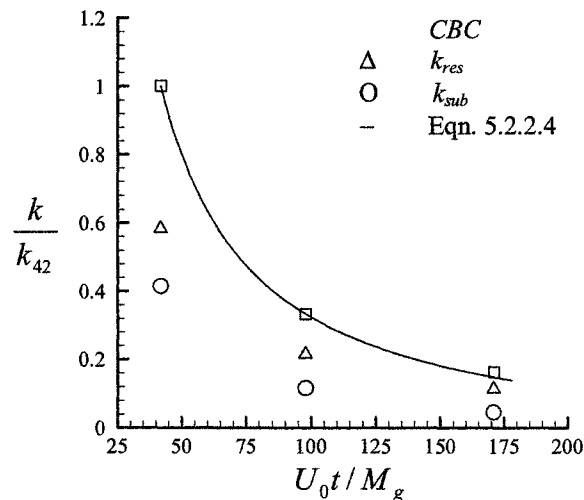


Figure 5.3.1: Measured and predicted rates of turbulence decay

Eqn. 5.2.2.4 agrees well with the experimental data of Comte-Bellot and Corrsin (*CBC*) as the decay regime is classified to be that before saturation. Since only the resolved turbulence kinetic energy can be monitored in *LES*, it is not appropriate to compare simulation results to Eqn. 5.2.2.4. Simulation results will instead be compared directly to

the resolved turbulence kinetic energy shown in Figure 5.3.1. With the quality of experimental data of Comte-Bellot and Corrsin (1971) confirmed, *LES* and Smagorinsky's sub-grid model will be discussed next.

5.4 *LES* and Smagorinsky's Turbulence Model

When the hat filter, presented in Section 2.3.1, is applied to the Navier-Stokes equations, the filtered Navier-Stokes equations are derived:

$$\rho \frac{\partial \bar{u}_i}{\partial t} + \rho \frac{\partial (\overline{u_i u_j})}{\partial x_j} = -\frac{\partial (\bar{p})}{\partial x_i} + \mu \frac{\partial}{\partial x_j} \left(\frac{\partial \bar{u}_i}{\partial x_j} + \frac{\partial \bar{u}_j}{\partial x_i} \right) - \rho \frac{\partial \tau_{ij}}{\partial x_j} \quad (5.4.1)$$

where τ_{ij} is the sub-grid stress tensor. In Smagorinsky's model, the sub-grid stress tensor, τ_{ij} , is correlated to the resolved strain-rate tensor, \bar{S}_{ij} , using an eddy viscosity,

ν_T :

$$\tau_{ij} - \frac{1}{3} \delta_{ij} \tau_{kk} = -2\nu_T \bar{S}_{ij} = -\nu_T \left(\frac{\partial \bar{u}_i}{\partial x_j} + \frac{\partial \bar{u}_j}{\partial x_i} \right) \quad (5.4.2)$$

The eddy viscosity, ν_T , is determined from dimensional analysis:

$$\nu_T = (C_s \bar{\Delta})^2 |\bar{S}| \quad (5.4.3)$$

where C_s is the Smagorinsky constant and the resolved strain-rate magnitude is

$|\bar{S}| = (2\overline{S_{ij} S_{ij}})^{\frac{1}{2}}$. The filter width, $\bar{\Delta}$, is the characteristic length scale of the sub-grid

motion. Lilly (1967) derived a high-Reynolds-number expression for the Smagorinsky constant assuming a large inertial range for the isotropic decay of turbulence:

$$C_s = \frac{1}{\pi} \left(\frac{2}{3C_k} \right)^{\frac{3}{4}} = 0.18 \quad (5.4.4)$$

5.5 Computational Domain and Discretization

As shown in Figure 5.5.1, the computational domain for this study was chosen to be of cubic shape with an edge length of $L_{ref} = 11M_g$. This domain size contains approximately 4 integral length scales of turbulence, L_c . The choice of domain sizing is consistent with the work of Misra and Pullin (1997) and the inclusion of 4 integral scales in the domain was considered adequate to resolve the largest scales of turbulence.

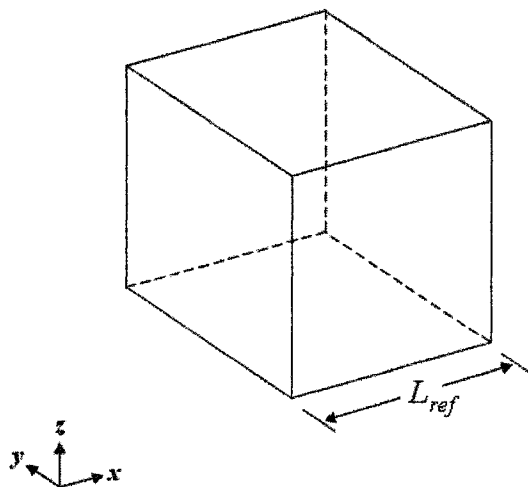


Figure 5.5.1: Computational domain

The convective and diffusive space derivatives were discretized with second-order accuracy using a central-differencing scheme. The central differencing scheme was recommended for *LES* in the user manual for *CFX 5.7*, since it is less dissipative than the high resolution scheme available in *CFX*. The discretization of the time derivative was selected to be second order backward Euler.

5.6 Boundary Conditions

The computational domain is enclosed by surfaces with periodic boundary conditions as shown in Figure 5.6.1. The periodic interface chosen in *CFX* is the one-to-one interface where identical grid-node distributions exist on each side of the interface. This type of connection allows the nodal values from one periodic surface to be applied to the nodal values at the other surface without the need for spatial interpolation.

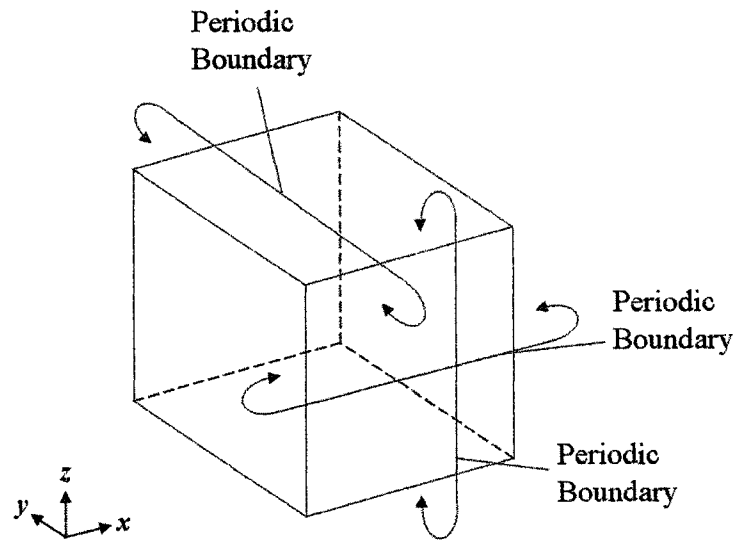


Figure 5.6.1: Boundary conditions

5.7 Initial Conditions

The computational domain was initialized to atmospheric pressure, zero mean velocity, and a specified velocity fluctuation. When the velocity fluctuation initialization option is used, *CFX* gives a homogeneous random distribution of the velocity field. The velocity fluctuation level is dependent on temporal resolution, which was a parameter that varied between simulations.

Ideally, the flow data of the first measurement location would be used for initialization, and the total time needed to run the transient simulation would then be 0.656 seconds. However, the initial turbulence field produced by *CFX* was found to be anisotropic and required approximately 100 to 200 time-steps to reach an isotropic state, with a difference between spatially-averaged velocity correlations, $\overline{u'_i u'_i}$, of less than one

percent. Therefore, the initial 200 time-steps of each simulation was considered to be a part of the initialization process. Also, during this initialization period, the magnitude of the decay rate was approximately one order of magnitude larger than the decay rate after this period. Therefore, it was required that simulations be initialized at levels of velocity fluctuation much higher than u'_{42} . This range of velocity-fluctuation initialization, u'_{init} , extended from $1.5u'_{42}$ to $10u'_{42}$. Figure 5.7.1 shows the initialization process for a typical simulation.

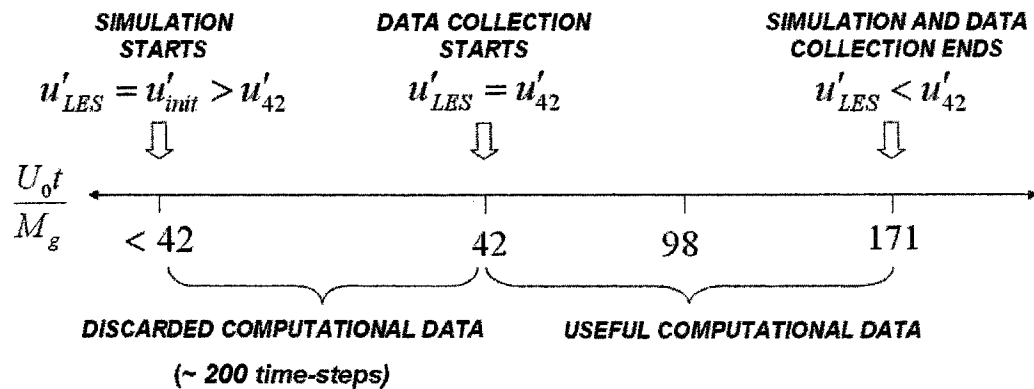


Figure 5.7.1: Simulation initialization process

In Figure 5.7.1, u'_{LES} is the velocity fluctuation predicted through *CFX*. It should be noted that u'_{init} and the extent of discarded computational data were chosen to ensure identical values of predicted and experimental turbulence levels at the first measurement location ($u'_{LES} = u'_{42}$). This is elaborated upon in Figure 5.7.2, which presents the sensitivity of turbulence decay rate to velocity-fluctuation initialization values. It appears

that the decay rate is not affected by the level of velocity fluctuation that each simulation is initialized to.

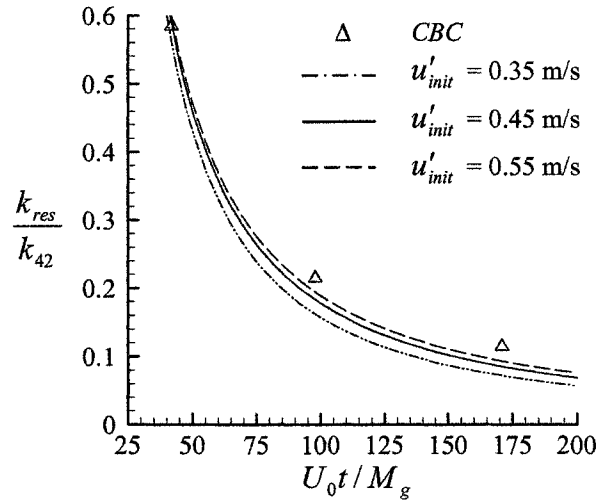


Figure 5.7.2: Sensitivity of decay rate to initialization
($\nu = 1.55 \times 10^{-5} \text{ m}^2/\text{s}$, $C_s = 0.18$, $\nu = 0.009$)

5.8 Spatial and Temporal Resolution

5.8.1 Spatial Resolution

The spatial resolution was set to resemble that of a similar study by Misra and Pullin (1997). In their decay predictions of Comte-Bellot and Corrsin's turbulence data, a structured grid in a cubic domain of 32^3 grid-nodes was used. The spatial resolution corresponds to:

$$\frac{\Delta}{\eta} = \frac{L_{ref} / N_d}{\left(\frac{\nu^3}{(k / L_{ref})^3} \right)^{\frac{1}{4}}} = 40 \quad (5.8.1.1)$$

where Δ , η , and N_d are the mean grid-node spacing, Kolmogorov length scale, and number of grid-nodes per edge length of the computational domain, respectively. This ratio of mean-grid-node spacing-to-Kolmogorov length scale is consistent with the choices of Moin *et al.* (1991) and Dailey *et al.* (1996). Furthermore, shown in a similar study by Misra and Pullin (1997), this spatial resolution corresponds to resolving 60 to 70% of the turbulence energy spectrum. Pope (2000) demonstrates a method of grouping types of *LES* based upon the amount of turbulence energy the computational grid resolves. According to Pope (2000), since less than 80% of the turbulence energy is resolved, this type of simulation is termed a very-large-eddy simulation. Due to the absence of wall boundaries or pressure gradients, the level of turbulence allocated to the sub-grid model is considered adequate.

One observation deduced from Figure 5.8.1.1 is that as turbulence decays, the portion of energy allocated to the sub-grid turbulence model decreases. This is expected as the ratio of mean-grid-node spacing-to-Kolmogorov length scale decreases as turbulence decays. Therefore, as the simulation proceeds in time, the prediction accuracy becomes less dependent on the sub-grid model performance.

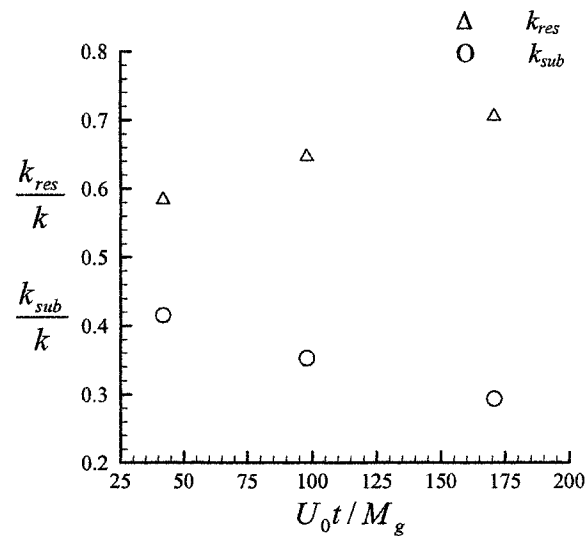


Figure 5.8.1.1: Decomposition of turbulence kinetic energy ($\nu = 1.55 \times 10^{-5} \text{ m}^2/\text{s}$, $C_s = 0.18$, $\nu = 0.009$), reproduced from Misra and Pullin (1997)

For this study, the Patran-Volume-Meshing method of *CFX* was used to create the spatial grid. The Patran-Volume-Meshing method uses either an unstructured Paver algorithm or a structured IsoMesh algorithm. The IsoMesh tool was used to create a structured hexahedral grid of 32 nodes in each principal direction. IsoMesh creates equally spaced nodes along each edge in real space and requires the domain to have either three or four sides. The node distribution is controlled by the grid seed specified by the user. A grid seed for an edge of a computational grid is defined by the total number of nodes or a mean-grid-node spacing. For the present study, a uniform grid seed of 32 nodes was applied to each edge of the computational grid corresponding to a mean grid-node spacing of $\Delta = 0.0175 \text{ m}$. Figure 5.8.1.2 shows the resultant structured grid.

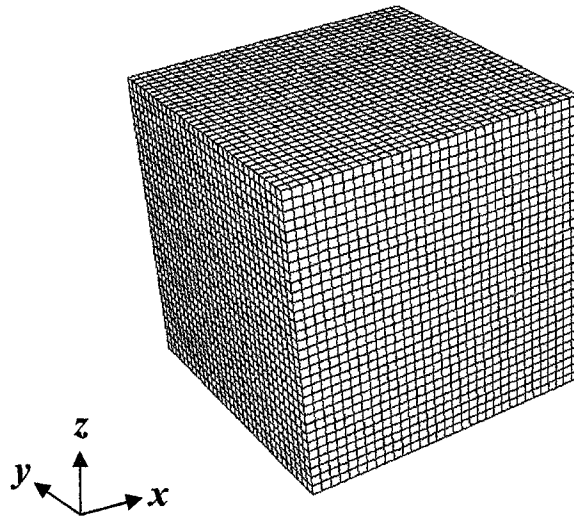


Figure 5.8.1.2: Computational grid for isotropic decay of turbulence

5.8.2 Temporal Resolution

The effects of temporal resolution on the decay of isotropic turbulence are investigated in this study. The range of temporal resolution is based upon a range of Courant number:

$$0.009 < \nu < 0.5 \quad (5.8.2.1)$$

The conventional Courant number was defined in Section 2.2.2, but when specifically applied to this study, it is defined as:

$$\nu = u'_{42} \frac{\Delta t}{\Delta x} \quad (5.8.2.2)$$

where u'_{42} is the fluctuating velocity corresponding to the first measurement location of Comte-Bellot and Corrsin (1971) shown in Table 5.1.1. Generally a Courant number in the range of 0.5 to 1 is recommended in the user manual for *CFX 5.7* for most *LES*. The

user manual claims that larger values can give stable results but the turbulence may be damped. In this case of isotropic decay of homogenous turbulence, CFX-SUPPORT (2004) recommended a Courant number less than 0.1. Kang *et al.* (2003) used Smagorinsky's sub-grid turbulence model to predict the decay of isotropic turbulence and used a Courant number of $\nu = 0.05$. For the present study, simulations using a Courant number of $\nu = 0.009$ and $\nu = 0.5$ corresponded to time-steps of 0.0007 and 0.04 seconds, respectively.

5.9 Solution Convergence

Monitoring solution convergence for *LES* is not as straight forward as that for *RANS* simulations, although certain techniques are shared by both. As *LES* is a transient simulation, at each time-step the filtered governing equations are solved iteratively. The number of iterations per time-step is either determined by a minimum *RMS* residual level or simply by an upper limit for the iteration count specified by the user. After the required iterations are completed at a time-step, the *CFX* algorithm proceeds to the next time-step using the flow data from the last iteration of the last time-step as an initial condition. For the present simulations, a minimum residual level of 10^{-4} and maximum number of 10 iterations was specified for each time-step. Typically, during the beginning of the simulations, the *RMS* residual levels for mass and momentum did not meet the time-step residual-convergence criterion of 10^{-4} before the algorithm proceeded to the next time-step. However, after approximately 10 time-steps, the simulation became

stable enough to meet the time-step residual convergence criteria before the maximum iteration count was reached. Solution sensitivity to the specified minimum residual level is shown in Figure 5.9.1.

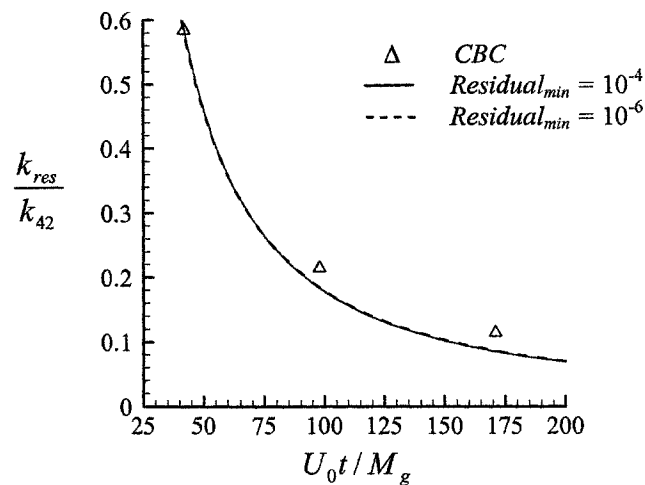


Figure 5.9.1: Solution sensitivity to time-step convergence criteria ($\nu = 1.55 \times 10^{-5} \text{ m}^2/\text{s}$, $C_s = 0.18$, $\nu = 0.009$)

From Figure 5.9.1 it can be seen that the minimum residual level of $Residual_{min} = 10^{-4}$ is adequate as a convergence criteria.

Figure 5.9.2 shows the time history of *RMS* residuals for a typical *LES* run of turbulence decay. As shown in the figure, during each time-step, the momentum *RMS* residuals drop at a faster rate than the *RMS* residuals corresponding to the continuity equation. However, both residuals are of the same order of magnitude when the algorithm proceeds to the next time-step.

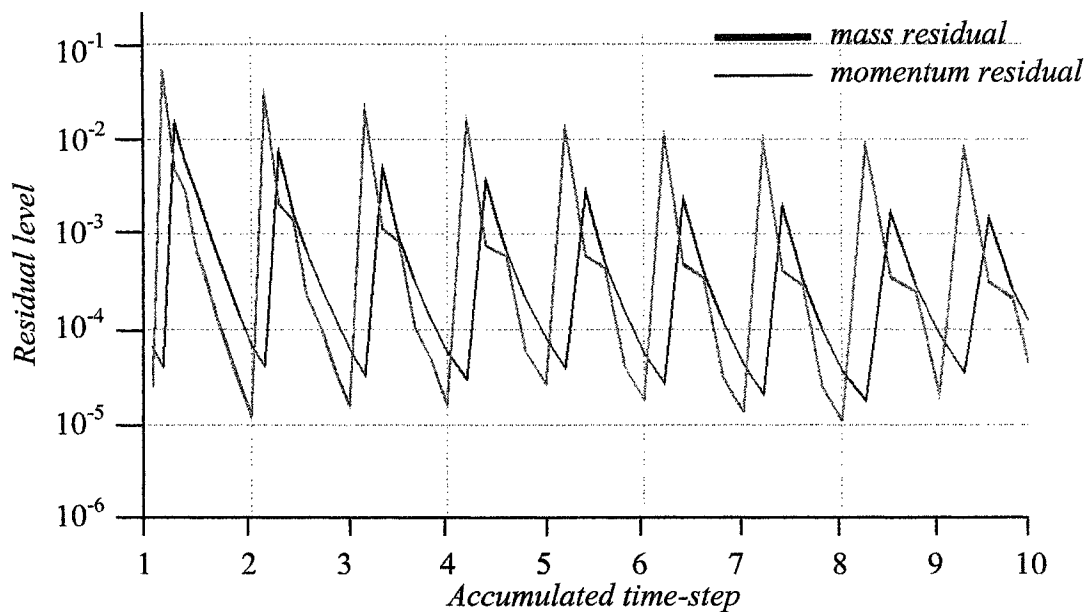


Figure 5.9.2: Typical residual plot for *LES* of turbulence decay
 $(\nu = 1.55 \times 10^{-5} \text{ m}^2/\text{s}, C_s = 0.18,$
 $\nu = 0.009, 2 \text{ iterations/time-step})$

The chosen residual convergence criteria resulted in a global mass conservation within one percent at each time increment. In the present study, typically between 1000 and 10000 time-steps were required to complete simulations from $U_0 t / M_g = 42$ to 171, with approximately 2 iterations per time-step. Although it appears that the residuals corresponding to the mass and momentum equations are not synchronized in Figure 5.9.2, *CFX* solves these equations simultaneously during iterations. The non-synchronization between these residual levels is merely due to how *CFX* presents them. Simulations requiring 1000 to 10000 time-steps took approximately 5 to 50 hours to complete on a Pentium 4, 2GHz computer with 1GB of RAM.

5.10 Simulation Results

The prediction capability of *LES* is assessed by investigating the effects of numerical dissipation and computational grid structure on the decay of isotropic turbulence. Upon determining optimum values for these simulation parameters, a direct comparison of simulation results to experimental data is presented.

5.10.1 Effects of Numerical Dissipation

The level of numerical dissipation has a large impact on the accuracy of an algorithm. For the simulations presented, it was found that the level of molecular viscosity and Courant number largely affect the level of numerical or artificial dissipation. This dissipation is caused by the truncated terms of the discretized partial-differential equations (*PDE*). It is well known that the truncated terms contain molecular viscosity and the Courant number, hence the noted sensitivity of numerical dissipation to these two parameters. As an example, the interrelation between truncated terms, numerical dissipation, Courant number, and molecular viscosity is demonstrated analytically on a simplified *PDE* and a well-established discretization scheme in Appendix H.

As noted in the example given in Appendix H, for second-order discretization in time and space, the truncated terms typically consist of dissipative and dispersive terms. The dissipative terms typically scale directly on the molecular viscosity, as is the case in

this example. Assuming that this holds true for the *CFX* algorithm, one can attempt to quantify the dispersive error by setting the molecular viscosity to zero, and vary the Courant number to determine the dependence of dispersion on this parameter (Figure 5.10.1.1).

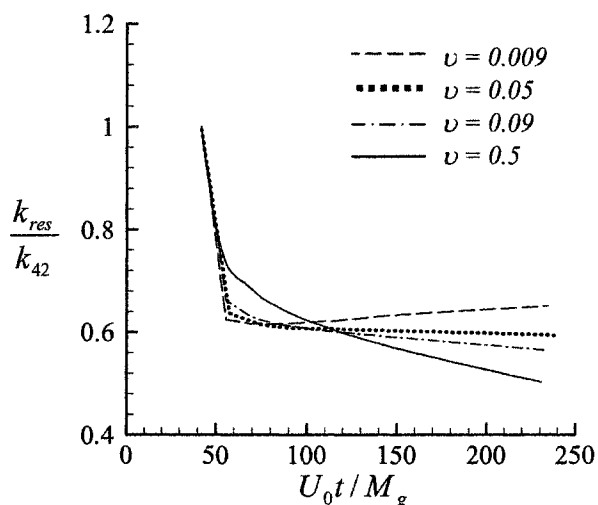


Figure 5.10.1.1: The effects of Courant number on turbulence decay ($C_s = 0$)

The results in Figure 5.10.1.1 demonstrate the presence of dispersion in the truncation error of the *CFX* algorithm, as is evident from the increase of turbulence energy in time for $\nu = 0.05$. Furthermore, the presence of decay for higher values of Courant number indicates that the functional form of the dissipative component of the truncation error is such that it is not eliminated by setting the molecular viscosity to zero. The simulation that corresponds to a Courant number of $\nu = 0.05$ is considered to be the most realistic as it yields a turbulence kinetic energy independent of time in the absence of a physical dissipation mechanism, i.e. molecular viscosity.

Figures 5.10.1.2 and 5.10.1.3 show the effects of molecular viscosity on the decay rate of turbulence for *LES* using a Smagorinsky constant of $C_s = 0.18$ and $C_s = 0$, respectively. In Figure 5.10.1.3, the range of $U_0 t / M_g$ extends from -400 to 300. This is due to the procedure of proper turbulence initialization so that a state of isotropic turbulence exists at the first measuring location as explained in Section 5.7. In previous figures, the data before the first measuring location was not presented as it was not necessary to show the initialization process.

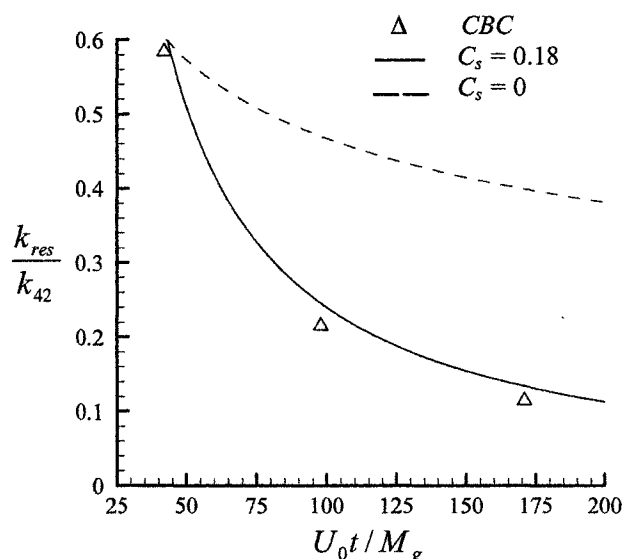


Figure 5.10.1.2: The effect of the sub-grid model on the rate of turbulence decay ($\nu = 0.05$, $\nu = 1.55 \times 10^{-5}$)

As is noted in Figure 5.10.1.2, in the presence of molecular viscosity, turbulence kinetic energy decays in time. While part of this trend may be due to physical dissipation, since the dissipative range (Kolmogorov scale) of turbulence activity was not

resolved, this effect is likely secondary. The noted decay is therefore hypothesized to be primarily due to numerical dissipation. As expected, with the introduction of Smagorinsky's sub-grid model into the computation, the correct level of turbulence decay rate is achieved. These results were quite similar to the results obtained by Misra and Pullin (1997), as they also successfully predicted decay on a similar computational grid.

5.10.2 Effects of Computational Grid Structure

For computational efficiency it is paramount that one optimizes the spatial grid. This optimization involves coarsening the grid as much as possible while maintaining adequate resolution of regions of high spatial gradients such as wall boundary layers. It is important to recognize that the criteria for optimizing a grid in *LES* computations are not necessarily the same as those used in *RANS* computations. Firstly, the concept of grid-independent solution does not exist in *LES* when the grid itself is being used as the filter. Instead, the choice of grid-node spacing dictates the proportions of resolved and modeled turbulence. Secondly, with the larger turbulence eddies being resolved in *LES*, the stretching, skewness, and aspect-ratio of the grid cells are likely to affect the solution more substantially than in *RANS* computations. It is therefore critical that the sensitivity of *LES* computations to such features of the spatial-grid structure be established. For example, in Figure 5.10.2.1, an anisotropic computational grid characterized by an expansion (stretching) factor of three is shown.

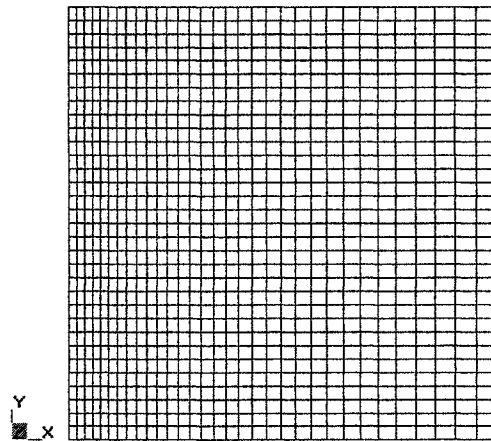


Figure 5.10.2.1: Spatial resolution for anisotropic grid (expansion factor = 3)

The grid-node spacing on the right side is three times larger than the grid-node spacing on the left side. The expansion factor is only applied to the x direction, resulting in cells with aspect ratios ranging from 0.54 to 1.66. Figure 5.10.2.2 shows these deviations from the uniform baseline grid (Figure 5.8.1.2) have no noticeable effect on the decay rate of isotropic turbulence.

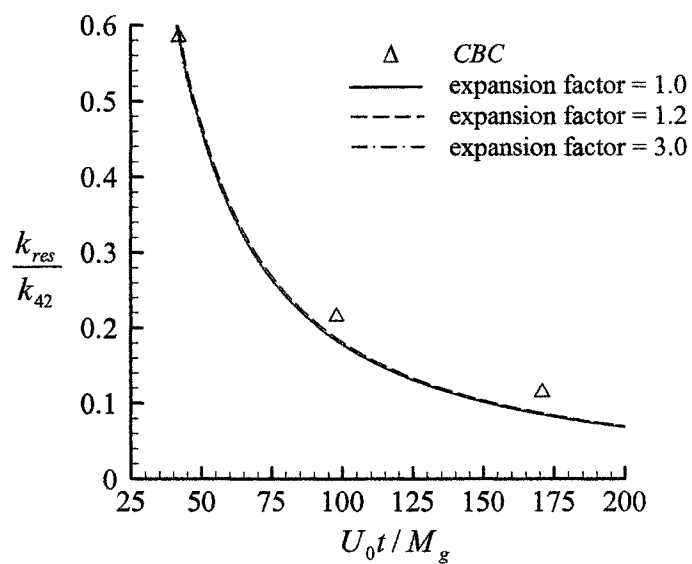


Figure 5.10.2.2: The effects of stretch ratio on the decay of turbulence
 ($\nu = 1.55 \times 10^{-5} \text{ m}^2/\text{s}$, $C_s = 0.18$, $\nu = 0.009$)

Chapter 6

INCLINED-JET-IN-CROSS-FLOW

In this chapter, the prediction capability of *RANS* (ω -Reynolds-stress turbulence model) and *LES* (Smagorinsky's sub-grid model) for the flow field of an inclined-jet-in-cross-flow are established. The predictions are compared to the experimental data of Yaras (2004).

6.1 Description of Test Case

The simulated jet, depicted schematically in Figure 6.1.1 has, perpendicular to the jet axis, a circular discharge cross-section of diameter $D_j = 0.06826$ m, with the jet inclined at a pitch angle of $\Phi = 45^\circ$ relative to the test surface. Measurements of mean flow variables along with turbulence properties obtained with a 4-wire probe are presented at y - z planes at streamwise locations over the range of $-5D_j < x < 11D_j$. In each measurement plane, the first and second measurement points off the test surface are located at $y = 6.6$ mm ($0.1D_j$) and $y=10$ mm, respectively. The next 14 measurement points in the y direction are spaced 10 mm apart, followed by 8 points of 20 mm spacing. In the lateral (z) direction, the spacing of measurement points is kept uniform at 10 mm. As shown in Figure 6.1.1, the cross sectional area of each measurement plane is smaller than the cross sectional area of the test section. To document the flow conditions in the

jet as it discharges from the test surface, the 4-wire probe is traversed 3 mm ($0.044D_j$) above the test surface with its axis aligned with the axis of the jet. Measurement points are slightly clustered towards the perimeter of the jet orifice where larger gradients in the velocity distribution are located.

The jet Reynolds number is $Re_{D_j} = 40800$, and is based on the spatially-averaged jet velocity of $V_j = 9$ m/s and jet diameter, D_j . The average jet velocity to cross-flow freestream velocity ratio (VR) is 1.1.

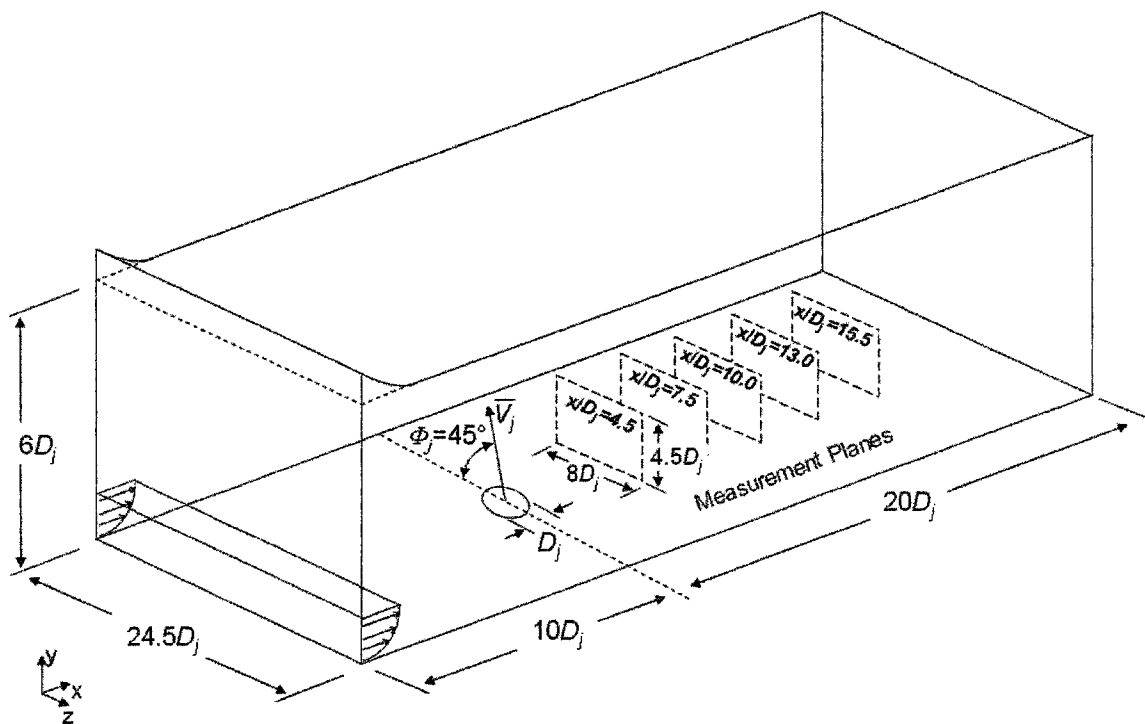


Figure 6.1.1: Geometry of experimental test section

The inclined-jet-in-cross-flow test section (Figure 6.1.1) consists of a frame of 2.04 m length, 1.67 m width, and 0.71 m height, housing a test surface with a single jet hole and

a contoured ceiling. The frame is sized to occupy the full length and full width of the test area in the wind tunnel. The purpose of the flexible, contoured ceiling is to allow the manipulation of the streamwise pressure distribution on the test surface. The current configuration provides a slightly converging flow path into the test section. Downstream of this region, the ceiling is kept at a constant distance of 0.47 m from the test surface. The jet hole is positioned just downstream of the converging section.

A 5 hp centrifugal fan supplies the airflow for the jet. After the air is discharged from the fan, it is directed through a 0.156 m – diameter basket diffuser into a 0.28 m x 0.28 m x 0.60 m stagnation chamber. Midway through the stagnation chamber, the air is passed through a honeycomb layer before being accelerated through a bell-mouth into a galvanized steel pipe of diameter D_j and 0.55 m length ($8D_j$).

A miniature 4-wire probe, controlled by a 4-channel constant-temperature anemometer, was used to measure the three-dimensional velocity and turbulence fields throughout the test section. The four (1.3 mm long) tungsten hot-wire sensors on the probe are positioned at approximately 45° relative to the probe axis and are circumferentially positioned at 90° from each other to form the shape of a pyramid. A measurement volume of approximately 2 mm diameter is created through the orientation of the four sensors.

The uncertainty of the time-averaged velocity magnitude and direction measured with the 4-wire probe are estimated to be within 3% and $\pm 2^\circ$ of actual values. The effective cooling velocities of the four wire sensors are normalized by V_{ref} , which is the reference velocity measured at $(x,y,z) = (-4.44D_j, 4.39D_j, 0.0D_j)$.

6.2 Turbulence Models

6.2.1 RANS Reynolds-Stress Turbulence Model

The first turbulence model tested in this benchmark is the ω -Reynolds-stress model. Such second order models solve a partial differential equation for each of the Reynolds-stresses in addition to a partial differential equation for the specific turbulence dissipation rate, ω . The transport equations for the Reynolds stresses are defined as:

$$\rho \frac{\partial(\overline{u'_i u'_j})}{\partial t} + \rho U_k \frac{\partial(\overline{u'_i u'_j})}{\partial x_k} = d_{ij} + P_{ij} + \phi_{ij} + \frac{2}{3} \beta' \rho k \omega \delta_{ij} \quad (6.2.1.1)$$

where k is the turbulence kinetic energy. The diffusion term, d_{ij} , the production term, P_{ij} and the pressure-strain term, ϕ_{ij} , are defined as:

$$d_{ij} = \frac{\partial}{\partial x_k} \left[\left(\mu + \frac{\mu_T}{\sigma_T} \right) \frac{\partial \overline{u'_i u'_j}}{\partial x_k} \right] \quad (6.2.1.2)$$

$$P_{ij} = -\overline{\rho u'_i u'_k} \frac{\partial U_j}{\partial x_k} - \overline{\rho u'_j u'_k} \frac{\partial U_i}{\partial x_k} \quad (6.2.1.3)$$

$$\begin{aligned} \phi_{ij} = & \rho \beta' C_\omega \omega \left(\overline{u'_i u'_j} + \frac{2}{3} k \delta_{ij} \right) - \rho \hat{\alpha} \left(P_{ij} - \frac{1}{3} P_{kk} \delta_{ij} \right) \\ & - \rho \hat{\beta} \left(D_{ij} - \frac{1}{3} P_{kk} \delta_{ij} \right) - \rho \hat{\gamma} k \left(S_{ij} - \frac{1}{3} S_{kk} \delta_{ij} \right) \end{aligned} \quad (6.2.1.4)$$

where the turbulent viscosity, μ_T , appearing in the diffusion term is calculated to be:

$$\mu_T = \rho \frac{k}{\omega} \quad (6.2.1.5)$$

In these expressions, S_{ij} is the mean strain rate tensor:

$$S_{ij} = \frac{1}{2} \left(\frac{\partial U_i}{\partial x_j} + \frac{\partial U_j}{\partial x_i} \right) \quad (6.2.1.6)$$

and D_{ij} is a tensor defined as:

$$D_{ij} = -\overline{\rho u'_i u'_k} \frac{\partial U_k}{\partial x_j} - \overline{\rho u'_j u'_k} \frac{\partial U_k}{\partial x_i} \quad (6.2.1.7)$$

In contrast to the *SSG* Reynolds-stress model (Section 4), which solves for the dissipation rate, ε , the ω -Reynolds-stress turbulence model solves for the specific dissipation rate, ω , through the transport equation:

$$\rho \frac{\partial \omega}{\partial t} + \rho U_j \frac{\partial \omega}{\partial x_j} = \alpha \frac{\omega}{k} \overline{\rho u'_i u'_j} \frac{\partial U_i}{\partial x_j} - \beta \rho \omega^2 + \frac{\partial}{\partial x_j} \left[\left(\mu + \frac{\mu_T}{\sigma} \right) \frac{\partial \omega}{\partial x_j} \right] \quad (6.2.1.8)$$

As shown in Section 3.3.3.2, the relationship between ε and ω is given as:

$$\varepsilon = k\omega \quad (6.2.1.9)$$

CFX's automatic wall treatment is used for this turbulence model, which consists of blending *CFX's* scalable wall function (Section 4.5) with a low-Reynolds-number near-wall formulation. Near the wall, the flux for each Reynolds-stress equation is artificially kept to be zero and the flux for the momentum equation, F_U , is specified as:

$$F_U = -\rho u_\tau u^* \quad (6.2.1.10)$$

The friction velocity, u_τ , the near wall velocity scale, u^* , and wall shear stress, τ_w , are defined as:

$$u_\tau = \left(\frac{\tau_w}{\rho} \right)^{\frac{1}{2}} \quad (6.2.1.11)$$

$$u^* = \max \left(\left(\frac{1}{2} \overline{\alpha u'_i u'_i} \right)^{\frac{1}{2}}, u_\tau \right) \quad (6.2.1.12)$$

$$\tau_w = \mu \frac{\partial u}{\partial y} \Big|_{y=0} \approx \mu \frac{U_t}{y_p} \quad (6.2.1.13)$$

where U_t is the velocity tangent to the wall at a distance of y_p from the wall. Near the wall, ω is estimated by:

$$\omega = \omega_s \left(1 + \left(\frac{\omega_l}{\omega_s} \right)^2 \right)^{\frac{1}{2}} \quad (6.2.1.14)$$

where ω_l and ω_s are analytical equations for ω in the logarithmic region and viscous sub-layer of the boundary layer, respectively:

$$\omega_l = \frac{u^*}{\alpha_1 \kappa y_p} \quad (6.2.1.15)$$

$$\omega_s = \frac{6\nu}{\beta y_p^2} \quad (6.2.1.16)$$

The empirical constants in Eqns. 6.2.1.1-16 are determined to be:

$$\hat{\alpha} = 0.78, \hat{\beta} = 0.2, \hat{\gamma} = 0.49, C_\omega = 1.8, \sigma_T = 2, \beta' = 0.09, \beta = 0.075, \sigma = 2, \alpha = 5/9$$

6.2.2 LES and Smagorinsky's Turbulence Model

In Smagorinsky's model (Section 2.3.1), the sub-grid stress tensor, τ_{ij} , is correlated to the resolved strain-rate tensor, \bar{S}_{ij} , using an eddy viscosity, ν_T . Since this type of flow is

wall bounded, Smagorinsky's constant is set to $C_s = 0.1$ (Ferziger, 1993). The discrepancy in C_s values used for this benchmark and the decay of isotropic turbulence (Section 5) is speculated to be related to an increase in backscatter in flows with mean strain or shear. Ferziger (1993) and McMillan *et al.* (1980) claim that Smagorinsky's model has a higher prediction capability for the decay of isotropic turbulence than it does for wall bounded flows because the model was designed to operate in exclusively dissipative environments. This is why Ferziger (1993) suggests that for inhomogeneous shear flows, Smagorinsky's constant must be adjusted to approximately $C_s = 0.1$.

In addition to the effects of backscatter, Smagorinsky's model overestimates sub-grid stresses near the wall due to the misrepresentation of turbulence length scales. The standard Smagorinsky model uses the local grid-node spacing, instead of the distance to the wall, as characteristic turbulence length scale. This is a poor choice of turbulence length scale near the wall, since it is known that the presence of the wall acts as a damping mechanism (Tennekes and Lumely, 1972). Therefore, turbulence wall damping functions are needed for wall bounded flows when Smagorinsky's model is used. For this study, the van-Driest (1956) wall damping function is used to calculate the eddy viscosity near walls:

$$\nu_T = \min(l_{mix}, f_v C_s \bar{\Delta})^2 |\bar{S}| \quad (6.2.2.1)$$

where f_v and l_{mix} are the wall damping function and turbulence mixing length scale, respectively. These terms are calculated as follows:

$$l_{mix} = k_v y_p \quad (6.2.2.2)$$

$$f_v = 1 - \exp\left(-\frac{\tilde{y}}{A_v}\right) \quad (6.2.2.3)$$

$$\tilde{y} = \frac{y_p U_t}{\nu} \quad (6.2.2.4)$$

\tilde{y} is the dimensionless distance from the wall. $k_\nu = 0.4$ and $A_\nu = 25$ are constants.

6.3 Computational Domain and Discretization

Figure 6.3.1 shows the dimensions of the computational domain used for both *LES* and *RANS* simulations. The computational domain was chosen to extend $2D_j$ upstream of the jet exit and $19D_j$ in the downstream direction. The inflow boundary location is considered to be far enough upstream of the jet where the cross-flow is still undisturbed. The location of the outflow boundary was chosen to be significantly far from the location of the last measurement plane ($x = 19D_j$) in order to have negligible effects on computational results. Initial lateral ($3D_j$) and vertical ($5D_j$) dimensions of the computational domain were set to resemble that of a similar study by Grosvenor (2000). Grosvenor's numerical study of an inclined jet-in-cross-flow was characterised by a rectangular jet inlet geometry, a jet-pitch angle of $\Phi = 30^\circ$, a jet Reynolds number $Re_{D_j} = 4910$, and a jet-to-cross-flow velocity ratio $VR = 1.5$. In contrast to free-slip wall boundaries used for *RANS* simulations in this study (Section 6.4), Grosvenor (2000) used a uniform static pressure outflow boundary, and periodic boundaries for the top and side surfaces, respectively. Free-slip wall boundaries used for both the side and top surfaces

may impose artificial effects on the development of the vortex. These artificial effects are avoided by placing the wall boundaries at distances sufficiently far away from the vortex. The lateral and vertical dimensions shown in Figure 6.3.1 were determined from a domain size sensitivity study based on *RANS* simulations, where free-slip wall boundaries were used. Since the damping of turbulence near walls prohibited the use of free-slip wall boundaries at the side surfaces during *LES*, periodic boundaries were used instead. It was found that *RANS* simulations were insensitive to the choice of either free-slip wall boundaries or periodic boundaries for the side surfaces. Therefore, the domain size sensitivity studies conducted using *RANS* simulations are also applicable to *LES*.

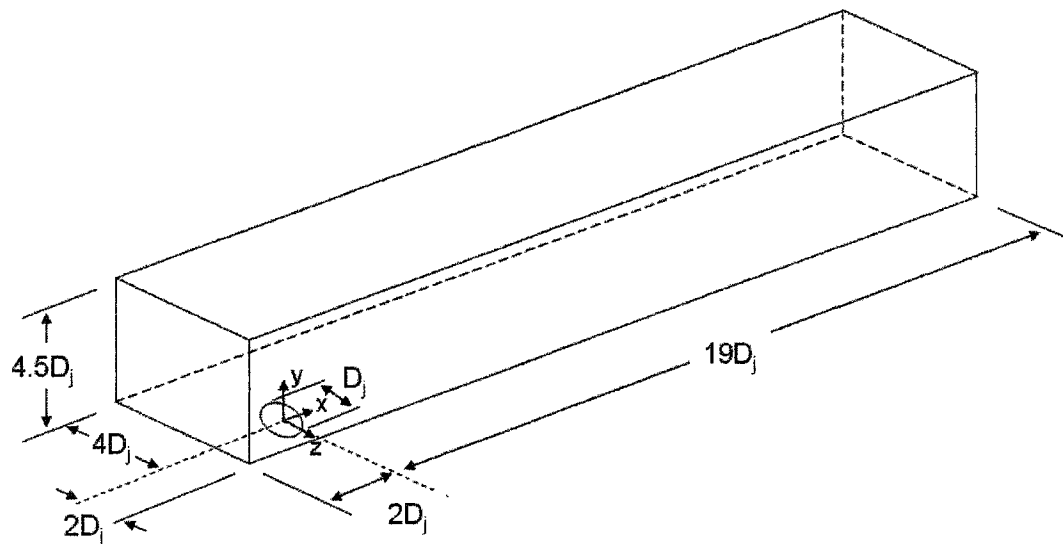


Figure 6.3.1: Computational domain for inclined jet-in-cross-flow

For both *LES* and *RANS* simulations, convective and diffusive space derivatives were discretized with second order accuracy (centered differencing). The discretization of the time derivative for *LES* was selected to be second order backward Euler.

6.4 Boundary Conditions

The inflow boundary conditions for the mean velocity and turbulence properties were specified using a two-dimensional cloud function available in *CFX*. The function executes by interpolating from a list of point coordinates and a list of flow-parameter values at those points. This type of function allows the user to specify discrete values at arbitrary locations.

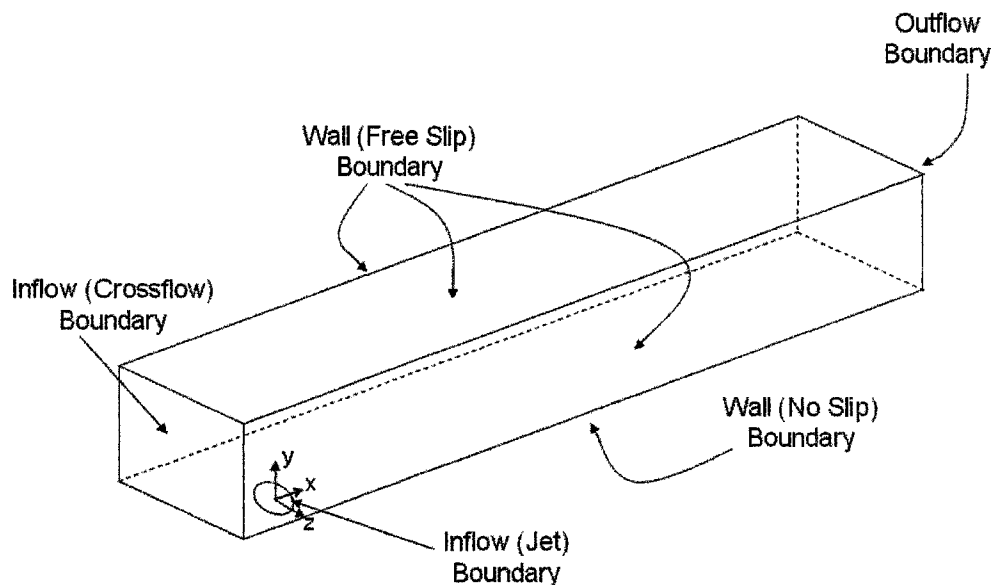


Figure 6.4.1: Boundary conditions for inclined-jet-in-cross-flow using *RANS*

The inflow boundary was located $2D_j$ upstream of the inclined jet. This choice was dictated by the availability of the flow measurements, experimental setup considerations and constraints on computational resources. Flow data existed at two cross-sectional planes upstream of the inclined jet: at $x=-2 D_j$ and $x=-5 D_j$. Choosing the

inflow boundary to be positioned at $x=-2 D_j$ avoided the problem of a converging cross-sectional area of the test section that existed upstream of the $x=-2 D_j$ location (Figure 6.1.1). Also, choosing the location at $x=-2 D_j$ reduced the total node count, hence computing time.

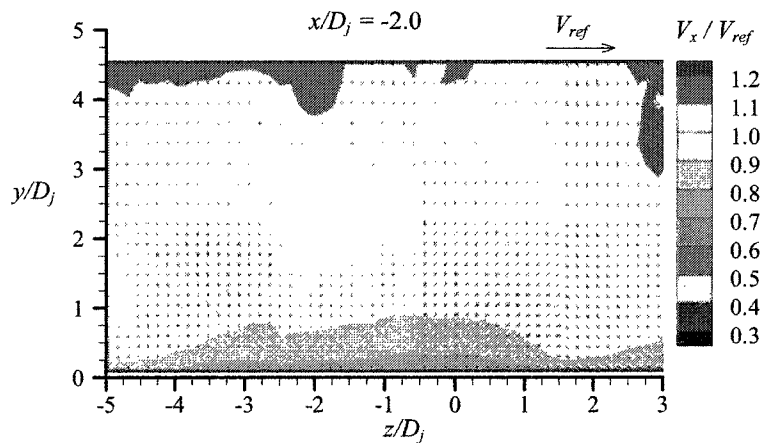


Figure 6.4.2: Mean velocity distributions at the inflow boundary

The velocity distribution (V_x , V_y , and V_z) shown in Figure 6.4.2 was specified at the inflow boundary. This velocity distribution corresponds to the experimental data of Yaras (2004) at $x/D_j = -2$. At this streamwise location, Yaras (2004) showed that lateral variations in boundary-layer momentum thickness, θ , and boundary-layer displacement thickness, δ^* , are within 10%, suggesting the presence of a fairly two-dimensional boundary layer. The reference velocity used to normalize the experimental and simulation data, is $V_{ref} = 7.44$ m/s.

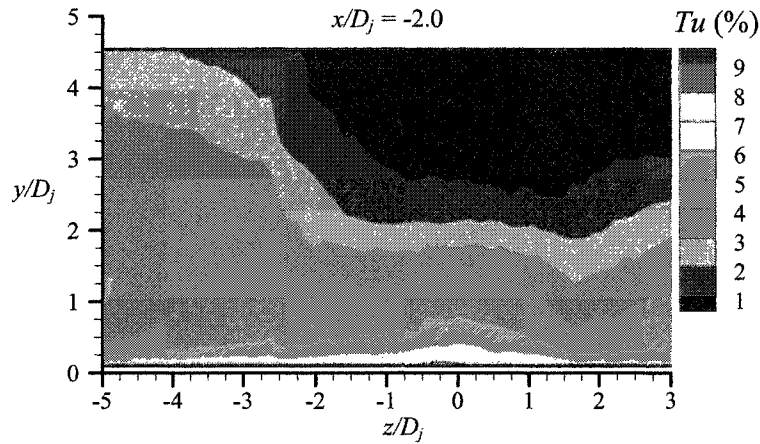


Figure 6.4.3: Turbulence intensity distribution at the cross-flow inflow boundary

The turbulence at the cross-flow inflow boundary was specified through a length scale and a turbulence intensity. The turbulence intensity, Tu , was provided in the experimental data (Figure 6.4.3) and was applied to the cross-flow inflow boundary using a cloud function. The length scale, L_{scale} , was used as the turbulence length scale:

$$L_{scale} = \min(L_i) = 4.5D_j \quad (6.4.1)$$

where L_i ($i = 1,2,3$) are the domain extents in the x , y , and z directions, respectively. For *RANS* simulations involving the k equation, the turbulence kinetic energy was estimated from the turbulence intensity, Tu , at the cross-flow inflow boundary by:

$$k = \frac{3}{2} Tu^2 V^2 \quad (6.4.2)$$

where V is the vector sum of the velocity components V_x , V_y , and V_z .

A no-slip (zero velocity) boundary condition was applied to the bottom wall boundary (x - z plane at $y=0$). For *RANS* simulations, a low-Reynolds-number turbulence modeling approach was used to resolve the details of the boundary layer profile. For

LES, the van-Driest wall damping function discussed in Section 6.2.2 was used. Both of these techniques required small grid-node spacing in the direction normal to the wall. The grid near the wall is created by making a structured “inflation layer” that allows for high aspect ratio prism elements. Applying the low-Reynolds-number wall formulation for both the *RANS* and *LES* typically requires $y^+ \leq 2$ for the first node off of the wall. Yang and Voke (2000) and Spalart (2000) used a $y^+ = 1$ to resolve the viscous sub-layer of a turbulent boundary layer in their numerical studies using *LES* and *RANS* based turbulence models, respectively. In the present study, y^+ values for the first node off the wall for *RANS* simulations and *LES* were approximately 1.2 and 1, respectively. The inflation layer near the wall contained 15 nodes in the normal (y) direction. This resulted in approximately 33 nodes in the boundary layer, which surpasses recommendations of a minimum of 15 nodes stated in the *CFX 5.7* user manual.

For the *RANS* simulations, the remaining surfaces (top, left, and right) were specified as free-slip wall boundaries. The choice of using free-slip wall boundaries is justified since the experimental data has revealed that the cross-stream component of velocity is negligible in comparison to the streamwise component of velocity near these boundaries. Furthermore, the domain size sensitivity study conducted in Section 6.3 has assured that these wall boundaries are placed sufficiently far from the vortex. For *LES*, the left and right boundaries were designated as *GGI* periodic boundaries. *GGI* boundary connections are used when the grid on either side of the two connected surfaces do not match. Nodal values from one periodic surface are applied to the nodal values at the other surface through spatial interpolation. It was found that *RANS* simulations were

insensitive to the treatment of the side wall boundaries (free-slip vs. periodic). *LES* simulations were only run with periodic boundaries since the presence of free-slip wall boundaries may interfere with development of the larger turbulence eddies.

On the outflow boundary, pressure was maintained at atmospheric level on a spatially-averaged basis. The *CFX* algorithm allows for non-uniform pressure distribution within the outflow boundary, with the pressure gradients extrapolated from the adjacent set of interior nodes.

The jet-inflow boundary conditions for the mean velocity and turbulence properties were also specified using the two-dimensional cloud function. The experimental data included distributions of both mean velocity and turbulence properties 3mm ($0.044D_j$) above the opening of the inclined jet. It was considered appropriate to use these measurements as boundary conditions for the jet-inflow since the mean velocity and turbulence properties are unlikely to change noticeably over a vertical distance of 4.4% of the jet diameter.

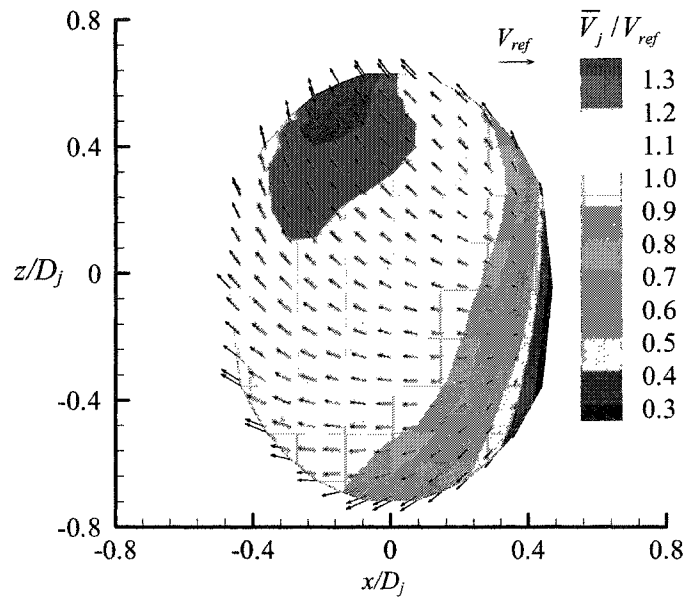


Figure 6.4.4: Mean velocity distributions at the jet-inflow boundary ($y/D_j = 0$)

The distribution of the mean velocity field at the jet-inflow boundary is presented in Figure 6.4.4. In this figure, the velocity distribution is presented using a combination of the (x, y', z') and (x, y, z) coordinate systems shown in Figure 6.4.5. Velocity components in the x, y', z' coordinate system are projected onto the elliptical jet boundary in the x, y, z coordinate system.

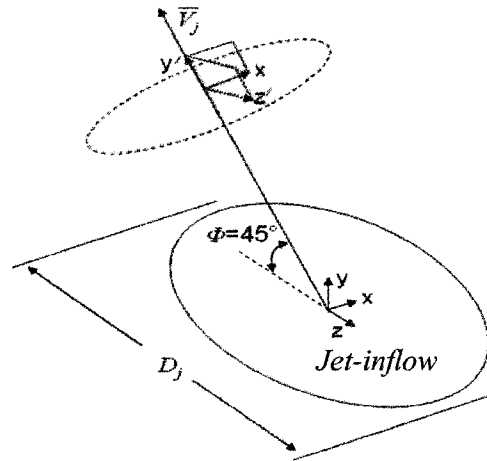
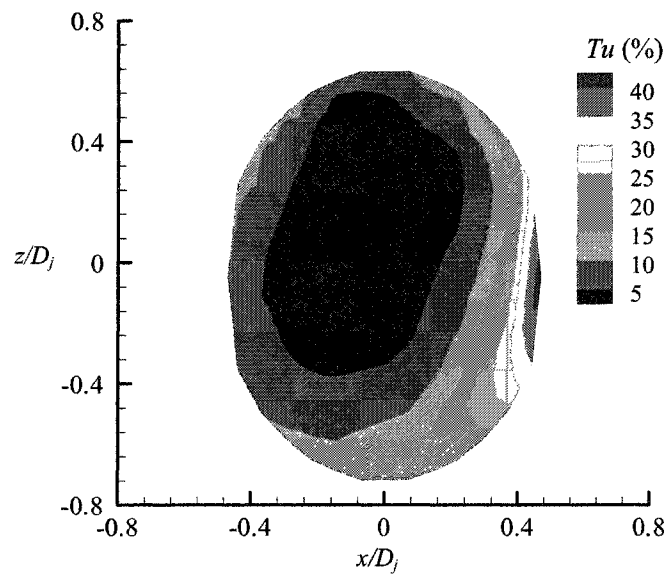


Figure 6.4.5: Jet-inflow boundary

It is noted that the velocity distribution is not uniform across the jet-inflow boundary, and this non-uniformity was accurately represented in the simulations by the use of the cloud function in *CFX*.

Figure 6.4.6: Turbulence intensity distribution at the jet-inflow boundary ($y/D_j = 0$)

The turbulence conditions at the jet-inflow boundary (Figure 6.4.6) were applied in the same manner as at the cross-flow inflow boundary. The turbulence intensity, Tu , was provided in the experimental results and a cloud function was used to apply this distribution as a boundary condition. The turbulence length scale, L_{scale} , was estimated using the Eqn. 6.4.1.

6.5 Initial Conditions

To initialise the simulations, the static pressure in the computational domain was set to a uniform atmospheric level. For the *RANS* simulations, the initial distributions of the Cartesian components of velocity within the computational domain were set uniformly to zero for both the y and z directions, and to $1.11V_{ref}$ for the x direction. For *LES*, a *RANS* solution with the *SST* turbulence model (Section 3.3.3.2) is used as an initial condition for velocity. Since the initial turbulence levels for *LES* were not specified, the initial 200 time-steps were discarded, during which turbulence developed. For *RANS* simulations, the initial turbulence properties were specified through the equation:

$$k = \frac{3}{2} Tu^2 (1.11V_{ref})^2 \quad (6.5.1)$$

where $Tu = 5\%$ is the turbulence intensity. This resulted in an initial turbulent kinetic energy value of $k = 0.256 \text{ m}^2/\text{s}^2$. The length scale, $L_{scale} = 4.5D_j$, was used as the initial turbulence length scale.

6.6 Spatial Resolution

6.6.1 Spatial Resolution for *RANS* Simulations

The initial spatial grid was set to resemble the optimum grid for a similar test case presented by Grosvenor (2000), which was undertaken using two-equation turbulence models. The grid consisted of 47 nodes in the x direction, 29 nodes in the y direction, and 37 nodes in the z direction. 20 nodes were placed in the cross-flow boundary-layer, 11 nodes in the jet core, and 7 nodes in the jet shear layer in the flow region just above the jet orifice. Figure 6.6.1.1 shows an isometric drawing of the computational domain used in Grosvenor's simulations.

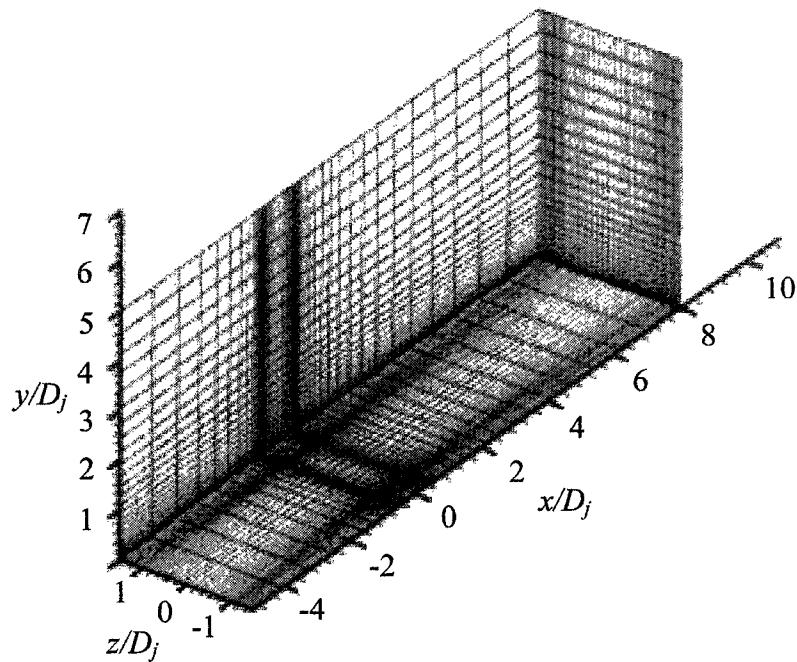


Figure 6.6.1.1: Computational grid for inclined jet-in-cross-flow, reproduced from Grosvenor (2000)

CFX allows for the use of a hybrid grid to minimize the grid-node count for a grid independent-solution. For the present simulation, a structured grid consisting of prismatic elements is used near the wall to resolve the boundary layer, and an unstructured grid consisting of tetrahedral elements is used elsewhere.

The structured grid is created by applying inflation layers to boundaries. An inflation layer is created by ‘inflating’ a two dimensional triangle into a three dimensional prism. The purpose of inflation layers is to minimize total node count while still adequately resolving the flow where spatial gradients are greatest normal to the boundary.

The computational grid contained one inflation layer and three grid controls. The inflation layer was used on the bottom surface, consisted of 15 nodes, and had an expansion factor of 1.2. Less than 10% of the undisturbed cross-flow boundary layer was discretized by the inflation layer. All three grid controls were aligned with the vortex trajectory. This trajectory was determined by locating the vortex center at each measurement plane in the experimental data.

The global length scale for the computational domain was set to $0.4 D_j$, which is the length scale applied to all locations in the domain that are outside the influence of grid controls or inflation layers. The grid controls were used to cluster nodes near the jet-inflow boundary since the magnitude of spatial gradients decreased as the vortex decayed downstream. The beginning of each grid control was placed at the center of the jet-inflow boundary. The first grid control had a radius of influence of $1.2 D_j$, an expansion factor of 1.05, a local length scale of $0.06D_j$, and a length that extended $4.4 D_j$ in the x direction. The second grid control had a radius of influence of $1.2 D_j$, an expansion factor of 1.05, a local length scale of $0.12D_j$, and a length that extended $8.8 D_j$ in the x direction. The third grid control had a radius of influence of $1.2 D_j$, an expansion factor of 1.05, a local length scale of $0.22D_j$, and a length that extended $23 D_j$ in the x direction. The use of low values for the expansion factors allowed for smooth transitions between elements of small scales specified by the grid control and elements of larger scales specified by the global length scale. The clustering of nodes on the vortex trajectory can be visualized through the node distribution at three cross-sectional planes shown in Figures 6.6.1.2-3.

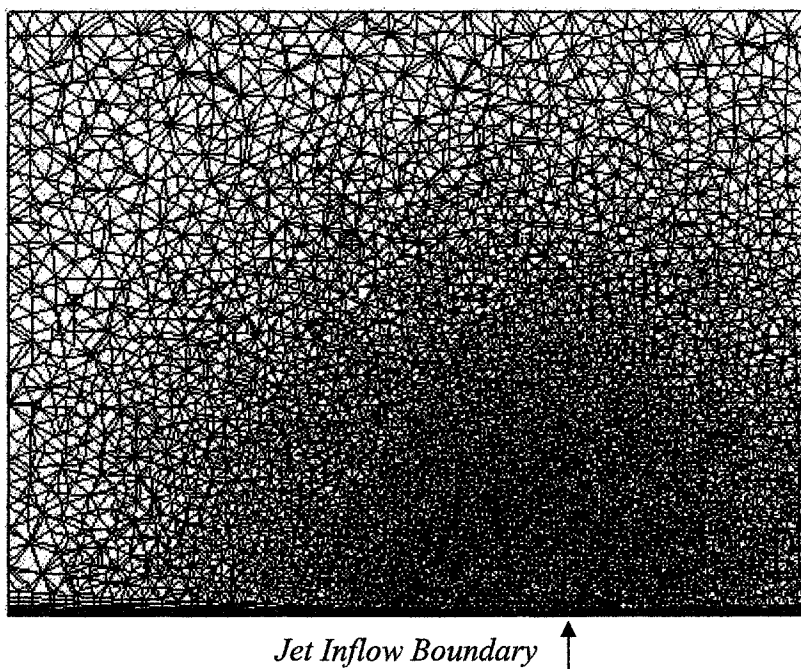


Figure 6.6.1.2: Optimized grid-node distribution in y - z plane at $x/D_j = 0$

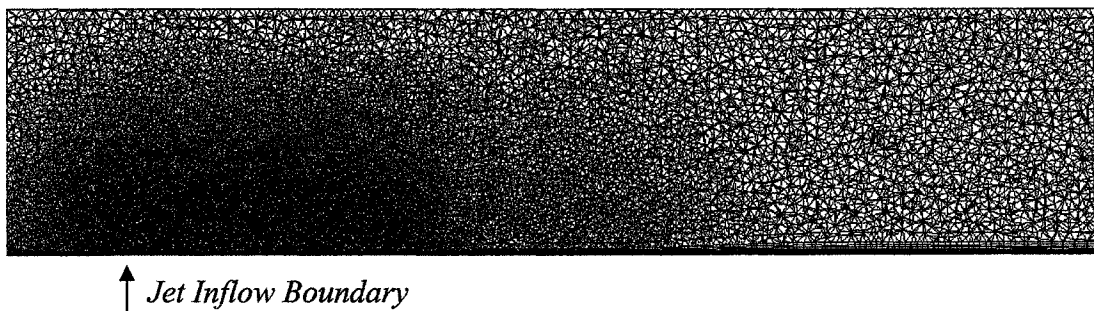


Figure 6.6.1.3: Optimized grid-node distribution in x - y plane at $z/D_j = 0$

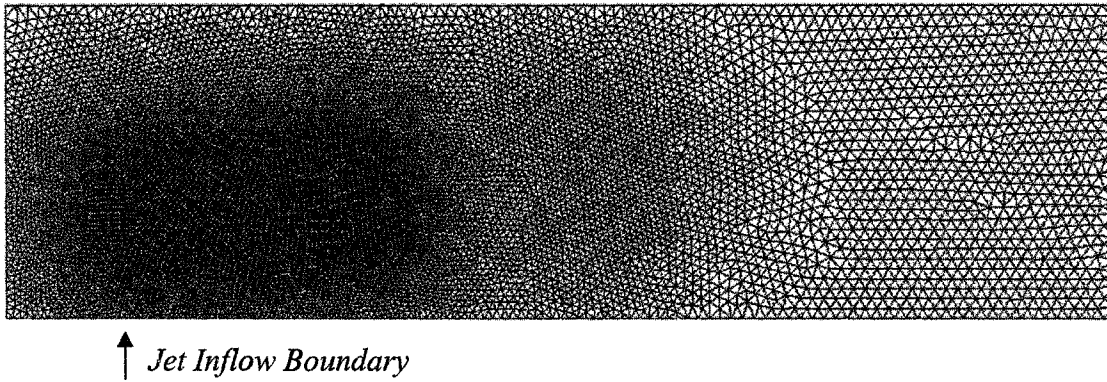


Figure 6.6.1.4: Optimized grid-node distribution in x - z plane at $y/D_j = 0.5$

As the grid resolution was adjusted, both mean velocity and turbulence properties were monitored until a grid independent solution was obtained. When the variation in velocity distribution from one grid to the next fell below one percent, the solution was deemed grid independent.

Figures 6.6.1.5 and 6.6.1.6 summarise the sensitivity of *RANS*-based predictions to two spatial resolutions, which are denoted as grid *A* and grid *B* and consist of 400,000 and 806,000 nodes respectively. The addition of nodes was distributed in the vicinity of the vortex through the use of grid controls. Based on these results, the final grid independent solution had a total of 400,000 nodes. This consisted of approximately 170 nodes, 53 nodes, and 51 nodes in the x , y , and z directions, respectively.

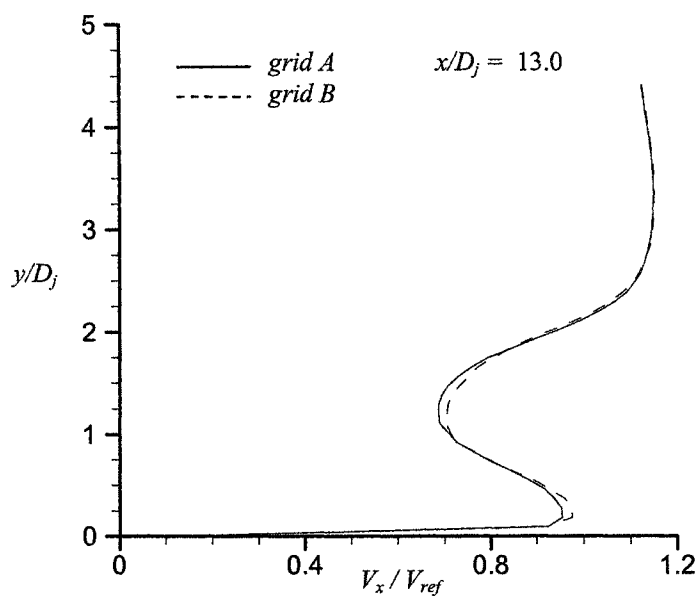


Figure 6.6.1.5: Predicted streamwise velocity; sensitivity to grid resolution

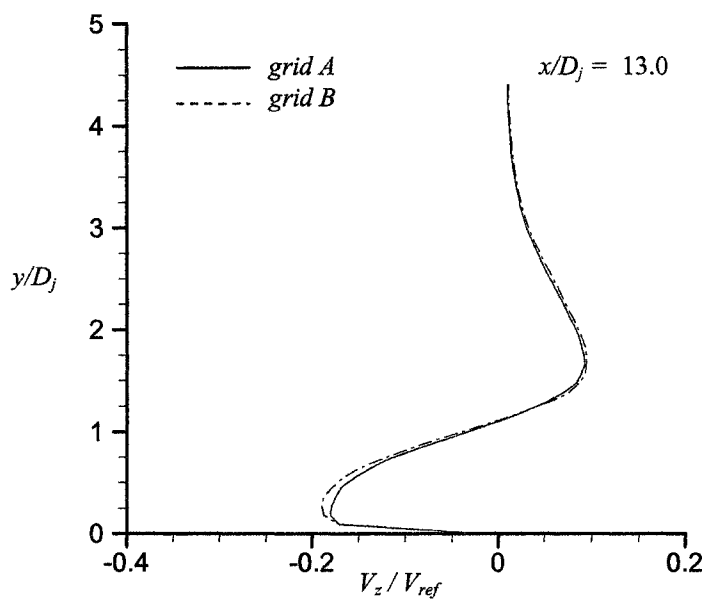


Figure 6.6.1.6: Predicted tangential velocity; sensitivity to grid resolution

6.6.2 Spatial Resolution for *LES*

The spatial resolution used for the *LES* corresponded to a grid-node mean spacing of $\Delta = 0.008$ m ($0.12D_j$). In a similar study by Yuan *et al.* (1999), where the development of a vortex produced from an normal jet in cross-flow was predicted using *LES*, the spatially averaged grid-node spacing corresponded to $\Delta = 0.1D_j$. The study was based on a velocity ratio and jet-Reynolds number of $VR = 2$ and $Re_{D_j} = 1050$, respectively. The spatial resolution for the present study was set as fine as possible given the computational resources at the author's disposal. Approximately 600,000 nodes for both *LES* and *RANS* simulations required over 1 GB (which exceeded available resources) of *RAM* memory. Unfortunately, the grid controls discussed in Section 6.2.1 could not be used in *LES* since it was suggested by both Ferziger (1993) and the *CFX 5.7* user manual to use isotropic grids. When anisotropic grids are used in *LES*, turbulence is no longer equally resolved in each spatial direction. Furthermore, the mean grid-node spacing for each spatial direction is no longer representative of the filter width. Essentially, the accuracy of sub-grid stresses calculated using Smagorinsky's model will deteriorate when anisotropic grids are used (Ferziger, 1993). Inflation layers were still used for the present simulation since an isotropic grid with a $y^+ < 2$ yielded a node count one order of magnitude larger than the present computational limit (600,000 nodes). This spatial resolution corresponds to:

$$\frac{\Delta}{\eta} = \frac{\Delta}{D_j} Re^{\frac{3}{4}} = 344 \quad (6.6.2.1)$$

where η is the Kolmogorov length scale. This ratio of mean-grid-node spacing-to-Kolmogorov length scale is similar to two studies of vortices in a turbulent boundary layer using *LES*. Yuan *et al.* (1999) investigated the decay of a turbulent vortex produced from a normal jet-in-cross-flow at a Reynolds number of 2100, based on the jet diameter, and used a grid corresponding to a spatial resolution of $\Delta/\eta = 30$. Liu *et al.* (1996) studied the development of streamwise vortices embedded in a turbulent boundary layer. In that study, the flow was characterized by a Reynolds number of 1245 based upon the boundary layer displacement thickness, and the grid corresponded to a spatial resolution of $\Delta/\eta = 409$.

6.7 Temporal Resolution

6.7.1 Temporal Resolution for *RANS* Simulations

For steady-state *RANS* simulations, the *CFX* algorithm uses a fully implicit formulation so that iterations through time marching can be performed with as large time steps as possible. The time-step for the *RANS* simulations was calculated $\Delta t = 0.01$ seconds. The *CFX* algorithm calculates the time-step based upon characteristic length and velocity scales determined from the domain geometry, initial domain conditions, and boundary conditions (Section 4.4). Due to stability problems with *RANS* simulations using the ω -Reynolds-stress turbulence model, the temporal resolution was reduced to $\Delta t = 0.001$ seconds.

6.7.2 Temporal Resolution for *LES*

It was determined that a time resolution of $\Delta t = 0.0005$ seconds was adequate for both stability and accuracy. Identical velocity distributions through the center of the vortex at several downstream positions ($x/D_j = 4.5$, $x/D_j = 10$) revealed that simulations were insensitive to temporal resolution variations over the $\Delta t = 0.0005$ to $\Delta t = 0.0001$ seconds range.

6.8 Solution Convergence

6.8.1 Solution Convergence for *RANS* Simulations

The criteria involved in determining solution convergence includes monitoring the *RMS* residuals of all governing equations solved for the flow simulation in question, checking solution development with iterations, and checking for global conservation of mass. The number of iterations (time-steps) required to reach converged solutions for Reynolds-stress simulations were approximately 1000. Typical computing times were approximately one week.

For a converged solution, *RMS* residual values for continuity, momentum, and turbulence equations were of the order of 10^{-6} . After the residual levels subsided, the simulation was continued for approximately 500 iterations. After the solution was determined to be independent of iterations, five cross-sectional planes were chosen along

the computational domain to conduct a global conservation of mass analysis. For each simulation, the plane-to-plane variation in mass flow rate was less than one percent.

6.8.2 Solution Convergence for *LES*

As discussed in Section 5.9, convergence requirements for *LES* were different than that for *RANS* simulations. For *LES*, a minimum residual level of 10^{-6} and maximum number of 10 iterations were specified for each time-step. The residual convergence criteria resulted in a global mass balance within one percent. During the beginning of simulations, similar to the decay-of-turbulence benchmark in Section 5.9, *RMS* residual levels for mass and momentum did not meet the time-step residual-convergence criterion of 10^{-6} before the algorithm proceeded to the next time-step. However, after approximately 10 time-steps, the simulation met the time-step residual convergence criterion before the maximum iteration level was reached.

In addition to specifying a minimum residual level and maximum number of iterations per time-step, several locations in the domain were monitored for convergence of the temporal average of velocity and pressure as well as Reynolds-stresses (Figure 6.8.2.1). The simulation is considered to be statistically converged once the difference in these quantities drops below one percent.

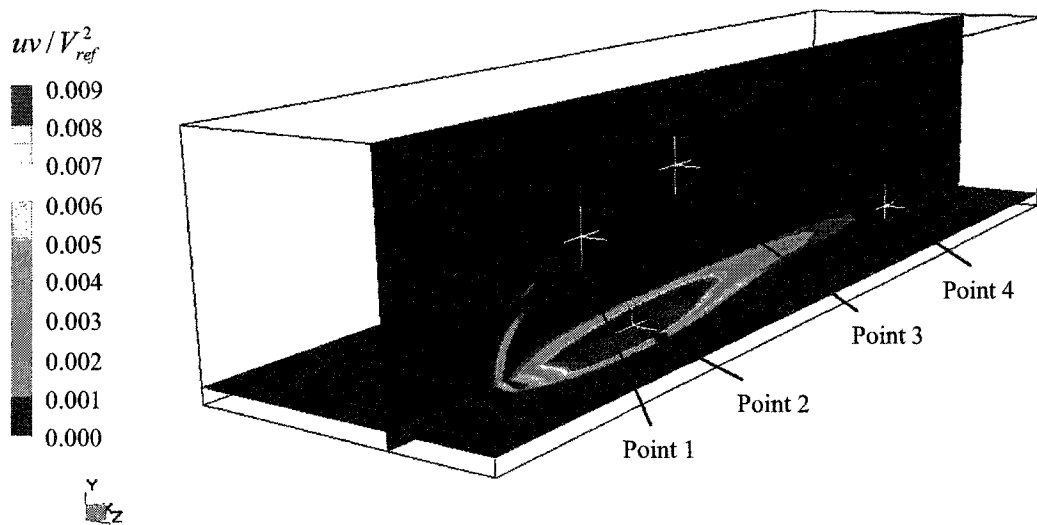


Figure 6.8.2.1: Location of monitor points

In Figure 6.8.2.1, contours of Reynolds-stress, uv , of a *RANS* simulation are shown to emphasize that locations of high turbulence activity are being monitored. *LES* required approximately 3000 time-steps to reach a statistically converged state, which corresponds to two weeks on a Pentium 4, 2GHz computer with 1GB of RAM.

6.9 Flow Physics

As described in Section 6.1, the flow configuration consists of a jet discharging at a pitch angle of $\Phi = 45^\circ$ and skew angle of $\theta = 90^\circ$ into a cross-flow at a Reynolds number $Re_{D_j} = 40800$ and velocity ratio $VR = 1.1$. In Figure 6.9.1, surface flow patterns based on oil flow visualizations of a similar study performed by Barberopoulos and Garry (1998) illustrate these features in the near field. In their study, the flow was characterized

by a jet Reynolds number of $Re_{D_j} = 26000$, a skew angle of $\theta = 60^\circ$, a pitch angle $\Phi = 45^\circ$, and a velocity ratio $VR = 1.4$.

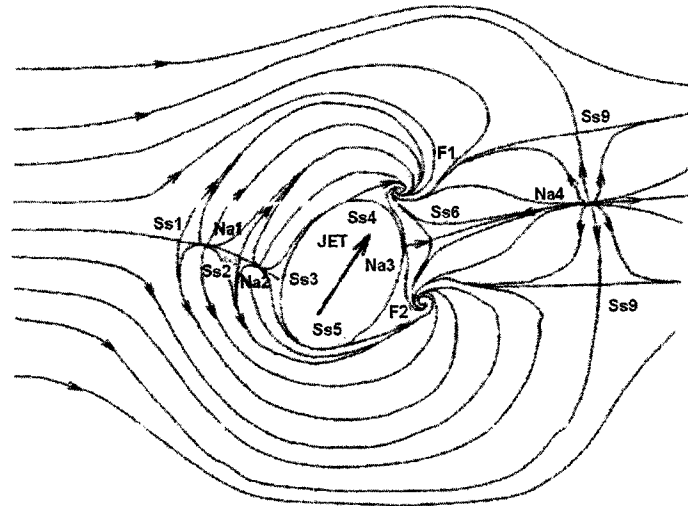


Figure 6.9.1: Flow topology of inclined jet-in-cross-flow, reproduced from Barberopoulos and Garry (1998)

In deducing the shear-stress topology, it is assumed that the velocity field forms a continuous vector field and the distribution of singular points must yield a possible flow pattern. In the shear-stress topology figure, a total of six nodes and eight saddle points are observed. Critical points of separation are marked as (*s*) while points of attachment are marked (*a*). The streamlines originating from the front stagnation point (*Ss1*) form a separation surface which engulfs the jet orifice. This separation surface spirals around two focal points *F1* and *F2*. The two attachment nodes *Na1* and *Na2* are needed to separate the saddle point of separation (*Ss2*) from saddles *Ss1* and *Ss3*. Barberopoulos and Garry (1998) argue that this configuration is similar to flows ahead of bluff bodies.

The main coherent structures that form due to the interaction between the jet and cross-flow is very similar to studies of jets discharging normal into a cross-flow ($\Phi = 90^\circ$), where a dominant counter-rotating vortex pair forms. When the jet is pitched relative to the test surface, only one dominant vortex is eventually formed while the other vortex either never forms or is dissipated. On the side where the dominant vortex is formed (upper side), large scale flow entrainment is induced by the vortex flow in the vertical direction. Transfer of high streamwise momentum towards the wall helps to prevent boundary layer separation (Khan *et al.*, 2000).

In addition to the dominant vortex that forms, other complex features include wake vortices and a horseshoe vortex. Although the coherent structures other than the dominant vortex are often called secondary vortices, and do not significantly affect the flow system, their effects are not negligible in the near field of the jet. In Figure 6.9.2, Bray and Garry (2000) show a schematic of the main coherent structures present in an inclined-jet-in-cross-flow.

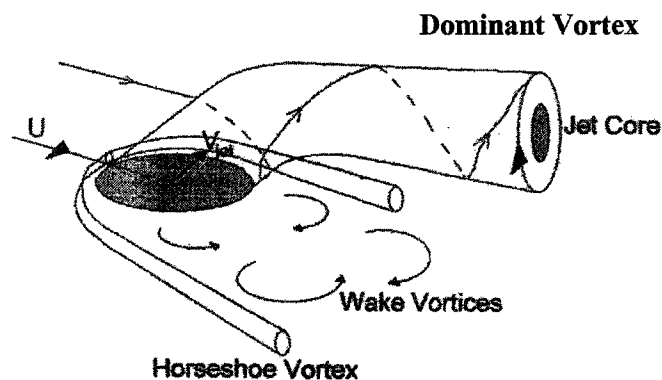


Figure 6.9.2: Vortical structures of inclined jet-in-cross-flow, reproduced from Bray and Garry (2000)

Investigating velocity distributions near the jet exit allows further understanding of the flow. It can be seen from Figure 6.4.4 that there is relatively high amount of axial-flow non-uniformity over the cross-section of the jet discharge. This is due to the interaction of the jet with the cross-flow. Upstream of the jet exit, the cross-flow near the test surface has a large z component of vorticity associated with the boundary layer. As the flow approaches the jet, the interaction between the boundary layer and jet discharge cause a horseshoe vortex system to form. This process is shown in Figure 6.9.3 where ζ_z is the z component of vorticity normalized by the reference velocity V_{ref} and jet diameter D_j .

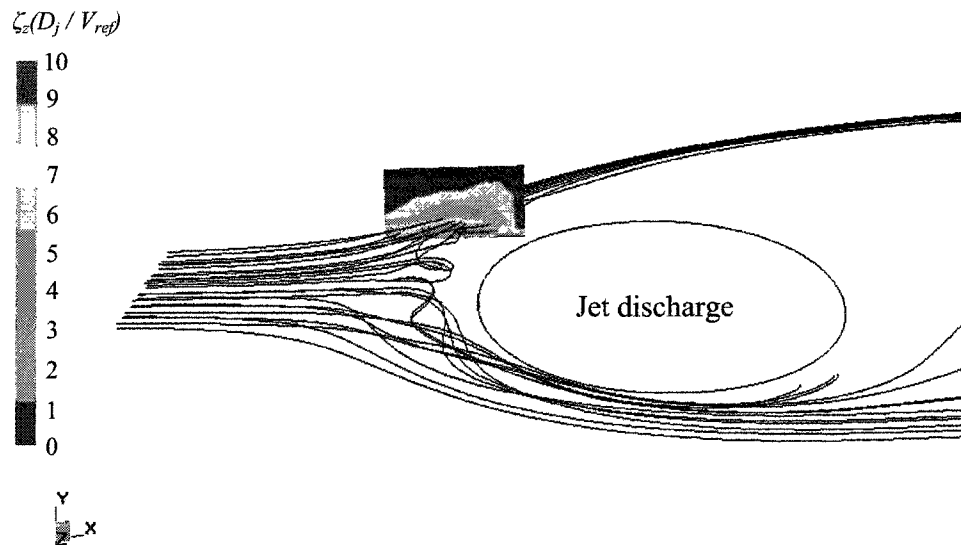


Figure 6.9.3: Formation of horseshoe vortex upstream of jet discharge

The maximum streamwise velocity peaks on the leeward side of the jet with respect to the cross-flow and is concentrated towards the upper side of the jet relative to the test surface. As the cross-flow approaches the jet, it is forced to decelerate due to the rise in static pressure. Analogous to flow around a cylinder, it accelerates around the perimeter of the jet on the upper and lower sides. As the flow passes the discharging jet, some of the flow is entrained into the forming vortex as shown in Figure 6.9.4.

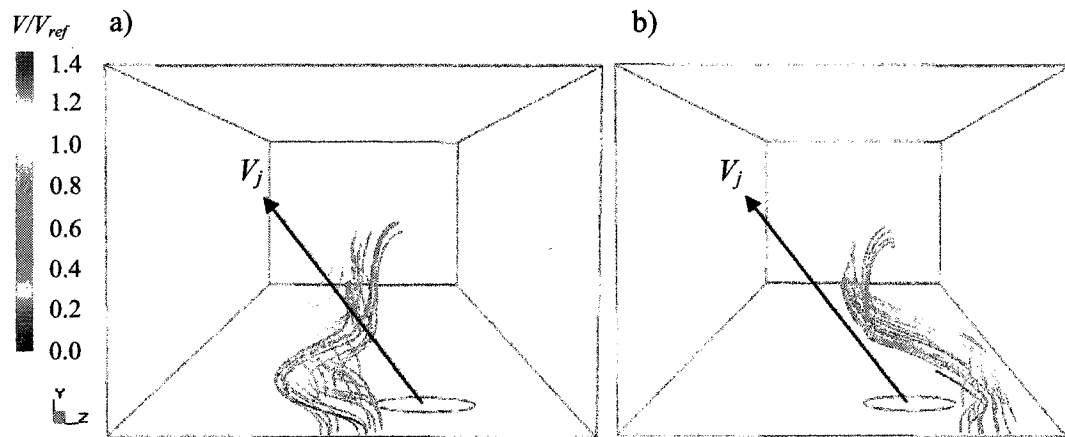


Figure 6.9.4: Streamlines around lower (a) and upper (b) side of jet inflow

The pressure distribution that results from the pitching of the jet forces the flow close to the test surface as it accelerates around the lower-side of the jet. Due to large viscous forces near the test surface, the acceleration around the upper side of the jet is considered to be higher than that around the lower side. Therefore, the static pressure distribution is lowest near the upper-leeward side, and highest near the windward side. This spatial

distribution of static pressure along the jet perimeter is responsible for the variation in axial velocity distribution observed at the jet discharge.

As mentioned above, one dominant streamwise vortex is produced by the interaction between an inclined jet and the cross-flow boundary layer. There are several mechanisms that are known to contribute to the streamwise trajectory of this vortex. These are the inviscid and viscous interactions of the vortex with the test surface, and the presence of turbulence eddies. The inviscid interaction can be quantified through consideration of an image vortex below the test surface, as is well established in potential flow theory. In the presence instance, such interaction would lead to spanwise movement of the vortex in the $-z$ direction. The prevailing viscous forces diffuse the vortex with downstream distance, result in production of vorticity of opposite sign beneath the vortex, and also impose a drag on the vortex as it is moved laterally by the aforementioned viscous mechanism. All of these viscous effects tend to oppose the influence of the inviscid mechanism mentioned above. Small scale turbulence complements the diffusion effect of molecular viscosity. While the large scale turbulence is expected to have a convective (induced) effect on the vortex, hence its instantaneous position in the cross-flow plane, this effect should average out in time.

Several of the physical features of this downstream vortex are evident in Figure 6.9.5. More details can be found in the work of Yaras (2002). With this preamble on flow physics, the prediction accuracy of the simulations is discussed next.

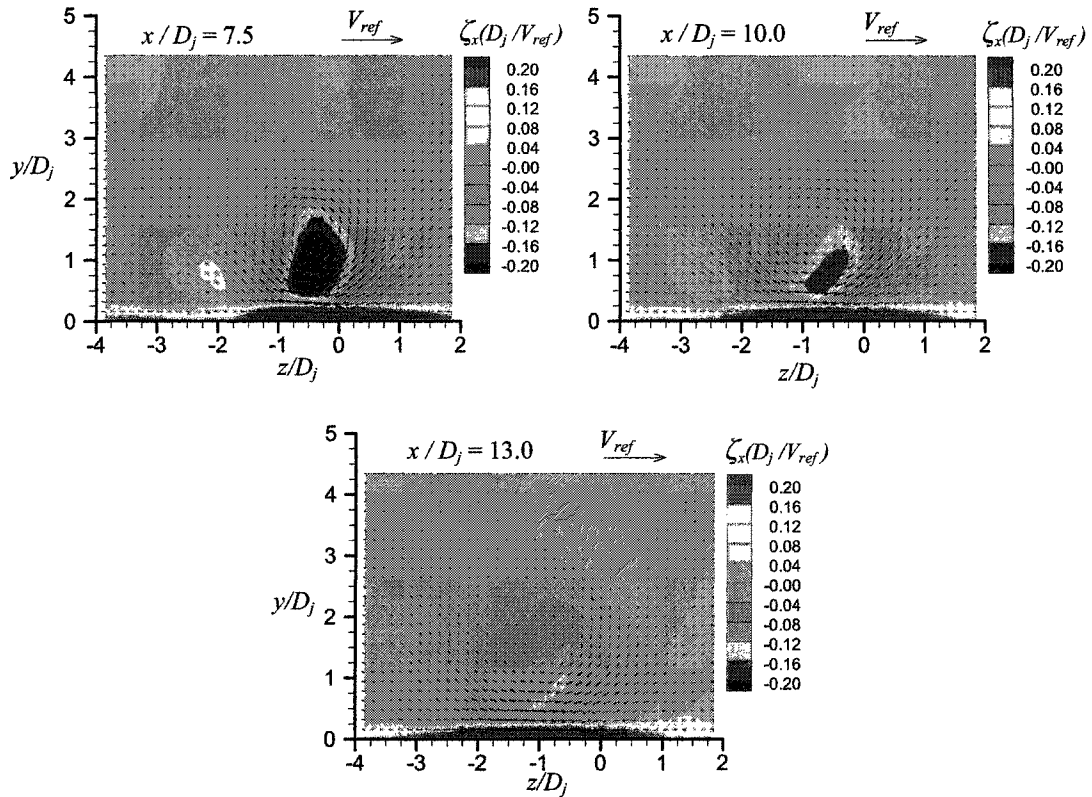


Figure 6.9.5: x -component vorticity distribution predicted using *LES*

6.10 Simulation Results

The predicted flow field based on *RANS* simulations with the ω -Reynolds-stress-turbulence model and *LES* with Smagorinsky's sub-grid model are presented and compared to the experimental data of Yaras (2004). Predictions of the mean flow field, vorticity field, and turbulence field are presented at y - z planes downstream of the location of jet discharge.

All two-dimensional comparisons between simulation and experimental data are made along lines parallel to the y axis at each y - z plane. The spanwise (z) positions of these lines in experimental and computed flow fields are chosen to be the same relative to the vortex center. The vortex center is located by studying the cross-stream velocity field. Although the location of peak vorticity is often used to locate the center of the vortex, in a similar study, Zhang (2000) demonstrated how the maximum vorticity and vortex center are in close proximity but are not at the same location.

6.10.1 Mean Flow Distribution

Figures 6.10.1.1-2 show the experimental and simulated velocity fields at two planes downstream of the inclined jet discharge. V_y and V_z are displayed as vector components in the y and z axis directions, respectively, and the axial velocity, V_x , is represented through contours. Each velocity component is normalized by the reference velocity, V_{ref} . While both *LES* and *RANS* computations fail to reproduce the experimental data precisely, it is clearly evident that the *LES* results are superior to those of the *RANS* computations. This is elaborated upon in the form of two-dimensional velocity-distribution comparisons next.

Figure 6.10.1.3 shows two components of velocity normalized by the reference velocity, V_{ref} , at three streamwise positions. For the spanwise component of velocity along a vertical line passing through the vortex center (Figure 6.10.1.3b), both *LES* and *RANS* simulations agree well with experimental data. However, the overall cross-flow

velocity field is not predicted with the same precision by both simulations as was observed in Figures 6.10.1.1-2, and is consistent with the streamwise vorticity field discussed next. The over-prediction of the axial velocity deficit by the *RANS* simulations (Figure 6.10.1.3a) is related to this discrepancy in the predicted cross-flow fields.

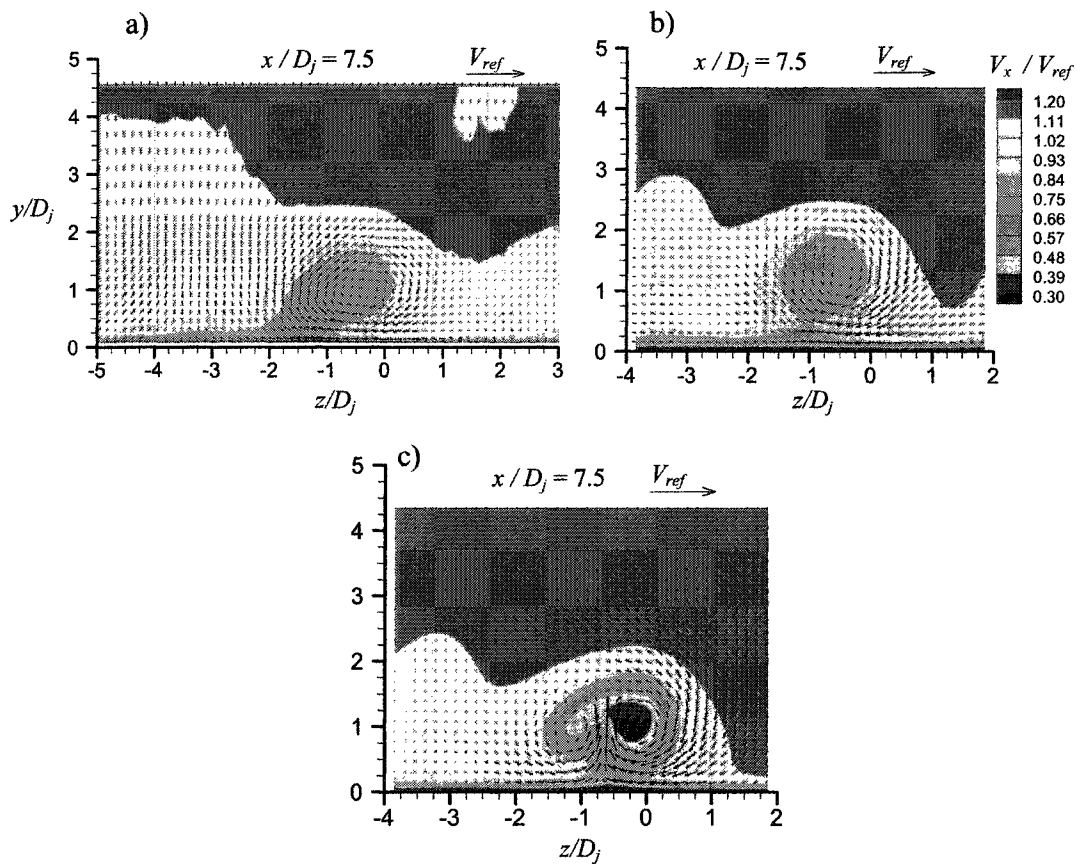


Figure 6.10.1.1: Velocity field of the vortex produced by the inclined jet-in-cross-flow interaction at $x/D_j = 7.5$
 (a) experimental data of Yaras (2004), (b) *LES*, (c) *RANS*

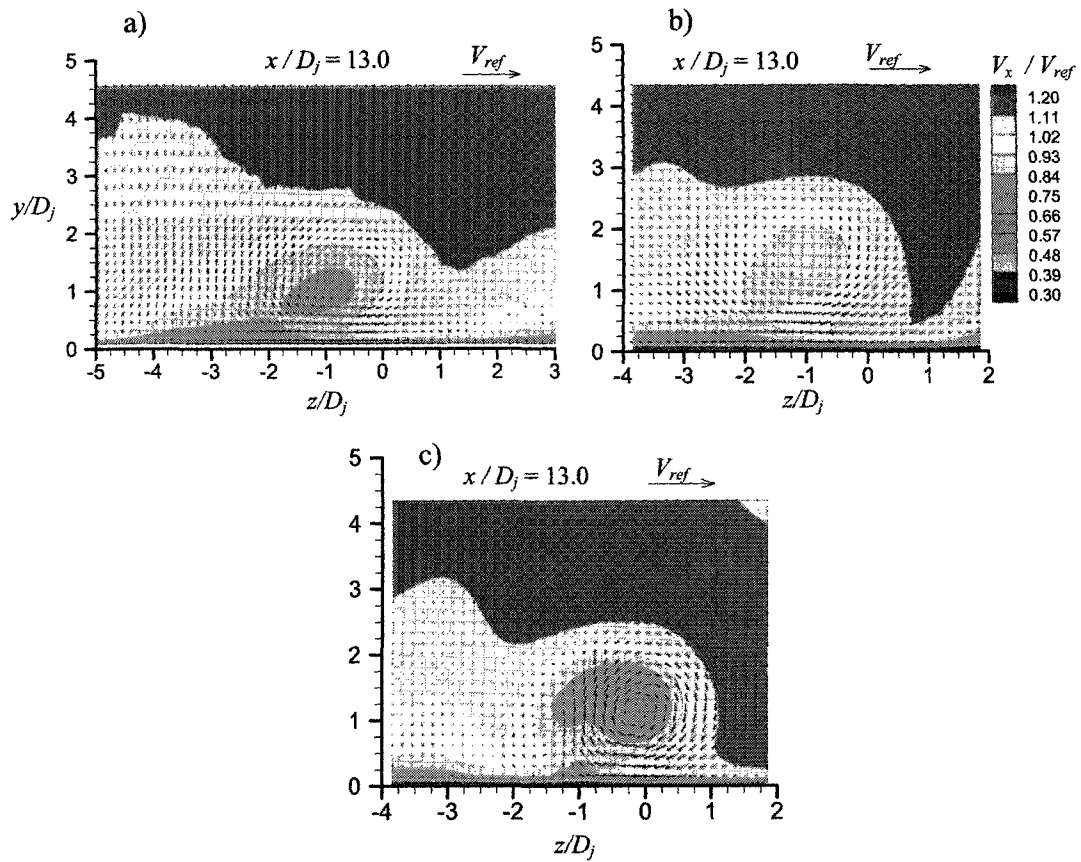


Figure 6.10.1.2: Velocity field of the vortex produced by the inclined jet-in-cross-flow interaction at $x/D_j = 13.0$
 (a) experimental data of Yaras (2004), (b) *LES*, (c) *RANS*

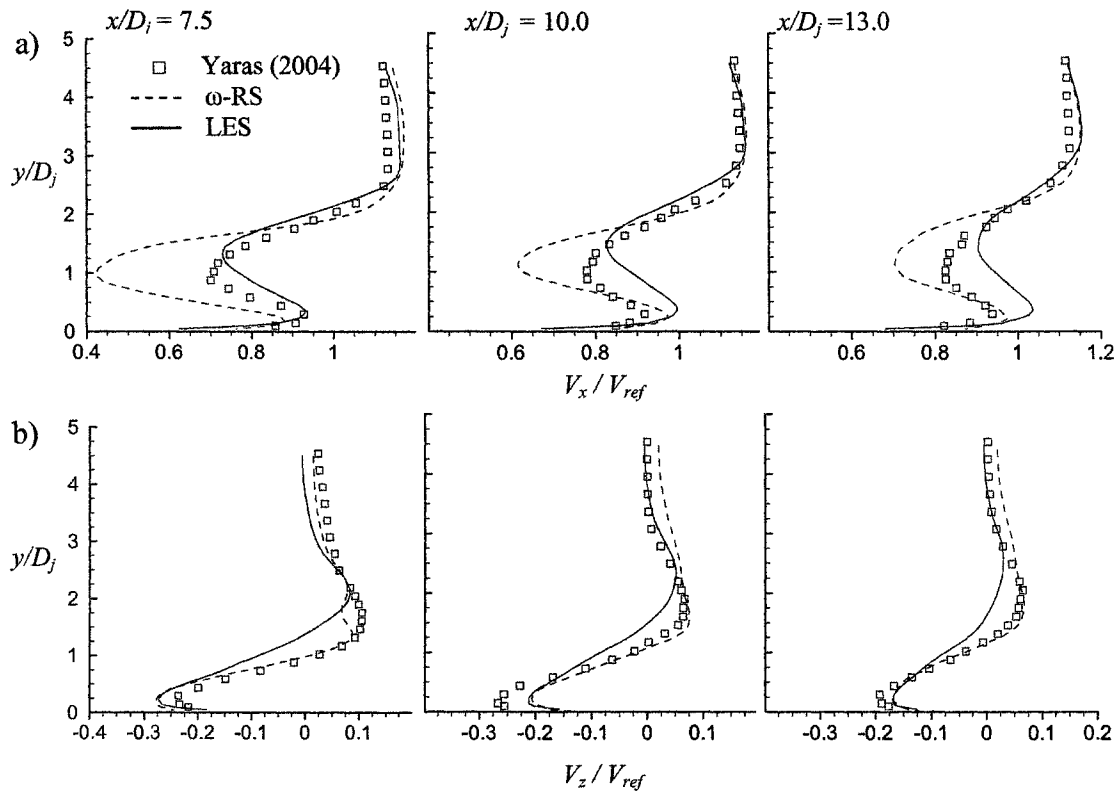


Figure 6.10.1.3: Velocity distributions through the center of the vortex

6.10.2 Vorticity Distribution and Decay

Figure 6.10.2.1 shows distributions of vorticity (ζ_x) at planes downstream of the jet discharge. Confirming observations made in the previous section pertaining to velocity distributions, vorticity associated with the vortex decreases in intensity and follows a shifted trajectory with respect to the cross-flow direction.

As the fluid accelerates beneath the vortex, the cross-stream shear layer eventually separates on the upward-sweep side of the vortex. During this process, vorticity of the opposite sign is produced near the lower portion of the upward-sweep side

of the vortex. The *LES* simulations capture this (6.10.2.1b), as negative vorticity is observed between the vortex and the test surface on the upward-sweep side. The accumulation of vorticity in this region affects the vortex trajectory, as the vorticity induces a velocity on the vortex and also influences its diffusion rate. It should be noted this vorticity of opposite sign along the test-surface is not as evident in the experimental results, partially because of the limited spatial resolution of the measurement grid in that region (Figure 6.10.2.1a). However, the higher streamwise decay rate of the vortex in *LES* compared to the experimental results suggests that the extent of vorticity production on the test surface beneath the vortex is over-estimated by the *LES* computations. The *RANS* simulation results, not shown in the vorticity plots, were in even lesser agreement with the experimental data in this regard. Despite the noted discrepancies in the cross-plane vorticity predictions, as shown in Figure 6.10.2.2, the spanwise vortex trajectory and decay of peak vorticity predicted by *LES* agree well with experimental data.

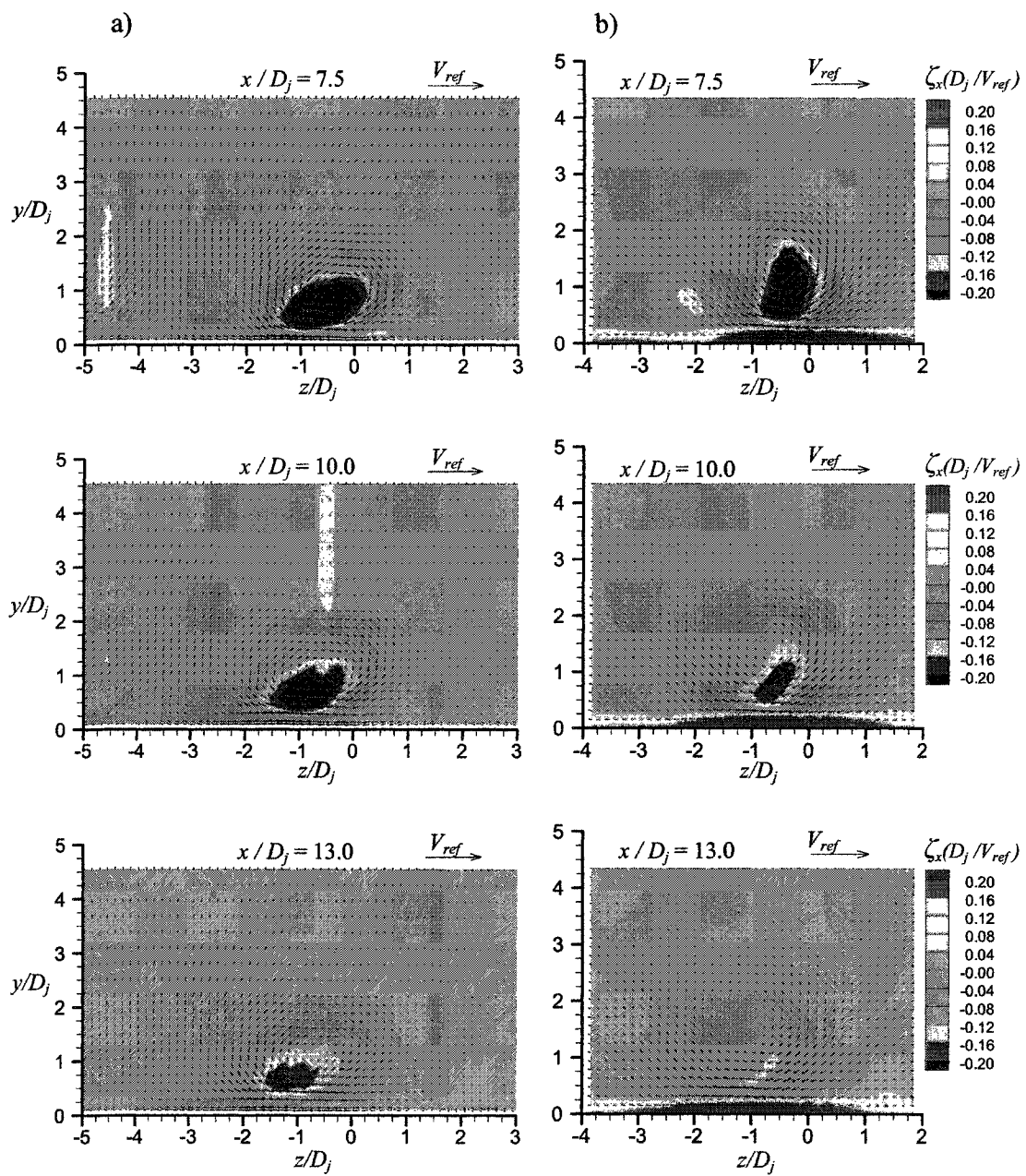


Figure 6.10.2.1: x -component vorticity distribution (a) experimental data of Yaras (2004) and (b) *LES*

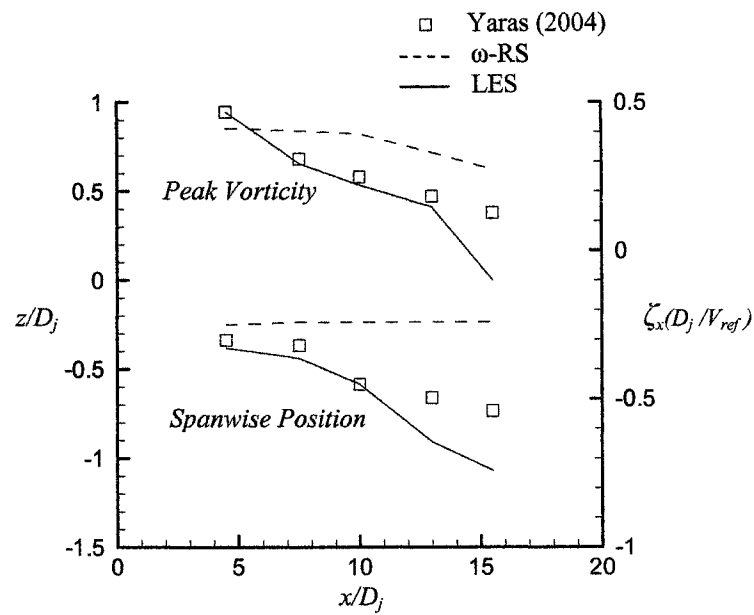


Figure 6.10.2.2: Streamwise decay of peak vorticity and spanwise movement of vortex center

Having demonstrated a favorable agreement between experimental data and *LES* computations in the context of the time-mean flow field, the *LES* results provide an opportunity to explore the effects of large scale turbulence eddies on the instantaneous flow field associated with the dominant streamwise vortex.

6.10.3 Turbulence Distribution

Milanovic and Zaman (2004), Khan *et al.* (2000), and Rixon and Johari (2003) agree that the mechanism responsible for the oval shaped time-averaged streamlines and high levels of turbulence in the vortex core are not well understood. The high levels of turbulence in the vortex core can be due to vortex wandering (Khan and Johnston, 2000),

entrainment of surrounding turbulence (Bandyopadhyay *et al.*, 1991), or the vortex core acting as a wave guide propagating disturbances that would have otherwise dissipated (Leibovich, 1984).

Since a favourable agreement has been demonstrated between the experimental time-mean velocity field and the predictions using *LES*, we can use the temporal development of the flow available in the simulation results to explore transient activity in the vortex and its vicinity. Figure 6.10.3.1 shows the evolution of the dominant streamwise vortex at $x/D_j = 4.5$, where cross-flow velocity components are represented by vectors, and vorticity is represented by contours. Each snapshot represents a temporally averaged flow field over 10 time-steps, culminating in the total duration of approximately $0.7T$. T is the realization time for a turbulent structure and is defined in Section 3. The concentration of negative vorticity and orientation of vectors allows one to follow the path of the dominant vortex in both spanwise and vertical directions.

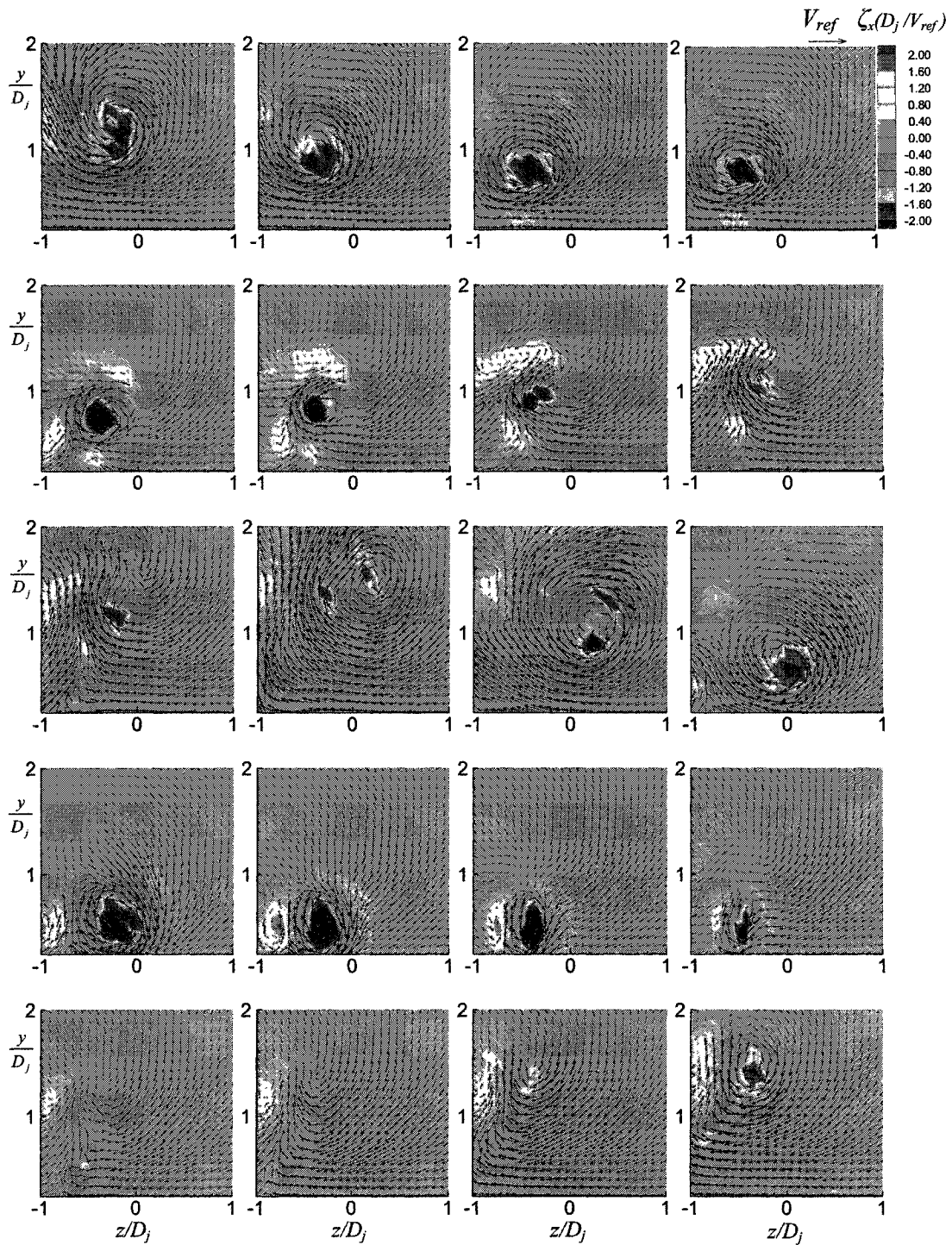


Figure 6.10.3.1: Movement of a vortex produced by an inclined jet-in-cross-flow ($x/D_j = 4.5$)

For the cycle of movement shown, larger displacements are measured in the vertical direction ($1.0 D_j$) than in the spanwise direction ($0.7 D_j$). This provides evidence against the theory that oval shaped streamlines are a result of vortex wandering as suggested by Khan (2000). In an experimental investigation of an inclined-jet-in-cross-flow using particle image velocimetry ($x/D_j = 30$), Rixon and Johari (2003) measured maximum spanwise and vertical displacements of $3.5 D_j$ and $4.3 D_j$, respectively. In that study, the flow was characterised by a jet-to-cross-flow velocity ratio of $VR = 2$ and a jet-Reynolds-number of 2040. In addition, a spectral analysis of peak vorticity fluctuations did not reveal any dominant frequencies.

The absence of any dominant frequencies in vorticity spectra suggests that the mechanism for vortex wandering is more likely the presence of large scale turbulence. Both Rixon and Johari (2003) and Yuan *et al.* (1999) believe that large scale turbulence originating in the jet, turbulence produced from the boundary layer, and turbulence produced by the vortex itself are responsible for vortex wandering. For example, on the top row of Figure 6.10.3.1, the vortex migrates in the negative z direction due to the induced velocity from the image vortex below the test surface. As the vortex approaches the test surface, the core diameter begins to decrease, which causes the peak vorticity to increase due to the conservation of angular momentum. Continuing to the second row, three distinct large scale eddies of opposite vorticity are produced around the vortex perimeter. As these eddies reduce the strength of the vortex, they also migrate in a clockwise direction concentrating on the lower side of the vortex. Collectively, the large

scale turbulence induces a velocity upon the vortex causing it to migrate in the positive vertical direction away from the test surface. At the end of the second row, the large scale eddies have dissipated, and the vortex is able to regain its strength and continue a similar type of movement in the remaining rows of Figure 6.10.3.1. Random spanwise movements of a vortex were also observed by Khan and Johnston (2000), where the flow was characterised by a velocity ratio of $VR = 1.0$ and a jet-Reynolds number of 5000. In many frames of Figure 6.10.3.1, it is not even possible to distinguish the dominant streamwise vortex from large scale turbulence. In an experimental study of an inclined jet-in-cross-flow using *PIV*, Johari (2004) observed instances where the vortex was not very clear and its strength varied significantly.

Yuan *et al.* (1999) studied the development of a vortex produced by a normal jet in cross-flow using *LES* based on a velocity ratio and jet-Reynolds number of $VR = 2$ and $Re_{D_j} = 1050$, respectively. The instantaneous flow field was dominated by large scale turbulence, and only after the numerical data was subjected to a low-pass filter, was the counter rotating pair visible. For the present simulation, the numerical data was temporally averaged over a series of time durations. It was found that for shorter averaging durations ($0.03 T$), the dominant vortex could still be tracked although peak vorticity changed by one order of magnitude relative to time-averaged experimental peak vorticity. For large averaging durations ($6.0 T$), the amplitude of vortex movement became negligible, and velocity and turbulence distributions resembled that of the time-averaged experimental data and steady *RANS* simulations (Figures 6.10.1.3 and 6.10.3.2).

Figure 6.10.3.2 shows distributions of turbulent kinetic energy (TKE), Reynolds-normal-stress (ww), and Reynolds-shear-stress (uv), all normalized by V_{ref}^2 . Statistical turbulence quantities from the *LES* were calculating over a duration of $6.0 T$. Since *LES* computes large scale turbulence directly from the Navier-Stokes equations, turbulence distributions were predicted better by *LES* than for *RANS* simulations. This is likely part of the explanation for the greater prediction accuracy of *LES* for the time-mean flow field. For both *LES* and *RANS* simulations, the largest discrepancies between experimental data and numerical predictions of Reynolds-stresses were near the test surface. This is not surprising since near-wall turbulence activity is more difficult to predict due to the damping effect of the wall.

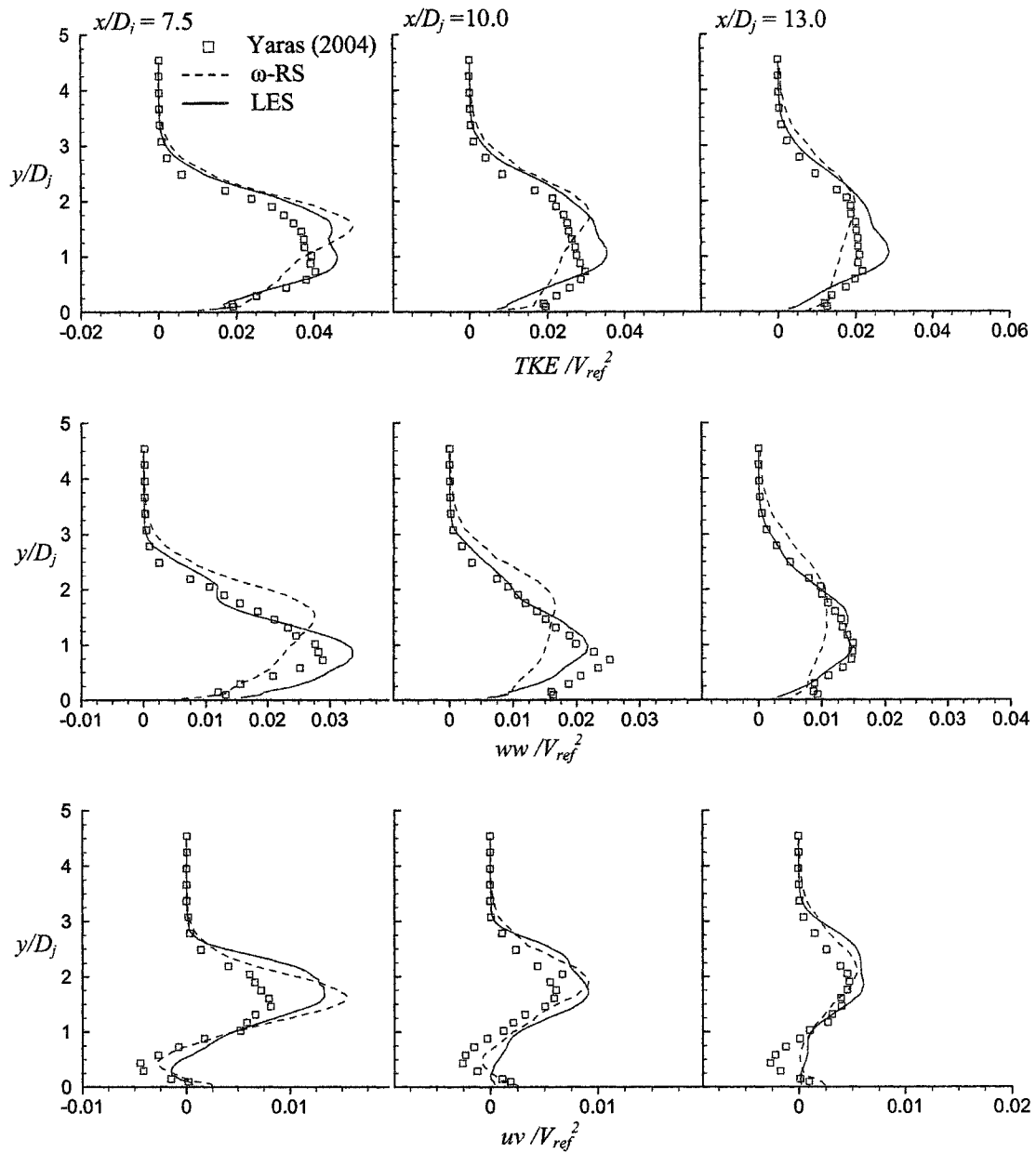


Figure 6.10.3.2: Turbulence distributions through the center of the vortex

Chapter 7

VORTEX GENERATOR

Through the series of benchmarks presented in Chapters 4-6, large-eddy simulation (*LES*) is identified as the most effective computational tool for simulating turbulent flows with substantial streamline curvature. In this chapter, the computational tool is used in the pre-diction rather than post-diction mode. The exercise involves the design of a vortex generator that generates vortical flows with prescribed velocity distributions in a laboratory environment. The design of the blade row for the vortex generator is based on established turbomachinery aerodynamic design practices. *LES* is used to estimate the flow development downstream of the blade row.

Lift generated by an aircraft is due to the pressure differential between the upper and lower surfaces of the wing. Immediately downstream of the wing, flow develops into a pair of wingtip vortices (Section 2.4.2). These wingtip vortices can interfere with the flight characteristics of smaller following aircraft. Understanding the far-field behaviour of these vortices is prerequisite to accurate prediction of safe and economical distances between aircraft at take-off and landing. The far-field corresponds to a streamwise distance of approximately 50 chord lengths (≈ 10 wingspans) downstream of the wing (Shekarriz *et al.*, 1993). Velocity measurements at 30 chord lengths (≈ 7 wingspans) downstream of a wing tested by Devenport *et al.* (1996) and Traub *et al.* (1998) indicate a maximum tangential velocity equal to 25% of the free-stream velocity (Figures 2.4.2.2 and 2.4.2.3), occurring at approximately 4% chord length from the center of the

vortex. The vortex generator shall be designed to produce a velocity distribution corresponding to this experimental data.

7.1 Configuration of the Vortex Generator

7.1.1 Vortex Generator General Setup

Figure 7.1.1.1 shows the general setup of the vortex generator installed in a wind tunnel. U_a , U_t , D_v , D_t , and r_c are the, axial flow velocity, tangential flow velocity after the vortex generator, vortex generator diameter, wind tunnel test-section diameter, and vortex core radius, respectively. Due to the adverse pressure gradient that the vortex generator imposes on the upstream flow, a velocity control mesh is installed between the vortex generator and walls of the wind tunnel. The purpose of this mesh is to ensure uniform axial velocity at the wind tunnel cross-section after the vortex generator. If the turbulence generated by the mesh is undesirable, a setup would be required where the core and bypass flows are separately delivered into the test section.

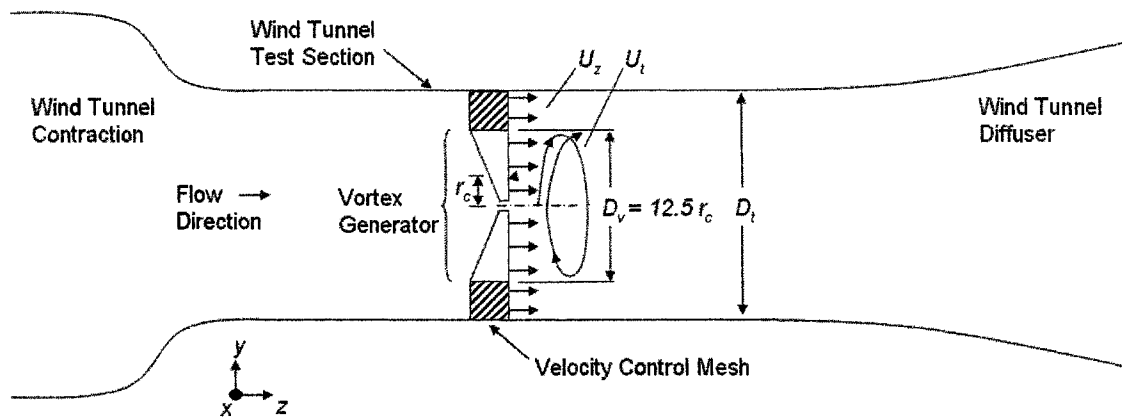


Figure 7.1.1.1: Vortex generator general setup

7.1.2 Vortex Generator Inflow and Outflow Conditions

The current design method is based upon established turbomachinery blade-design practices, as presented by Cohen *et al.* (1972) among others. The starting point in the design process is to establish the inflow and outflow conditions of the vortex generator blade row. The inlet flow consists of a uniform axial velocity distribution with no flow angularity. The turbulence distribution upstream of the vortex generator is also considered to be uniform with an approximate turbulence intensity of one percent.

The outflow conditions are to approximate the flow in the far field of a wing-tip vortex, which can be divided into two regions. In the inner section of the vortex, the tangential velocity varies proportionally with radius from the centerline to the edge of the vortex core, r_c :

$$(U_t)_{FOV} = k_1 r \quad (7.1.2.1)$$

where FOV denotes forced vortex rotation and k_1 is a constant. Experimental studies of wingtip vortices in the far field, such as those by Traub *et al.* (1998) and Devenport *et al.* (1996), provide an estimate to the size of the vortex core as:

$$\frac{r_c}{c_w} \approx 0.04 \quad (7.1.2.2)$$

It has been observed that the core region undergoes relatively small amount of diffusion with downstream distance, hence the noted r_c value may be used for the wing-tip vortex at any location in the far field. Beyond the edge of the vortex core, the tangential velocity profile, $(U_t)_{FRV}$, follows a free-vortex distribution:

$$(U_t)_{FRV} = \frac{k_2}{r} \quad (7.1.2.3)$$

where FRV denotes a free-vortex distribution and k_2 is a constant. The tangential velocity at the edge of the vortex core, as shown in Figures 7.1.2.1 and 7.1.2.2, is estimated as:

$$\frac{(U_t)_{r=r_c}}{U_\infty} \approx 0.25 \quad (7.1.2.4)$$

The flow is characterised by a vortex-core Reynolds number of $Re = 20886$ and a swirl number of $S = 0.145$. The vortex-core Reynolds number is based upon a vortex-core radius of $r_c = 0.04$ m and a spatially averaged axial velocity of $\bar{U}_z = 8.1$ m/s.

The flow exiting the vortex generator must satisfy the radial equilibrium condition. In a vortex, the sum of the forces acting upon a fluid element in the radial direction must be equal to its radial acceleration. This is the essence of the radial equilibrium condition, and can be expressed mathematically as:

$$\frac{dh_o}{dr} = U_z \frac{dU_z}{dr} + U_t \frac{dU_t}{dr} + \frac{U_t^2}{r} \quad (7.1.2.5)$$

where h_o and U_z are stagnation enthalpy and axial velocity, respectively. Substituting Eqn. 7.1.2.1 into Eqn. 7.1.2.5, the radial equilibrium equation for the core region of the vortex simplifies to:

$$0 = U_z \frac{dU_z}{dr} + 2k_1^2 r \quad (7.1.2.6)$$

$\partial h_o / \partial r$ is set to zero since the inflow has uniform stagnation enthalpy, and no energy is imparted to the flow in the vortex generator. Integrating and solving for the axial velocity yields:

$$(U_z)_{r < r_c} = \sqrt{k_3 - 2k_1^2 r^2} \quad (7.1.2.7)$$

where k_1 and k_3 are constants determined from the following relations:

$$k_1 = \frac{(U_t)_{r=r_c}}{r_c} \quad (7.1.2.8)$$

$$k_3 = U_\infty^2 + 2k_1^2 r_c^2 \quad (7.1.2.9)$$

Beyond the edge of the vortex core, assuming a constant axial velocity and constant stagnation enthalpy, the radial equilibrium equation reduces to:

$$0 = U_t \frac{dU_t}{dr} + \frac{U_t^2}{r} \quad (7.1.2.10)$$

A free-vortex velocity distribution, as given in Eqn. 7.1.2.3, satisfies this radial equilibrium equation and the constant k_2 is solved as:

$$k_2 = r_c (U_t)_{r=r_c} \quad (7.1.2.11)$$

The tangential velocity profiles described by Eqns. 7.1.2.1 and 7.1.2.3 are denoted as the K -Vortex design. Unfortunately, a slight discontinuity exists in the tangential velocity profile of the K -Vortex at $r = r_c$. An alternative is the Q -Vortex that was proposed by Batchelor (1964):

$$U_t = (U_t)_{r=r_c} (1 + 0.5/\gamma) \frac{r_c}{r} \left[1 - \exp\left(-\gamma \frac{r^2}{r_c^2}\right) \right] \quad (7.1.2.12)$$

where $\gamma = 1.25643$ is a constant. As shown in Figure 7.1.2.1, the difference between the tangential velocity distributions of the Q and K vortices is not substantial. In this figure, the tangential velocity is normalized by the axial velocity spatially-averaged over the cross-sectional area of the vortex generator. Figure 7.1.2.2 shows the flow angularity in the Q vortex.

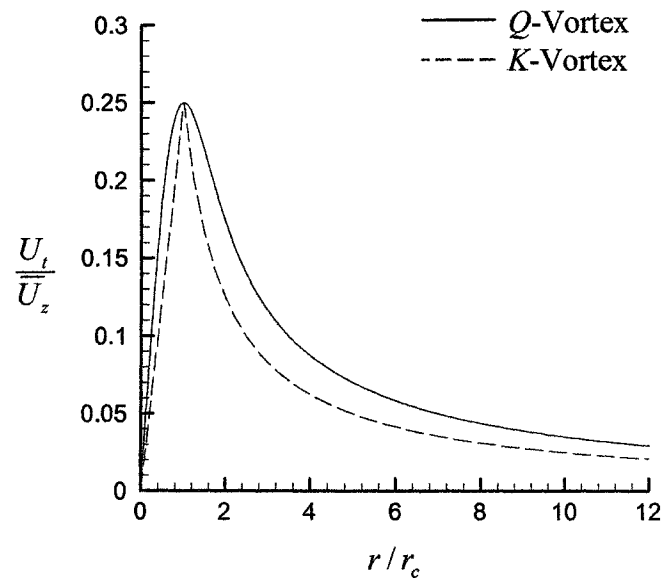


Figure 7.1.2.1: Tangential velocity distribution for Q and K vortices

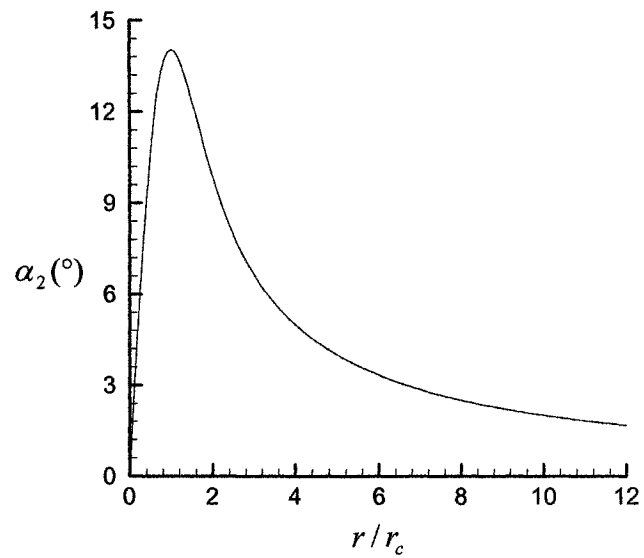


Figure 7.1.2.2: Flow angularity in a Q -vortex

7.1.3 Choices of Overall Design Configuration, Blade Aspect Ratio and Pitch-to-Chord Ratio

The conventional terminology used in the design and analysis of blades is shown in Figure 7.1.3.1.

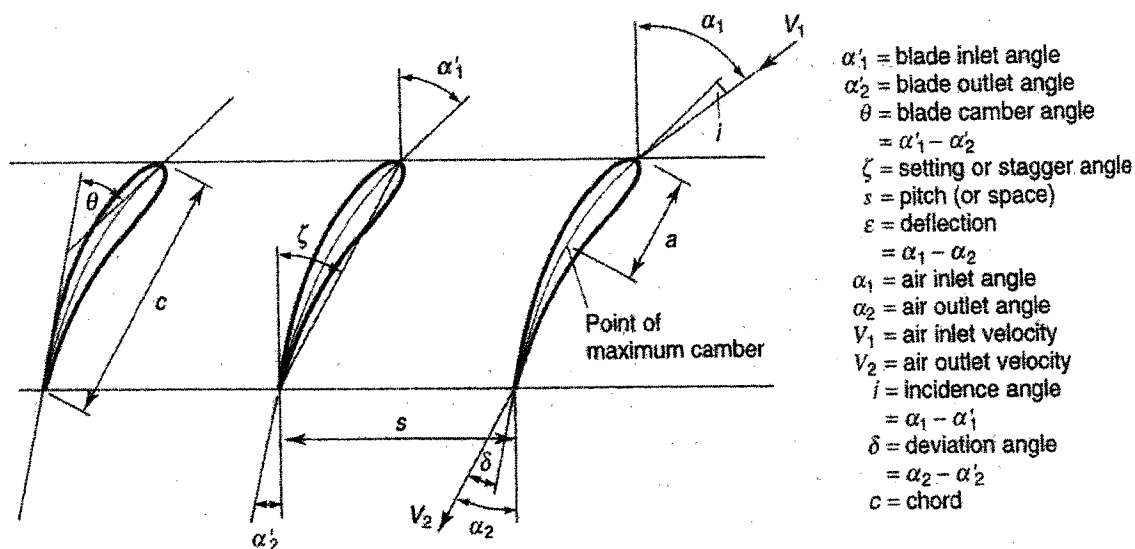


Figure 7.1.3.1: Cascade notation for vortex generator, reproduced from Cohen *et al.* (1972)

In turbomachinery practice, the goal is to minimize frictional losses for maximum efficiency. For the present vortex-generator application, although frictional losses are not crucial, designing for minimum losses remains beneficial. This is because such a design strategy will result in minimum effects of blade wakes, passage vortices, etc., on the downstream flow. The aspect ratio is defined as:

$$AR = \frac{(\text{blade span})^2}{\text{blade planform area}} \quad (7.1.3.1)$$

If a constant-chord assumption is used, Eqn. 7.1.3.2 can be reduced to:

$$AR = \frac{b}{c} \quad (7.1.3.2)$$

where b is the span of the blade and c is the blade chord length. To minimize losses, it is recommended by Cohen *et al.* (1972) that:

$$3 < AR < 4 \quad (7.1.3.3)$$

Following the recommendations of Cohen *et al.* (1972), an aspect ratio of 3.5 was selected for this initial design.

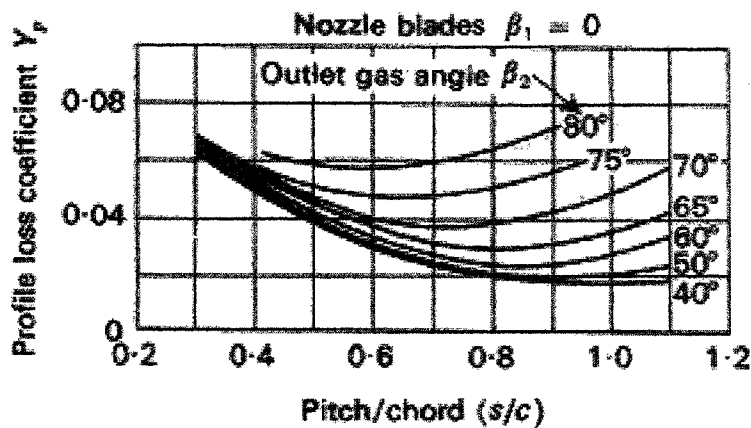


Figure 7.1.3.2: Profile loss coefficient variation with pitch/chord ratio, reproduced from Cohen *et al.* (1972)

Figure 7.1.3.2 shows the empirical relationship between the profile loss coefficient, Y_p , and the pitch to chord ratio, s/c . Since the outlet flow angle of the vortex generator is smaller than 40° (Figure 7.1.2.2), it can be assumed that the profile loss coefficient is minimized with $s/c = 1.0$. The angle of incidence is taken as zero at all radial positions of the vortex generator. The angle of incidence, i , is defined as:

$$i = \alpha_1 - \alpha'_1 \quad (7.1.3.4)$$

where α_1 is the inlet flow angle and α'_1 is the inlet metal angle of the blade. The incoming flow is taken to be uniform and free of swirl, which should be achievable with the chosen wind-tunnel setup (Figure 7.1.1.1).

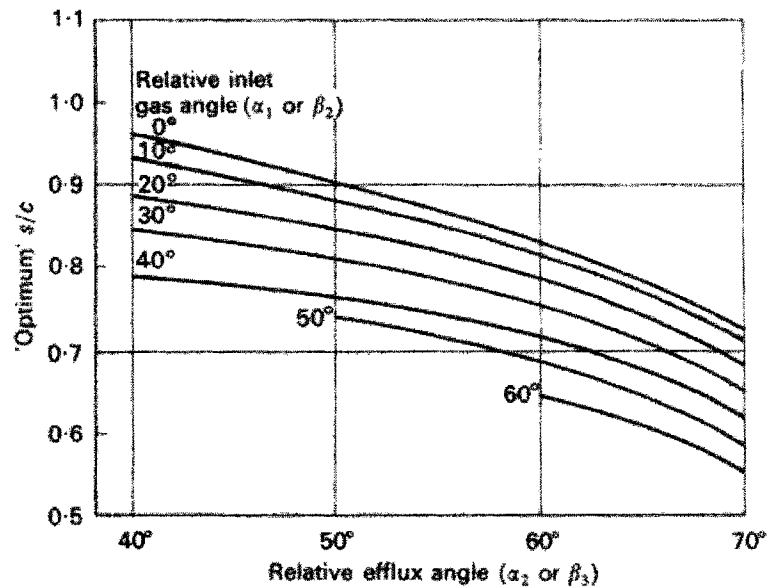


Figure 7.1.3.3: Optimum pitch/chord ratio as a function of efflux angle, reproduced from Cohen *et al.* (1972)

The choice of $s/c = 1.0$ is supported by the information reproduced in Figure 7.1.3.3. Here, an optimum s/c value is correlated to the relative efflux angle. The relative efflux angle refers to the outlet flow angle in the context of this design. For the present design, the relative inlet angle is zero and the relative efflux angle is less than 40° . An estimate of the optimum s/c ratio at outflow angles less than 40° is obtained from Figure 7.1.3.3 through extrapolation. This resulted in a pitch-to-chord ratio of approximately 1.0.

For a constant-chord design, maintaining that the optimum s/c value of 1.0 at all radial positions, r , clearly requires the use of different blade counts at different r . This option is presented in Figure 7.1.3.4a. This will keep each section's profile loss at a minimum but the discontinuities between sections will have their own associated loss. Second, a design with a blade of varying chord length can be implemented to yield

$s/c = 1.0$ at all radial positions, as shown in Figure 7.1.3.4b. Finally, a blend of the two above options can be designed which consists of two sections, each of which has a varying chord length to yield $s/c = 1.0$ (Figure 7.1.3.4c). A quantitative functional analysis is undertaken to help guide this optimization process.

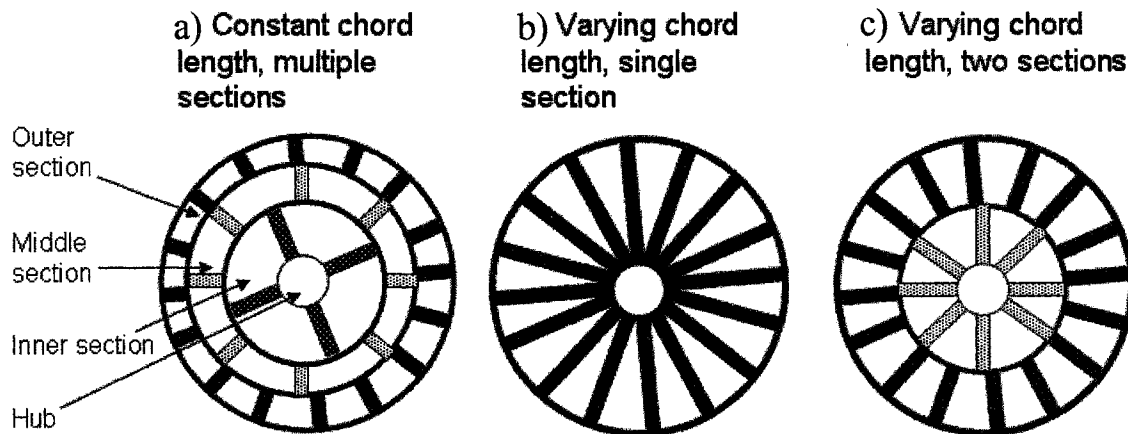


Figure 7.1.3.4: Vortex-generator design options

7.1.4 Quantitative Functional Analysis (QFA)

Four key factors that determine which design will be further investigated are velocity profile accuracy, ease of manufacture, structural integrity, and design simplicity. The vortex generator must be designed to deliver the downstream velocity profile with minimum disturbances (bladewakes, secondary flows, etc.), and this characteristic is identified as the profile accuracy. Although the vortex generator is not moving, there are forces acting upon the blades resulting from the imparting of swirl onto the fluid. If the

blade chord length decreases below a minimum strength value ($c_{min} = 0.5$ cm), the risk of elastic deformation of the blades during testing becomes a concern. Finally, the simplicity of the design is desirable for it allows for straight forward representation of the geometry through computational fluid dynamics (*CFD*). A *CFD* analysis is relevant since it will validate the design, which is based upon empirical correlations only. Each section of the *QFA* has a quantitative value ranging between 1 and 5 where 1 denotes a weakness in the design and 5 denotes a strength, as shown in Table 7.1.4.1.

Design Option	Profile Accuracy	Ease of Manufacture	Strength	Simplicity	Total Score
Multiple Sections	3	5	4	1	13
Single Section	5	3	2	4	14
Two Sections	4	4	3	2	13

Table 7.1.4.1: Quantitative functional analysis of vortex design options

The *QFA* analysis shown in Table 7.1.4.1 allows the first design of multiple sections and third design of two sections to be discarded. Further analysis of the single section option is now explored in greater detail.

7.1.5 Selection of Hub and Tip Radii and Blade Chord Length

The diameter of the vortex generator, $D_v = 0.5$ m, was chosen to easily fit inside of a typical wind-tunnel test section. This diameter corresponds to approximately 6.25

vortex core diameters. A fixed number of blades and an s/c ratio equal to unity at all radial positions yield a chord length that is linearly proportional to radius. Due to structural reasons, the vortex-generator blade should not be extended through the entire vortex generator. Aiming for a hub chord length greater than $c_{min} = 0.5$ cm, the radial position of the blade hub, r_{min} , is 0.66 cm, which corresponds to approximately 15% of the vortex core radius.

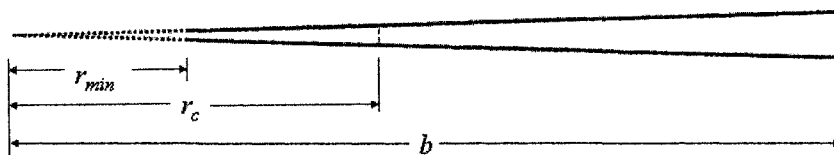


Figure 7.1.5.1: Blade dimensions

Based upon an aspect ratio, AR , of approximately 3.5 and a blade span, b , of 0.25 m, the mean chord length, c_{mean} , and mean radius, r_{mean} are calculated to be 0.074 m and 0.125 m, respectively. The number of blades, $N = 10$, can be calculated from c_{mean} , an s/c ratio equal to unity, and an aspect ratio, AR , equal to 3.5. With these constraints defined, the chord length and pitch for the rest of the blade can be ascertained.

7.1.6 Blade Outlet Angle Calculations

Even with an optimized blade design with minimal associated losses, the exit flow angle does not follow the exit blade metal angle. This deviation needs to be accounted

for in the design if the correct tangential velocity profile downstream of the vortex generator is to be obtained. The deviation for a turbine nozzle blade is defined as:

$$\delta = \beta_2 - \alpha_2 \quad (7.1.6.1)$$

where β_2 is the blade exit metal angle, α_2 is the exit flow angle, and δ is the deviation. As the deflection of the flow through the blade row increases and/or flow guidance by the blades decreases, the deviation increases. An empirical formula provided by Cohen *et al.* (1972) estimates deviation as a function of blade camber angle and pitch-to-chord ratio:

$$\delta = 0.19\theta \frac{s}{c} \quad (7.1.6.2)$$

$$\epsilon = \beta_1 - \beta_2 \quad (7.1.6.3)$$

where θ is the camber angle and β_1 is the blade metal angle at the inlet. For $\beta_1 = 0^\circ$, as is chosen for the present design (through $\alpha_1 = 0$ and $i = 0$), Eqns. 7.1.6.1-3 yield:

$$\theta = -\beta_2 = \frac{\alpha_2}{1 - 0.19 \frac{s}{c}} \quad (7.1.6.4)$$

Figure 7.1.6.1 shows the calculated blade exit angles along the blade span.

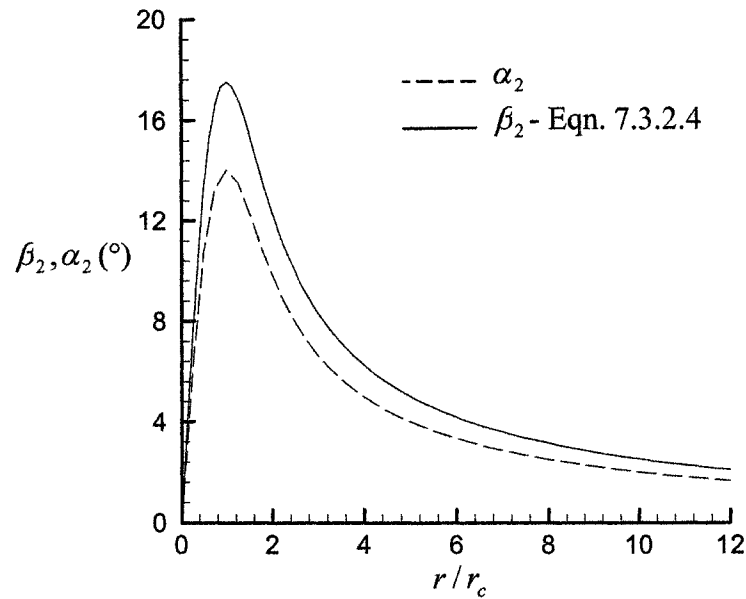


Figure 7.1.6.1: Outlet flow and blade angles

7.1.7 Blade Profile

After the blade chord length, pitch-to-chord ratio, and inlet and outlet blade metal angles are determined, the blade profile must be designed. The blade profile selected for the vortex generator is a *T6* base profile with a circular arc camber line. This blade has a thickness/chord ratio of $t/c = 0.1$, a leading edge radius of $0.12t$, and a trailing edge radius of $0.06t$. The *T6* base profile is shown in Figure 7.1.7.1 for a zero-camber configuration.

7.2 Simulation of the Vortex-Generator Downstream Flow

It is of interest to establish the streamwise rate of change of the flow field downstream of the vortex generator. If the vortex generator is to be used to produce vortical oncoming flow in wind-tunnel testing of model aircraft, it is important that the streamwise decay rate of the vortical flow be consistent with the decay rate of the full scale flow being simulated, e.g. the wingtip vortex of a leading airplane. The *LES* results presented herein are intended to be a first step in the study of the vortex-generator downstream flow development. Smagorinsky's sub-grid turbulence model was used with a constant, C_s , value of 0.1.

7.2.1 Computational Domain and Discretization

As shown in Figure 7.2.1.1, the computational domain used in this investigation consists of a cylinder of diameter and length equal to 25 and 62.5 vortex core radius, r_c , respectively. The domain diameter is twice the diameter of the vortex generator, and was chosen such that a conservative amount of flow bypassing the vortex generator in a wind-tunnel setting is included in the computations. This will ensure that the simulated development and decay of the vortical flow exiting the vortex generator is performed in an environment representative of the flow conditions in a wind-tunnel test section.

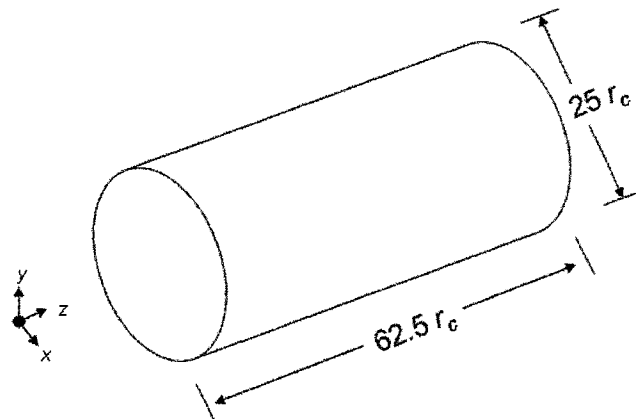


Figure 7.2.1.1: Computational domain of vortex generator simulation

The domain length has to be of adequate length to meet the objective of undertaking this numerical simulation, as outlined in the opening paragraph of Section 7.2. It is desirable to select this length conservatively, to ensure absence of non-physical effects in the region of interest that may be caused by the approximate treatment of the outflow boundary conditions. The present choice of domain length, corresponding to five vortex-generator diameters, is judged to meet these requirements.

7.2.2 Boundary Conditions

The boundaries of the computational domain are shown in Figure 7.2.2.1. The inflow boundary condition was specified to correspond to the outlet velocity field of the vortex-generator design.

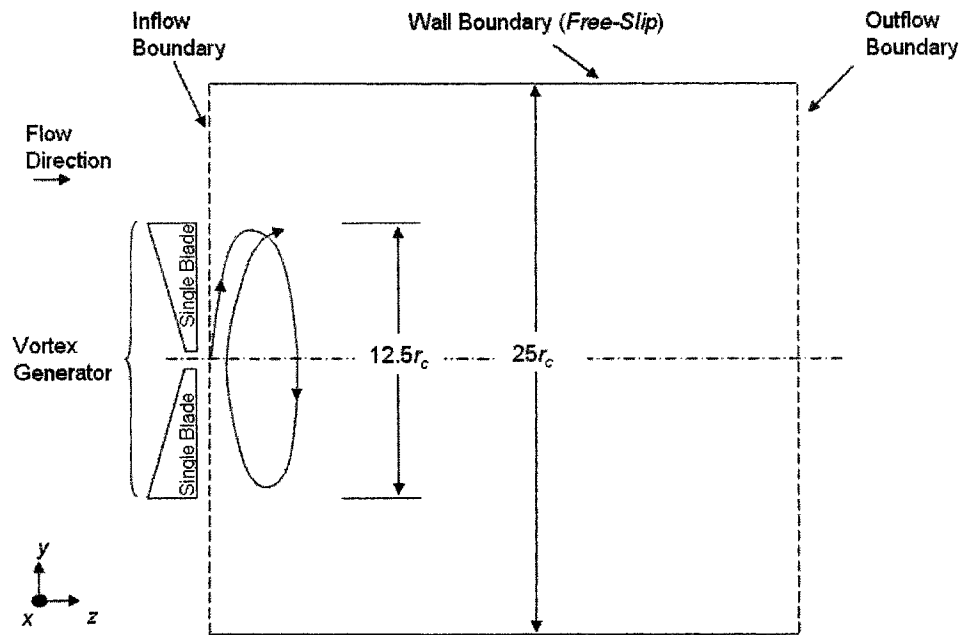


Figure 7.2.2.1: Boundary conditions for vortex generator simulation

As the vortex generator was designed for radial equilibrium discharge flow with constant axial velocity, the computational domain inflow radial and axial velocity components are $U_r = 0$ m/s and $U_z = 8.1$ m/s, respectively. The tangential velocity is specified at the inflow boundary using *CFX's* one-dimensional interpolation function. It should be noted that inlet-boundary flow non-uniformities associated with blade-passage discharge flow conditions (e.g. secondary flows) are not accounted for in the present simulation simulations. Such effects are expected to be small due to the very mild flow turning in the vortex generator. Nonetheless, sensitivity of the present simulation results to such non-uniformities should be investigated in future efforts.

The inflow turbulence intensity is set to a uniform value of one percent. This is based on the assumption of low-turbulence conditions at the vortex-generator inlet and neglecting the turbulence associated with the end-wall and blade-surface boundary layer. Future sensitivity studies are recommended to establish the effect of inflow turbulence levels on the streamwise decay rate of the downstream vortical flow.

A free-slip condition was applied to the wall boundary, which requires all spatial derivatives normal to the boundary to be zero. Since the computational domain-to-vortex-generator diameter ratio is large and the expected diffusion rate is low, it is reasonable to assume that the stream tube corresponding to the computational domain perimeter experiences negligible expansion with downstream distance. In addition, low levels of turbulence near the domain perimeter support the assumption of steadiness for this stream tube. On the outflow boundary, pressure was maintained at atmospheric level on a spatially-averaged basis.

7.2.3 Initial Conditions

The initial conditions for all *LES* flow variables within the computational domain were obtained from a *RANS* simulation using a k - ε turbulence model (Section 3.3.3.1). Although the k - ε turbulence model has prediction limitations in flow fields of streamline curvature, it was considered to have the highest accuracy-to-cost ratio of all the turbulence models the author has tested. For the *RANS* simulation, identical computational domain, boundary conditions, and grid resolution specifications as for the

LES were used. The initial distribution of flow variables for the *RANS* simulation was identical to those specified at the inflow boundary. The pressure distribution was initialized at standard atmospheric level throughout the computational domain. *RMS* residuals levelled off at a magnitude of 10^{-8} and velocity and turbulence quantities were monitored to confirm negligible changes with iterations.

7.2.4 Spatial Resolution

The spatial resolution in the vicinity of the vortex core is similar to that used in the inclined-jet-in-cross-flow benchmark. In that benchmark, the grid-node spacing in the vortex was set to about 340 times the Kolmogorov scale. The mean grid-node spacing, Δ , used for the present study corresponds to:

$$\frac{\Delta}{\eta} = \frac{\Delta \text{Re}^{\frac{3}{4}}}{r_c} = 584 \quad (7.2.4.1)$$

where η is the Kolmogorov length scale. This spatial resolution ($\Delta = 0.008$ m) corresponds to approximately 10 nodes across the vortex core. In an investigation of far-field decay of an isolated trailing vortex by Wallin and Girimaji (2000), 10 nodes were used to adequately resolve the vortex core.

Outside of the core, the grid-node spacing expands in the radial direction at an exponential rate of 1.3. This was applied uniformly at all axial positions. Although an expanding grid in the axial direction would decrease the load on computational resources, limitations in the *CFX* Build algorithm prohibited this. As the wall boundaries on the

computational domain were free-slip conditions, near-wall grid refinement was not needed.

The above specifications resulted in with 600,000 nodes, with approximately 60 nodes in the radial direction and approximately 250 nodes in the axial direction. Figures 7.2.4.1 and 7.2.4.2 show the radial and axial distribution of nodes in the computational domain.

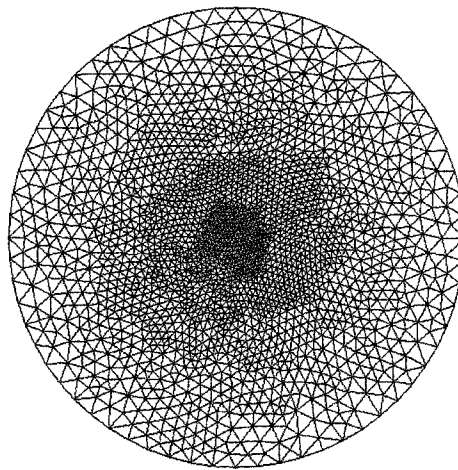


Figure 7.2.4.1: Radial grid-node distribution for vortex generator downstream flow simulation

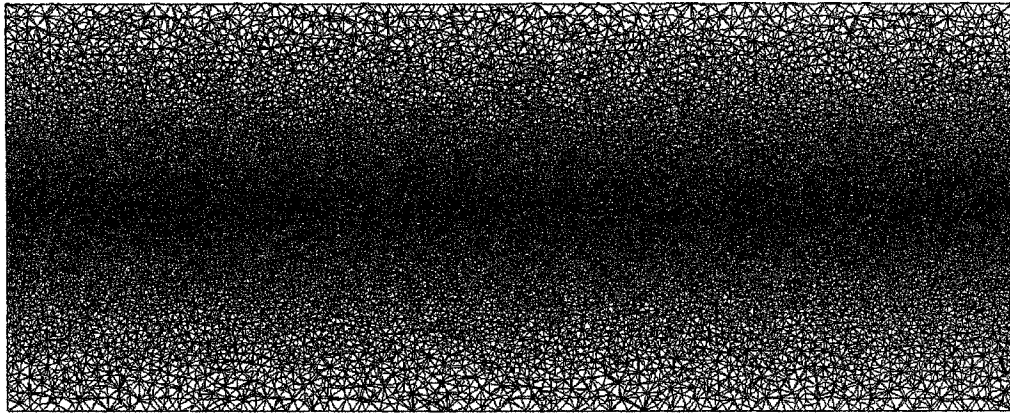


Figure 7.2.4.2: Axial grid-node distribution for vortex generator downstream flow simulation

7.2.5 Temporal Resolution

Parametric studies over the range of $\Delta t = 0.0001$ sec to $\Delta t = 0.0005$ sec revealed the results to be insensitive to the choice of time-step size in this range. The results presented herein correspond to a courant number and time-step of $\nu = 0.58$ and $\Delta t = 0.001$ seconds, respectively.

7.2.6 Solution Convergence

A minimum residual level of 10^{-6} and maximum number of 10 iterations were specified for each time-step. In contrast to previous benchmark studies (Chapter 6), the simulation began very stable and *RMS* residual levels for mass and momentum were able to reach convergence criteria at the first time-step. Nonetheless, as a precaution, the first

100 time steps were excluded from the calculation of flow statistics. Approximately four iterations per time-step were required to meet the minimum residual level throughout the simulation.

Approximately one week was required to complete a simulation on a Pentium 4, 2GHz computer with 1GB of RAM. This simulation time corresponds to 1000 time-steps. Based upon the selected time step size of $\Delta t = 0.001\text{s}$, a spatially-averaged axial velocity of $\overline{U}_z = 8.1\text{ m/s}$, and a domain length of $62.5 r_c$, 1000 time steps is equivalent to 3 realization times. The realization time is the time required for a particle to travel through the computational domain at $U_z = 8.1\text{ m/s}$.

7.2.7 Simulation Results

In this section, $k\text{-}\varepsilon$ and LES predictions of vortical flow development downstream of the vortex generator are presented. In the results presented, velocity is normalized by the spatially-averaged axial velocity component, \overline{U}_z , and vorticity ζ_z is normalized by \overline{U}_z / D_c . Figure 7.2.7.1 shows the axial locations ($z/r_c = 20$, $z/r_c = 40$) where variables are measured or calculated.

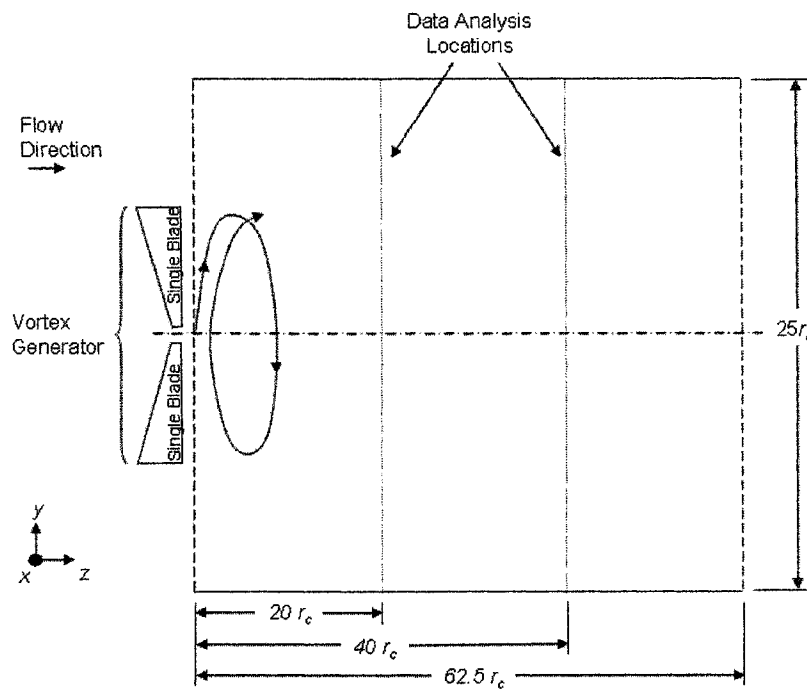


Figure 7.2.7.1: Streamwise location of data-analysis planes

Figure 7.2.7.2 shows the streamwise decay of the tangential velocity component, U_t . It is observed that at $z/r_c = 40$, the maximum tangential velocity has decreased by 6% and 24% of its initial value for *LES* and *RANS- $k-\epsilon$* , respectively. Over the same length ($40r_c$) and measured at the same streamwise distance from the wingtip, Devenport *et al.* (1996) measured 1.3% decay of maximum tangential velocity in a wingtip vortex, where the vortex Reynolds number was $Re_{c_w} = 6 \times 10^5$.

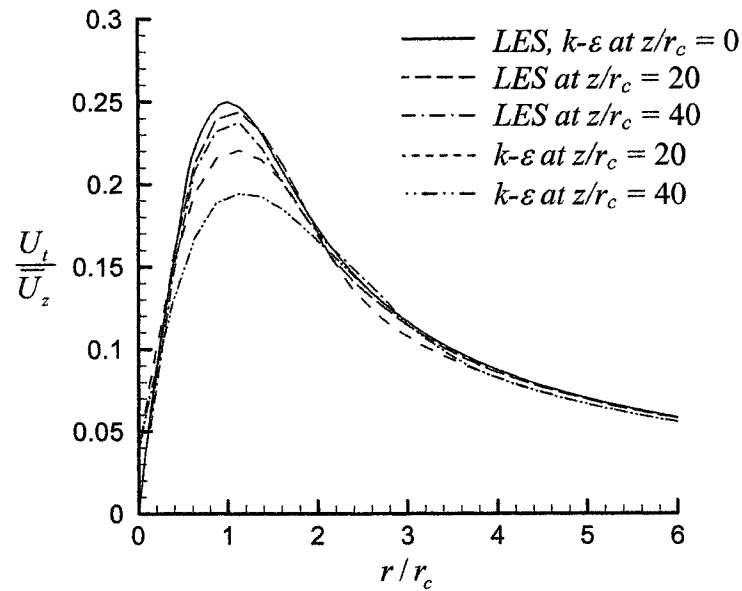


Figure 7.2.7.2: Decay of tangential velocity component

Over the initial axial distance of $z/r_c = 40$, the growth in vortex core radius was approximately 8% and 20% for *LES* and *RANS- $k-\varepsilon$* , respectively. Moore and Saffman (1973) developed a relationship between vortex-core-radius growth and downstream distance measured from the wingtip:

$$\frac{r_c}{c_w} = 2.92 \left(\frac{z}{c_w} \right)^{\frac{1}{2}} (\text{Re}_{c_w})^{\frac{1}{2}} \quad (7.2.7.1)$$

Applied to the present flow, ($r_c/c_w = 0.04$, $z/c_w = 30$, $\text{Re}_{c_w} = 6 \times 10^5$), Eqn. 7.2.7.1 corresponds to 2.6% increase in vortex core radius over a distance of $z/r_c = 40$. The decay of tangential velocity component and growth of the vortex core radius is related to the redistribution of vorticity, as shown in Figure 7.2.7.3. The more rapid diffusion of the vortex in the *RANS- $k-\varepsilon$* simulation is clearly evident in this figure.

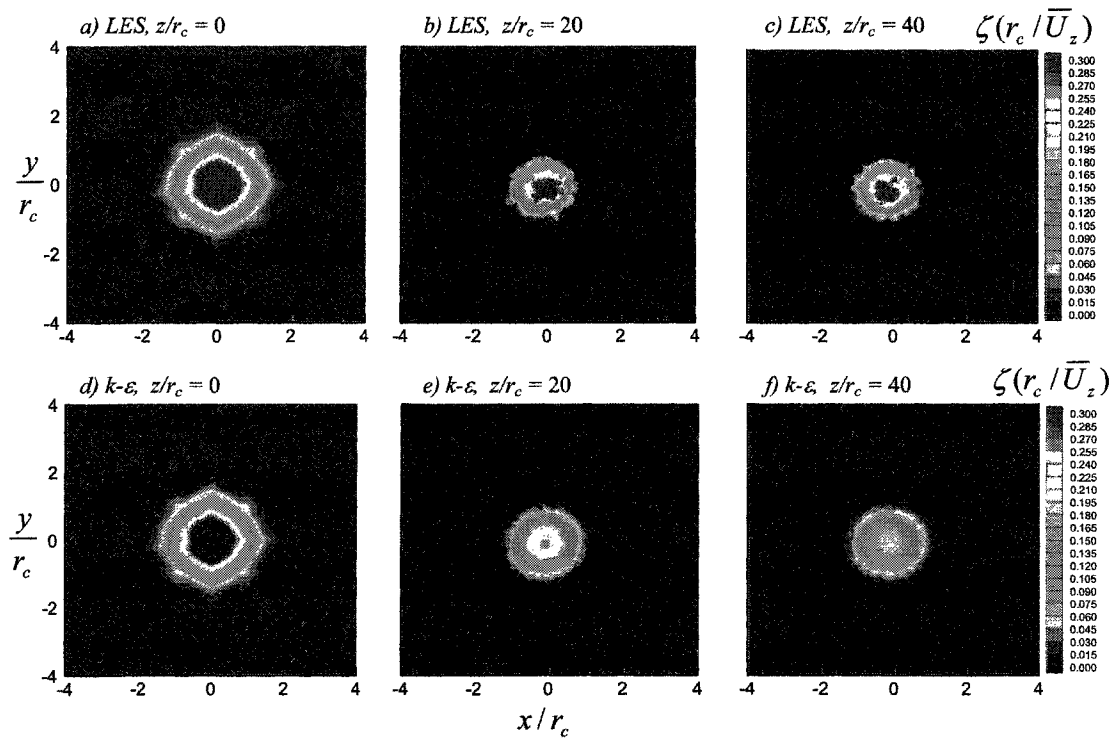


Figure 7.2.7.3: Decay of vorticity

It is not surprising that the *RANS- $k-\epsilon$* computations predict a larger decay rate than the *LES*, since the *k- ϵ* turbulence model is known to fail in situations of streamline curvature, predicting excess turbulent production and diffusion (Section 3.3.3.1). It is therefore concluded that the *LES* results are considerably more realistic than the *RANS- $k-\epsilon$* results.

The presence of vortex wandering has important consequences for the accuracy of measurements, since using a simple temporal average can lead to incorrect values of peak velocity and vortex core size (Devenport, 1996). Jacquin *et al.* (2001) proposed four mechanisms responsible for wandering. These included perturbation of the core by wind-

tunnel unsteadiness, perturbation of the core by turbulence in the surrounding shear layer (as the layer rolls up around the core), long-wave instabilities such as the Crow instability, or propagation of unsteadiness from the turbulence model.

Baker *et al.* (1974) and Devenport *et al.* (1996) estimated vortex wandering to exist at amplitudes up to $0.4r_c$ at 5-36 chord lengths downstream of a wing. No wandering was detected in the present simulation. Since the inflow boundary conditions for the present simulation were steady and the domain length is insufficient for Crow instability to develop, the only possible mechanism that can promote vortex wandering is the larger eddies present in the shear layer surrounding the vortex core. Such eddies were not observed in the simulation results. Since large scale turbulence was not specified as part of the inflow boundary conditions, such eddies would have to develop naturally under the influence of the prevailing strain-field in the vortex. Presumably, the computed streamwise distance was insufficient for this process to occur.

It is therefore concluded that the vortical flow produced by the vortex generator experiences little diffusion or wandering over a streamwise distance of 4 vortex generator diameters. It would be beneficial to undertake further *LES* studies with inflow conditions that are unsteady or of high turbulence intensity and length scale to determine whether the present results remain applicable under such conditions. These results can then be used to guide further optimization of the proposed vortex-generator setup.

Chapter 8

CONCLUSIONS AND RECOMMENDATIONS

The prediction performance of *RANS*- and *LES*-based turbulence models were evaluated using the commercial *CFX* software for confined swirling flow, the decay of isotropic turbulence and an inclined jet in cross-flow. Upon evaluation, *LES* with Smagorinsky's sub-grid turbulence model was chosen as the optimum numerical simulation, and was used to predict the downstream development of a wind-tunnel vortex generator.

LES was able to successfully predict the decay of isotropic turbulence. This was demonstrated to hold true for a range of spatial grid structures. However, the simulation results were found to be sensitive to the choices of Courant number and discretization scheme.

Through predictions of the flow field produced by an inclined jet in cross-flow, *LES* was shown to be superior to *RANS*-type computations, even when full Reynolds-stress modelling was used for turbulence closure. The *LES* computations provided accurate predictions of the development and decay of the dominant streamwise vortex behind the inclined jet. Additionally, it provided insight on the role of large scale turbulence in the convective and diffusive development of this vortex. While the *LES* results were found to be insensitive to the Courant number in this instance, they remained to be sensitive to the choice of discretization scheme for the convective derivatives. For

best results, it was also observed that the constant in Smagorinsky's sub-grid model had to be adjusted from its original value used in the turbulence decay study.

Having demonstrated the superiority of *LES* over *RANS* through these benchmarks, and the ability to undertake such demanding computations using a commercial software, *LES* was used in a design exercise involving the development of a vortex generator to produce vortical flow patterns in a wind-tunnel setting. Specifically, *LES* was utilized to predict the streamwise decay rate of the flow field downstream of the vortex generator. The proposed vortex generator was shown to produce a cross-flow pattern that experiences little variation with streamwise distance over 4-vortex-generator diameters.

It is important to point out that the choices of flow initialization, boundary conditions, discretization scheme, and sub-grid turbulence models utilized in the *LES* study were limited to the few available in *CFX 5.7*. It is recommended that similar efforts be undertaken with the present benchmarks (turbulence decay and inclined jet in cross-flow) as a wider range of choices becomes available in future versions of *CFX* software.

The vortex-generator design effort presented herein should be considered to be preliminary. While the proposed blade design was based on established design practices using semi-empirical tools, it is considered worthwhile to validate this design by undertaking an *LES* study of the blade-passage flow. Furthermore, the downstream flow development predicted in the present study is limited to relatively idealized vortex generator discharge flow conditions. It is recommended that this exercise be repeated

with more realistic discharge conditions that would become available through the blade passage *LES* predictions.

References

Ahmed, S. A. , 1998, "Velocity measurements and turbulence statistics of a confined isothermal swirling flow," *Experimental Thermal and Fluid Science*, Vol. 17, pp. 256-264.

Ajersch, P., Zhou, J. M., Ketler, S., Salcudean, M. & Gartshore, I. S. , 1997, "Multiple jets in a crossflow: Detailed measurements and numerical simulations.", Trans. ASME: *Journal of Turbomachinery*, Vol 119, pp. 330–342.

Akanni, S. D., and Hentry, F.S. , 1995, "Numerical calculations for air-jet vortex generators in turbulent boundary layers," CEAS European Forum on High Lift and Separation Control.

Alvarez, J., Jones, W.P., and Seoud, R.. , 1993, "Prediction of momentum and scalar fields in a jet in cross flow using first and second order turbulence closures.", *Computational and Experimental Assessment of Jets in Cross Flow*, number CP-534. AGARD.

Andreopoulos, J. , 1982, "Measurements in a jet-pipe flow issuing perpendicularly into a cross stream," *Journal of Fluid Mechanics*, vol. 104, pp. 493-499.

Andreopoulos, J., and Rodi, W. , 1984, "Experimental investigation of jets in a crossflow." *Journal of Fluid Mechanics*, Vol 138, pp. 93-127.

Armfield, S. W., and Fletcher, C. A. J. , 1989, "Comparison of k- ϵ and algebraic Reynolds-stress models for swirling diffuser flow," *International Journal for Numerical Methods in Fluids*, Vol. 9, 987-1009.

Baker, G. R., Barker, S. J, Bofah, K.K., Saffman, P.G., 1974, "Laser anemometer measurements of trailing vortices in water," *Journal of Fluid Mechanics*, Vol. 65, p. 325-336.

Baker, C. J. , 1979, "The laminar horseshoe vortex.," *Journal of Fluid Mechanics*, Vol 95 pp. 347-367.

Baldwin, B. S., and Lomax, H. , 1978, "Thin-layer approximation and algebraic model for separated turbulent flows," *AIAA Paper No. 78-257*.

Bandyopadhyay, P. R., Stead, D. J., and Ash, R. L. , 1991, "The Organized Nature of a Turbulent Trailing Vortex," *AIAA Journal*, Vol. 29, No. 10., pp. 1627-1633.

Bardina, J., Ferziger, J. H. and Reynolds, W. C. , 1983, "Improved turbulence models based on large-eddy simulation of homogenous, incompressible turbulent flows," Stanford University Tech. Rep. TF-19.

Barberopoulos, A. A., and Garry, K. P. , 1998, "The effect of skewing on the vorticity produced by an airjet vortex generator," *The Aeronautical Journal*, Paper No. 2275, pp. 171-177.

Barlow, R. S., and Johnston, J. P. , 1988, "Structure of a turbulent boundary layer on a concave surface," *Journal of Fluid Mechanics*, Vol. 191, p 137.

Basara, B., Cokljat, D., and Younis, B. A. , 1995, "Assessment of eddy-viscosity and Reynolds-stress transport closures in two- and three-dimensional turn-around ducts", ASME, FED-Vol 217, Separated and Complex Flows.

Bayly, B. J. , 1986, "Three-dimensional instability of elliptical flow," *Phys. Rev. Lett.*, Vol 57, pp. 2160.

Benjamin, T. B. , 1962, "Theory of vortex breakdown phenomenon," *Journal of Fluid Mechanics*, Vol 14, pp. 593-629.

Benz, E., Beeck, A., Fottner, L., and Wittig, S. , 1993, "Analysis of cooling jets near the leading edge of turbine blades," *Computational and Experimental Assessment of Jets in Cross Flow*, number CP-534. AGARD.

Bertoglio, J. P. , 1982, "Homogenous turbulent field within a rotating frame," *AIAA Journal*, Vol 20, p. 1175.

Betz, A. , 1932, "Verhalten von Wirbelsystemen," *Z. angew. Math. Mech.*, Vol. 12, No. 164.

Bossel, H. H. K. , 1967, "Inviscid and Viscous Models of the Vortex Breakdown Phenomenon," PhD thesis, University of California at Berkeley.

Boussinesq, J., 1877, "Theorie de l'Ecoulement Tourbillant," Mem. Presentes par Divers Savants Acad. Sci. Inst. Fr., Vol. 23, pp. 46-50.

Bray, T. P., and Garry, K. P. , 2000, "On the velocity profile of inclined jets in a boundary layer for vorticity production," College of Aeronautics, Cranfield University, IMechE.

Broadwell, J. E., and Breidenthal, R. E. , 1984, "Structure and mixing of a transverse jet in incompressible flow." *Journal of Fluid Mechanics*, Vol 148, pp. 405-412.

Cebeci, T., and Meier, H. V. , 1979, "Modelling requirements for the calculation of the turbulent flow around airfoils, wings and bodies of high revolution," AGARD CP 271, paper 16.

Cebeci, T., Chang, K. C., Li C. , 1986, and Whitelaw J.H., “Turbulence Models for Wall Boundary Layers.” *AIAA Journal*, Vol 24, Number 3, pp. 359-360.

CFX-SUPPORT, 2004, *Personal Communication with CFX user support*.

Chaouat, B. , 1999, “Numerical simulations of fully developed channel flows by using $k - \epsilon$, algebraic and Reynolds stress models,” *37th AIAA Aerospace Sciences Meeting and Exhibit*, AIAA 99-0158.

Chen, J. C., and Lin, C. A. , 1999, “Computations of strongly swirling flows with second-moment closures,” *International Journal for Numerical Methods in Fluids*, Vol 30, pp 493 -508.

Chen, J. C., and Jaw, S. , 1998, *Fundamentals of Turbulence Modeling*, Taylor & Francis.

Chiu S. H., Roth, K. R., Margason, R. J., and Tso, J. , 1993, “A numerical investigation of a subsonic jet in a crossflow.”, *Computational and Experimental Assessment of Jets in Cross Flow*, number CP-534. AGARD.

Chow, J. S., Zilliac, G. G., Bradshaw, P. , 1997, “Mean and Turbulence Measurements in the Near Field of a Wingtip Vortex”, *AIAA Journal*, Vol 35, No. 10.

Clausen, P. , 1987, “Measurement and predictions of swirling flow behind turbine blades and through axisymmetric diffusers,” *Ph. D. thesis*, University of Newcastle, Australia.

Cohen, H., Rogers, G. F. C., Saravanamuttoo, H. I. H. , 1972, *Gas Turbine Theory*, Longman Group Limited.

Compton, D. A., and Johnston, J.P. , 1991, “Streamwise vortex production by

pitched and skewed jets in a turbulent boundary layer,” Paper AIAA-91-0038.

Comte-Bellot, G., and Corrsin, S. , 1971, “Simple eulerian time correlation of full- and narrow-band velocity signals in grid-generated, ‘isotropic’ turbulence,” *Journal of Fluid Mechanics*, Vol. 48, part 2, pp. 273-337.

Crow, S.C, 1971., “Stability Theory for a Pair of Trailing Vortices”, *AIAA Journal*, Vol. 8, pp. 2172.

Dailey, L.D., Simons, T.A., and Pletcher, R.H. , 1996, “Large eddy simulation of isotropic decaying turbulence with structured and unstructured grid finite volume methods,” ASME Winter meeting in Atlanta, GA.

Davenport, W. J., Rife, M. C., Stergios L. I., and Follin G. J. , 1996, “The structure and development of a wing-tip vortex,” *Journal of Fluid Mechanics*, Vol 312, pp. 67-106.

Davenport, W. J., Rife, M. C., Liapis, S. I., and Folin G. J. , 1995, “Turbulent Structure and Scaling in Trailing Vortices,” *AIAA 33rd Aerospace Sciences Meeting and Exhibit*, Reno, NV.

Deardorff, J.W. , 1970, “A numerical study of three-dimensional turbulence channel flow at large Reynolds numbers.” *Journal of Fluid Mechanics*, Vol. 41, pp. 453-480.

Eloy C., 2000. *Instabilit'e multipolaire de tourbillons*. PhD thesis. Universit'e Aix-Marseille II

Eloy C., le Dize, Stephane , 1999 “Three-dimensional instability of Burgers and Lamb-Oseen vortices in a strain field,” *Journal of Fluid Mechanics*, Vol. 378, pp. 145-

166.

Escudier, M. P. , 1988 “Vortex breakdown: Observations and explanations” *Prog. Aerospace Science*, Vol. 25, 189-229

Faler, J. H. and Leibovich, S. , 1978 “An experimental map of the internal structures of a vortex breakdown,” *Journal of Fluid Mechanics*, Vol. 86, pp. 313-335.

Ferziger, J. H. , 1993, “Subgrid-Scale Modeling,” *Large Eddy Simulation of Complex Engineering and Geophysical Flows*, Cambridge University Press.

Ferziger, J. H., Peric, M, 1999., “Computational Methods for Fluid Dynamics,” Springer-Verlag Berlin Heidelberg.

Findlay, M. J., Salcudean, M. & Gartshore, I. , 1999, “Jets in a crossflow: Effects of geometry and blowing ratio.”, *Trans. ASME: Journal of Fluids Engineering*, Vol 121, pp. 373–378.

Fric, T. F., and Roshko, A. , 1994, “Vortical structure in the wake of a transverse jet.” *Journal of Fluid Mechanics*, Vol 279, pp.1-47.

Fu, S., Launder B. E., and Leschziner, M. A. , 1987, “Modelling strongly swirling recirculating jet with Reynolds stress transport closure,” *Proc. 6th Symposium on Turbulent Shear Flows*, Toulouse, pp. 17.6.1 - 17.6.6.

Gallardo, J-F., and Lakshminarayana, B. , 1993, “Computation of curved flows using a modified k - ϵ model of turbulence based on algebraic Reynolds stress relations,” 31st Aerospace Sciences Meeting & Exhibit, AIAA 93-0202.

Gatski, T. B., Hussaini, M. Y., Lumley, J. L., 1996, *Simulation and Modeling of Turbulent Flows*, Oxford Univeristy Press, New York.

Gatski, T. B., and Speziale, C. G. , 1993, “On explicit algebraic stress models for complex turbulent flows,” *Journal of Fluid Mechanics*, Vol. 254, pp. 59-78.

Germano, M., Piomelli, U., Moin, P., and Cabot, W. H. , 1991, “A dynamic subgrid scale eddy viscosity model” *Physics of Fluids*, Vol. 3, p. 1760.

Gerz, T., and Holzapfel, F., 1999, “Wing-tip vortices, turbulence, and the distribution of emissions,” *AIAA Journal*, Vol. 37, No. 10, pp. 1270-1276.

Gibson, M. M., and Launder, B. E. , 1978, “Ground effects on pressure fluctuations in the atmospheric boundary layer,” *Journal of Fluid Mechanics*, Vol. 86, pp. 491-511.

Gogineni, S., Goss, L. & Roquemore, M., 1998, “Manipulation of a jet in cross flow.”, *Journal of Experimental Thermal & Fluid Science*, Vol 16, pp. 209–219.

Govindaraju, S. P., and Saffman, P. G., 1971, “Flow in a turbulent trailing vortex,” *Physics of Fluids*, Vol 14, No. 10, pp. 2074 – 2080.

Graham, J.M.R, 1984, International Workshop on Numerical Simulation of Bluff Body Aerodynamics, Meersburg, Germany.

Grosvenor, A.D., 2000, “Numerical simulations of diffusing s-duct and vortex-generator-jet flows”, Master’s Thesis, Carleton University.

Grosvenor, A.D. , 2003, “Numerical Simulations of Diffusing S-Duct and Vortex-Generator-Jet Flows,” *International Journal for Numerical Methods in Fluids*, Vol 42., pp 1293 – 1319.

Gupta, A.K., Lilley, D.G., and Syred, N., 1984, “Swirl Flows,” *Abacus Press Energy and Engineering Series*.

Hanjalic, K., and Launder, B. E. , 1972, "A Reynolds stress model and its applications to this shear flow," *Journal of Fluid Mechanics*, Vol 52, pp. 609-638.

Havelock, T. H. , 1931, "The Stability of Motion of Rectilinear Vortices in Ring Formation" *Phil. Mag. S.7.*, Vol. 11, no. 70.

Haven, B. A., and Kurosaka, M. , 1997, "Kidney and anti-kidney vortices in crossflow jets." *Journal of Fluid Mechanics*, Vol 352 pp. 27-64.

Hellsten, A. , 1998, "Some improvements in Menter's $k - \omega$ SST turbulence model," AIAA 98 - 2554.

Henry, F. S., and Pearcey, H. H. , 1994, "Numerical model of boundary-layer control using air-jet generated vortices," AIAA Journal Vol 32, No. 12, pp. 2415-2425

Heyes, A.L., Jones, R.F., and Smith, D.A.R. , 2004, "Wandering of wing-tip vortices," *Applications of Laser Techniques to Fluid Mechanics*, 12th International Symposium, Portugal.

Hinze, O. , 1975, *Turbulence* McGraw-Hill, New York.

Hogg, S., and Leschziner, M. A. , 1989, "Computation of highly swirling confined flow with a Reynolds-stress turbulence model," *AIAA*, Vol. 27, No. 1.

Hughes, T. J. R., Mazzei, L., Oberai, A. A. , 2001, "The multiscale formulation of large eddy simulation: Decay of homogeneous isotropic turbulence," *Physics of Fluids*, Vol. 13, Number 2, pp. 505-512.

Hytopoulos, E., and Simpson, R. L., 1993, "Critical Evaluation of Recent Second-Order Closure Models," *31st Aerospace Sciences Meeting & Exhibit*, AIAA 93 - 0081,.

Jacob, D., 1995, "Experimental Investigation of the Trailing Vortex of

Rectangular Airfoils,” Ph.D. Thesis, University of California at Berkley.

Jacquín, L., Fabre, D., Geffroy, P., Coustols, E. , 2001, “The properties of a transport aircraft wake in the extended near field: An experimental study,” *AIAA conference proceedings*, p. 1038.

Johari, V., 2004, Personal Communication.

John, V. , 2004, “Large Eddy Simulation of Turbulent Incompressible Flows,” Springer-Verlag Berlin Heidelberg.

Johnston, J., and Nishi, M. , 1989, “Vortex generator jets- a means for passive and active control of boundary layer separation,” Paper AIAA-89-0564

Jiminez, J. , 1975, “Stability of a Pair of Co-Rotating Vortices”, *Physics of Fluids*, Vol. 18, no. 11.

Jones, W. P., and Pascau, A. , 1989, “Calculation of confined swirling flows with a second moment closure,” *Journal of Fluid Engineering*, Vol. 111, p. 248.

Kamotani, Y. & Greber, I., 1972, “Experiments on a turbulent jet in a cross flow.”, *AIAA Journal.*, Vol 10, pp. 1425–1429.

Kang, H. S., Chester, S., Charles, M. , 2003, “Decaying turbulence in an active-grid-generated flow and comparisons with large-eddy-simulation,” *Journal of Fluid Mechanics*, Vol. 480, pp. 129-160.

Kármán, V. T. , 1911, “*Göttinger Nachrichten*,” Math. Phys. K1. pp. 509-517

Kármán, V. T. , 1912, “*Göttinger Nachrichten*,” Math. Phys. K1. pp. 547-556

Kelso, R. M. & Smits, A. J. , 1995, “Horseshoe vortex systems resulting from the interaction between a laminar boundary layer and a transverse jet.”, *Physics of Fluids*,

Vol 7, pp. 153–158.

Kelso, R. M., Lim, T. T. & Perry, A. E. , 1996, “An experimental study of round jets in cross-flow.”, *Journal of Fluid Mechanics*, Vol 306, pp. 111–144.

Khan, Z. U., and Johnston, J. P., 2000, “On vortex generating jets,” *International Journal of Heat and Fluid Flow*, Vol 21, pp. 506-511.

Kim, J., Moin, P., and Moser, R., 1987, “Turbulence statistics in fully developed channel flow at low Reynolds numbers,” *Journal of Fluid Mechanics*, Vol. 177, pp. 137-166.

Kitoh, O. , 1991, “Experimental study of turbulent swirling flow in a straight pipe,” *Journal of Fluid Mechanics*, Vol 225, pp 445 -479.

Kolmogorov, A. N. , 1942, “The equations of turbulent motion in an incompressible fluid,” *Isv. Acad. Sci. USSR, Phys.* Vol 6, pp. 56-58.

Kupper, C., and Henry, F.S. , 2001, “A numerical study of the application of vane and air-jet vortex generator,” *Aeronautical Journal* 105, pp. 255-265.

Kupper, C., and Henry, F.S., 2003, “Numerical study of air-jet vortex generators in a turbulent boundary layer,” *Applied Mathematical Modelling*, Vol. 27, pp. 359-377.

Launder, B. E., Reece G., and Rodi, W. , 1975, “Progress in the development of a Reynolds stress turbulence closure,” *Journal of Fluid Mechanics*, Vol 68, p 537.

Launder, B. E., and Spalding, D. B. , 1974, “The numerical computation of turbulent flows.” *Computational Methods of Applied Mechanical Engineering*, Vol 3, pp. 269-289.

Launder, B. E., and Craft, 1991, “Progress and paradoxes in modelling near-wall

turbulence,” 8th Symposium for Turbulent Shear Flow, Munich.

Launder, B. E., Priddin, C. H., and Sharma, B. , 1977, “The calculation of turbulent boundary layers on curved and spinning surfaces,” *Journal of Fluids Engineering*, Vol. 98, p. 753.

Laurence, D. , 1992, “Modelling turbulent flows in engineering applications,” *Computational Methods in Applied Sciences*, pp 103-116.

Leibovich, S., 1984, “Vortex Stability and Breakdown: Survey and Extension,” *AIAA Journal*, Vol. 22, No. 9, pp. 1192-1206.

Lenoard, A. , 1974, “Energy cascade in large-eddy simulation of turbulent flows,” *Advances in Geophysics*, A 18, pp. 237-248.

Leschziner, M. A. , 1990, “Modelling engineering flows with Reynolds stress turbulence closure,” *Journal of Wind Engineering and Industrial Aerodynamics*, Vol. 35 pp. 21-47.

Leweke, T., and Williamson, C. H. K. , 1998, “Cooperative elliptic instability of a vortex pair,” *Journal of Fluid Mechanics*, vol. 360, pp. 85-119.

Lilly, D.K. , 1966, “On the application of the eddy viscosity concept in the inertial sub-range of turbulence,” NCAR Manuscript 123.

Lilly, D. K.. , 1967, “The representation of small-scale turbulence in numerical simulation experiments,” In Proceedings of the IBM Scientific Computing Symposium on Environmental Science, IBM Form No. 320-1951, page 195.

Lilly, D.K. , 1992, “A proposed modification of the Germano subgrid-scale closure,” *Physics of Fluids*, Vol. 3, pp. 2746-2757.

Lim, T. T., New, T. H. & Luo, S. C. , 2001, "On the development of large-scale structures of a jet normal to a cross flow.", *Physics of Fluids*, Vol 13, 770–775.

Lin, C. A., and Lu, C. M. , 1994, "Modelling three-dimensional gas-turbine combustor model flow using second-moment closure," *AIAA Journal*, Vol 32, No 7.

Liu, J. Piomelli, U., and Spalart, P. , 1996, "Interaction between a spatially growing turbulent boundary layer and embedded streamwise vortices," *Journal of Fluid Mechanics*, Vol. 326, pp. 151-179.

Loitsianskii, L. F. , 1939, "Some basic laws of isotropic turbulent flow," *Cent. Aero Hydro. Inst Moscow*, pp. 440.

Lumley, J. L. , 1978, "Computational modeling of turbulent flows," *Advanced Applied Mathematics*, Vol 18, pp. 123-176.

Lumley, J. L. , 1983, "Turbulence Modelling," *Journal of Applied Mechanics*, Vol. 50, 1097.

Lumley, J. L. , 1992, "Some comments on turbulence," *Physics of Fluids, A*, Vol. 4, p. 203

Lumley, J. L. and Newman, G. R. , 1977, "The return to isotropy of homogeneous turbulence," *Journal of Fluid Mechanics*, Vol. 82, p. 161.

Luo, J., and Lakshminarayana, B. , 1997, "Analysis of streamline curvature effects on wall-bounded turbulent flows," *AIAA Journal*, Vol 35, No 8.

Margason, R. J, 1993, "Fifty years of jet in cross flow research." *Computational and Experimental Assessment of Jets in Cross Flow*, number CP-534. AGARD.

Mayer, E.W., and Powell, K.G. , 1992, "Viscous and inviscid instabilities of a

trailing vortex,” *Journal of Fluid Mechanics*, Vol. 245, pp. 91-114.

McMillan, O.J. , 1980, Ferziger, J.H., and Rogallo, R.S., “Test of new subgrid scale models in strained turbulence,” AIAA Paper 80-1339.

Menter, F. R. , 1994, “Two equation eddy-viscosity turbulence models for engineering applications,” *AIAA Journal*, Vol 32, No 8.

Milanovic, I. M., and Zaman, K. B. M. Q., 2004, “Fluid Dynamics of Highly Pitched and Yawed Jets in Crossflow,” *ALAA Journal*, Vol. 42, No. 5, pp. 874-882.

Misra, A., and Pullin, D. I. , 1997, “A vortex-based subgrid stress model for large-eddy simulation,” *Physics of Fluids*, Vol 9, No. 8, pp. 2443-2454.

Moin, P. K., Squires, W., Cabot, Lee, S. , 1991, “A dynamic subgrid-scale model for compressible turbulence and scalar transport,” *Physics of Fluids*, A 3, Vol. 11, pp. 2746-2757.

Moore, D. W., and Saffman, P. G. , 1973, “Axial Flow in Laminar Trailing Vortices,” *Proceedings of the Royal Society of London, Series A.*, Vol. 333, pp. 491-508.

Moore D. W., and Saffman P. G. , 1975, “The instability of a straight vortex filament in a strain field,” *Proc. R. Soc. Lond. A*, Vol. 25, pp.346-413

New, T. H., Lim, T. T. & Luo, S. C. , 1999, “On the effects of velocity profiles on the topological structures of a jet in cross flow.”, TSFP-1 Proc, pp. 647–652.

New, T.H., Lim, T.T., and Luo, S.C., 2003, “Elliptic jets in cross-flow,” *Journal of Fluid Mechanics*, Vol. 494, pp. 119-140.

Newman, B. G. , 1959, “Flow in a viscous trailing vortex,” *Aeronautical Quarterly*, pp. 140-160.

Pearcey, H.H. , 1961, "Shock induced separation and its prevention by design and boundary layer control," *Boundary Layer and Flow Control*, Pergamon Press, Oxford.

Perry, A.E., Kelso, R.M., and Lim, T.T. , 1993, "Topological structure of a jet in cross flow," *Computational and Experimental Assessment of Jets in Cross Flow*, number CP-534. AGARD.

Pierrehumbert, R. T. , 1986, "Universal short-wave instability of two-dimensional eddies in an inviscid fluid," *Phys. Rev. Lett.* Vol 57, pp. 2157.

Pope, S. B., 1975, "A more general effective eddy viscosity hypothesis," *Journal of Fluid Mechanics*, Vol. 41, pp. 413-434.

Pope, S. B., 2000, *Turbulent Flows*, Cambridge University Press, United Kingdom.

Prandtl, L., 1925, "Bericht uber Untersuchungen zur ausgebildeten Turbulenz," *ZAMM*, p. 136-139.

Prandtl, L. , 1945, "Ube rein neues formelsystem fur die ausgebildete turbulenz," *Nachr. Akad. Wiss. Gottingen Math. Phys. Kl*, pp. 6-19.

Proctor, F.H. , 1998, "The NASA-Langely Wake vortex Modelling Effort in Support of an Operational Aircraft Spacing System," AIAA Paper 98-0589.

Proudman, I., and Reid, W. H., 1954, "On the decay of a normally distributed and homogeneous turbulent velocity field," *Proc. R. Soc. London. Ser*, Vol. 247, p. 163.

Rixon, G. S., and Johari, H, 2003, "Development of a steady vortex generator jet in a turbulent boundary layer," *Transactions of the ASME*, Vol. 125, pp. 1006 – 1015.

Rogers, M. M., Moin, P., and Reynolds, W. C. , 1986, "The structure and

modelling of the hydrodynamic and passive scalar fields in homogenous turbulent shear flow, Dept. Mech. Engng., Rep. TF-25, Stanford University, Stanford, California.

Rotta, J. C. , 1951, "Statistische theory nichthomogener turbulence," *Z. Phys.*, Vol. 129, pp. 547-572.

Saffman, P. G., 1967, "The large-scale structure of homogeneous turbulence," *Journal of Fluid Mechanics*, Vol. 27, p. 581

Saffman, P. G. 1992 *Vortex Dynamics*. Cambridge University Press.

Sagaut, P. , 2002, *Large Eddy Simulation for Incompressible Flows*, Springer-Verlag Berlin Heidelberg.

Sarkar, S. and Speziale, C. G. , 1990, "A simple nonlinear model for the return to isotropy in turbulence," *Journal of Physics Fluids*, pp. 84-93.

Sarpkaya, T. , 1998, "Decay of Wake Vortices of Large Aircraft," *AIAA Journal*, Vol. 26, No. 9, pp. 1671-1679.

Sarpkaya, T., and Daly, J. J. , 1987, "Effect of Ambient Turbulence on Trailing Vortices," *Journal of Aircraft*, Vol. 24., No. 6, pp. 399-404.

Scorer, R. S. 1958 *Natural Aerodynamics*. Pergamon.

Selby, G., Lin, J.C., and Howard, F.G. , 1992, "Control of low-speed turbulent separated flow using jet vortex generators," *Experiments in Fluids*, Vol 12, pp. 394-400.

Shekarriz, A., Fu, T. C., Katz, J., and Huang, T. T. , 1993, "Near-Field Behaviour of a Tip Vortex," *AIAA Journal*, Vol. 31, No. 1, pp. 112-118.

Shih, T. H., Liou, W. W., Shabbir, A., Yang, Z., and Zhu, J. , 1995, "A new k- ϵ eddy viscosity model for high Reynolds number turbulent flows," *Computers and Fluids*,

Vol. 24, No. 3, pp. 227-238.

Skrbek, L., and Stalp, S. R., 2000, "On the decay of homogeneous isotropic turbulence," *Physics of Fluids*, Vol. 12, No. 8, pp. 1997-2018.

Smagorinsky, J., 1963, "General circulation experiments with the primitive equations, Part I: The basic experiment," *Mon. Wea. Rev.*, Vol 91, p. 99.

So, R.M.C., Ahmed, S.A., Mongia, H.C. , 1984, "An experimental investigation of gas jets in confined swirling air flow," NASA CR 3832.

Spalart, P. R. and Allmaras, S. R. , 1992, "A one-equation turbulence model for aerodynamic flows," *AIAA Paper No. 92-439*.

Spalart, P. R. , 1998, "Airplane trailing vortices," *Annual Review of Fluid Mechanics*, Vol. 30, pp. 107-138.

Spalart, P. R., 2000, "Strategies for Turbulence Modeling and Simulations," *International Journal of Heat and Fluid Flow*, Vol. 21, pp. 252-263.

Speziale, C. G. , Gatski, T. B., and Mac Giolla Mhuiris, N. , 1990, "A critical comparison of turbulence models for homogenous shear flows in a rotating frame," *Physic Fluids*, A 2, p. 1678.

Speziale, C. G., Sarkar, S., and Gatski, T. B. , 1991, "Modelling the pressure-strain correlation of turbulence: an invariant dynamical systems approach," *Journal of Fluid Mechanics.*, Vol 227, pp 245 - 272.

Squire, H. B. , 1960, "Analysis of the vortex breakdown phenomena," *Technical Report Aeronautics Department Report 102*, Imperical College, University of London.

Sutton, O. G. , 1932, "A theory of eddy diffusion in the atmosphere," *Proc. Roy.*

Soc., A(CXXXV) pp. 143-165.

Sykes, R. I., Lewellen, W. S., and Parker, S. F. , 1986, "On the vorticity dynamics of a turbulent jet in a crossflow.," *Journal of Fluid Mechanics*, Vol 168, pp. 393-413.

Talbot, L. , 1954, "Laminar swirling pipe flow," *Journal of Applied Mechanics, Transactions of the ASME*, Vol. 21, pp. 1-7.

Tannehil, J. C., Pletcher, R. H., Anderson, D. A. , 1997, "Computational Fluid Mechanics and Heat Transfer," Taylor and Francis.

Tavoularis, S., and Corrsin, S. , 1981, "Experiments in nearly homogenous turbulent shear flows with a uniform mean temperature gradient," Part 1, *Journal of Fluid Mechanics*, Vol 104, p. 311.

Tennekes H., and Lumley J. L. , 1972, *A First Course in Turbulence*, 1st Edition, The MIT Press.

Thomas, P. J., and Auerbach, D., 1994, "The observation of the simultaneous development of a long- and short-wave instability mode of a vortex pair," *Journal of Fluid Mechanics*, Vol. 265, p. 289

Toy, N., Savory, E., and McCusker, S. , 1993, "The interaction region associated with twin jets and a normal cross-flow." *Computational and Experimental Assessment of Jets in Cross Flow*, number CP-534. AGARD.

Traub, L. W., Mani, S., Galls, S. F., and Rediniotis, O. K. , 1998, "Application of the vortex breakdown phenomenon in the attenuation of trailing vortices," *The Aeronautical Journal*, pp 439 - 444.

Tsai, C.-Y., and Widnall, S. E. , 1976, "The stability of short waves on a straight

vortex filament in a weak externally imposed strain field,” *Journal of Fluid Mechanics*, Vol. 73, pp. 721-733.

Uchida S., Nakamura, Y., and Oshawa, M. , 1985, “Experiments on the axisymmetric vortex breakdown in a swirling air flow,” *Trans. Jpn. Soc. Aero. Sci.*, Vol. 27, pp. 206-216.

Van Driest, E.R. , 1956, “On Turbulent Flow Near a Wall,” *Journal of Aeronautical Sciences*, Vol. 23, pp. 1007-1011.

Von Dyke, M. , 1982, *An Album of Fluid Motion*, Parabolic Press, Stanford, CA.

Vreman, A. W., Geurts, B. J., Kuerten, J. G. M., and Zandbergen, P. J. , 1992, “A finite volume approach to large eddy simulation of compressible, homogeneous, isotropic, decaying turbulence,” *International Journal for Numerical Methods in Fluids*, Vol 15, pp. 799-816.

Wallin, S., and Girimaji, S. S. , 2000, “Evolution of an Isolated Trailing Vortex,” *AIAA Journal*, Vol. 38, No. 4, pp. 657-665.

Wallis, R.A., 1952, “The Use of Air Jets fro Boundary Layer Control,” Tech. Note ARL 110, Australia.

Wallis, R.A., 1956, “A preliminary note on a modified type of air-jet for boundary-layer control,” *ARC, CP-153*, London, UK.

Warming, R., and Hyett, B. , 1974, “The Modified Equation Approach to the Stability and Accuracy of Finite-Difference Methods,” *Journal of Computational Physics*, Vol. 14, pp. 159-179.

Westphal, T. V., and Mehta, R. D. , 1989, “Interaction of an Oscillating Vortex

with a Turbulent Boundary Layer,” *Experiments in Fluids*, Vol. 7, No. 6, pp. 405-411.

Widnall, S. E. , 1972, “The Stability of a Helical Vortex Filament”, *Journal of Fluid Mechanics*, Vol. 54, part 4, pp. 641-663

Widnall, S. E., and Sullivan, J. P. , 1972, “On the Stability of Vortex Rings,” *Proc. Roy. Soc. London*, A332, pp. 335-353.

Widnall, S. E. , 1985, “Review of Three-Dimensional Vortex Dynamic: Implications for the Computation of Separated and Turbulent Flows,” *Proceedings of the Symposium on Vortex Dominated Flows*, Nasa Langley Research Center, Hampton Virginia.

Widnall, S. E., Bliss, D. B., and Tsai, C.-Y. , 1974, “The instability of short waves on a vortex ring,” *Journal of Fluid Mechanics*, Vol. 66 pp. 35-47.

Widnall, S. E., Bliss, D. B. ,1971, “Slender-body analysis of the motion and stability of a vortex filament containing an axial flow,” *Journal of Fluid Mechanics*, Vol. 50, pp.335-353.

Wilcox, D. C, 1998, *Turbulence Modeling for CFD*, Dwc Industries, Inc..

Xia, J.L., and Yadigaroglu, G. , 1998, “Numerical and experimental study of swirling flow in a model combustor,” *International Journal of Heat Mass Transfer*, Vol. 41, No. 11, pp. 1485-1497.

Yang, Z., and Voke, P., 2001, “Large-Eddy Simulation of Boundary-Layer Separation and Transition at a Change of Surface Curvature,” *Journal of Fluid Mechanics*, Vol 493, pp. 305-333.

Yaras, M.I., Grosvenor, A.D. , 2003, "Evaluation of one and two - equation low Re turbulence models. Part I - Axisymmetric separating and swirling flows,"

International Journal for Numerical Methods in Fluids, Vol 42., pp 1293 – 1319.

Yaras, M.I., Grosvenor, A.D. , 2003, "Evaluation of one and two - equation low Re turbulence models. Part II – Vortex-generator jet and diffusing S-duct flows,"

International Journal for Numerical Methods in Fluids, Vol 42., pp 1321 – 1343.

Yaras, M.I. , 2004, "Measurements of Surface-Roughness Effects on the Development of a Vortex Produced by an Inclined-Jet in Cross-Flow," *Journal of Fluids Engineering*, Vol 126, Issue 3, pp. 346-354.

Yuan, L. L. , 1997, "Large eddy simulations of a jet in crossflow." PhD thesis, Department of Mechanical Engineering, Stanford University.

Yuan, L. L. , 1999, Street, T. L., and Ferziger, J. H., "Large eddy simulations of a round jet in crossflow," *Journal of Fluid Mechanics*, Vol. 379, pp. 71-104.

Yin, M., Shi, F., and Xu, Z. , 1996, "Renormalization group based $k - \epsilon$ turbulence model for flows in a duct with strong curvature," *International Journal of Engineering Science*. Vol 34, No 2, pp 243 - 248.

Zaman, K. B. M. Q. & Foss, J. K. , 1997, "The effect of vortex generators on a jet in a cross-flow", *Physics of Fluids*, Vol 9, pp. 106–114.

Zhang, X. , 1993, "Computational analysis of co- and contra-rotating streamwise vortices in a turbulent boundary layer," AIAA Paper no. 93-3035.

Zhang, X., and Collins, M. W., 1993, "Flow and Heat Transfer in a Turbulent Boundary Layer Through Skewed and Pitched Jets," *AIAA Journal*, Vol. 31, No. 9, pp.

1590-1599.

Zhang, X., 1998, "Turbulence Measurements of a Longitudinal Vortex Generated by an Inclined Jet in a Turbulent Boundary Layer," *Journal of Fluids Engineering*, Vol 120, pp. 765-772.

Zhang, X., 2000, "An inclined rectangular jet in a turbulent boundary layer-vortex flow," *Experiments in Fluids*, Vol. 28, pp. 344-354.

Appendices

Appendix A

Vortex Generator Design Specifications

Radius r [m]	r/D_v	Gas Angle α_2 [°]	Blade Angle β_2 [°]	Optimum s/c	Span s [m]	Chord c [m]
0.000	0.00	0.0000	NA	NA	NA	NA
0.005	0.01	3.1111	NA	NA	NA	NA
0.010	0.02	6.0268	7.5376	1.0549	0.006283	0.005956
0.015	0.03	8.5833	10.7295	1.0527	0.009425	0.008953
0.020	0.04	10.6703	13.3310	1.0504	0.012566	0.011963
0.025	0.05	12.2370	15.2808	1.0484	0.015708	0.014983
0.030	0.06	13.2863	16.5850	1.0468	0.018850	0.018006
0.035	0.07	13.8625	17.3005	1.0459	0.021991	0.021026
0.040	0.08	14.0362	17.5162	1.0456	0.025133	0.024036
0.050	0.10	13.5138	16.8675	1.0465	0.031416	0.030021
0.060	0.12	12.3637	15.4384	1.0482	0.037699	0.035966
0.070	0.14	11.0590	13.8149	1.0499	0.043982	0.041890
0.080	0.16	9.8482	12.3067	1.0514	0.050265	0.047808
0.090	0.18	8.8141	11.0173	1.0525	0.056549	0.053727
0.100	0.20	7.9551	9.9455	1.0533	0.062832	0.059650
0.110	0.22	7.2422	9.0556	1.0540	0.069115	0.065576
0.120	0.24	6.6447	8.3095	1.0544	0.075398	0.071505
0.130	0.26	6.1377	7.6761	1.0548	0.081681	0.077437
0.140	0.28	5.7023	7.1321	1.0551	0.087965	0.083370
0.150	0.30	5.3244	6.6598	1.0553	0.094248	0.089305
0.160	0.32	4.9934	6.2460	1.0555	0.100531	0.095241
0.170	0.34	4.7010	5.8805	1.0557	0.106814	0.101178
0.180	0.36	4.4409	5.5554	1.0558	0.113097	0.107116
0.190	0.38	4.2080	5.2642	1.0560	0.119381	0.113054
0.200	0.40	3.9983	5.0020	1.0561	0.125664	0.118993
0.210	0.42	3.8085	4.7646	1.0561	0.131947	0.124933
0.220	0.44	3.6359	4.5487	1.0562	0.138230	0.130873
0.230	0.46	3.4782	4.3515	1.0563	0.144513	0.136813
0.240	0.48	3.3336	4.1707	1.0563	0.150796	0.142754
0.250	0.50	3.2005	4.0042	1.0564	0.157080	0.148695

Table A.1: Vortex generator design specifications

Appendix B

3D Isometric View of Vortex Generator (using BladeGen)

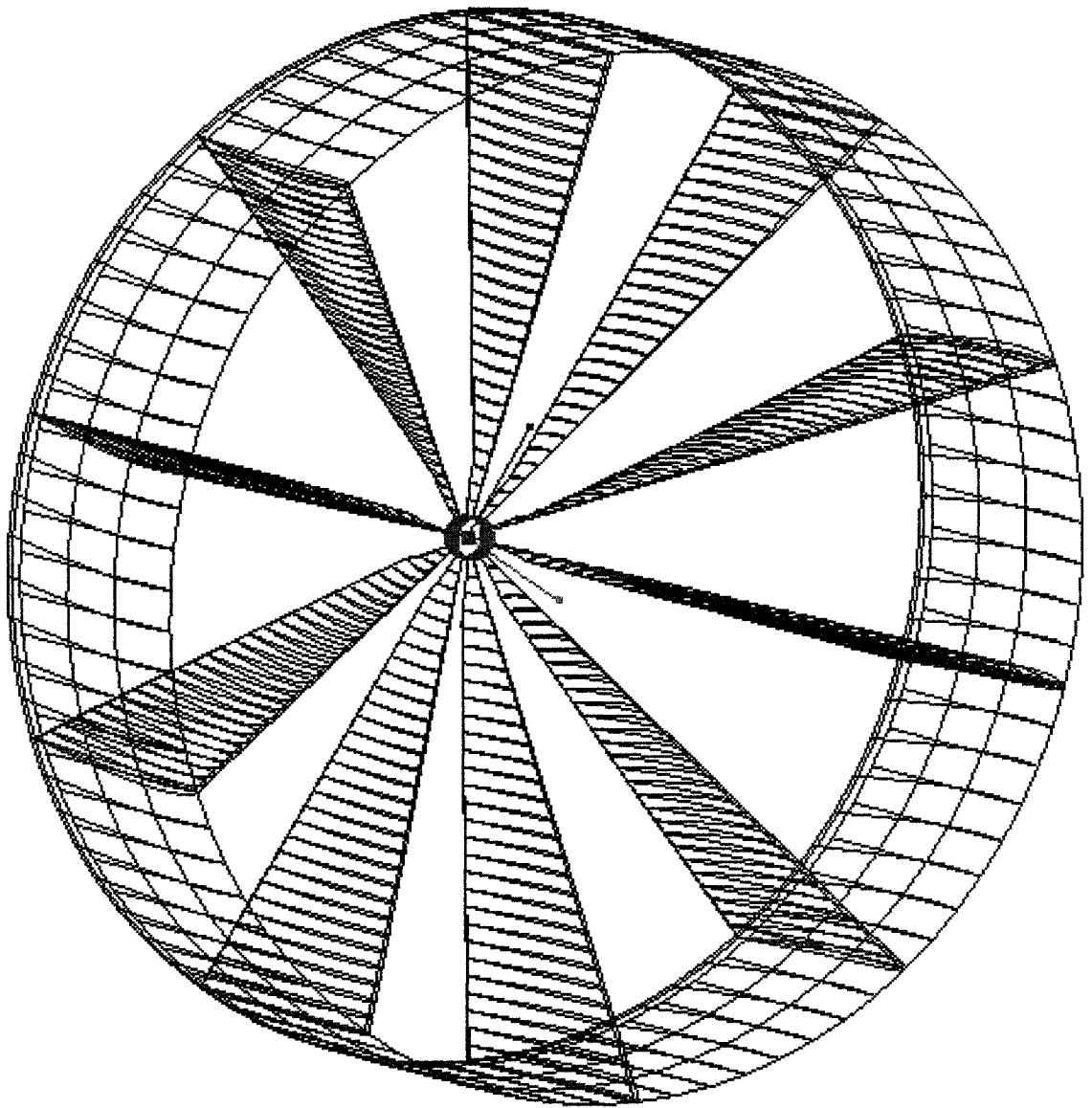


Figure B.1: 3D isometric view of vortex generator

Appendix C

Monitor Point Generation Program (Matlab)

%Generates a text file used as a CFX CCL file in defining monitor points

%GENERAL INFORMATION

%GRID IS YMIN < Y < YMAX
%GRID IS ZMIN < Z < ZMAX
%THERE IS A TOTAL OF JMAX+1 NODES IN THE Y DIRECTION
%THERE IS A TOTAL OF KMAX+1 NODES IN THE Z DIRECTION
%CARTESIAN COORDINATES IN X,Y,Z
%J=0 CORRESPONDS TO Y=YMIN
%J=JMAX CORRESPONDS TO Y=YMAX
%K=0 CORRESPONDS TO Z=ZMIN
%K=KMAX CORRESPONDS TO Z=ZMAX

%FORMAT OF CCL FILE

% MONITOR POINT: PointP
% Cartesian Coordinates = X [m], Y [m], Z [m]
% Option = Cartesian Coordinates
% Output Variables List = Velocity v
% END

%CLEARING ALL MEMORY AND SCREEN

clc
clear all

%DEFINING VARIABLES

X = 1.058;
Q = 0;
YMIN = 0.00674;
YMAX = 0.14326;
ZMIN = -0.14652;
ZMAX = 0.12652;
JMAX = 24;
KMAX = 49;

```

%CALCULATED VARIABLES

DY = (YMAX-YMIN)/JMAX;
DZ = (ZMAX-ZMIN)/KMAX;
QMAX = KMAX*JMAX;

%ALGORITHM

%SETTING ZEROS

%CALCULATING X AND Y COORDINATES

for K = 1:KMAX,
    for J = 1:JMAX,
        Q = Q+1;
        YCORD(Q) = J*DY+YMIN;
        ZCORD(Q) = K*DZ+ZMIN;
    end
end

%OUTPUT TO TEXT FILE

fid = fopen('MONITORPOINTCCL_10.txt','w');
for Q = 1:QMAX,
    fprintf(fid, 'MONITOR POINT: SPoint%G',Q);
    fprintf(fid, '\n Cartesian Coordinates = %G [m], %G [m], %G
[m]',X,YCORD(Q),ZCORD(Q));
    fprintf(fid, '\n Option = Cartesian Coordinates');
    fprintf(fid, '\n Output Variables List = Velocity v');
    fprintf(fid, '\nEND\n');
end

for Q = 1:QMAX,
    QNAME = Q+QMAX;
    fprintf(fid, 'MONITOR POINT: SPoint%G',QNAME);
    fprintf(fid, '\n Cartesian Coordinates = %G [m], %G [m], %G
[m]',X,YCORD(Q),ZCORD(Q));
    fprintf(fid, '\n Option = Cartesian Coordinates');
    fprintf(fid, '\n Output Variables List = Velocity w');
    fprintf(fid, '\nEND\n');
end
fclose(fid);

```

Appendix D

LES Inclined Jet Data Reduction Program (Matlab)

% Takes output data from CFX specified by the Monitor program in Appendix C and
% puts it into a 4 columns (x, y, Vx, Vy). Data is averaged over several periods of
% time and written to corresponding folders

```
clear all  
clc
```

%READING IN THE CFX OUTPUT TXT FILE

```
CFX= csvread('FINALJICF_LES_1Cs_Hires_0to2683_noheader.txt');
```

%SETTING THE TOTAL AMOUNT OF TIMESTEPS IN ABOVE FILE

```
timestepmax = 2683; %set a variable (MODIFY THIS NUMBER)
```

%NUMBER OF MONITOR POINTS AND CONTROLLING THE OUTPUT

```
N=1176  
outputcontrol = [1 1 1 1 1 1 1];
```

%ARRANGING DATA FOR TECPLOT

%DEFINING VARIABLES

```
X = 1.058;  
QQ = 0;
```

```
YMIN = 0.00674;  
YMAX = 0.14326;  
ZMIN = -0.14652;  
ZMAX = 0.12652;
```

```
JMAX = 24;  
KMAX = 49;
```

%CALCULATED VARIABLES

```
DY = (YMAX-YMIN)/JMAX;
```

```
DZ = (ZMAX-ZMIN)/KMAX;
QQMAX = KMAX*JMAX;
```

```
%ALGORITHM
```

```
%CALCULATING X AND Y COORDINATES
```

```
for K = 1:KMAX,
  for J = 1:JMAX,
    QQ = QQ+1;
    YCORD(QQ) = J*DY+YMIN;
    ZCORD(QQ) = K*DZ+ZMIN;
  end
end
```

```
for w=1:timestepmax
  for v=1:QQMAX
    YS=R(v);
    ps=v+1;
    pss=v+1+QQMAX;

    F(w,v,2)=YCORD(YS);
    F(w,v,1)=ZCORD(YS);
    F(w,v,4)=CFX(w,ps);
    F(w,v,3)=CFX(w,pss);
  end
end
```

```
%WRITING FILES FOR TECPLOT
```

```
dt=0.00075;
maxf=1/dt;
```

```
%1 TIMESTEP PER FILE
```

```
if outputcontrol(1)==1
  for w = 1:timestepmax
    number = num2str(w,'%4i');
    name = 'timeavg_';
    timea = 1;
    timeavg = num2str(timea);
```

```

extension = '.txt';
timest = '_timestep_';
directory = 'files\1\';
filename = [directory name timeavg timest number extension];

fid = fopen(filename,'w');

for v = 1:QQMAX
    fprintf(fid, '%G, %G, %G, %G\n',F(w,v,1), F(w,v,2), F(w,v,3), F(w,v,4));
end

fclose(fid);
end

FT=0; %average velocity v
for i = 1:QQMAX %average velocity v
    FT = F(w,v,4)+FT; %average velocity v
end %average velocity v

clc
'FINISHED WRITNG 1 TIMESTEP PER FILE'
end

%5 TIMESTEP PER FILE
if outputcontrol(2)==1
numtime = 5;
tmax = floor(timestepmax/numtime);
    w=0;

for z = 1:tmax
    F_5(z,v,3)=0;
    F_5(z,v,4)=0;
end

for z = 1:tmax
    for k=1:numtime
        w=w+1;
        for v=1:QQMAX
            F_5(z,v,3)=F_5(z,v,3)+F(w,v,3)/numtime;
            F_5(z,v,4)=F_5(z,v,4)+F(w,v,4)/numtime;
        end
    end
end
end
end

```

```

for z = 1:tmax
    number = num2str(z,'%4i');
    directory = 'files\5\';
    name = 'timeavg_';
    timea = 5;
    timeavg = num2str(timea);
    extension = '.txt';
    timest = '_timestep_';
    filename = [directory name timeavg timest number extension];

    fid = fopen(filename,'w');

    for v = 1:QQMAX
        fprintf(fid, '%G, %G, %G, %G\n',F(z,v,1), F(z,v,2), F_5(z,v,3), F_5(z,v,4));
    end

    fclose(fid);
end

clc
'FINISHED WRITNG 5 TIMESTEPS PER FILE'

    %500 TIMESTEP PER FILE
if outputcontrol(7)==1
    numtime = 500;
    tmax = floor(timestepmax/numtime);
        w=0;

    for z = 1:tmax
        F_500(z,v,3)=0;
        F_500(z,v,4)=0;
    end

    for z = 1:tmax
        for k=1:numtime
            w=w+1;
            for v=1:QQMAX
                F_500(z,v,3)=F_500(z,v,3)+F(w,v,3)/numtime;
                F_500(z,v,4)=F_500(z,v,4)+F(w,v,4)/numtime;
            end
        end
    end
end

for z = 1:tmax

```

```
number = num2str(z, '%.4i');
directory = 'files\500\';
name = 'timeavg_';
timea = numtime;
timeavg = num2str(timea);
extension = '.txt';
timest = '_timestep_';
filename = [directory name timeavg timest number extension];

fid = fopen(filename, 'w');

for v = 1:QQMAX
    fprintf(fid, '%G, %G, %G, %G\n', F(z,v,1), F(z,v,2), F_500(z,v,3),
F_500(z,v,4));
end

fclose(fid);
end
end
clc
```

Appendix E Simulation Fact Sheet

Benchmark	Confined Swirling Flow (k-e)	Confined Swirling Flow (R-S)	Decay of Turbulence	Inclined Jet in Cross-Flow (R-S)	Inclined Jet in Cross-Flow (LES)	Vortex Generator
Turbulence Model	<i>RANS k-e</i>	<i>RANS SSG-Reynolds-Stress</i>	<i>LES Smagorinsky</i>	<i>RANS ω-Reynolds-Stress</i>	<i>LES Smagorinsky</i>	<i>LES Smagorinsky</i>
Simulation Type	Steady State	Steady State	Transient	Steady State	Transient	Transient
Domain Dimensions [m]	D = 0.125, Dj = 0.00873, L=45Dj	D = 0.125, Dj = 0.00873, L=45Dj	Lref = 0.55	Dj = 0.068, L = 21Dj, W = 6Dj, H = 4.5Dj	Dj = 0.068, L = 21Dj, W = 6Dj, H = 4.5Dj	Dv = 0.5, rc = 0.04, L = 2.5
Reynolds Number	164000	164000	33867	40800	40800	41909
Characteristic Velocity [m/s]	19.8	19.8	10	9	9	8.1
Number of Nodes	144659	62000	32768	400000	600000	600000
Grid Spacing (Δ) [m]	0.0025	0.0015625	0.0171875	0.004-0.027	0.008	0.008-0.02
Kolmogorov Scale (h) [m]	1.53383E-05	1.53383E-05	0.000429688	2.32558E-05	2.32558E-05	0.000571429
Δ/h	162.9907213	101.8692008	40	666.5	344	293
Number of Time-Steps (N_s)	400	3000	1000-10000	1000	3000	1000
Time-Step Size [s]	0.001	0.001	0.0007-0.04	0.001	0.0005	0.001
Courant Number (u)	7.92	12.672	0.009-0.5	0.45	0.45-0.09	0.58
Run Time [hrs]	12	72	12	168	336	168
Realization Time (T) [s]	0.019840909	0.019840909	2.5	0.158	0.158	0.3049
Advection Scheme	Upwind/HighResolution	HighResolution	Central Difference	HighResolution	Central Difference/HighResolution	Central Differencing
Convergence Criteria	1.00E-07	1.00E-06	1.00E-04	1.00E-06	1.00E-06	1.00E-06
Inlet Boundary	Ut (cloud), Ux(cloud), k(cloud)	Ut (cloud), Ux(cloud), k(cloud)	None	Ut (cloud), Ux(cloud), Tu(cloud)	Ut (cloud), Ux(cloud), Tu(cloud)	Ut (cloud), Ux(8.12 m/s), Tu(cloud)
Outlet Boundary	Pressure = 0kPa	Pressure = 0kPa	None	Pressure = 0kPa	Pressure = 0kPa	Pressure = 0kPa
Wall Boundary	No-Slip	No-slip	None	No-Slip/Free-Slip	No-Slip/Free-Slip	No-Slip/Free-Slip
Periodic Boundary	None	1 periodic pair	3 periodic pairs	None	None	None

Table E.1: Simulation fact sheet

Appendix F

Practical Issues in Turbulence Modelling

The numerical investigations presented in this thesis highlight the importance of turbulence modelling in computational fluid dynamics. Information pertaining to numerical stability, computational cost, and solution accuracy of *LES*- and *RANS*-based computations is summarized. Based upon the experience gained from this study, the future role of *LES* in academic and industrial settings is then discussed.

F.1 Numerical Stability

The complexity of the flow, choice of turbulence model, spatial resolution, temporal resolution, and discretization all affect the numerical stability of an algorithm. Table F.1.1 shows the relative complexity for each of the benchmarks in this thesis.

Simulation Name	Type	Turbulence Model	Complexity
Confined Swirling Flow	<i>RANS</i>	Two-equation	Medium
Confined Swirling Flow	<i>RANS</i>	Reynolds-stress	High
Isotropic Decay of Turbulence	<i>LES</i>	Smagorinsky	Low
Inclined Jet in Cross-Flow	<i>RANS</i>	Reynolds-stress	High
Inclined Jet in Cross-Flow	<i>LES</i>	Smagorinsky	High
Vortex Generator	<i>LES</i>	Smagorinsky	Medium

Table F.1.1 Simulation complexity

The boundary conditions of the computation were the most significant factor in determining the complexity of the flow. Essentially, if the spatial gradients of velocity, pressure, and turbulence are high, the flow is considered to be more complex. Examples include the high spatial gradients near the jet inflow boundary of the inclined jet in cross-flow, high spatial gradients of the non-linear region of the vortex generator, and high spatial gradients near the wall boundary in the confined swirling flow benchmark. Furthermore, if the boundary conditions describe an unstable flow configuration, then the flow is considered to be more complex. In contrast, low swirl associated with the vortex-generator flow allowed the vortex to maintain its structure and avoid flow reversal. Finally, the amount of unsteadiness in the flow determines its complexity. For the inclined jet in cross-flow, the nature of the flow led to vortex wandering, thus increasing its complexity.

The choice of turbulence model was another important factor in determining numerical stability. For the confined swirling flow study, *RANS* simulations with two-equation turbulence models converged at much faster rates than with a differential Reynolds-stress model, and was stable on much coarser grids. The inclined jet in cross-flow was the only study to directly compare a *RANS* simulation to *LES*. Due to the unsteady nature of the flow, the Reynolds-stress model was subjected to numerical instability that *LES* was able to avoid.

To combat numerical instability, a combination of techniques was employed. It was found that each technique either increased computational time, increased

computational resources, or increased numerical error. For the *RANS* simulations used in the confined swirling flow study and inclined jet in cross-flow study, refining both spatial and temporal resolutions were needed to improve numerical stability. In addition, the size of the computational domain was increased to decrease spatial gradients near the outflow boundaries. Both of these techniques increased computational time and computational resources significantly. The Courant number, which determines the stable ratio of temporal and spatial resolutions, was a determining factor in the decay of isotropic turbulence. The Courant number needed to be decreased below a value of $\nu = 0.5$ for the simulation to become stable. For the inclined jet in cross-flow using *LES*, the choice of advection scheme greatly affected simulation results. The high-resolution scheme that implicitly introduces an artificial viscosity in the simulation was needed in order to arrive at a converged solution. Unfortunately, this blend of first and second order accurate schemes introduces a numerical truncation error that does not exist with the second order accurate central differencing scheme.

F.2 Computational Cost and Solution Accuracy

Issues such as computational cost and solution accuracy need to be considered in addition to numerical stability. Table F.2.1 shows the relationship between computational cost and solution accuracy for the simulations investigated.

Simulation	Type	Turbulence Model	Cost (hrs)	Accuracy
Confined Swirling Flow	<i>RANS</i>	Two-equation	12	Low
Confined Swirling Flow	<i>RANS</i>	Reynolds-stress	72	Medium
Isotropic Decay of Turbulence	<i>LES</i>	Smagorinsky	12	High
Inclined Jet in Cross-Flow	<i>RANS</i>	Reynolds-stress	168	Medium
Inclined Jet in Cross-Flow	<i>LES</i>	Smagorinsky	336	High
Vortex Generator	<i>LES</i>	Smagorinsky	168	High

Table F.2.1: Computational cost and solution accuracy

As expected, the computational cost of two-equation *RANS* models, differential Reynolds-stress *RANS* models, and large eddy simulations were extremely different. From Table F.2.1, it is obvious that improved solution accuracy is obtained at a high computational price. For example, the investigation of the decay of confined swirling flow shows that the more accurate Reynolds-stress model requires approximately 6 times more computational time than the two-equation model.

Although it might be surprising that the computational requirements for the decay of isotropic turbulence were comparatively small since *LES* was used, the flow was characterized as being relatively simple (Table F.2.1). It should be noted that the author is not implying that the decay of isotropic turbulence is an easy problem, but that the absence of a mean flow, pressure gradient, or wall boundaries simplified defining the problem in *CFX*. The calibration of Smagorinsky's model for the decay of turbulence allowed a relatively small computational grid of 32^3 nodes to be used. This spatial resolution was approximately 20 times less than that for the confined swirling flow benchmark and 40 times less than that of the inclined jet in cross-flow benchmark.

Smagorinsky's sub-grid model was ideal for this type of flow and accurate results were achieved with a relatively small computational cost.

For wall-bounded flows (i.e. inclined jet in cross-flow and confined swirling flow), the computational time required was an order of magnitude larger than the *RANS* simulations. These flows are quite complex and available computational resources were insufficient to obtain more accurate solutions. The *LES* inclined jet in cross-flow was designated as being more accurate than the *RANS* simulation since the latter was unable to capture the transient motion of the dominant vortex.

The relatively low computational requirements for the vortex generator flow are due to the absence of no-slip wall boundaries. The simulations for this flow are quite stable and meet time-step convergence criteria after only a few time-steps. The spatial resolution requirement near the vortex core is the main source of computational cost for this flow. This *LES* solution is considered accurate since spatial and temporal resolutions are consistent with simulations used throughout the entire work and in literature.

F.3 The Future of *LES* in Vortical Flow Predictions

The numerical simulations conducted in this study demonstrate the need for an appropriate turbulence model selection. Obviously, this type of decision is based upon the application. The use of robust *RANS* type turbulence models is appropriate for early design calculations where computational speed is the primary goal. Unfortunately, for many *RANS* simulations, including the confined swirling flow benchmark, the addition of

extra computational power will not improve accuracy as the solution was independent of temporal and spatial resolutions. This is not the case with *LES*. The main advantage of *LES* is that the solution can be improved until its accuracy is comparable to that of *DNS*. However, there are two main problems when using *LES* as a design tool.

The most obvious problem is the computational cost of using *LES*. Fortunately, this problem is decreasing as computer technology improves. As technology continues to improve, the majority of engineering problems at high Reynolds number will be solved with the use of *LES*. Until this time arrives, *LES* is restricted to low Reynolds-number flows, or requires allocating large amounts of turbulence to the sub-grid model. This is the second major problem of *LES*. When large amounts of energy are allocated to the sub-grid model, similar issues seen in *RANS* simulations begin to surface. For instance, even the simplest of sub-grid models require calibration of constants. The Smagorinsky model uses a constant that is not only dependent on flow conditions ($C_s = 0.18$ for isotropic decay of turbulence, $C_s = 0.1$ for channel flow), it is grid dependent. However, it was found in the isotropic decay benchmark that the model was insensitive to convergence criteria, grid structure, and initial conditions. When applied to the inclined jet in cross flow, the model was quite sensitive to each of these conditions. This type of performance is very inconsistent. The use of more complicated models requires yet more computational power, and relies more on empirical constants. The use of coarse spatial and temporal resolutions in *LES* also leads to numerical instabilities.

For the purpose of fundamental research, the choice to use *LES* over *RANS* simulations is clearer. In an academic setting, solution accuracy is a high priority, and

the simplicity of *LES* assures the user that most of the turbulence is predicted directly from the Navier-Stokes equations. In the author's opinion, *LES* will continue to be used in academic settings until computational resources allow for *DNS* to become a replacement.

A few helpful tips have been compiled to assist the newcomer to *CFD* who wishes to use *CFX* as their algorithm. Although online tutorials and the user manual are sufficient to start a numerical problem, there are situations when further assistance is needed.

G.1 Getting Technical Help

After completely reading the user manual, there are times when help professional technical help with *CFX* is needed. Technical support over the telephone was extremely frustrating and inefficient in solving problems. During the beginning stages of the thesis, the technical support staff became irritated with questions regarding simulation setup. The author found that for more than 50% of the time that *CFX* was contacted using the telephone, there was simply no technical support available. In addition, contact by email typically took more than one week to receive a response to questions. During later stages of the thesis, it was found that the technical support available through telephone and email were unable to answer any questions. Although it may seem that *CFX's* technical support through the telephone is quite poor, at least for academic users, two online sites have proved to be quite useful and efficient. The online community site at:

<http://www-waterloo.ansys.com/cfx/community/default.asp>

took approximately 2-5 days to receive a response. The best site for user support is:

<http://www.cfd-online.com/Forum/cfx.cgi>

where responses typically take from 1-3 days. The author has received a satisfactory answer for each of the many questions posted on this online forum. Since questions can be answered by both *CFX* moderators and *CFX* clients, responses are quick.

G.2 Turbulence Intensity at Boundaries for *LES*

Through the benchmark studies and from technical support from *CFX*, turbulence boundary conditions for *LES* perform poorly. Specifically, simulations have shown to be insensitive to the level of turbulence intensity specified at the inflow boundary. Although a list of advantages and disadvantages of *LES* are listed in the user manual, information pertaining to turbulence boundary conditions has been omitted. To counter this problem the author is aware of two solutions. First, by placing inflow boundaries far away from the area of interest, turbulence is able to develop naturally. Unfortunately, this results in high computing times. The inflow boundary allows for time varying functions to be specified for velocity, where turbulence can be simulated. A function simulating turbulence is not available in *CFX* and the user would have to manually configure this if this option is to be used.

G.3 Conservative and Hybrid Values Near Boundaries

In the event that the user wants to double check that *CFX* is correctly imposing distributions of velocity, turbulence, etc., near boundaries it is important to specify either a conservative or hybrid option. The hybrid option, which is the default, will give the value of the first node away from the boundary. If the node distribution near the inflow boundary is adequate, hybrid values should be equal to conservative values. Conservative values correspond to what was specified in *CFX Pre*. If there are large spatial gradients near the inflow boundary, e.g. recirculation zone, then there will be noticeable differences between conservative and hybrid values.

G.4 Output Control Options

CFX allows the user to output specified variables at nodes corresponding to either the entire domain or individual points at specified time intervals. If the user wishes to output variables over a two-dimensional plane inside the domain, this option is not available. Large amounts hard-disk space are needed if data corresponding to the entire domain is outputted frequently. A more practical option is for the user to monitor a series of points that correspond to discrete locations over the desired plane. Essentially, a cloud of points is specified and the user is required reassemble these points in a program external to *CFX* (Appendices C-D).

Statistical quantities of turbulence such as Reynolds-stresses are automatically calculated when using *LES*. To avoid unrealistic flow statistics during the initialization process (first 100 time-steps), *CFX* has an option to delay the computation of these statistics. Based upon experience and online *CFX* support, *CFX* does not allow for the option to start, stop, and then restart calculation of these statistics. If the user believes that there is some low frequency unsteadiness in the flow that is not considered to be turbulence, it is not possible to calculate turbulence statistics over multiple ranges simply by specifying these ranges in the output control box in *CFX Pre*.

G.5 CFX on Linux Workstations

It is strongly recommended to run *CFX* simulations on Linux workstations. If many runs are required and need to be monitored remotely, Linux provides the best platform. To free memory for the simulation, it is recommended to stop monitoring the simulation after execution. In contrast to Windows, the user is able to log out of the workstation and allow other users to log in, all while the simulation is running in the background. To run these simulations remotely, a shell script needs to be written in order to execute the *CFX* solver:

```
#!/bin/sh  
  
/usr/local/cfx56/bin/cfx5solve -def [filename]  
  
done
```

Appendix H

Numerical Truncation Error

The numerical truncation error of an algorithm can be separated into dissipation and dispersion errors. Dispersion errors are common in second order accurate schemes and cause ‘wiggles’ in places of high gradients. For first order schemes, dissipation errors dominate and cause smearing or smoothing in places of high gradients. Dissipation is the direct result of even derivative terms in the truncation error and dispersion is the direct result of odd derivatives in the truncation error. Figure G.1 shows the effects of numerical dissipation and dispersion on a step function.

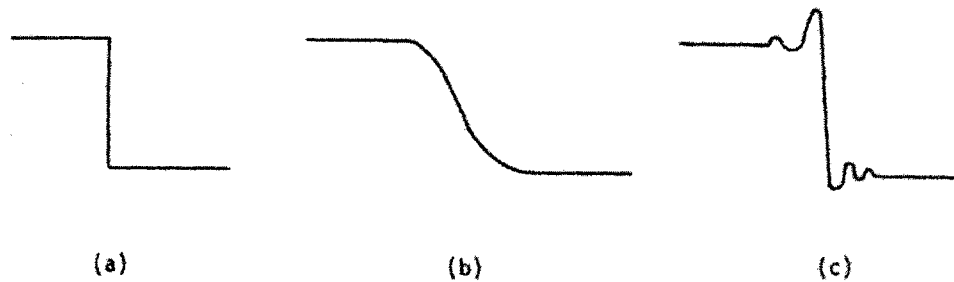


Figure H.1: Effects of dissipation and dispersion. (a) exact solution, (b) dissipation error, (c) dispersion error, reproduced Tannehill (1997)

A more in depth analysis of dispersion and dissipation errors can be carried out by analyzing the modified equation. The modified equation is the partial differential equation which is actually solved when a finite difference method is applied to a partial differential equation (Warming and Hyett, 1974). It allows for a rigorous analysis of the truncation error, in which dispersive and diffusive errors are identified. Information

available through the user manual for *CFX 5.7* has revealed that the recommended time discretization scheme is second order backward implicit Euler and the space discretization scheme is central differencing. Unfortunately, due to the proprietary reasons, more information about the discretization schemes could not be determined. Therefore, a scheme will be analyzed that solves a partial differential equation similar to the Navier-Stokes equation. The one-dimensional-viscous-burgers-equation is considered to be adequate for this analysis:

$$\frac{\partial u}{\partial t} + A \frac{\partial u}{\partial x} = \mu \frac{\partial^2 u}{\partial x^2} \quad (\text{H.1})$$

where $A=c$ and $A=u$ for the linear and non-linear case respectively. The Leap Frog/DuFort-Frankel Method is a scheme that solves a linearized version of the viscous burgers equation:

$$\frac{u_j^{n+1} - u_j^{n-1}}{2\Delta t} + A_j^n \frac{u_{j+1}^n - u_{j-1}^n}{2\Delta x} = \mu \frac{u_{j+1}^n - u_j^{n+1} - u_j^{n-1} + u_{j-1}^n}{(\Delta x)^2} \quad (\text{H.2})$$

The modified equation associated with this scheme is written as:

$$u_t + cu_x = \underbrace{\mu(1-\nu^2)}_{\text{dominant term}} u_{xx} + \left[\frac{2\mu^2 c (\Delta t)^2}{(\Delta x)^2} - \frac{1}{6} c (\Delta x)^2 + \frac{1}{6} c^3 (\Delta t)^2 - \frac{2\mu^2 c^3 (\Delta t)^4}{(\Delta x)^4} \right] u_{xxx} + \dots \quad (\text{H.3})$$

where $u_x = \frac{\partial u}{\partial x}$ and $\nu = c \frac{\Delta t}{\Delta x}$. From the modified equation it can be determined that this scheme has a truncation error of $O[(\Delta t / \Delta x)^2, (\Delta t)^2, (\Delta x)^2]$, which is similar to the truncation error of the *CFX* algorithm. However, from the user manual in *CFX 5.7*, it

was assured that the truncation error associated with the *CFX* discretization scheme used in the present simulations had no cross-terms such as $(\Delta t / \Delta x)^2$.

The dominant term in Eqn. H.3 is considered to be a dissipation error as it includes the even derivative u_{xx} . However, the effects of the dominant term can be reduced and even disappear if the molecular viscosity is set to $\mu = 0$ or if the Courant number is set to $\nu = 1$. If this is the case, the second term in the modified equation that includes an odd derivative u_{xxx} will be the leading contributor to the total truncation error. It should be noted the dispersive term in Eqn. H.3 is also dependent on molecular viscosity, making it difficult to quantify each type of truncation error.